Mineral Magnetism of Environmental Reference Materials: Iron Oxyhydroxide Nanoparticles

by

Fedora González-Lucena

A thesis submitted to the Faculty of Graduate and Postdoctoral Studies, University of Ottawa,

in partial fulfillment of the requirements for the degree of Ph.D. in Earth Sciences

Ottawa-Carleton Geoscience Centre

and

University of Ottawa

Ottawa, Canada

Dedicada a mi querida abuela, Elba Vidarte

[Dedicated to my beloved grandmother, Elba Vidarte]

Abstract

Iron oxyhydroxides are ubiquitous in surface environments, playing a key role in many biogeochemical processes. Their characterization is made challenging by their nanophase nature. Magnetometry serves as a sensitive non-destructive characterization technique that can elucidate intrinsic physical properties, taking advantage of the superparamagnetic behaviour that nanoparticles may exhibit. In this work, synthetic analogues of common iron oxyhydroxide minerals (ferrihydrite, goethite, lepidocrocite, schwertmannite and akaganéite) are characterized using DC and AC magnetometry (cryogenic, room temperature), along with complementary analyses from Mössbauer spectroscopy (cryogenic, room temperature), powder X-ray diffraction and scanning electron microscopy. It was found that all of the iron oxyhydroxide mineral nanoparticles, including lepidocrocite, schwertmannite and akaganéite were superparamagnetic and therefore magnetically ordered at room temperature. Previous estimates of Néel temperatures for these three minerals are relatively low and are understood as misinterpreted magnetic blocking temperatures. This has important implications in environmental geoscience due to this mineral group's potential as magnetic remanence carriers. Analysis of the data enabled the extraction of the intrinsic physical parameters of the nanoparticles, including magnetic sizes. The study also showed the possible effect on these parameters of crystal-chemical variations, due to elemental structural incorporation, providing a nanoscale mineralogical characterization of these iron oxyhydroxides. The analysis of the intrinsic parameters showed that all of the iron oxyhydroxide mineral nanoparticles considered here have a common magnetic moment formation mechanism associated with a random spatial distribution of uncompensated magnetic spins, and with different degrees of structural disorder and compositional stoichiometry variability, which give rise to relatively large intrinsic magnetization values. The elucidation of the magnetic nanostructure also contributes to the study of the surface region of the nanoparticles, which affects the particles’ reactivity in the environment.

Résumé

Les oxyhydroxydes de fer sont des composants communs des environnements de surfaces où ils jouent un rôle important dans les cycles biogéochimiques. Leur caractérisation est toutefois difficile car ils sont souvent présents sous forme de nano particules. La magnétométrie est une technique très sensible qui ne détruit pas les échantillons. Elle permet d'élucider les propriétés intrinsèques physiques, car elle prend en compte le comportement super paramagnétique des minéraux. Dans cette étude, des composés analogues synthétiques d'oxyhydroxydes de fer (ferrihydrite, goethite, lépidocrocite, schwertmannite et akaganéite) ont été caractérisés en utilisant la magnétométrie DC et AC (cryogénique et à la température de la pièce), la spectroscopie Mössbauer (cryogénique et à la température de la pièce), ainsi que la diffraction X et la microscopie à balayage. Les résultats ont démontré que les nano particules d'oxyhydroxydes de fer, incluant la lépidocrocite, la schwertmannite et l'akaganéite, étaient super paramagnétiques et ordonnées magnétiquement à la température de la pièce. Les basses températures de Néel de ces minéraux sont donc expliquées par une mauvaise interprétation des températures de blocage du moment magnétique. Ces résultats ont des répercussions importantes dans le domaine des géosciences environnementales car certains oxyhydroxydes de fer peuvent donc garder leur rémanence magnétique. Les analyses complémentaires de ces résultats ont aussi permis d'extraire les paramètres physiques intrinsèques des nano particules, dont la taille. La présente étude a aussi démontré l'effet de ces paramètres de variation chimique des cristaux causés par l'incorporation structurale d'éléments, permettant ainsi une caractérisation minéralogique des oxyhydroxydes de fer à l'échelle du nanomètre. L'analyse des paramètres intrinsèques a indiqué que tous les

oxyhydroxydes de fer analysés dans cette étude ont un mécanisme de formation de moment magnétique commun, lequel est associé à la distribution spatiale aléatoire des spins magnétiques non-compensés, ainsi qu’à différents niveaux de désordre structural et chimique, lesquels produisent des valeurs de magnétisation intrinsèques relativement élevées. Une meilleure compréhension des nano structures magnétiques permet aussi une meilleure étude de la surface réactive des nano particules, laquelle affecte la réactivité des particules dans l’environnement.

Resumen

Los oxihidróxidos de hierro son minerales comunes que tienen un rol esencial en muchos procesos biogeoquímicos en ambientes de la superficie terrestre. La naturaleza nanométrica de estos minerales usualmente dificulta su caracterización mineralógica. La magnetometría es una técnica de caracterización sensible y no destructiva que puede proveer propiedades físicas intrínsecas de este tipo de materiales, tomando en cuenta su comportamiento superparamagnético. En este trabajo, análogos sintéticos de minerales de oxihidróxidos de hierro comunes (ferrihidrita, goetita, lepidocrocita, schwertmannita y akaganeíta) son caracterizados utilizando magnetometría AC y DC (criogénica y a temperatura ambiente) y análisis complementarios de espectroscopía Mössbauer (criogénica y a temperatura ambiente), difracción de rayos-X y microscopía electrónica de escaneo. Los resultados demuestran que todas las nano-partículas minerales de oxihidróxidos de hierro, incluyendo la lepidocrocita, schwertmannita y akaganeíta, son superparamagnéticas y por lo tanto, presentan orden magnético a temperatura ambiente. Las bajas temperaturas de Néel previamente asociadas a estos minerales se explican como una interpretación errada de temperaturas de bloqueo magnético. Estos resultados tienen implicaciones importantes dentro de las geociencias ambientales debido al potencial que estos minerales tienen de ser portadores de remanencia magnética. El análisis complementario de los datos permitió la extracción de parámetros intrínsecos de las nano-partículas, incluyendo tamaños (magnéticos) de las mismas. Este estudio también demuestra el efecto que tienen las variaciones cristalo-químicas, asociadas a la incorporación estructural de elementos, en estos parámetros, proporcionando de esta manera, una caracterización mineralógica a escala nanométrica de estos oxihidróxidos de hierro. El análisis de los parámetros intrínsecos demuestra que todas las nano-partículas minerales de oxihidróxidos de hierro consideradas en este trabajo, poseen un mecanismo común del origen del momento magnético en la partícula, asociado a la presencia de espines magnéticos no compensados, distribuidos en una forma aleatoria dentro del volumen, y a diferentes grados de desorden estructural y químico, lo cual origina valores de magnetización intrínseca relativamente grandes. El estudio de la nano-estructura magnética también contribuye al estudio de la región superficial de las nano-partículas, la cual afecta la reactividad de las mismas en el ambiente.

Statement of Authorship

I, the undersigned, hereby declare that I am the sole author of this thesis, having performed all experimental work, analyses, interpretation and writing. The work contributed by other persons has been fully acknowledged within the text of the thesis. The thesis does not contain material published elsewhere or previously submitted for any other degree at this or any other university.

……………………………………………………………………………

Fedora González-Lucena

Ottawa, April 26, 2010

Table of Contents

List of Tables

List of Figures

List of Symbols, Acronyms and Abbreviations

μ	Intrinsic magnetic moment of the superparamagnetic particle
$<\mu>$	Equilibrium thermal average magnetic moment of the superparamagnetic particle
μ'	Number of magnetic ions (Fe^{3+}) contributing to net moment of the superparamagnetic sample
$\{\mu\}$	Average magnetic moment of the superparamagnetic particle
μ_B	Bohr Magneton: 9.274×10^{-24} Am^2
$\{\mu\}/\{m\}$	Intrinsic magnetization of the superparamagnetic particle
μ'/n	Percentage of magnetic ions in the superparamagnetic particle that are contributing to the net moment
θ	Diffraction angle (in X-ray diffraction)
ρ	Density of the mineral
τ	Relaxation time (of the superparamagnetic particle)
τ_0	Pre-factor in Néel-Brown expression
φ	Phase shift of the susceptibility relative to the drive field (AC-magnetometry)

χ	(Mass) Magnetic susceptibility
χ'	In-phase component of the susceptibility
χ''	Out-of-phase component of the susceptibility
A	Pre-factor in $\mu' \propto n^{\alpha}$ relationship
AC	Alternating current
Akg	Akaganéite
A_r	Atomic weight of Fe: 55.85 g/mol
B_1	Intercept used in the "x >> 1" magnetic analysis method
B_2	Slope used in the "x >> 1" magnetic analysis method
BET	Brunauer-Emmett-Teller (surface area measurements)
C	Curie-Weiss constant
C_1	Intercept used in "x < 1" magnetic analysis method
C_2	Magnitude of the slope used in the "x < 1" magnetic analysis method
CANMET	Canada Centre for Mineral and Energy Technology
d	Diameter
DC	Direct current
EDS	Energy-dispersive X-ray spectroscopy

FC	Field-cooled (curve)
f_{Fe}	Iron fraction
FWHM	Full width at half maximum
g	Landé g-factor
Gt	Goethite
H	Applied magnetic field
HFO	Hydrous ferric oxide
H_{max}	Maximum magnetic field applied (in a field cycle)
J	Atomic total angular momentum quantum number
JCPDS	Joint Committee on Powder Diffraction Standards
K	Magnetic anisotropy energy constant per unit volume
k_B	Boltzmann constant: 1.3807×10^{-23} J/K
L	Coherence length (of the diffracting domain in X-ray diffraction)
Lp	Lepidocrocite
M	(Mass) Magnetization or Molar (molarity unit)
m	Mass of the superparamagnetic particle
{m}	Average mass of the superparamagnetic particle

M_{max}	Maximum value of magnetization reached in a field cycle
MMSL	Mining and Mineral Sciences Laboratories
MPMS	Magnetic Property Measurement System
MPS	Morpholinopropane sulfonic acid
M_W	Molecular weight
N	Number of magnetic cations (Fe^{3+}) per unit mass of sample
n	Number of magnetic ions (Fe^{3+}) in the superparamagnetic particle
N_A	Avogadro’s number (6.022×10^{23})
N/A	Not applicable
PDF	Powder Diffraction File
pXRD	Powder X-ray diffraction/diffractogram
S	Atomic spin quantum number
SEM	Scanning electron microscopy
SQUID	Superconducting quantum interference device (magnetometer)
Sw	Schwertmannite
T	Temperature
T_{CW}	Curie-Weiss temperature

TEM	Transmission electron microscopy
T_N	Néel temperature
V	Volume
VSM	Vibrating sample magnetometer
wt %	Weight percentage
XRF	X-ray fluorescence
x	Argument of the Langevin function, $x = \mu H/k_B T$
ZFC	Zero field-cooled (curve)
2L-Fh	Two-line ferrihydrite
4L-Fh	Four-line ferrihydrite
6L-Fh	Six-line ferrihydrite
#Fe	Number of Fe in nominal chemical formula

Chapter 1

1.1 Introduction

Iron oxyhydroxides are ubiquitous minerals in a wide range of natural environments, including rocks, sediments, soils and natural waters (e.g., Thompson, 1986). They also occur on the surface of Mars (Morris et al., 2000), as alteration products in meteorites (Jambor and Dutrizac, 1998; Pedersen, 1999), in acid mine drainage sites (Murad and Rojík, 2005) and even in many types of organisms, including mammals, as the core of the iron-storage protein ferritin (Webb et al., 1996).

In near-surface or surface environments, the iron cycle is coupled to other main elemental cycles, such as the oxygen and phosphorous cycles (e.g., Dutkiewicz et al., 2005; Hochella et al., 2008). The latter and the fact that iron oxyhydroxides usually occur as nanoparticles with a high specific surface area, makes them reactive phases playing a key role in biogeochemical reactions (e.g., Fortin and Langley, 2005; Waychunas et al., 2005). For instance, the bioavailability of phosphorous in natural waters can be limited by the precipitation of iron oxyhydroxide nanoparticles (e.g., Hochella et al., 2008), such as colloidal phosphate-bearing hydrous ferric oxides (HFO) (e.g., Buffle et al., 1989; Fox, 1989; Föllmi, 1996; Rose et al., 1996).

Iron oxyhydroxides have a high sorptive capacity and a high affinity for organic, radioactive and metal contaminants, adsorbing and sequestering them, therefore determining their fate and bioavailability. This attribute makes iron oxyhydroxides useful materials in environmental remediation technologies (e.g., Cundy et al., 2008). For example, uranium can be adsorbed onto ferrihydrite ($5Fe_2O_3 \cdot 9H_2O$) and subsequently be immobilized in a stable phase when the ferrihydrite transforms to nanoparticles of hematite (α-Fe_2O_3) or goethite (α-

FeOOH), providing long term storage for low concentrations of uranium (Murakami et al. 2005). In addition, adsorbents containing akaganéite (β-FeOOH) have been shown to remove arsenic from groundwater (Guo and Chen, 2005).

Considering the relevance that iron oxyhydroxides have in biogeochemical systems, it is imperative to study these mineral nanoparticles in order to elucidate their physical properties. This is fundamental for their accurate detection and quantification and subsequent understanding of their behaviour in the environment. In particular, environmental magnetic studies, rely on the measured magnetic signal of surface samples to determine the type of magnetic mineral present, domain state, particle size and concentration (e.g., Peters and Dekkers, 2003), all of which are affected by variations in environmental conditions. The characterization of iron oxyhydroxide nanoparticles is pertinent not only within the environmental geosciences and nanogeosciences but also in other fields, such as corrosion science, materials science (e.g., pigments characterization) and applied technology (e.g, nanotechnology).

Magnetometry can serve as a useful non-destructive tool for the nanoscale characterization of iron oxyhydroxide mineral nanoparticles, since it is sensitive to the arrangement of the Fe^{3+} cations within the nanoparticles and therefore to any chemical and/or structural variation within the latter. Particularly, the nanophase nature of these minerals does not pose a challenge or add complexity to the magnetic analysis. In fact, magnetic nanoparticles can exhibit a particular magnetic behaviour i.e., superparamagnetism, for which direct analysis can provide intrinsic physical properties of these materials (González-Lucena et al., 2004).

The present work constitutes a mineral magnetic study of the common iron oxyhydroxides: goethite, akaganéite, lepidocrocite, schwertmannite, ferrihydrite and phosphate-bearing hydrous ferric oxides, using complementary analysis of powder X-ray diffraction, Mössbauer spectroscopy and electron microscopy. The structure of the present work is organized as follows: the following section (Section 1.2) discusses the fundamental magnetic concepts used in this study; whereas Section 1.3 and 1.4 provide a literature review of iron oxyhydroxides and their magnetic properties and the objectives of the present work, respectively. Chapter 2 explains the different experimental characterization methods used and the magnetic analysis methods. Chapter 3 presents the results and analysis of the data for each mineral group and Chapter 4 provides an integrated discussion for all of the samples, after which the conclusions are presented.

1.2 Magnetic Principles

1.2.1 Antiferromagnetism

The magnetic properties of minerals are determined by the content of magnetic atoms, the arrangement of these within the crystalline structure and the interactions between them. The magnetic interaction or magnetic exchange coupling is an interdependence of the electrostatic energies of the magnetic moments that creates an effect on the relative directions of the magnetic moments, thereby creating a magnetic structure (Ashcroft and Mermin, 1976). In iron oxyhydroxides, the Fe^{3+} cations, which have a spin magnetic moment, are coupled magnetically through a superexchange mechanism, whereby the exchange coupling is achieved through the non-magnetic ions, i.e., O^{2-} and OH^{-}, forming an antiferromagnetic structure in which the spins are ordered in an antiparallel fashion (Cornell and Schwertmann, 2003).

Antiferromagnetic materials have a magnetic ordering temperature, called the Néel temperature (T_N) , above which the material behaves as a paramagnet. The magnitude of the Néel temperature is a measure of the strength of the magnetic interactions in the material. Above the Néel temperature, the magnetic moment vector of each magnetic atom averages zero, due to the fact that the magnetic interactions are overcome by the thermal energy. The magnetic behaviour of the material follows the Curie-Weiss law (Morrish, 1965):

$$\chi = \frac{C}{T - T_{CW}} \tag{1.1}$$

$$C = \frac{Ng^2 \mu_B{}^2 J(J+1)}{3k_B} \tag{1.2}$$

where:

χ is the (mass) magnetic susceptibility

T is the temperature

T_{CW} is the Curie-Weiss temperature (< 0, for antiferromagnets)

N is the number of magnetic cations (Fe^{3+}) per unit mass of sample

g is the Landé g-factor (= 2, for Fe^{3+} cations)

μ_B is the Bohr magneton

J is the atomic total angular momentum quantum number (equal to the spin number S = 5/2, for Fe^{3+} cations)

k_B is the Boltzmann constant

For the simple case of two antiparallel sublattices in a body-centered cubic (bcc) lattice and a rutile-type structure, the molecular field theory predicts a $|T_{CW}|:T_N$ ratio between 1 and 3. For the case of a face-centered cubic (fcc) lattice with a more complex magnetic structure (four simple cubic lattices), this ratio is predicted to be between 1 and 5 (Morrish, 1965), These ratio values have been confirmed by experimental studies for a variety of antiferromagnetic compounds (e.g., Lidiard, 1954; Morrish, 1965; De Jongh and Miedema, 1974). The difference between $|T_{CW}|$ and T_N is related to the presence of contributions of antiferromagnetic interactions with next-nearest neighbours as opposed to antiferromagnetic interactions exclusively with nearest neighbours, which represents the case where $|T_{CW}| = T_N$.

Ideally, a perfect antiferromagnetic single-domain mineral particle will have the same number of spins in each of the antiparallel sublattices, causing every spin to compensate with another one that is in the opposite direction. However, the presence of crystalline defects can disrupt this “perfect” compensation and therefore create a net magnetic moment of the particle due to the contribution of the uncompensated spins in the magnetic structure. This is especially true for nanoparticles, which, among other things, have a considerable proportion of atoms at or near the surface, where uncompensation of spins can occur (e.g., Waychunas and Zhang, 2008).

In the absence of any other external force (e.g., applied magnetic field, thermal energy), the direction of the net magnetic moment of the particle is determined by the magnetic anisotropy energy. For antiferromagnetic nanoparticles, the main contribution to this energy is the magnetocrystalline anisotropy, which is the effect of the arrangement of ions within the crystalline structure (Bocquet et al., 1995). Additionally, for very small nanoparticles (< 4 - 5 nm), the surface anisotropy is also a relevant contribution to the total magnetic anisotropy energy (Dormann et al., 1997).

1.2.2 Superparamagnetism

Due to the small size of nanoparticles, the thermal energy can overcome the magnetic anisotropy energy barrier of the magnetic moment of the particle. In this condition, the direction of the moment of the particle becomes unstable and fluctuates in a similar way to the case of a paramagnet but with a moment magnitude that can be much bigger than that of a single atom. This phenomenon is called superparamagnetism.

In this thermally activated state, the average time between reversals of the direction of the magnetic moment, called the relaxation time (τ), is given by the Néel – Brown expression (e.g., Morup and Hansen., 2007):

$$\tau = \tau_0 \exp\left(\frac{KV}{k_B T}\right) \tag{1.3}$$

where:

τ_0 is a pre-factor that typically ranges between 10^{-12} and 10^{-13} s (Dormann et al., 1997)

K is the magnetic anisotropy energy constant per unit volume of the material

V is the particle volume

Based on Equation 1.3, for a given particle volume, the relaxation time becomes longer at lower temperatures. The temperature below which there are no more fluctuations (on the time scale of the measurement) when the particle is magnetically blocked, due to the lower thermal energy, is called the blocking temperature. A distribution of particle volumes therefore has an associated distribution of magnetic blocking temperatures.

The magnetization (M) of a superparamagnetic material follows Langevin behaviour and is represented as (e.g., Morup and Hansen, 2007):

$$M = \frac{N}{n}\mu L\left(\frac{\mu H}{k_B T}\right) \qquad (1.4)$$

where:

$L(x) = \coth(x) - 1/x$, is the Langevin function with $x = \mu H/k_B T$

μ is the magnetic moment of the superparamagnetic particle

n is the number of magnetic ions (Fe^{3+}) in the superparamagnetic particle

H is the applied magnetic field

The magnetic moment μ is determined by the number of magnetic cations whose moments are not compensated within the antiferromagnetic structure of the particle (μ’). For Fe^{3+} cations, which have an individual magnetic moment of $5\mu_B$ (e.g., Ashcroft and Mermin, 1976), μ is equal to $\mu' \times 5\mu_B$.

Appendix A shows simulations of the field-dependent behaviour of the magnetization, along with curvature graphs (explained in Section 2.6.2), for a FeOOH superparamagnetic sample based on a simple moment formation mechanism where μ' is linearly proportional to n (where $100 \leq n \leq 10{,}000$) with a proportionality factor (A) varying from 0.01 to 0.1:

$$\mu' = A\, n \tag{1.5}$$

Figures A.1 and A.2 show the increase in both M values and curvature with larger n (i.e., particle size) and μ', at a given temperature. For a given particle size, an increasing trend for both M and the curvature is also seen for decreasing temperatures in Figures A.3 and A.4.

In field-dependent magnetic measurements or field cycles, magnetic blocking of a superparamagnetic particle system is evidenced by the appearance of a hysteresis in the measurements done at lower temperatures, which represents the presence of both magnetic coercivity and remanence. In temperature-dependent measurements performed on a zero-field cooled (ZFC) sample, the blocking phenomenon is evidenced as a maximum or a peak in the curve. When the sample is cooled down to low temperatures (e.g., liquid helium temperature) in zero field, the moment direction of all of the particles in the sample becomes blocked or fixed at random directions. When a constant external magnetic field is applied while increasing the temperature, the measured moment increases due to the gradual alignment of the blocked magnetic moments with the applied field up to a maximum at the blocking temperature, above which the thermal energy overcomes the tendency of alignment with the applied field causing a continuous decrease in the measured magnetic moment. In temperature cycles, the ZFC curve and the field-cooled (FC) curve diverge or show hysteresis below the blocking temperature (e.g., Zhang, 2006).

In principle, the temperature associated with the maximum in the temperature runs is the blocking temperature and as expected from Equation 1.3, smaller particles have a lower blocking temperature than larger particles. The latter has been found experimentally for antiferromagnetic nanoparticles such as ferrihydrites (e.g., Duarte et al., 2006). However, the peak in the temperature curve can be shifted to lower or higher temperature values depending on the magnitude of the constant applied field, the time scale of the measurement (i.e., characteristic measurement time), and the presence of inter-particle interactions. Additionally, the peak broadening and the overall intensity of the trends in the temperature curves can also be affected by the magnitude of the applied field and the temperature sweep rate. For instance, small kinks in the FC curve near the blocking temperature, associated with a quench effect, can be noticeable or not depending on the latter parameters (Zhang, 2006).

A useful tool for exploring relaxation effects in nanoparticles is AC magnetometry. In this technique, the magnetic moment is measured while a small alternating drive field is applied. The frequency of the alternating field can be varied providing a way to vary the characteristic measurement time and looking at the effect on the magnitude of the measured moment (e.g., Thompson, 1986). During the magnetic blocking process, the relaxation time associated with the superparamagnetic fluctuations increases; this involves dissipation of energy since there is loss of energy as there are fewer fluctuations over time. This situation may cause a decrease in the magnitude of the measured quantity for higher operating frequencies since the magnetization of the particle lags behind the drive field creating a phase shift and an out-of-phase contribution of the measured quantity. Therefore AC-temperature runs for a superparamagnetic material will show a maximum associated with magnetic blocking and frequency-dependence of the measured quantity near the blocking temperature (e.g., Morup and Hansen, 2007).

1.3 Literature Review

1.3.1 Crystalline and Magnetic Structure of the Iron Oxyhydroxides

The building structural unit of the iron oxyhydroxides is the $Fe(O,OH)_6$ octahedron (Figure 1.1). The octahedra can be linked by their corners, edges or faces and the different structures consist of a structural array of one or more type of these octahedra linkages (Cornell and Schwertmann, 2003).

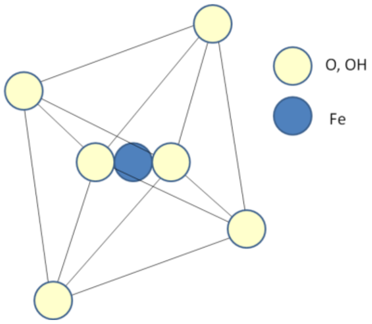

Figure 1.1 Schematic representation of the $Fe(O,OH)_6$ octahedron

Goethite is orthorhombic with space group Pnma. In this structure, double chains (parallel to [010]) of edge-sharing octahedra are linked by their corners forming an alternating sequence of chains with vacant and filled octahedra sites as depicted in Figure 1.2. The magnetic structure of goethite is antiferromagnetic with spins aligned along the [010] direction (e.g., Szytula et al., 1968); the latter being also the direction of elongation of the particles (Coey et al., 1995).

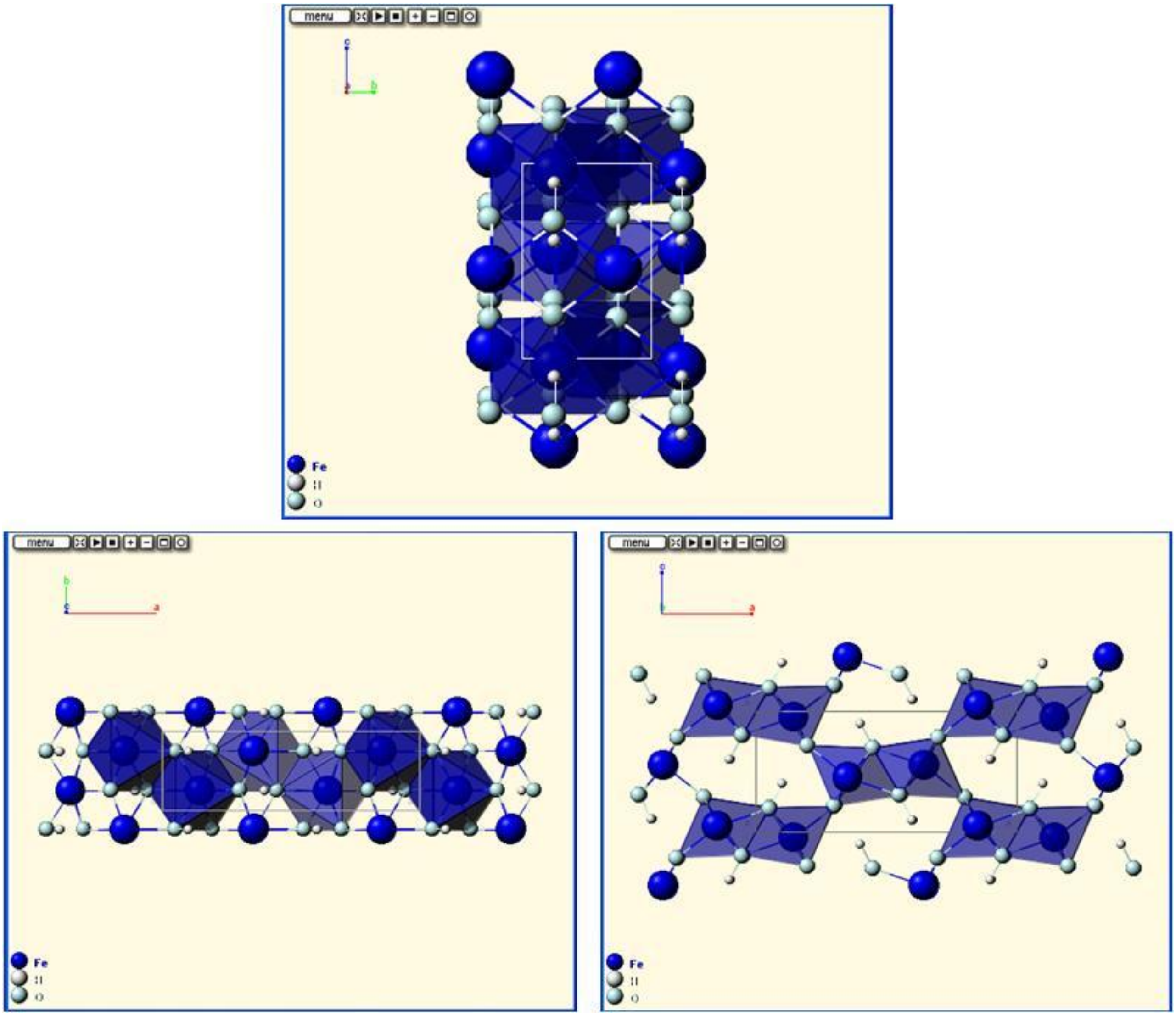

Figure 1.2 Crystallographic structure of goethite viewed from the three different axes (Gualtieri and Venturelli, 1999; modified from webmineral.com)

The crystal structure of ferrihydrite has been an issue of debate for many years (e.g., Towe and Bradley, 1967; Eggleton and Fitzpatrick, 1988; Drits et al., 1993; Jansen et al., 2002). Even the most recently proposed structure (Michel et al., 2007a) has been a source of further debate (Rancourt and Meunier, 2008; Carta et al., 2009; Manceau et al., 2009). However, most studies agree on a trigonal/hexagonal crystal system (e.g., Jansen et al., 2002; Michel et al., 2007a). The phase structure of ferrihydrite has also been a source of debate; both multi-phase (e.g., Drits et al., 1993; Janney et al., 2000) and single-phase structures have been proposed (Michel et al., 2007b, 2010). In addition, there is no consensus on whether the Fe is only in octahedral coordination (e.g., Pankhurst and Pollard, 1992; Pan et al., 2006) or in both tetrahedral and octahedral coordination (e.g., Michel et al., 2007a, 2010). It is also the case for the compositional stoichiometry representing the relative amounts of Fe, O/OH and structural water which has not been resolved. However, one of the commonly referred nominal formulas is $5Fe_2O_3 \cdot 9H_2O$ (e.g., Jambor and Dutrizac, 1998). The magnetic structure of ferrihydrite was thought to be speromagnetic, having non-collinear spins with random orientation (Coey and Readman, 1973). However, more recent Mössbauer and neutron diffraction studies have shown the collinearity of the spins in an antiferromagnetic structure (e.g., Pollard and Pankhurst, 1992; Jansen et al., 2002).

Lepidocrocite is orthorhombic with space group Bbmm. The crystal structure consists of corrugated layers made up of edge-sharing double chains of octahedra, which also share edges with the other double chains in the layer. The layers are parallel to the (100) plane and the double chains follow the [010] direction (Figure 1.3). These layers are held together by a network of hydrogen bonds (Cornell and Schwertmann, 2003). The preferential direction of growth of lepidocrocite particles is along the [001] direction (Manceau et al., 2000). In terms of its magnetic structure, an antiferromagnetic arrangement with spins aligned along the [001] direction has been established for lepidocrocite based on Mössbauer and neutron diffraction studies (Johnson, 1969; Olés et al., 1970).

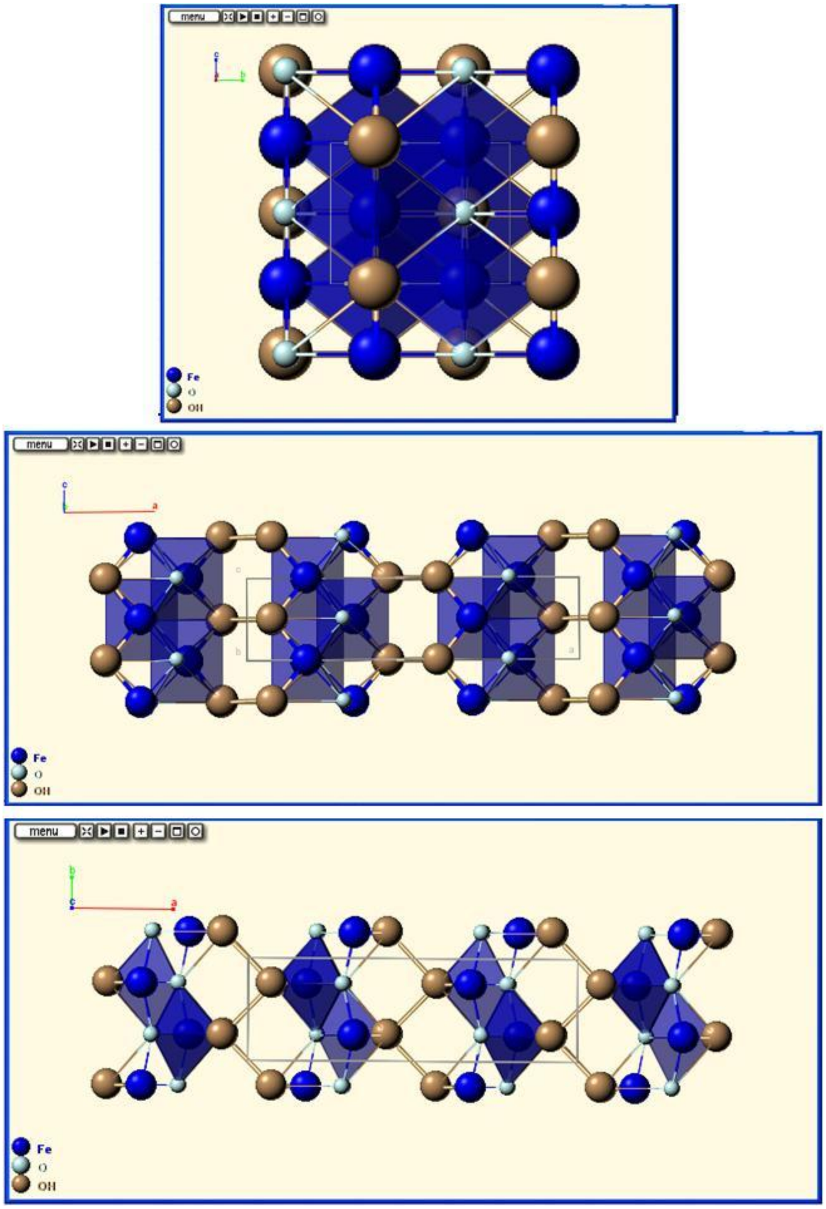

Figure 1.3 Crystallographic structure of lepidocrocite viewed from the three different axes (Wyckoff, 1963; modified from webmineral.com)

Akaganéite can have a tetragonal or monoclinic crystal structure with space groups I4/m and I2/m, respectively (e.g., Mackay, 1960; García et al., 2004). Figure 1.4 depicts the monoclinic structure showing edge-sharing double chains of octahedra along the [010] direction linked by their corners forming a tunnel-like structure with a chloride anion in the interior. The magnetic structure is antiferromagnetic with spins aligned along the [010] direction. The spin ordering is layered, i.e., within the layers, the moments are coupled ferromagnetically and there is antiferromagnetic coupling between the layers (Yamamoto et al., 1968; Szytula et al., 1970; Vlasov et al., 1974). The [010] is also the direction of elongation of the particles (e.g., Gallagher, 1970).

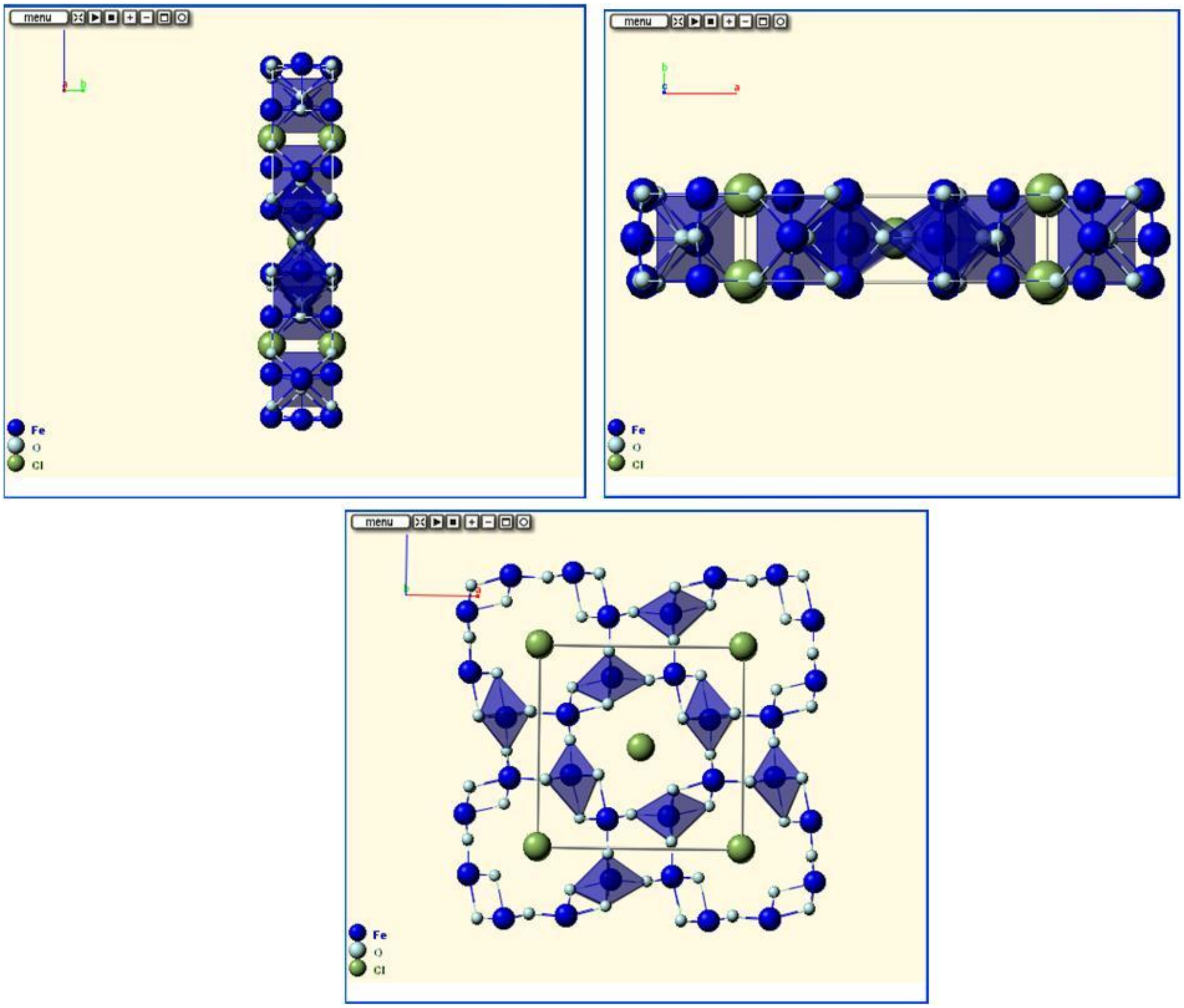

Figure 1.4 Crystallographic structure of akaganéite viewed from the three different axes (Post et al., 2003; modified from webmineral.com)

The crystal structure of schwertmannite has been the subject of debate. Bigham et al. (1994) proposed a structure analogous to that of akaganéite but with sulphate anions in the tunnel sites, instead of the chloride anions. Loan et al. (2004) indicated that the schwertmannite structure is not analogous to that of akaganéite. Their electron nanodiffraction studies showed that akaganéite is a multi-phase structure consisting of a dense core and radiating whiskers; the latter having a structure similar to that of ferrihydrite. Thus far, the magnetic structure of schwertmannite has not been studied in detail; only Mössbauer studies have shown the magnetically blocked and non-blocked state with temperature; these will be discussed in the following section (Section 1.3.2).

The variety and complexity of the crystallographic structures of the iron oxyhydroxides, along with their variable water content and their nanophase nature makes them complex mineral phases. This complexity extends to the extraction of accurate thermodynamic data and stability fields. The stability of these minerals at the nanoscale is directly related to their particle size and degree of hydration. Particularly, small particles with large surface areas have higher degrees of hydration, especially at their surface, lowering their free energy and increasing their stability (Navrotsky et al., 2008).

1.3.2 Magnetic Ordering Temperatures

Table 1.1 shows the magnetic ordering temperatures for all of the iron oxides and iron oxyhydroxides. Most of these temperatures are relatively high, suggesting fairly strong magnetic exchange coupling in these minerals (Section 1.2.1). Lepidocrocite, schwertmannite and akaganéite stand out due to their relatively low Néel temperatures. These low Néel temperatures are not representative of the strong antiferromagnetic exchange coupling found for lepidocrocite and akaganéite, along with goethite, as supported by applied-field Mössbauer spectroscopy studies (Pollard et al., 1992). A similar strength of the magnetic exchange coupling for these three minerals is in agreement with the fact that they share similar Fe-Fe distances and inter-octahedral angles (Manceau and Combs, 1988).

The low Néel temperature of lepidocrocite has been linked to its characteristic layer-like crystalline structure and the associated weak interlayer bonding, which would account for the weak magnetic exchange mechanism (Johnson, 1969). However, Weckler and Lutz (1998) have found that the interlayer hydrogen bonding in lepidocrocite is a strong one, even stronger than the hydrogen bonding present in both goethite and akaganéite. Additionally, the layer-like nature of the crystal structure does not necessarily imply a low magnetic ordering temperature since, for instance, the layered iron oxyhydroxides (feroxyhyte and the related synthetic form δ-FeOOH) have high magnetic ordering temperatures (Table 1.1.; Cornell and Schwertmann, 2003).

Tables 1.2, 1.3 and 1.4 show the claimed Néel temperatures for lepidocrocite, schwertmannite and akaganéite, respectively, based on the commonly used magnetic and Mössbauer studies. The features used to claim the Néel temperatures for both experimental techniques are not exclusively associated with magnetic ordering phenomena. For instance, the presence of a doublet in the Mössbauer spectra, indicating an unblocked magnetic state, which is also associated with a decrease in the absorption of gamma-rays in the sample, can be due to either paramagnetism or superparamagnetism (e.g., Rancourt, 1998). In addition, the development of a sextet in the spectra on applying a magnetic field can be hindered by either phenomenon (Afanas’ev and Chuev, 2003; Madsen et al., 2009), whereas the maxima in the magnetic susceptibility data can also be due to either phenomenon (Morrish, 1965; Section 1.2.2).

Table 1.1 Magnetic ordering temperatures (Néel and Curie) of the iron oxides and iron oxyhydroxides

Mineral	Nominal Formula	Néel / Curie Temperature (K)	Reference
Goethite	α-FeOOH	350-400	Szytula et al. (1968); Forsyth et al. (1968); Vlasov et al. (1974)
Feroxyhyte	δ'-FeOOH	440-460	Cornell and Schwertmann (2003)
Hematite	α-Fe_2O_3	956	Cornell and Schwertmann (2003)
Magnetite	Fe_3O_4	850	Cornell and Schwertmann (2003)
Maghemite	γ-Fe_2O_3	820-986	Cornell and Schwertmann (2003)
Ferrihydrite	$5Fe_2O_3 \cdot 9H_2O$	330-500	Seehra et al. (2000); Jansen et al. (2002); Punnoose et al. (2004); Guyodo et al. (2006)
Lepidocrocite	γ-FeOOH	(44-77)	(See Table 1.2)
Schwertmannite	$Fe_8O_8(OH)_6(SO_4)$	(70-80)	(See Table 1.3)
Akaganéite	β-FeOOH	(15 –300)	(See Table 1.4)

Table 1.2 Previously claimed Néel temperatures (T_N) for lepidocrocite

Claimed T_N (K)	**Reference**	**Technique**	**Main feature(s) used to claim T_N**
~50	Yamamoto (1968)	AC susceptibility; Mössbauer spectroscopy	Small broad peak in susceptibility. Sextet at 4.2 K and doublet at 77 K.
73	Johnson (1969)	Mössbauer spectroscopy	Gradual transition from doublet to sextet on decreasing the temperature.
50 (5)	Olés et al. (1970)	Susceptibility; Mössbauer spectroscopy	Sudden drop of susceptibility at 50 K on increasing the temperature. Doublet above 77 K.
~50 – 77 (1)	Murad and Schwertmann (1984)	Mössbauer spectroscopy	Gradual transition from doublet to sextet on decreasing the temperature. Gamma-ray transmission at zero source velocity drops on increasing the temperature.
60 (5)	De Grave et al. (1986)	Mössbauer spectroscopy	Gradual transition from doublet to sextet on decreasing the temperature. Gamma-ray transmission at zero source velocity at 0 T and 4 T drops on increasing the temperature. At 180 K, a field of 6 T splits the spectrum into a triplet instead of a sextet.
~44-~50	De Grave et al. (1996)	Mössbauer spectroscopy	Gamma-ray transmission at zero source velocity drops on increasing the temperature.
~52	Hirt et al. (2002)	AC susceptibility	Peak in the in-phase susceptibility.
53	Lee et al. (2004)	Magnetometry	Maximum in the zero-field-cooled curve.

Table 1.3 Previously claimed Néel temperatures (T_N) for schwertmannite

Claimed T_N (K)	**Reference**	**Technique**	**Main feature (s) used to claim T_N**
75	Bigham et al. (1990)	Mössbauer spectroscopy	Gradual transition from doublet to sextet on decreasing the temperature. Above 77 K, a field of 6 T did not split the spectrum into a sextet.
75	Murad et al. (1990) Bigham et al. (1994)	Mössbauer spectroscopy	Gradual transition from doublet to sextet on decreasing the temperature.
70 – 80	Eneroth and Koch (2004)	Mössbauer spectroscopy	Gradual transition from doublet to sextet on decreasing the temperature.

Table 1.4 Previous claims of Néel temperature (T_N) for akaganéite

Claimed T_N (K)	**Reference**	**Technique**	**Main feature(s) used to claim T_N**
295 (4)	Dészi et al. (1967)	Mössbauer spectroscopy	Gradual transition from doublet to sextet on decreasing the temperature.
~285	Kulgawczuk et al. (1968)	Susceptibility	Weak peak in susceptibility.
273	Yamamoto (1968)	Mössbauer spectroscopy	Transition from doublet to sextet on decreasing the temperature.
296 (5)	Hogg et al. (1975)	Mössbauer spectroscopy	Gradual transition from doublet to sextet on decreasing the temperature.
295	Murad (1979)	Mössbauer spectroscopy	Sextet below 295 K
~250 – 299 (3)	Chambaere and De Grave (1984)	Mössbauer spectroscopy	Gamma-ray transmission at zero source velocity drops on increasing the temperature. At 278 K, a field of up to 6 T splits the spectrum into a triplet instead of a sextet.
15 - 25	Zhang et al. (2006)	Magnetometry	Kinks near the blocking temperature in the field-cooled curve. Curie-Weiss law fit with T_{CW} = +7 K

The ambiguousness between superparamagnetism (which implies magnetic order in the material) and paramagnetism (which implies lack of this magnetic order) can be resolved using neutron diffraction. A strong antiferromagnetic exchange coupling was found for lepidocrocite based on neutron diffraction studies at 4.2 K and 77 K (Olés et al., 1970), but the magnetic structure at higher temperatures has yet to be probed. For akaganéite, the magnetic reflections in the neutron diffractograms at 77 K and 300 K are superposed with nuclear reflections (Szytula et al., 1970; Vlasov et al., 1974), which makes it hard to interpret the absence of a magnetic reflection, upon increasing the temperature, since these two contributions have not been resolved and separated. Additionally, the presence of hydrogen in the sample contributes to a fairly high background signal (e.g., Szytula et al., 1970) that can mask the presence of small magnetic contributions at 300 K.

Heat capacity measurements (from 4.2 K to 390 K) for lepidocrocite do not show any sharp anomaly (Majzlan et al., 2003), usually associated with a magnetic ordering transition (e.g., De Jongh and Miedema, 1974). Majzlan et al. (2003) showed that there is a broad anomaly at ~ 68 K, which they associated with the previous claims of Néel temperature, suggesting that it represents the magnetic ordering of lepidocrocite. However, broad anomalies in heat capacity measurements have been associated with the magnetic blocking of superparamagnetic particles due to the entropy change associated with this phenomenon (e.g., Poddar et al., 2006). Heat capacity measurements of lepidocrocite between 300 K and 500 K, above which there is transformation to maghemite, do not report any type of anomaly due to a magnetic transition (e.g., Diakonov, 1998). Lang (2005) measured the heat capacity of akaganéite and did not find any anomaly near the previously claimed Néel temperatures; instead, the author found an inflection in the specific heat around 310 K and interpreted it as the onset of magnetic ordering. The same author did however state that the results were not conclusive.

Thermomagnetic measurements above 300 K for lepidocrocite do not show changes in the magnetization due to magnetic ordering up to 520 K, where transformation to maghemite occurs (Hanesch et al., 2006). In addition, Guyodo (2007) has shown evidence of magnetic remanence in lepidocrocite up to 150 K, above the previously claimed Néel temperatures, suggesting the need for further study of the magnetic behaviour of this mineral.

1.3.3 Néel Models of Moment Formation Mechanism

Any antiferromagnetic particle can have a net moment if there is uncompensation of spins due to the presence of crystalline defects (Section 1.2.1). In nanometric antiferromagnetic particles, this net moment can be enhanced due to the greater presence of defects associated with smaller particles, such as the presence of a higher degree of strain within the structure and greater proportion of spins at the surface of the particle (e.g., Waychunas and Zhang, 2008). Néel (1961) proposed a hypothesis regarding the origin of the magnetization of small (< 10 nm) antiferromagnetic particles that are superparamagnetic. He proposed different models representing the moment formation mechanism for a simple two-sublattice antiferromagnetic structure. The models are based on a relationship between the total number of magnetic cations in a particle (n) and the number of magnetic cations for which magnetic spins are uncompensated within the antiferromagnetic structure (μ') and therefore contribute to the net magnetic moment of the particle. These models are summarized in Table 1.5.

Table 1.5 Models of moment formation mechanism in antiferromagnetic nanoparticles proposed by Néel (1961)

Model	**Origin of net moment**
$\mu' \propto n^{1/3}$	Random spatial distribution of uncompensated spins at the surface.
$\mu' \propto n^{1/2}$	Random spatial distribution of uncompensated spins throughout the volume of the particle.
$\mu' \propto n^{2/3}$	All of the spins at the surface are uncompensated.

Magnetic studies done on metal oxide nanoparticles have explored the presence of those types of moment formation mechanisms. For instance, the model based on the exponent 1/3 has been proposed and found for NiO and CuO nanoparticles (Richardson et al., 1991; Punnoose et al., 2001) and the model based on the exponent 1/2 has been found in MnO nanoparticles (Sako et al., 1995).

Those models have also been explored in iron oxides and iron oxyhydroxides. Bødker et al. (2000) found that the net moment of superparamagnetic hematite is in agreement with a model based on an exponent between 1/3 and 1/2. Based on a preliminary study of a few ferrihydrite samples, Rancourt et al. (2004) suggested the model with an exponent of 2/3. Assuming a stoichiometry and particle size for ferrihydrite, Seehra et al. (2000) found agreement in the model based on the 1/2 exponent and the measured magnetic moment. The latter agreement was also found by Kilcoyne and Cywinski (1995) and Makhlouf et al. (1997) for ferritin. Assuming a value for n, Harris et al. (1999) also obtained the same result with a measured value of n. In addition, the assumption of this model has been used to fit magnetic and Mössbauer data for ferritin (Gilles et al., 2000).

1.4 Objectives

Main objective:

The main objective of the present work is to systematically study the magnetic properties of synthetic analogues of common iron oxyhydroxide nanoparticulate minerals (ferrihydrite, goethite, lepidocrocite, schwertmannite and akaganéite) as a function of field and temperature.

Specific objectives:

- Elucidate the magnetic state of these minerals in the temperature range from liquid helium temperature to room temperature.
- Extract intrinsic physical parameters of the nanoparticles using a superparamagnetic granulometry analysis.
- Explore the possible magnetic moment formation mechanism(s) that give origin to the observed magnetization in these nanoparticles.

Chapter 2 – Methods: Experimental and Analysis

2.1 Sample Synthesis

The samples studied in the present work are listed in Table 2.1. They include several ferrihydrite samples covering the crystallinity series from the 2-line to the 6-line varieties; a series of hydrous ferric oxides (HFO) with increasing concentration of P co-precipitation, starting from a 4-line ferrihydrite; a series of goethites with decreasing surface area and a pair of lepidocrocite, schwertmannite and akaganéite samples.

Table 2.1 List of samples

Sample Name	Mineral / Description
2L-Fh	2-line ferrihydrite
6L-Fh-1	6-line ferrihydrite
6L-Fh-2	6-line ferrihydrite
4L-Fh	4-line ferrihydrite
P-HFO-0	4-line ferrihydrite (Control sample of P-HFO series: [P] = 0 M)[1]
P-HFO-0.01	P-bearing hydrous ferric oxide (HFO); [P] = 0.01 M[1]
P-HFO-0.025	P-bearing HFO; [P] = 0.025 M[1]
P-HFO-0.05	P-bearing HFO; [P] = 0.05 M[1]
P-HFO-0.075	P-bearing HFO; [P] = 0.075 M[1]
P-HFO-0.1	P-bearing HFO; [P] = 0.1 M[1]
Gt-1	Goethite
Gt-2	Goethite
Gt-3	Goethite
Gt-4	Goethite
Gt-5	Goethite
Gt-6	Goethite
Lp-1	Lepidocrocite
Lp-2	Lepidocrocite
Sw-1	Schwertmannite
Sw-2	Schwertmannite
Akg-1	Akaganéite
Akg-2	Akaganéite

[1] P concentrations are those of the solutions from which the P-HFO samples were precipitated

2.1.1 Ferrihydrites

The 2-line ferrihydrite sample (2L-Fh) was synthesized by P.-J. Thibault in Dr. J. Dutrizac's laboratory at the CANMET-MMSL in Ottawa. A 0.1 M solution of $Fe(NO_3)_3 \cdot 9H_2O$ was stirred at 60 °C. The pH was increased to 4.0 by adding an 8 M solution of NaOH at a constant rate and maintained at this value for 2 h. The precipitate was suction-filtered and oven-dried at 100 °C overnight. The resultant sample was manually ground to a loose powder.

The 6-line ferrihydrite sample, 6L-Fh-1, was synthesized by S. Bonneville and Dr. T. Behrens at Utrecht University following the Cornell and Schwertmann (2003) procedure. Twenty grams of $Fe(NO_3)_3 \cdot 9H_2O$ were added to 2 L of water heated at 75 °C under constant stirring. The solution was further heated in the oven (at 75 °C) for 10 minutes during which the initial Fe hydroxyl-polymers were formed. The solution was then cooled by plunging it into iced water. The suspension was dialyzed for three days, changing the water several times a day. The final suspension was freeze-dried to produce a dry powder for analysis.

The 6-line ferrihydrite sample, 6L-Fh-2, was also synthesized at Utrecht University. The sample is the result of a test synthesis aimed at obtaining nanogoethite, which was not formed and instead a 6-line ferrihydrite was obtained. 500 mL of a solution of 0.1 M MPS (3-Morpholinopropane sulfonic acid, organic buffering substance) was adjusted to a pH of 7.2. The solution was purged with Ar for 1 h, after which a 0.2 M $FeCl_2$ solution was added and then circulated by a peristaltic pump through a long silicon tube into a dialysis bag. Over time, the Fe (II) concentration decreased due to the oxidation caused by the oxygen diffusion into the solution. After 70 h, about 90 % of the Fe (II) was oxidized and the reaction was stopped by adding 2 mL of concentrated HCl. The suspension was allowed to settle; the initial iron oxyhydroxide formed may have transformed due to the presence of Fe (II). During sub-sampling, the unintentional entry of 2 N HCl and oxygen dropped the pH (< 3) and may have further transformed the precipitate. The resultant sample was repeatedly centrifuged, re-suspended in de-mineralized water and finally freeze-dried.

The 4-line ferrihydrites and P-HFO series were synthesized at the CANMET-MMSL in Ottawa. For the 4-line ferrihydrites (4L-Fh and P-HFO-0), a solution of 0.1 M $Fe(NO_3)_3{\cdot}9H_2O$ was stirred at 60 °C; the pH increased from 1.3 to 4.0 by adding 8 M NaOH at a constant rate (1.1 mL/min). The solution was maintained for about 2 h, after which it was suction-filtered. The precipitate was oven-dried at 110 °C overnight and manually ground to a fine powder. The P-HFO series with increasing P were prepared in the same way, except for the addition of P before the addition of NaOH, using a solution of sodium phosphate ($NaH_2PO_4{\cdot}H_2O$), in increasing concentrations (0.01 M; 0.025 M; 0.05 M; 0.075 M; 0.1 M) for the different samples in the series.

2.1.2 Goethites

The goethite samples were synthesized by Dr. E. Roden. The Gt-1 and Gt-2 samples were synthesized by the slow oxidation of a 50 mM solution of $FeCl_2$, with the pH maintained at circumneutral values (pH ~ 7) through buffering with a 5 mM bicarbonate solution. The precipitate was washed from the suspension by dialysis, freeze-dried and passed through a 100 μm sieve.

The synthesis of the rest of the goethite samples (Gt-3 to Gt-6) was done using a 0.4 M solution of $FeCl_3{\cdot}6H_2O$; the pH was increased to 13 by adding 4 N NaOH. The solution was incubated for 16 h at 7 °C, 20 °C, 30 °C and 90 °C for the cases of Gt-3, Gt-4, Gt-5 and Gt-6, respectively. The suspensions were centrifuged until the Cl^- concentrations were below

0.5 mM. The precipitates were freeze-dried and passed through a 100 μm sieve. The specific surface area data of the goethite sample, measured using multipoint BET analysis with N_2 as the adsorbate, was also provided and they are shown in Table 2.2.

Table 2.2 Specific surface area of the goethite samples

Sample	**Surface Area (m^2/g)**
Gt-1	211
Gt-2	135
Gt-3	96
Gt-4	73
Gt-5	62
Gt-6	38

2.1.3 Lepidocrocites

The Lp-1 sample was synthesized at Utrecht University following the Schwertmann and Cornell (2000) procedure. $FeCl_2$ (39.76 g) was dissolved in 1 L of de-mineralized water and the solution was filtered to remove the early onset of precipitated akaganéite. The solution was purged with Ar (200 mL/min) for 30 min, after which a pH-stat instrument adjusted the pH to 6.8 with 1 M NaOH and a greenish precipitate formed. There was an overshooting of the target pH (6.8), so the automatic pH adjustment was manually stopped and the gas stream was changed from Ar to air (300 mL/min). After this, the pH-stat instrument was re-started. The pH decreased to 5.5 and remained constant despite increasing the rate of addition of NaOH. After 3 h, the pH increased to 6.8 and the colour of the precipitate changed from green to orange. The resulting precipitate was purified by repeated centrifugation and re-suspension in de-mineralized water until the conductivity in the supernatant was below 160 μS/cm. The resultant sample was freeze-dried.

The Lp-2 sample was synthesized by the slow oxidation of a 0.1 M solution of $FeCl_2 \cdot 4H_2O$ in 0.009 M $NaHCO_3$ at a pH of 5.3 – 6.1 for approximately 2 h. The suspension was sealed and left to age for 6 days (Fortin, 1992). The resulting precipitate was repeatedly centrifuged and re-suspended in deionised water and air-dried at room temperature.

2.1.4 Schwertmannites

The schwertmannite samples, Sw-1 and Sw-2, were synthesized following the procedure in Cornell and Schwertmann (2003) (Sw-1 was synthesized by Dr. D.L. Sparks at the University of Delaware). For each synthesis, 10.8 g of $FeCl_3 \cdot 6H_2O$ and 3 g of Na_2SO_4 (1000 mg SO_4 per L) were quickly added to 2 L of distilled water preheated in an oven to 60 °C. The solution was kept at this temperature for 12 more minutes and then was left to cool at room temperature. The suspension was then dialyzed for several days, after which it was freeze-dried.

2.1.5 Akaganéites

The protocol to synthesize the akaganéite sample Akg-1 is described in Bigham et al. (1990) (named "B-0S"). Its synthesis involved the hydrolysis of a 0.02 M $FeCl_3$ solution for 12 min at 60 °C, with an initial pH of 2.09. After cooling to room temperature, the sample was dialyzed for 30 days, and then freeze-dried.

The akaganéite Akg-2 was synthesized following the procedure of Schwertmann and Cornell (2000). A 0.1 M $FeCl_3 \cdot 6H_2O$ solution was heated to 40 °C in an oven for 8 days. The precipitates were dialyzed for 2 weeks and then freeze-dried.

2.2 Powder X-ray Diffraction

Powder X-ray diffraction (pXRD) patterns for all of the samples were collected using a Bragg-Brentano geometry (θ-2θ). All of the samples, excluding the 4L-Fh sample and P-HFO series, were run at the University of Ottawa using an automated Phillips X'pert PW3710 powder diffractometer with a Kevex™ solid state detector and Cu Kα radiation (1.5405 Å) at 45 kV and 40 mA, equipped with an automatic variable divergence slit, a fixed 1° anti-scatter slit and a rotating sample stage. The parameters that varied include: the 2θ measuring range, from 2° to 120° (typically, 5° to 75°); the receiving slit, 0.1 mm or 0.2 mm; the 2θ step size, from 0.02° to 0.04° and the time per step, from 2 sec/step to 18 sec/step.

The 4L-Fh and the P-HFO series were run by Dr. John Wilson at the CANMET-MMSL, using a Phillips diffractometer with a Rigaku rotating anode and Cu Kα radiation at 50 kV and 180 mA, equipped with a fixed divergence slit and a stationary sample stage. The runs were done with a 2θ range from 5° to 70°, a step size of 0.02° and a scan rate of 4°/min.

At the University of Ottawa, most of the samples were ground under acetone and prepared as thin smears on a low background holder, while the 2L-Fh sample and all of the goethite samples were prepared as filled troughs. The use of an automatic variable divergence slit provides a fixed irradiated area throughout the 2θ range measured, which for a thin sample (i.e., thin smear), also provides a constant irradiated volume. However, this is not the case for a semi-infinite sample (i.e., filled trough), and therefore the diffraction intensities for the latter case had to be corrected by a Sinθ factor (Kimmel, 1987).

Additionally, for increasing 2θ, the use of an automatic variable divergent slit increases the divergence of the diffracted beam, which can be partially blocked by the fixed anti-scatter slit of 1°. Consequently, at angles higher than those where the aperture of the anti-scatter slit is equal to the divergence of the diffracted beam (i.e., 2θ = 29.1° for a 1° aperture), the beam is partially blocked and, therefore, causes a decrease in the diffracted intensities above 2θ = 29.1°. In this sense, the intensities were corrected for this effect using a geometric factor based on the Bragg-Brentano geometry set-up used (Bowden and Ryan, 1991).

At the CANMET-MMSL, the samples were mounted in a cylindrical cavity using a capillary tube. The use of a fixed divergence slit and the semi-infinite sample geometry directly provide a constant irradiated volume and, therefore, does not require an anti-scatter slit correction.

The mineralogy of the samples was confirmed by the identification of the diffraction peaks and relative intensities of known iron oxyhydroxides (e.g., Cornell and Schwertmann, 2003) and powder diffraction files (PDF) from the Joint Committee on Powder Diffraction Standards (JCPDS) database.

A semi-quantitative estimation of the coherence length (L) of the diffracting domain was done using the Scherrer equation (e.g., Reynolds, 1989), which relates the broadening of the diffraction peaks to the size of the diffracting domain. For nanoparticles, the size broadening is expected to dominate over instrumental broadening and as a result, the latter is not taken into account in this particle size estimation. In addition, it does not consider the potential effect of the presence of structural strain in the crystalline structure. Particle size estimation was done for all of the samples except for the ferrihydrites and P-HFO series, due to the fact that they show very broad and/or overlapping peaks. For the rest of the samples, the Scherrer equation was applied to single (i.e., non-overlapping) peaks in the diffractograms. The peaks were fitted using the OriginLab software with Gaussian, Lorentzian or Gaussian-Lorentzian cross product lineshapes in order to obtain the FWHM used in the Scherrer equation.

2.3 Mössbauer Spectroscopy

Mössbauer spectroscopy is a nuclear resonant spectroscopy technique based on the recoil-free absorption of gamma rays in solids. It has a very fine resolution detecting changes in the nuclear energy levels. Particularly, it provides resolution of the magnetic hyperfine field in the probed nucleus in an experimental time window of the order of 10^{-8} seconds (e.g., Rancourt, 1998).

Room temperature and cryogenic (4.2 K) ^{57}Fe Mössbauer spectroscopy was performed by various members of the Lake Sediment and Structure Evolution research group (Dr. M.-Z. Dang; Dr. P. Hargraves; J.-F. Meunier; Dr. D. Roberts; P.-J. Thibault; Dr. C. van der Zee) at the University of Ottawa. The spectra were collected in transmission mode using a 10 to 50 mCi ^{57}Co-Rh source with the transducer operating in a constant acceleration mode and a velocity range of 11 mm/s or 4 mm/s. The samples (absorbers) were mounted in 0.5 inch diameter holders, using the ideal absorber thickness, specific to the sample, in order to maximize the signal to noise ratio (Rancourt et al., 1993). The raw data was folded in order to obtain a flat background.

The qualitative analysis of the spectra was based on the inspection of the type of absorption spectrum. In particular, the presence of six resonance lines (sextet) indicates the presence of a magnetic hyperfine field, which represents a spontaneous magnetic order in the material, as seen within the measurement time of the technique (~ 10^{-8} s). The presence of two resonance lines in the spectrum (a doublet) indicates the lack of a magnetically blocked state, which can represent either the lack of magnetic order (paramagnetism) or thermal instability (with respect to the measurement time of the technique) of the net moment of a magnetically ordered material (superparamagnetism) (e.g., Rancourt, 1998).

2.4 Iron Concentration

The iron concentration, represented by the Fe weight percentage (Fe wt %) in the samples, was estimated by measuring the weight loss in the samples after heating them under ambient conditions up to temperatures above 900 °C. The weight loss of a number of samples was measured using thermogravimetric analysis performed by A.H. Delgado of the Institute for Research in Construction at the National Research Council in Ottawa. Other samples were heated in a furnace and the weight loss was estimated from the difference in weight before and after the heating process. The weight loss was used to estimate the Fe wt % taking into consideration that the end product for all of the iron oxyhydroxides is hematite (α-Fe_2O_3) (Cornell and Schwertmann, 2003).

2.5 Scanning Electron Microscopy (SEM)

SEM micrographs were obtained for most of the samples to qualitatively characterize the morphology of the particles and/or aggregates and estimate the range of sizes. Additionally, for the P-HFO series, the estimation of the P/Fe ratios was done by energy-dispersive X-ray spectroscopy (EDS). The samples were mounted on a carbon tape and then gold-coated. These measurements were done at Carleton University, Ottawa on a Tescan-Vega II electron microscope operating at 30 kV.

2.6 Magnetometry

Field cycles showing the variation of the magnetization (M) with applied magnetic field (H) and temperature cycles/runs showing the variation of the magnetic susceptibility (χ) with temperature were obtained using DC and AC magnetometry. A Lake Shore 7304 vibrating sample magnetometer (VSM), which uses a DC or constant magnetic field, was used to obtain field cycles within a maximum applied field (H_{max}) range of ±1 T and temperature cycles between 4.2 K and 300 K with a constant applied field of 0.5 T. A number of samples were sent to Dr. M. Murugesu's laboratory of the Chemistry Department (University of Ottawa) and measured using a Quantum Design superconducting quantum interference device (SQUID) magnetometer MPMS-XL. The use of the latter magnetometer enabled the measurement of field cycles reaching a H_{max} range of ±7 T, DC temperature cycles between 1.8 K and 300 K with a constant applied field of 0.5 T and AC-temperature runs in the same temperature range using an alternating field with a frequency range between 1 Hz and 1500 Hz.

In all of the magnetic measurements, the magnetic moment measured was corrected for the diamagnetic signal of the sample holder and then normalized by the mass of the sample in order to obtain the mass magnetization (M). In the case of the temperature cycles/runs, the data is presented as the magnetic susceptibility, which is the magnetization divided by the applied field.

2.6.1 Temperature Cycles/Runs Parameters and Analysis

The (DC) temperature cycles include a zero-field cooled (ZFC) run and a field-cooled (FC) run. The ZFC run was done by first quenching the sample down to 1.8 K or 4.2 K under zero applied magnetic field; subsequently, a magnetic field of 0.5 T was applied and the magnetic moment was measured as the temperature increased to 300 K while maintaining this constant applied field. Following the ZFC run, the FC run was obtained by setting again the 0.5 T constant field and measuring the magnetic moment while decreasing the temperature from 300 K down to 1.8 K or 4.2 K.

The AC-susceptibility measurements consisted of first quenching the sample down to 1.8 K and then measuring the magnetic moment as the temperature increased to 300 K while a small (3×10^{-4} T) alternating drive field was applied at the following different frequencies: 1 Hz, 50 Hz, 100 Hz, 500 Hz, 1000 Hz, and 1500 Hz. For each frequency probed, the measurement gives the real or in-phase component (χ') and the imaginary or out-of-phase component (χ'') of the magnetic susceptibility (χ). The following expressions give the relationships between these parameters, where φ is the phase shift or lag of the susceptibility relative to drive field:

$$\chi = \chi' + i\chi'' \tag{2.1}$$

$$\chi' = \chi \mathrm{Cos}(\varphi) \tag{2.2}$$

$$\chi'' = \chi \mathrm{Sin}(\varphi) \tag{2.3}$$

The ZFC and FC curves were inspected for the presence of hysteresis and maxima in the susceptibility. The AC-susceptibility runs were also inspected for the presence of maxima in the susceptibility components and for their frequency-dependence, the latter which is indicative of relaxation processes (Section 1.2.2).

2.6.2 Field Cycles Parameters and Analysis

The applied field sequence in the VSM field cycles was: 0 to $+H_{max}$ to $–H_{max}$ to $+H_{max}$. The sequence in the SQUID magnetometer was $+H_{max}$ to $–H_{max}$ to $+H_{max}$, with an initial magnetization curve, from 0.5 T to $+H_{max}$, measured only at 1.8 K.

The field cycles were inspected for the presence of hysteresis and sigmoidal curvature. In many cases, these are obvious features in a field cycle graph, but sometimes they are not obvious. Thus, in order to confirm the existence or absence of hysteresis and/or curvature in the field cycles, “curvature graphs” are shown along with them. The construction of these curvature graphs involved doing a least square linear regression of the magnetization data. For each magnetic field value sampled, magnetization values along the best line fit were subtracted from the measured magnetization dataset. The curvature graphs show the deviation of this measured data from the best line fit of the dataset. This deviation is represented as a percentage of the maximum M value reached (M_{max}) at the highest magnetic field applied (Figure 2.1).

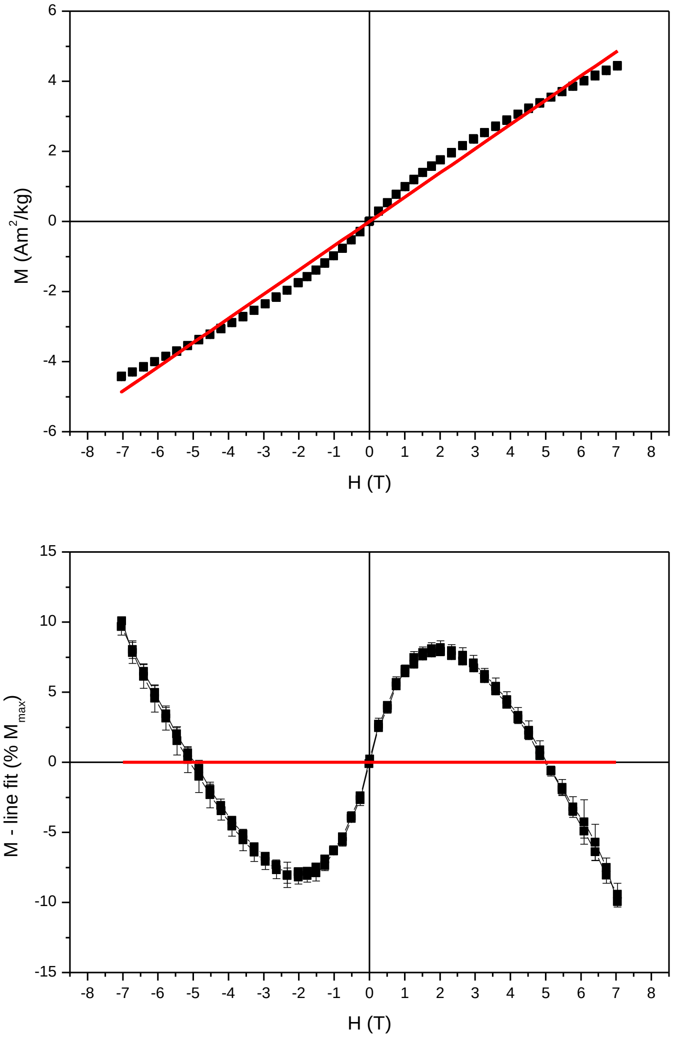

Figure 2.1 Example of the construction of a curvature graph (sample 6L-Fh-1, 300 K). Red line represents the error-weighted linear fit of the data

A quantitative analysis of the field cycles showing superparamagnetism was done using the magnetic granulometry method of Rancourt et al. (2004) in order to extract physical parameters of the superparamagnetic particles. In this analysis, the variation of the equilibrium thermal average magnetic moment (or time-average moment) of a superparamagnetic particle as a function of applied field (H) and temperature (T) is expressed as:

$$<\mu> = \mu L(\mu H/ k_B T) \qquad (2.4)$$

where μ is the intrinsic magnetic moment of the particle and $L(x) = \coth(x) - 1/x$ is the Langevin function with $x = \mu H/k_B T$. This expression is based on the fact that, although the magnetic anisotropy energy barrier can be significant, the defining term in the supermoment energy is the energy of interaction between the supermoment and the applied field, since the inversion point symmetry of the anisotropy energy barrier does not affect the thermal average moment, $<\mu>$.

For the case of $x < 1$, μH is smaller than $k_B T$, which implies that the thermal energy of the particle overcomes the magnetic energy associated with the alignment with the applied field. In this case, Equation 2.4 can be expressed, using a Taylor series approximation of coth(x), in terms of the mass magnetic susceptibility (χ) as:

$$\chi = \frac{\mu^2}{m\, k_B T}\left[\frac{1}{3} - \frac{1}{45}\left(\frac{\mu H}{k_B T}\right)^2 + \frac{2}{945}\left(\frac{\mu H}{k_B T}\right)^4\right] \qquad (2.5)$$

This expression is the basis for the “$x < 1$” analysis method; which shows that a χ vs. H^2 graph can display an initial straight line with a negative slope at low H^2 values, which deviates into a curve at higher H^2 values. The magnitude of μ will have an effect on the extent of this initial straight line and the magnitude of its slope (Figure 2.2). For the case of a sample with an unimodal distribution of magnetic moment (μ) and particle mass (m), the intercept (C_1) and slope ($-C_2$) of this straight line can be used to estimate the average magnetic moment $\{\mu\}$ and the average mass $\{m\}$ of the superparamagnetic particles:

$$\{\mu\} = k_B T \left(15 \frac{C_2}{C_1}\right)^{1/2} \tag{2.6}$$

$$\{m\} = 5 k_B T \frac{C_2}{(C_1)^2} \tag{2.7}$$

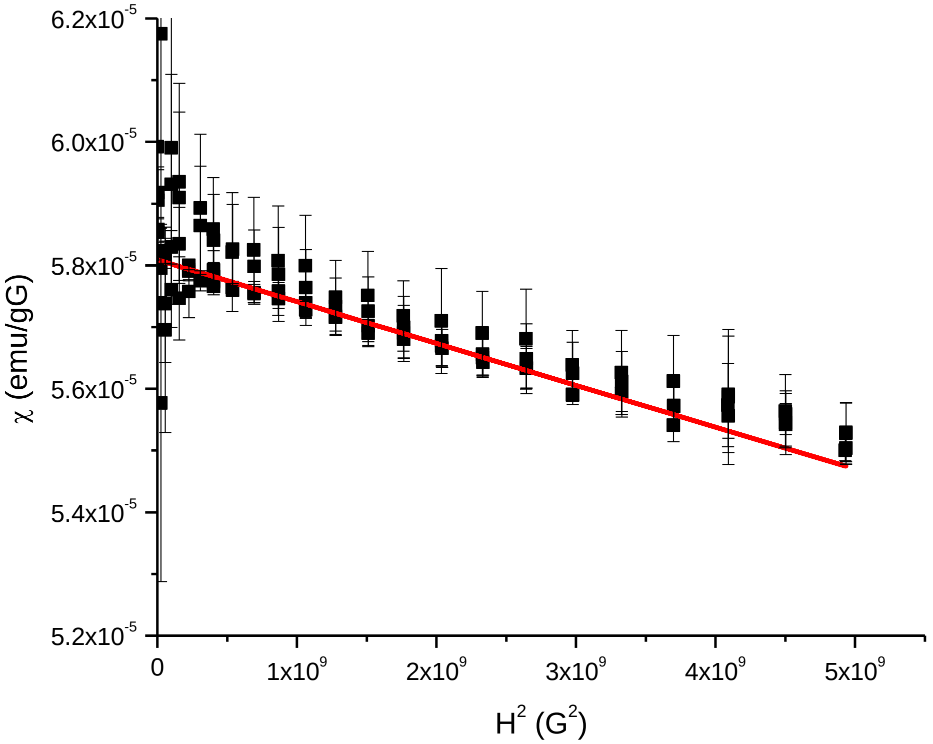

Figure 2.2 Example of graphical analysis for the "x < 1" method (sample Lp-2, 200 K). The red line represents the error-weighted linear fit of the data considered, which for this case is the H^2 range of 0.4-1.8 × 10^9 G^2

For the case of x >> 1, μH is much bigger than k_BT, which implies that the alignment of the magnetic moment of the particle with the applied field dominates over the thermal fluctuations. This is expected at either low temperatures and/or high applied magnetic fields.

In this case, Equation 2.4 can be expressed, using the x >>1 approximation of coth(x), in terms of the magnetization (M) as:

$$M = \frac{\{\mu\}}{\{m\}} - \frac{k_B T}{\{m\}H} \tag{2.8}$$

This expression is the basis for the “x >> 1” analysis method. In this case, the latter expression shows that a graph of |M| vs. |1/H| will display a straight line with a negative slope (Figure 2.3). For any distribution of magnetic moment and particle mass, the intercept (B_1) and slope (B_2) of this line can be used to directly calculate the average magnetic moment {μ} and the average mass {m} of the superparamagnetic particles:

$$\{\mu\} = -k_B T \left(\frac{B_1}{B_2} \right) \tag{2.9}$$

$$\{m\} = -k_B T \left(\frac{1}{B_2} \right) \tag{2.10}$$

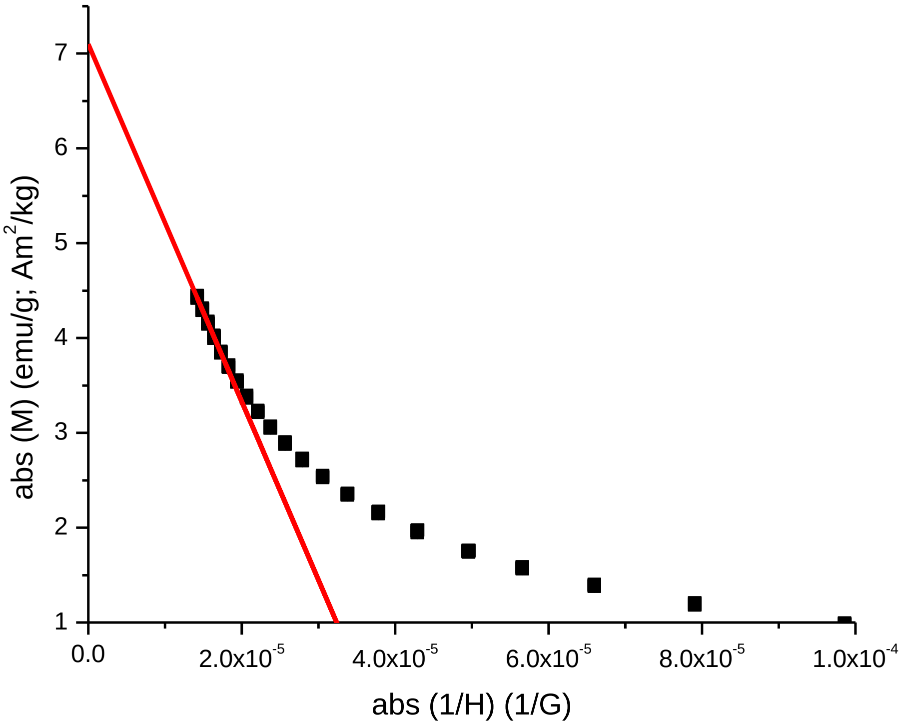

Figure 2.3 Example of graphical analysis for the “x >> 1” method (sample 6L-Fh-1, 300 K). The red line represents the error-weighted linear fit of the data considered

The intrinsic magnetization {μ}/{m} of the superparamagnetic particles is directly obtained from the {μ} and {m} extracted from the field cycles analysis. Additionally, other physical parameters can be estimated from these parameters. The size of the particle can be estimated from the average mass {m} using the density of the mineral (ρ) (Cornell and Schwertmann, 2003) and assuming a spherical shape of the particle; in this case, the diameter (d) of the particles is expressed as:

$$d = \left(\frac{6\{m\}}{\pi\rho} \right)^{1/3} \tag{2.11}$$

From {m}, the total number of Fe^{3+} cations in the particle (n) can also be estimated. Using the molecular weight of the mineral (M_W) according to its nominal formula (Section 1.3), n can be expressed as:

$$n = \frac{\{m\} N_A \# Fe}{M_W} \tag{2.12}$$

where N_A refers to Avogadro's number and #Fe is the number of Fe in the nominal chemical formula of the mineral. Using the Fe fraction (f_{Fe}) from the measured Fe wt % and the atomic weight of Fe (A_r), n can be expressed as:

$$n = \frac{\{m\} N_A f_{Fe}}{A_r} \tag{2.13}$$

The extracted {μ} of the superparamagnetic particles can be considered as the sum of the magnetic moments of the Fe^{3+} cations that are not compensated within the antiferromagnetic structure of the particle and therefore contribute to a net moment (Section 1.2.1). Using the magnetic moment of a Fe^{3+} of 5 μ_B, the number of Fe^{3+} cations in the particle contributing to the net moment (μ') can be estimated:

$$\mu' = \frac{\{\mu\}}{5\mu_B} \tag{2.14}$$

The ratio of the latter two parameters can be converted to a percentage in order to represent the proportion of Fe^{3+} cations in the superparamagnetic particle contributing to the net moment, μ'/n.

Chapter 3 – Results and Interpretation

3.1 Ferrihydrites

3.1.1 2-line and 6-line Ferrihydrites

The 2-line ferrihydrite (2L-Fh) and the 6-line ferrihydrites (6L-Fh-1 and 6L-Fh-2) show the characteristic two and six peaks, respectively, in their powder X-ray diffractograms (pXRD) (Cornell and Schwertmann, 2003) (Figures B.1 and B.2, Appendix B). The 6L-Fh-1 sample shows an impurity of goethite which was estimated to be approximately 10 wt % based on the relative intensities of the most intense diffraction peaks.

Scanning electron microscopy (SEM) images show dense aggregates for the 2L-Fh and 6L-Fh-1 samples (Figures C.1 and C.2 (a), Appendix C). The SEM micrographs for the 6L-Fh-2 sample also show chunks which appear to be composed of globular aggregates that range from 100 nm to 1 μm (Figure C.2 (b)). The resolution obtained for these images was above 10 nm, so individual ferrihydrite particles were not resolved.

Based on the temperature cycles of these samples (Figures D.1, D.2 and D.3, Appendix D), it can be seen that they all depict the typical behaviour of magnetic blocking phenomena in a superparamagnetic particle system (Section 1.2.2), where magnetic blocking is evidenced by the maxima in the zero-field-cooled (ZFC) curve in conjunction with hysteresis, which is the separation of the latter curve and the field-cooled (FC) curve.

The AC-susceptibility data for the three samples (Figures 3.1, 3.2 and 3.3) also show evidence of magnetic blocking in a superparamagnetic particle system, showing peaks in the in-phase component of the susceptibility (χ'), frequency-dependence of χ' and the associated non-zero values of the out-of-phase component of the susceptibility (χ'') (Section 1.2.2).

For the 2L-Fh sample, the temperature where the ZFC peak occurs coincides with the temperature below which there is hysteresis (i.e., separation between the ZFC and FC curves) (Figure D.1). In the AC-susceptibility data, the sample shows a very narrow peak in χ’, below which there is a frequency-dependence of χ’ and a non-zero value of χ” (Figure 3.4). In addition, the frequency-dependence decreases and ends as the lowest temperature is reached (i.e., 1.8 K).

The hysteresis in the temperature cycle, for both 6L-Fh-1 and 6L-Fh-2, starts at higher temperatures than the temperature associated with the peak in their corresponding ZFC curve (Figures D.2 and D.3), suggesting that magnetic blocking occurs as a gradual process for these two samples. Their corresponding AC–susceptibility data show a broad peak in χ’ at low temperatures. Unlike 2L-Fh, the frequency-dependence for these two samples does not occur suddenly below the temperature of the χ’ peaks, instead, it takes place gradually, covering temperatures below and above the temperature of the χ’ peak. The frequency-dependence of χ’ in 6L-Fh-1 is more obvious than in 6L-Fh-2, but the trend is evident in the latter (Figures 3.3 and 3.5). Additionally, the frequency-dependence ends at 1.8 K. With regards to χ”, 6L-Fh-1 clearly shows non-zero values at the same temperature range where there is a frequency-dependence of χ’. But 6L-Fh-2 does not; however, it does show more dispersion in the data at low temperatures.

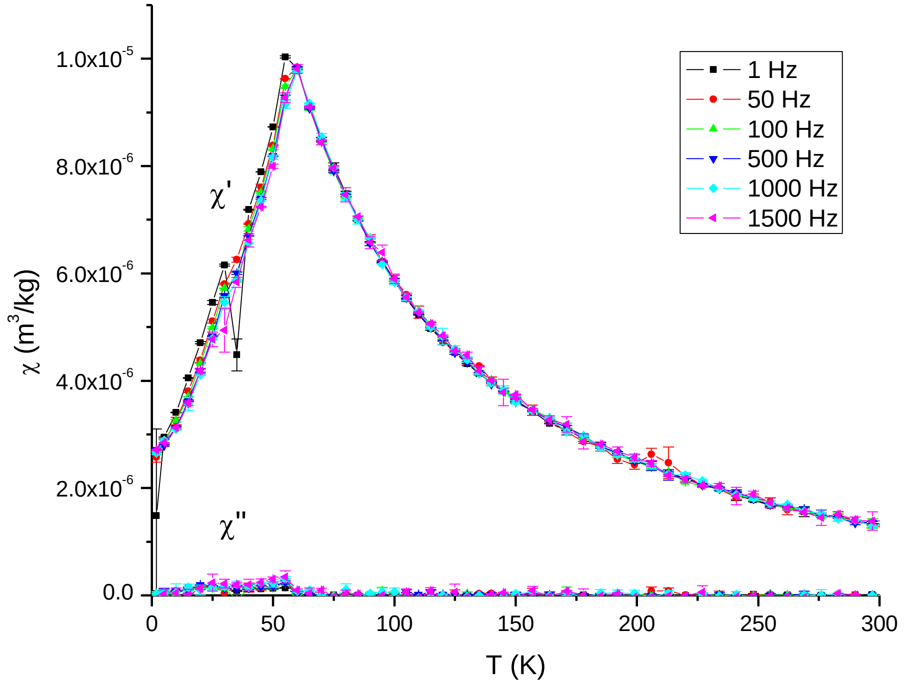

Figure 3.1 AC-susceptibility temperature runs (χ’ and χ”) of 2L-Fh

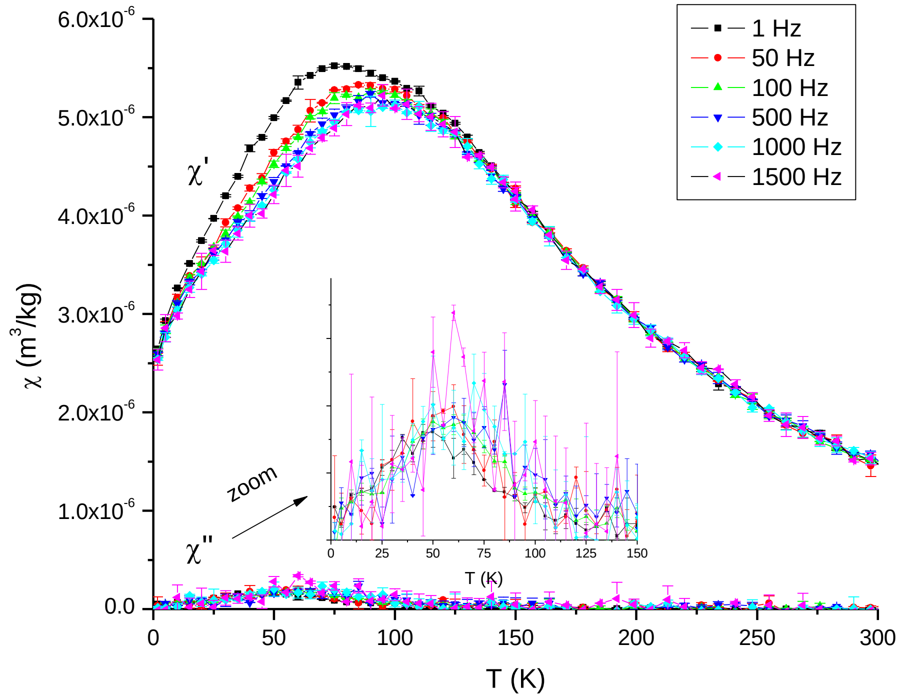

Figure 3.2 AC-susceptibility temperature runs (χ’ and χ”) of 6L-Fh-1 with zoom (between 0 and 150 K) of χ” (inset)

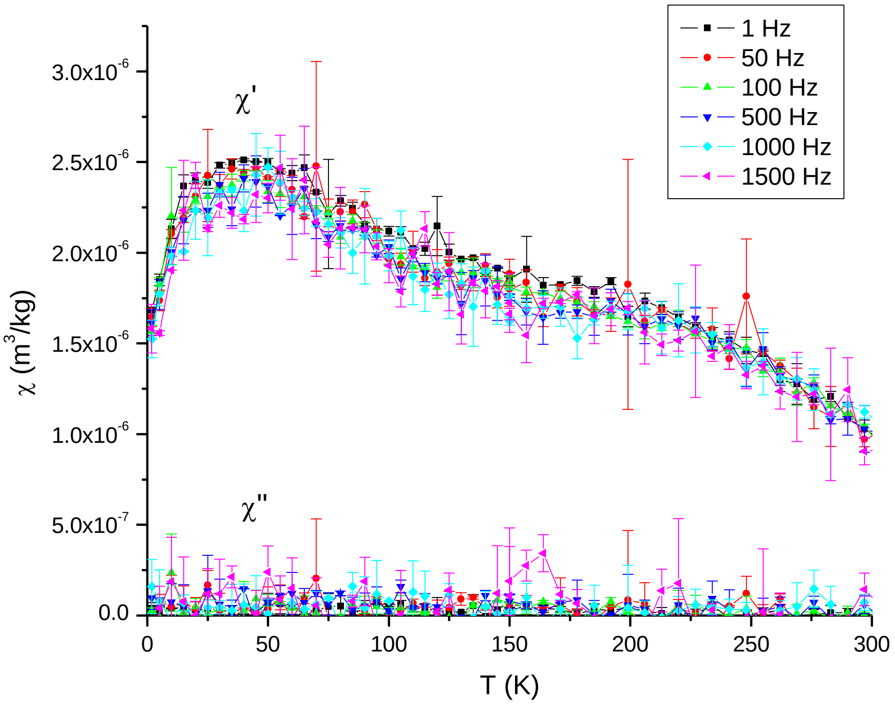

Figure 3.3 AC-susceptibility temperature runs (χ’ and χ”) of 6L-Fh-2

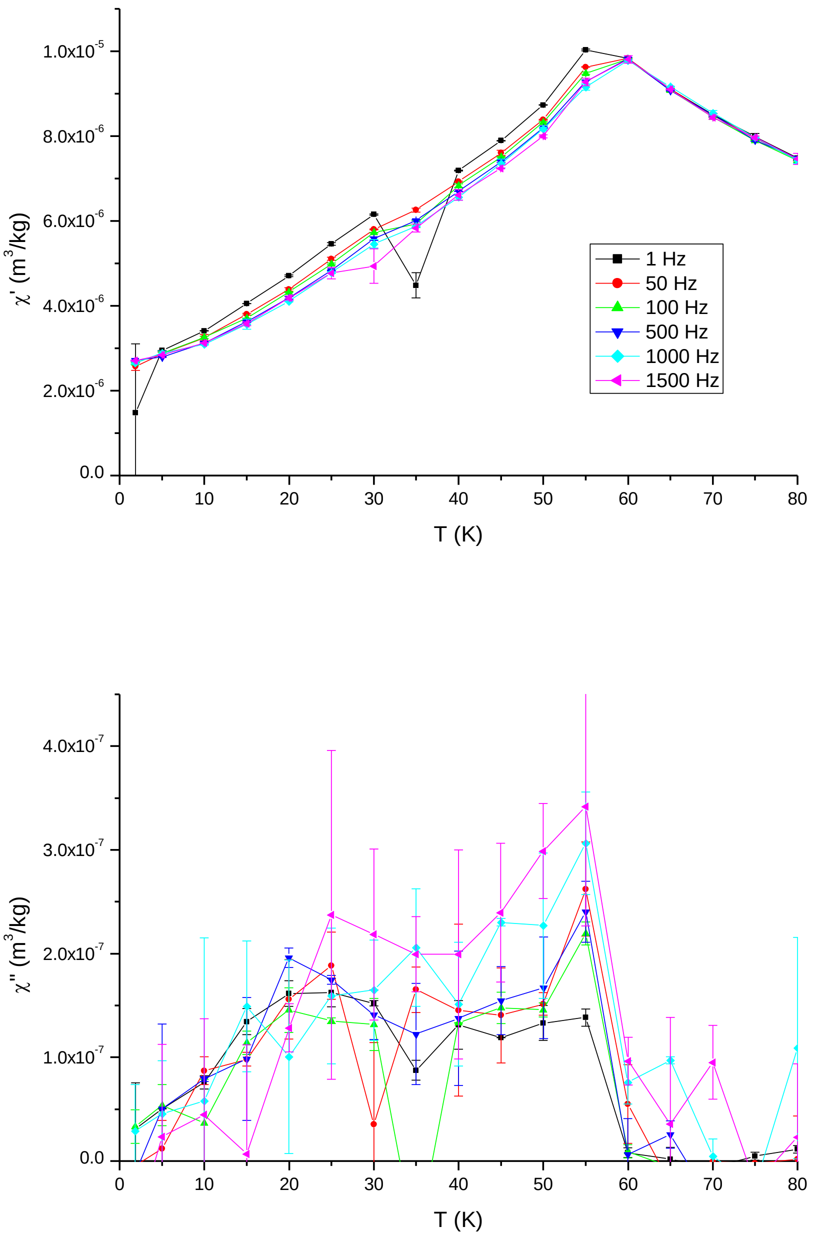

Figure 3.4 Zoom between 0 and 80 K of χ' (top) and χ'' (bottom) of 2L-Fh

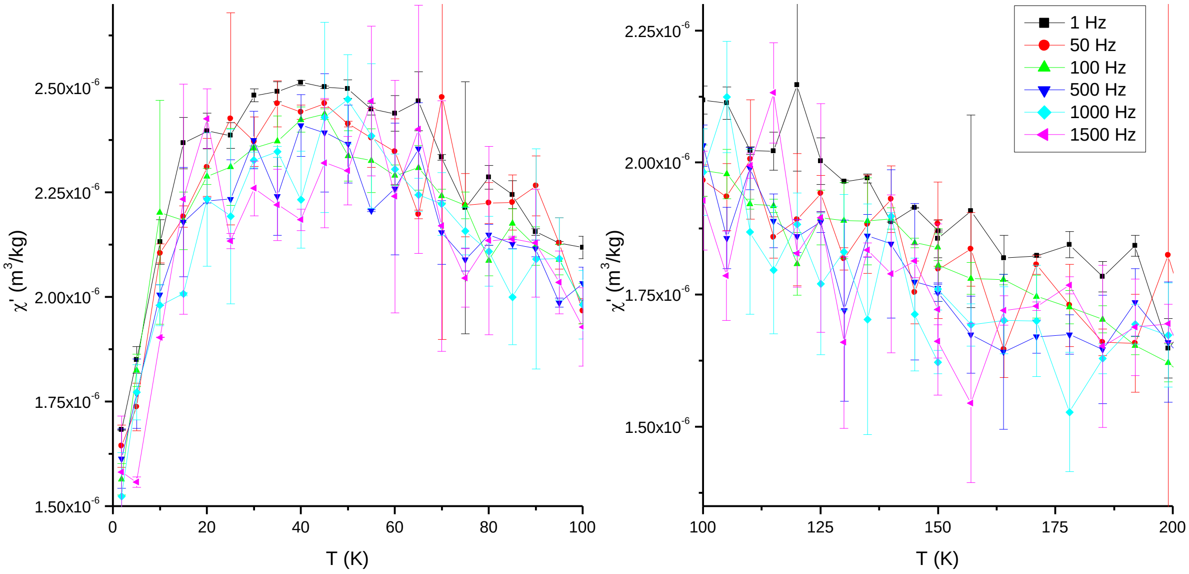

Figure 3.5 Zoom of χ' of 6L-Fh-2 from 0 to 100 K (left) and from 100 K to 200 K (right)

Both (DC) temperature cycles and AC-susceptibility runs for these ferrihydrites agree with the interpretation of a sudden magnetic blocking process in 2L-Fh at a low temperature and a more gradual blocking process for the 6-line ferrihydrites covering higher temperatures.

The magnetic blocked state at low temperatures is confirmed by the hysteresis in the field cycles measured at 1.8 K for the three samples (Figures E.4, E.8 and E.12, Appendix E). For the 6L-Fh-1 and 6L-Fh-2 samples, the latter is also confirmed by the existence of a well-developed sextet in their corresponding Mössbauer spectra at 4.2 K (Figures F.1 and F.2, Appendix F). The latter and the fact that there is no more frequency-dependence of χ' near 4.2 K, suggest that at this temperature, the magnetic blocking process has been completed, meaning that all of the particles are magnetically blocked. The Mössbauer spectrum for the 6L-Fh-1 sample at 4.2 K does not qualitatively resolve the contribution of the goethite impurity detected by pXRD because goethite has a sextet with an associated hyperfine field that is very similar to that of 6-line ferrihydrite (Cornell and Schwertmann, 2003).

Even though the temperature cycle data for both the 6L-Fh-1 and 6L-Fh2 samples shows magnetic blocking evidence at 100 K, their field cycles at this temperature do not show hysteresis (Figures E.7 and E.11), suggesting that the temperature cycle data for these samples has a better resolution with respect to magnetic blocking.

Based on the above data and interpretation, it can be determined, for each sample, the temperature above which there is no magnetic blocking evidence and therefore where superparamagnetic behaviour is expected. For these samples, this upper temperature limit of the transition from a blocked state to a superparamagnetic state is given by the temperature below which there is frequency-dependence of χ' and it is ~ 60 K, ~ 125 K and ~ 190 K, for 2L-Fh, 6L-Fh-1 and 6L-Fh-2, respectively.

At 300 K, the Mössbauer spectra for the 6L-Fh-1 and 6L-Fh-2 samples show a doublet (Figures F.1 and F.2), evidencing the lack of magnetic blocking. For the 6L-Fh-1 sample, the latter also shows that the goethite impurity must be superparamagnetic, since there is no evidence of a sextet representing a magnetically blocked goethite. The field cycles of 2L-Fh at 300 K, 200 K and 100 K show non-hysteretic cycles reaching larger magnetization (M) values and systematically show a more pronounced sigmoidal curvature with decreasing temperature (Figures E.1, E.2 and E.3). This behaviour agrees with the theoretical simulations of superparamagnetic behaviour shown in Appendix A. The 6L-Fh-1 and 6L-Fh-2 samples also show this superparamagnetic behaviour at 300 K and at 200 K (Figures E.5, E.6, E.9 and E.10). These field cycles were analyzed using the magnetic granulometry method described in Section 2.6.2; the extracted physical parameters are shown in Table 3.1. For the 6L-Fh-1 sample, these parameters represent an average that includes the contribution of the superparamagnetic goethite impurity.

Overall, it can be seen that the results for the 2L-Fh sample show higher intrinsic magnetization values ({μ}/{m}) and smaller particle sizes (d) than those for the 6L-Fh-1 and 6L-Fh-2 samples and that the estimated dimensions for all three samples are below 9 nm, which is below the resolution obtained with the SEM images.

Figure 3.6 shows the average of all of the extracted and estimated parameters for the three samples using the “x >> 1” analysis method at 300 and 200 K, since this set of results was common to all three samples and comes from a similar applied field (H) range; this figure also includes the weight percentage of Fe (Fe wt %) (Appendix G).

Table 3.1 Physical parameters of 2-line and 6-line ferrihydrites extracted from field cycles using $H_{max} = 7$ T

	T	**Analysis Method**	**H range**	**{μ}**		**{m}**	**{μ}/{m}**	**d**	**n**	**μ’**	**μ’/n**	**Comment**
	(K)	$x=\mu H/k_BT$	(T)	$x10^{-21}$ (Am^2)	(μ_B)	$x10^{-21}$ (kg)	(Am^2/kg)	(nm)	$x10^3$		(%)	
2L-Fh	300	< 1	1.5-2.6	1.15 (7)	124 (7)	0.09 (1)	13 (2)	3.5 (1)	0.57 (7)	25 (1)	4.4 (6)	
	200	< 1	0.8-1.8	1.67 (2)	180 (2)	0.154 (4)	10.9 (3)	4.20 (4)	0.96 (3)	36 (1)	3.7 (1)	
	100	< 1										N/A[1]
	300	>> 1	5.8-7	1.46 (4)	157 (4)	0.125 (3)	11.7 (1)	3.92 (3)	0.78 (2)	31 (1)	4.0 (1)	
	200	>> 1	5.8-7	1.09 (3)	118 (3)	0.069 (2)	15.8 (2)	3.22 (3)	0.43 (1)	24 (1)	5.5 (2)	
	100	>> 1	5.5-7	0.66 (1)	72 (2)	0.0346 (7)	19.2 (1)	2.55 (2)	0.217 (5)	14 (1)	6.6 (2)	
6L-Fh-1	300	< 1	0.5-1.3	4.2 (2)	455 (19)	1.4 (1)	3.1 (3)	8.7 (2)	8.5 (7)	91 (4)	1.1 (1)	
	200	< 1										N/A[1]
	300	>> 1	5.8-7	1.56 (4)	168 (4)	0.220 (5)	7.10 (6)	4.73 (3)	1.38 (3)	34 (1)	2.44 (8)	
	200	>> 1	5.8-7	1.14 (3)	122 (4)	0.130 (4)	8.70 (9)	3.98 (4)	0.82 (2)	24 (1)	3.0 (1)	
6L-Fh-2	300	< 1										N/A[1]
	200	< 1										N/A[1]
	300	>> 1	5.8-7	1.41 (6)	152 (7)	0.232 (9)	6.1 (1)	4.82 (2)	1.45 (6)	30 (1)	2.1 (1)	
	200	>> 1	5.8-7	0.98 (3)	105 (3)	0.128 (4)	7.6 (1)	3.95 (4)	0.80 (2)	21 (1)	2.6 (1)	

[1] Method was not applicable due to the lack of an initial straight line in the χ vs. H^2 graph

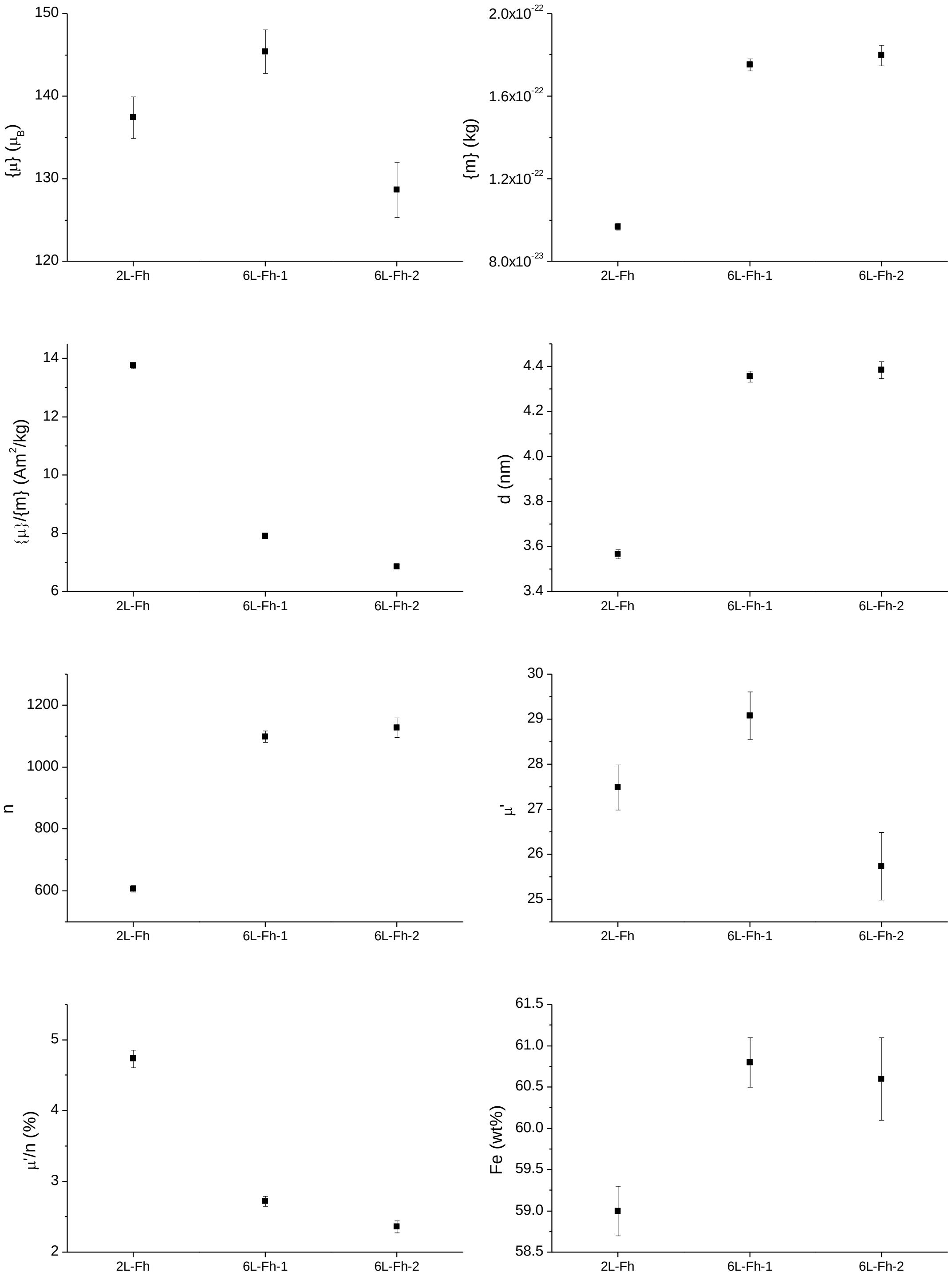

Figure 3.6 Average values of the physical parameters for 2L-Fh, 6L-Fh-1 and 6L-Fh-2 extracted using the "x >> 1" analysis method at 300 K and 200 K

Figure 3.6 shows that the superparamagnetic particle magnetic moment ({μ}) and its related parameter, the number of Fe^{3+} cations contributing to the moment (μ'), vary for each sample; there is not an evident trend between 2L-Fh and both 6L-Fh-1 and 6L-Fh-2 for these parameters. The superparamagnetic particle mass ({m}) and its related parameters, the number of total Fe^{3+} cations in the particle (n) and the particle diameter (d), of both 6L-Fh-1 and 6L-Fh-2 are larger than those of 2L-Fh. On the other hand, for 2L-Fh, the intrinsic magnetization ({μ}/{m}) and its derived parameter, the percentage of Fe^{3+} cations in the superparamagnetic particle contributing to the net moment (μ'/n), are larger than those of 6L-Fh-1 and 6L-Fh-2. In other words, the smaller 2L-Fh particles have more magnetic ions contributing to its intrinsic magnetization than the larger 6-line ferrihydrite particles.

3.1.2 4-line Ferrihydrites and "P-HFO Series"

The pXRD of samples 4L-Fh and P-HFO-0 (Figures B.3 and B.4) display four of the characteristic peaks for ferrihydrite. These samples are part of the crystallinity series of ferrihydrite, between 2-line and 6-line ferrihydrite (Schwertmann et al., 2004), namely 4-line ferrihydrites.

The "P-HFO Series" ferrihydrites includes the 4-line ferrihydrite sample, P-HFO-0, as the control sample with no P added, and five additional samples with increasing P concentration (from 0 to 0.1 mol/L (M)): P-HFO-0.01; P-HFO-0.025; P-HFO-0.05; P-HFO-0.075; P-HFO-0.1. Their X-ray diffractograms show that there is a gradual loss in both intensity and sharpness of the peaks with increasing P concentration, especially at higher 2θ angles. Additionally, the position of the low 2θ peak gradually shifts to lower angles with increasing P concentration (Figure B.4).

SEM images of 4L-Fh and P-HFO-0 show large dense smooth aggregates (Figures C.3 and C.4 (a)). With increasing P concentrations, the aggregates show a coarser texture and seem more loosely packed (Figure C.4).

The temperature cycles of 4L-Fh and P-HFO-0 are very similar (Figures D.4 and D.5); they both show the typical superparamagnetic blocking process described in the previous section for the 2-line and 6-line ferrihydrites. As in the case for 2L-Fh, on decreasing the temperature, the hysteresis appears at the temperature associated with the peak of the ZFC curve, so there is no evidence of a gradual blocking process as seen in the 6-line ferrihydrites. On the other hand, when decreasing the temperature from 300 K to the main blocking temperature, the increase in χ in the ZFC and FC curves is more gradual than for 2L-Fh, and similar to that observed for the 6-line ferrihydrites. For both samples, the ZFC curve is slightly above the FC curve for different portions of the temperature range above the blocking temperature; this is suspected to be an effect of an instrumental artefact that shifted the curve up or down.

The temperature cycles of the samples with the lowest concentrations of P ([P] from 0.01 to 0.05 M) also show a superparamagnetic magnetic blocking event at low temperatures (Figures D.6, D.7 and D.8). In these samples, the peak of the ZFC curve shifts to lower temperatures and becomes narrower with increasing P concentration. For the samples with even higher P concentration ([P]: 0.075 and 0.1 M), the blocking event is less evident and probably not completed at the lowest temperatures attained (Figures D.9 and D.10).

The magnetic blocked state at low temperatures for 4L-Fh, P-HFO-0, P-HFO-0.01, P-HFO-0.025 and P-HFO-0.05 is confirmed by the hysteresis in their corresponding field cycles at 4.2 K (Figures E.14, E.16, E.18, E.20 and E.22). In these cycles, the hysteresis decreases with increasing P concentration. Although the temperature cycles for the samples with the highest P concentrations ([P]: 0.075 and 0.1 M) did not clearly show the blocking process, their hysteresis cycles at 4.2 K show a small hysteresis on further inspection, confirming that the samples are blocked or partially blocked (Figures E.24 and E.26). The Mössbauer spectra at 4.2 K complement the latter analysis by showing that the samples with P concentrations from 0 to 0.025 M are blocked as evidenced by the well-developed sextet in their spectra (Figures F.4, F.5 and F.6). For higher P concentrations, the Mössbauer spectra show partially-developed sextets, indicating that the particles are in the process of blocking but have not blocked completely yet (Figures F.7, F.8 and F.9). The degree of non-development of the sextet increases with higher P concentrations, suggesting that the blocking temperature decreases with increasing P concentration.

At 300 K, all of the samples show features of superparamagnetic behaviour. They show a doublet in their Mössbauer spectra (Figures F.3, F.4, F.5, F.6, F.7, F.8 and F.9) and non-hysteretic field cycles (Figures E.13, E.15, E.17, E.19, E.21, E.23, E.25). The field cycles show curvature for 4L-Fh and the P-HFO series samples with P concentrations up to 0.025 M. For higher P concentrations, the curvature in the field cycle is not resolved. The physical parameters extracted through the magnetic granulometry method are shown in Table 3.2. Figure 3.7 shows the results for the "x >> 1" analysis method, which was applied to all of the samples within the same field range; this figure includes the Fe wt % and P/Fe ratios. The latter include the theoretical or molar ratios based on the synthesis of the samples, the values measured with X-ray fluorescence (XRF) by Thibault et al. (2009) and the values obtained through energy-dispersive X-ray spectroscopy (EDS).

Table 3.2 Physical parameters for the 4-line ferrihydrites and the P-HFO series from field cycles using a H_{max} of 1 T at 300 K

	Analysis Method	**H range**	**{μ}**		**{m}**	**{μ}/{m}**	**d**	**n**	**μ’**	**μ’/n**	**Comment**
	$x=\mu H/k_BT$	(T)	$x10^{-21}$ (Am^2)	(μ_B)	$x10^{-21}$ (kg)	(Am^2/kg)	(nm)	$x10^3$		(%)	
4L-Fh	< 1										N/A[1]
	>> 1	0.8-1	9.7 (2)	1046 (18)	2.99 (5)	3.24 (2)	11.30 (6)	18.8 (3)	209 (4)	1.12 (2)	
P-HFO-0	< 1	0.3-1	3.33 (5)	359 (5)	0.58 (2)	5.7 (2)	6.54 (6)	3.6 (1)	72 (1)	1.97 (6)	
	>> 1	0.8-1	9.6 (2)	1030 (25)	3.71 (8)	2.58 (3)	12.14 (9)	23.2 (5)	206 (5)	0.89 (3)	
P-HFO-0.01	< 1										N/A[2]
	>> 1	0.8-1	9.2 (2)	996 (17)	9.3 (1)	0.992 (8)	16.50 (8)	58.4 (9)	201 (3)	0.344 (8)	
P-HFO-0.025	< 1										N/A[2]
	>> 1	0.8-1	9.2 (2)	990 (21)	11.3 (2)	0.814 (8)	17.6 (1)	70.7 (1)	198 (4)	0.280 (8)	
P-HFO-0.05	< 1										N/A[2]
	>> 1	0.8-1	9.2 (3)	990 (37)	12.8 (4)	0.72 (1)	18.4 (2)	80 (3)	198 (7)	0.25 (1)	
P-HFO-0.075	< 1										N/A[2]
	>> 1	0.8-1	9.2 (4)	988 (40)	11.6 (4)	0.79 (1)	17.8 (2)	73 (3)	250 (9)	0.34 (2)	
P-HFO-0.1	< 1										N/A[2]
	>> 1	0.8-1	9.2 (4)	991 (44)	11.4 (4)	0.80 (2)	17.7 (2)	72 (3)	198 (9)	0.28 (2)	

[1] Method not applicable due to lack of an initial straight line in the χ vs. H^2 graph

[2] Method not applicable due to a zero slope in the χ vs. H^2 graph (C_2=0)

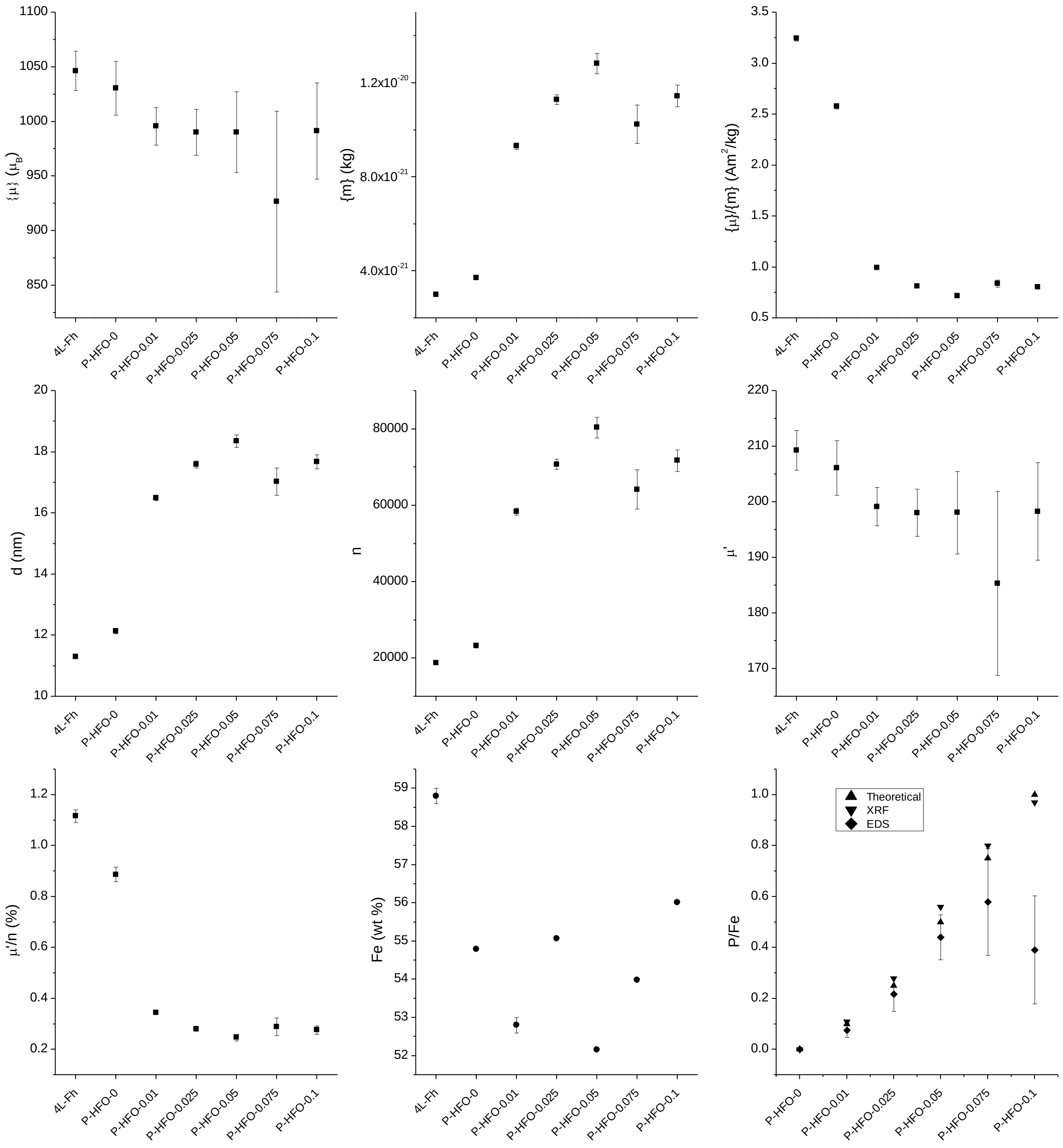

Figure 3.7 Physical parameters for 4L-Fh and the P-HFO series extracted using the "x >> 1" analysis method at 300 K

The trend in {μ} and μ' with increasing P concentration is inversely proportional to the P/Fe ratio measured by EDS, which indicates that it is in agreement with the Fe/P ratio measured with this technique. In this trend, Fe/P and the net magnetic moment of the superparamagnetic particle {μ} are lower for samples with higher P concentration up to 0.075 M; above this concentration, the values are similar to those for 0.05 M. At the highest P concentrations, both the XRF and molar P/Fe ratios are in disagreement with the EDS P/Fe. In contrast to XRF (which is a bulk characterization technique) and the molar ratio (which represent the total elemental content) the EDS technique probes a very small surface area (depending on the size of the X-ray beam, typically in the order of 1,000 nm) and therefore quantifies the elemental composition at a smaller scale, which minimizes the analytical error.

The {m}, n and d of the superparamagnetic particles increase considerably with the smallest P concentration and keep increasing until the P concentration reaches 0.05 M. Above this P concentration the parameters vary within relatively high values. The estimated particle sizes are between 10 to 20 nm and, for the analysis method used ("x >> 1"), they represent the particles that have aligned with the applied field in the range between 0.8 and 1 T. These estimated magnetic particles sizes are smaller than the resolution of the SEM images (Figure C.4).

The {μ}/{m} and μ'/n show the inverse trend of {m}, n and d, with P concentration. The intrinsic magnetization decreases with P concentrations up to 0.05 M, above which it no longer decreases and remains at low values. For most of the parameters in Figure 3.7 there seems to be a trend with P concentration that is not continued at concentrations above 0.05 and 0.075 M, where the corresponding parameter varies around a constant value.

3.2 Goethites

The pXRD patterns of the goethite samples show goethite as the only crystalline phase present (Figure B.5). The BET specific surface area values associated with these samples (Table 2.2), suggest that they go from a very small particle size in Gt-1 to a larger particle size in Gt-6. This trend of increasing particle size is supported by the increasing sharpness of the diffracting peaks; the estimates of the size or coherence length (L) of the diffracting domain based on the Scherrer formula (Section 2.2) are shown in Figure 3.8.

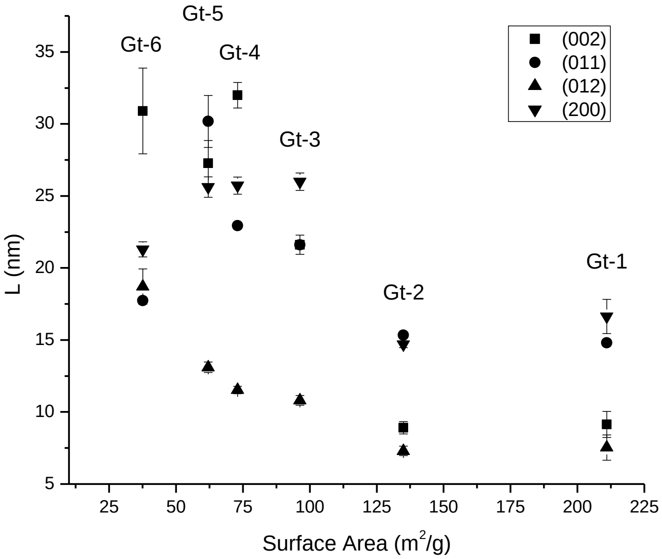

Figure 3.8 Coherence length (L) estimates for the goethites from the pXRD diffraction peaks indicated

SEM images for Gt-1 and Gt-2 show irregular aggregates (Figure C.5 (a) and (b)). For the larger goethites, Gt-3 to Gt-6, the SEM images do show individual laths with approximate dimensions given in Table 3.3 (Figure C.5 (c), (d), (e) and (f)).

Table 3.3 Dimensions of goethite laths observed by SEM

Sample	**Range of dimensions (nm)**
Gt-3	300 x 100 – 400 x 150
Gt-4	400 x 100 – 550 x 150
Gt-5	400 x 100 – 500 x 150
Gt-6	700 x 75 – 1000 x 150

The temperature cycles for Gt-1 and Gt-2 show superposed ZFC and FC curves down to ~ 250 K, below which there is hysteresis (Figures D.11 and D.12). Above 250 K, Gt-1 and Gt-2 show superparamagnetic behaviour in their field cycles; this is supported by the lack of hysteresis and the presence of curvature (Figures E.27, E.28 and E.30). Additionally, their Mössbauer spectra at 300 K shows a doublet (Figures F.10 and F.11), which is typical of superparamagnetism. Thus, both Gt-1 and Gt-2 show evidence of superparamagnetic behaviour down to 250 K; the latter marking the onset of the magnetic blocking process in these samples.

Below 250 K, Gt-1 shows a peak in the ZFC curve at ~ 30 K representing a main superparamagnetic blocking event. Gt-2 shows two low-temperature peaks in the ZFC curve, one at ~ 60 K and an additional one near the lowest temperatures reached and which is not completed at 1.8 K. This suggests that for Gt-2 the magnetic blocking takes place in more than one main event at different temperatures. In fact, the temperature where hysteresis starts (i.e., 250 K) may be seen as being associated with the first maximum, on decreasing the temperature, in the ZFC curve, representing the first main blocking event, which is followed by the one at 60 K, and subsequently, the one near 1.8 K. The field cycles of Gt-2 at 200 and 100 K show hysteresis, indicating magnetic blocking (Figures E.31 and E.32). Additionally, the shapes of these hysteresis curves provide evidence that there is also a gradual blocking process taking place in addition to the main blocking events described above. The cycle at 200 K shows that the hysteresis curve becomes constricted near its intercept with the y-axis; this type of shape has been termed as “wasp-waisted” and indicates the presence of single-domain particles (the particles that have already blocked at 200 K) and large superparamagnetic particles (Tauxe et al., 1996). At 100 K, the hysteresis curve becomes broadened near its intercept with the y-axis or “pot-bellied”. This kind of shape has been associated with the presence of single-domain particles and small superparamagnetic particles (Tauxe et al., 1996). In the latter case, the single-domain particles include the particles that were already blocked at 200 K and the large superparamagnetic particles that were giving the wasp-waisted shape to the hysteresis curve at 200 K and that have become blocked at 100 K.

The AC-susceptibility data for Gt-2 (Figure 3.9) does not illustrate the typical features associated with a superparamagnetic blocking process, as seen with the 2-line and 6-line ferrihydrites (Section 3.1.1). Below 250 K, the data do not show either frequency-dependence of χ’ or non-zero values of χ”. Moreover, there are no evident maxima in the χ’ associated with the ones seen in the ZFC curve. Given the fact that the blocking process mainly takes place in different events, the resultant effect of the previously mentioned features may not be sufficient to be resolved, as only a fraction of the particles are being blocked in each main event. Additionally, once the particles are blocked for each event, there is no more cause for frequency-dependence of χ’ or non-zero χ” related to the blocking event (as seen in the low temperature limit of the AC-data for the 2-line and 6-line ferrihydrites in Section 3.1.1) and so there is no cumulative effect that can be resolved in the data at lower temperatures.

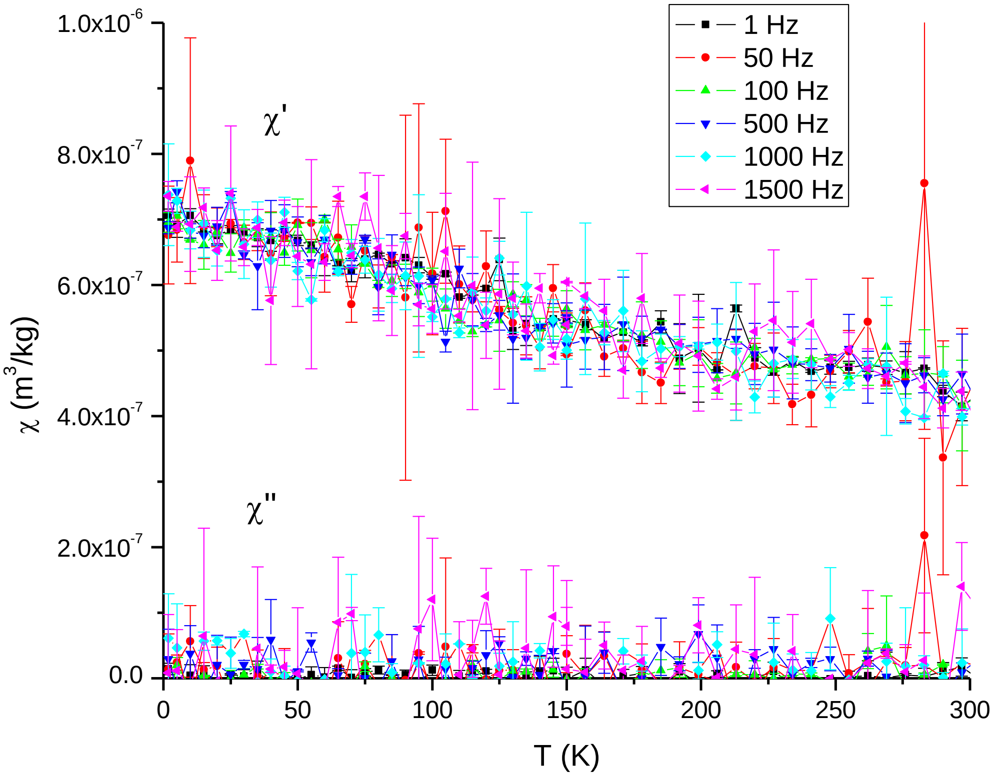

Figure 3.9 AC-susceptibility temperature runs (χ' and χ") of Gt-2

The magnetic blocked state of Gt-1 at 4.2 K is evidenced by the hysteresis in its field cycle (Figure E.29) and the well-developed sextet in its Mössbauer spectrum (Figure F.10). For Gt-2, the field cycle at 1.8 K shows hysteresis indicating magnetic blocking (Figure E.33). At 4.2 K its Mössbauer spectrum shows what can be qualitatively called as a well-developed sextet (Figure F.11) even though the temperature cycle suggests that at this temperature there is one blocking event that has not been completed. Given the fact that only a fraction of the particles have not been blocked yet, the effect may not be large enough to be qualitatively resolved in the spectrum as an evident contribution of a partially-developed sextet.

The temperature cycle of Gt-3 shows ZFC and FC curves superposed down to ~ 175 K (Figure D.13) and a very broad ZFC curve. At 4.2 K, the sample shows hysteresis in its field cycle (Figure E.35), indicating a blocked state. The field cycle at 300 K is non-hysteretic and shows curvature (Figure E.34), suggesting superparamagnetism; but its Mössbauer spectrum shows a partially-developed sextet (Figure F.12), which suggests that the sample is in the process of blocking and not completely superparamagnetic. (DC) Magnetometry and Mössbauer spectroscopy have different characteristic instrumental measurement times and as a result, the blocking temperatures suggested by either technique, may differ. The characteristic time for Mössbauer spectroscopy is much smaller (~ 10^{-8} s) than that of magnetometry (~ 1 s), which means that the former can resolve the slowing down of the superparamagnetic moment reversals or the decrease in thermal instability due to magnetic blocking while the latter still detects it as a thermally unstable state because it measures during a longer time window. In light of the above, it can be said that Gt-3 is in the process of blocking magnetically at 300 K.

The larger particle size goethites, Gt-4, Gt-5 and Gt-6, show temperature cycles with ZFC and FC curves superposed down to 150 K – 250 K and very broad or virtually flat ZFC curves at lower temperatures (Figures D.14, D.15 and D.16). At 4.2 K, they are all magnetically blocked according to their field cycles showing hysteresis (Figures E.37, E.39 and E.41) and Mössbauer spectra showing well-developed sextets (Figures F.13, F.14 and F.15). At 300 K, their field cycles suggest superparamagnetic behaviour since they do not show hysteresis and do show curvature (Figures E.36, E.38 and E.40); however, as in the case of Gt-3, their Mössbauer spectra show partially-developed sextets, indicating that magnetic blocking is occurring at this temperature (Figures F.13, F.14 and F.15). These sextets are better developed with increasing particle size. Accordingly, as in the case of Gt-3, samples Gt-4 to Gt-6 are in the transition from a blocked state to a superparamagnetic state at 300 K.

Table 3.4 shows the resultant physical parameters of Gt-1 and Gt-2 estimated using the magnetic granulometry method. The results for Gt-1 at 300 K and 270 K are in agreement with each other. Overall, the results show that the Gt-1 superparamagnetic particles have a larger moment, larger size and smaller intrinsic magnetization than the Gt-2 superparamagnetic particles, but it should be noted that the results for each sample are extracted using different field ranges. The results for Gt-1 are based on a lower field range (~ 0.8 – 1 T) than those for Gt-2 (5.8 - 7 T). For the applied method used ("x >> 1"), the results correspond to the particles that have aligned with the applied field at the range indicated. For a particle size distribution and at a given temperature, smaller superparamagnetic particles have a higher thermal energy than larger superparamagnetic particles. Consequently, the smaller particles need higher field strengths in order to become aligned with the applied field. Both Gt-1 and Gt-2 show evidence of magnetic blocking taking place over a broad temperature range, indicating than different particles block at different temperatures. Since blocking temperature is intrinsically related to the volume of the particle (Section 1.2.2), the data suggest that these two samples have a variable particle size distribution. The results for Gt-1 represent the larger particles in its size distribution and the results for Gt-2 represent an average of the particles that have aligned at 5.8 – 7 T, small and big. The range of sizes estimated for these two samples through magnetometry are between 5 and 18 nm, which agrees with the range of sizes estimated from pXRD (Figure 3.8), but they are smaller than the range of sizes estimated with the SEM (Figure C.5; Table 3.3). The latter sizes may be representing a type of oriented aggregate of the smaller crystallite sizes.

Table 3.4 Physical parameters of goethite samples

	T	**H_{max}**	**Analysis Method**	**H range**	**{μ}**		**{m}**	**{μ}/{m}**	**d**	**n**	**μ'**	**μ'/n**	**Comment**
	(K)	(T)	$x=\mu H/k_BT$	(T)	$x10^{-21}$ (Am^2)	(μ_B)	$x10^{-21}$ (kg)	(Am^2/kg)	(nm)	$x10^3$		(%)	
Gt-1	300	1	< 1										N/A[1]
	270	1	< 1										N/A[1]
	300	1	>> 1	0.9-1	8.8 (3)	954 (28)	12.3 (3)	0.718 (9)	17.7 (2)	84 (2)	191 (6)	0.228 (9)	
	270	1	>> 1	0.8-1	9.0 (1)	974 (12)	11.3 (1)	0.796 (4)	17.20 (7)	76.9 (9)	195 (2)	0.253 (4)	
Gt-2	300	7	< 1										N/A[2]
		7	>> 1	5.8-7	1.35 (5)	145 (6)	0.32 (1)	4.22 (7)	5.23 (6)	2.16 (7)	29 (1)	1.34 (7)	

[1] Method not applicable due to lack of an initial straight line in the χ vs. H^2 graph

[2] Method not applicable due to a zero slope in the χ vs. H^2 graph (C_2=0)

3.3 Lepidocrocites

The pXRD patterns of both Lp-1 and Lp-2 show lepidocrocite as the only crystalline phase present (Figure B.6). Lp-1 shows sharper peaks than Lp-2, suggesting bigger and/or more crystalline particles than Lp-2. An estimate of the coherence length of the diffracting domain based on the Scherrer formula is given in Table 3.5. The SEM micrographs show needle-like particles with resolved dimensions between 100 x 10 nm and 200 x 20 nm (Figure C.6).

Table 3.5 Coherence length estimates (L) from pXRD for the lepidocrocites

	L (nm)	
Miller index	**Lp-1**	**Lp-2**
(200)	9.42 (5)	4.5 (3)
(210)	14.3 (1)	7.8 (2)
(511)	11.1 (2)	4.9 (6)

The temperature cycle for Lp-1 shows superposed ZFC and FC curves down to ~ 75 K, below which there is hysteresis and a maximum in the ZFC curve (Figure D.17). The ZFC and FC curves for Lp-2 are superposed down to ~ 25 K. This temperature coincides with the one associated with the maximum in the ZFC curve and marks the onset of hysteresis (Figure D.18). These features agree with the magnetic blocking of superparamagnetic particles.

The field cycle of Lp-1 at 300 K shows a noticeable but small ferrimagnetic or ferromagnetic contribution, evidenced by a low-field ($|H| < 1$ T) saturation feature (Figure E.42). As indicated in Section 2.1.3, there was an overshooting of the pH during the hydrolysis process in the synthesis of this sample; this usually results in the formation of magnetite (Schwertmann and Cornell, 2000). The weight fraction of the magnetite precipitated should be small enough to not be resolved by either pXRD (Figure B.6) or Mössbauer spectroscopy (Figure F.16) and to not create an evident coercivity in the field cycles above 75 K (Figures E.42, E.43 and E.44). Assuming a saturation magnetization for magnetite of 90 Am^2/kg (Dunlop and Özdemir, 1997), the weight percentage of magnetite was estimated from the saturation magnetization of the impurity in the field cycle data at 300 K and found to be less than 1%. The curvature of magnetite is limited to a low-field range; the field cycles at 200 K and 100 K for Lp-1 do not show hysteresis and show an increased curvature throughout all of the field range measured, which is related to the superparamagnetic behaviour of the lepidocrocite (Figures E.43 and E.44). The blocked behaviour at low temperatures is evidenced by the presence of a well-developed sextet at 4.2 K (Figure F.16) and a hysteretic field cycle at 1.8 K (Figure E.45).

The field cycles at 300 K, 200 K and 100 K for Lp-2 are non-hysteretic and show curvature; as with Lp-1, they also reach higher magnetization values and show an increased curvature with decreasing temperature (Figures E.46, E.47 and E.48), in agreement with superparamagnetic behaviour. In the field cycle at 1.8 K, Lp-2 shows hysteresis indicating magnetic blocking (Figure E.49).

The AC-susceptibility data for Lp-2 is in agreement with superparamagnetic behaviour. It shows a peak in χ' at ~ 25 K associated with the peak in the ZFC curve; it also shows frequency-dependence of χ' and non-zero χ'' from 35 K down to 1.8 K (Figures 3.10 and 3.11). The magnetic granulometry method was applied to the Lp-2 field cycles showing superparamagnetic behaviour. The results are shown in Table 3.6.

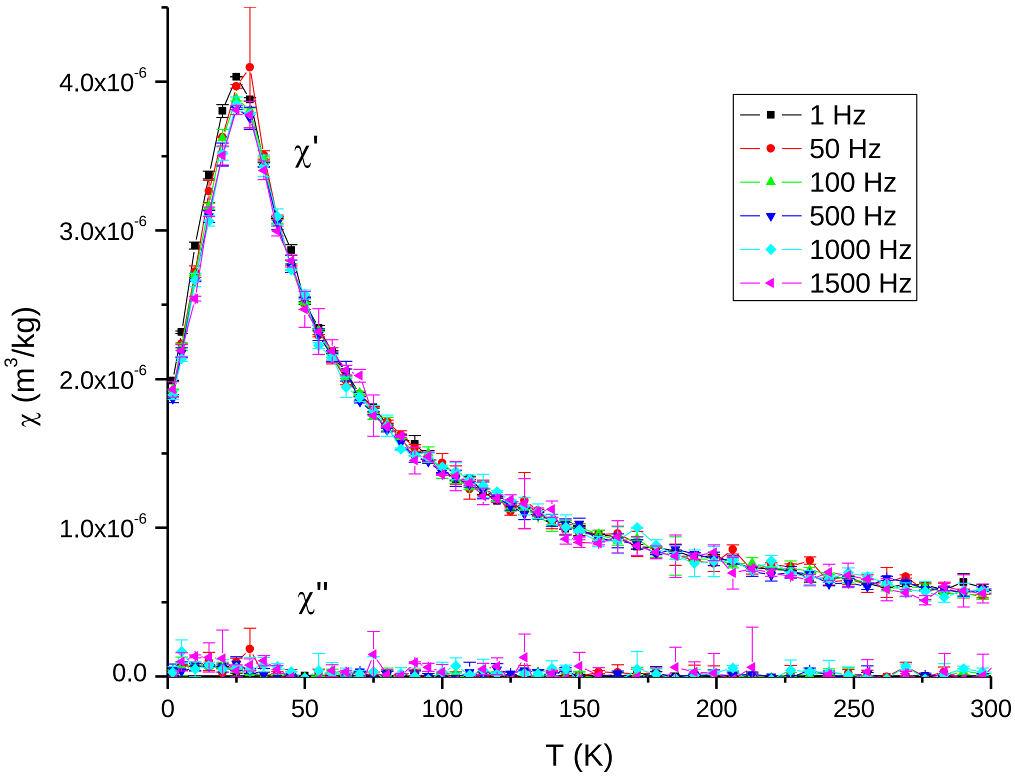

Figure 3.10 AC-susceptibility temperature runs (χ' and χ'') of Lp-2

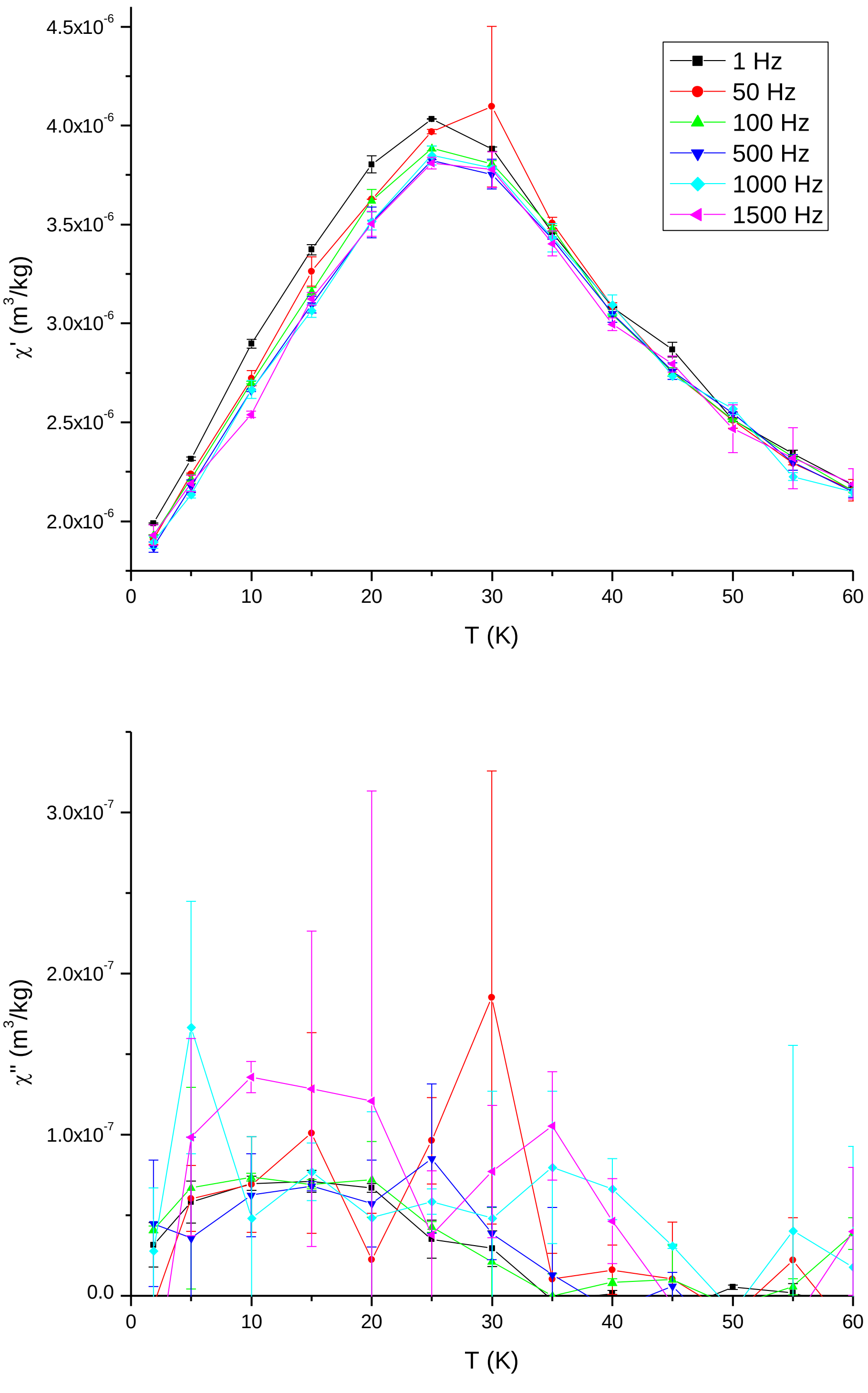

Figure 3.11 Zoom from 0 to 60 K of χ' (top) and χ'' (bottom) of Lp-2

Table 3.6 Physical parameters of lepidocrocite, Lp-2, extracted from field cycles using H_{max} = 7 T

T	**Analysis Method**	**H range**	**{μ}**		**{m}**	**{μ}/{m}**	**d**	**n**	**μ'**	**μ'/n**
(K)	$x=\mu H/k_BT$	(T)	$\times 10^{-21}$ (Am^2)	(μ_B)	$\times 10^{-21}$ (kg)	(Am^2/kg)	(nm)	$\times 10^3$		(%)
300	< 1	3.2-7	0.22 (4)	24 (5)	0.010 (4)	23 (10)	1.6 (2)	0.06 (2)	5 (1)	7 (3)
200	< 1	2-4	0.36 (4)	39 (5)	0.028 (7)	13 (4)	2.3 (2)	0.19 (4)	8 (1)	4 (1)
100	< 1	0.5-2	0.62 (4)	67 (4)	0.09 (1)	7.1 (9)	3.4 (1)	0.59 (7)	13 (1)	2.2 (3)
300	>> 1	6.1–7	1.29 (4)	140 (4)	0.241 (6)	5.37 (7)	4.79 (4)	1.63 (4)	28 (1)	1.71 (7)
200	>> 1	6.1–7	0.88 (3)	95 (3)	0.126 (4)	7.00 (9)	3.86 (4)	0.85 (2)	19 (1)	2.23 (9)
100	>> 1	6.1–7	0.49 (2)	53 (2)	0.052(2)	9.5 (1)	2.87 (3)	0.35 (1)	11 (1)	3.0 (1)

A general observation from Table 3.6 is that the trend of the calculated parameters with temperature is different for each analysis method used. The results obtained using the "x < 1" method are based on different field ranges. The shift of the lower limit of each field range to lower values with decreasing temperature is related to the decreasing effect of instrumental artefacts at low fields with the larger magnetization values. The shift to lower values of the high limit of the field ranges with decreasing temperature, implies that the field range where the assumption "x < 1" is applicable is limited to lower fields at lower temperatures. The "x < 1" method represents the situation where the thermal energy of the superparamagnetic particle is dominant over its magnetic energy, where the latter is associated with the alignment of the moment with the applied field (Section 2.6.2). At lower temperatures, there is less thermal energy and the magnetic energy can dominate the energy of the superparamagnetic particle at lower field strengths, therefore invalidating the “x < 1” assumption above a lower field limit. The results show that as the field range is limited to lower field strengths the resultant average sizes are larger. This is in agreement with the idea that at the lowest field strengths, the particles that first contribute to the magnetization, and start the process of alignment with the field while still fluctuating, are the bigger particles that have less thermal energy.

The results obtained using the “x >> 1” method are all based on the same field range. The results show smaller particles with smaller moments and larger intrinsic magnetization with decreasing temperature. The “x >> 1” method represents the case where the thermal energy is overcome by the magnetic energy due to the alignment of the magnetic moment of the superparamagnetic particle with the applied field. Because at lower temperatures the particles have less thermal energy, an increasing portion of the smaller particles is able to align with the field and therefore contribute to the estimated average values of the physical parameters.

At a given temperature, the results obtained from each of the two analysis methods differ because they are representing different processes. For instance, each of the physical parameters obtained using the “x < 1” method at 300 K represents the average associated with the particles that are in the process of aligning with the applied field, between 3.2 – 7 T, while still fluctuating due to their relative high thermal energy. Each of the physical parameters obtained with the “x >> 1” is the average associated with all of the particles that have aligned with the applied field, between 6.1 – 7 T, in this case. At this temperature, the results using the “x < 1” method give smaller sizes representing the particles that are still fluctuating in the 3.2 – 7 T field range due to their higher thermal energy, while the “x >> 1” method gives bigger sizes representing the particles that have aligned with the field between 6.1 – 7 T, because of their relatively lower thermal energy.

The range of particle sizes estimated with magnetic granulometry is between approximately 2 – 5 nm and is in the same order of magnitude of the size range estimated from pXRD with slightly lower values (Table 3.5). However, the magnetic sizes are much smaller than the dimensions estimated with SEM (Figure C.6), which could be representing a type of oriented aggregate of smaller crystallites.

3.4 Schwertmannites

The diffractogram for Sw-1 shows a small contribution of goethite (Figure B.7). This goethite impurity was also detected by Mössbauer spectroscopy, where it is seen as outer shoulders in lines 1 and 6 of the sextet obtained at 4.2 K (Figure F.17). This goethite contribution was quantified by the spectral analysis method of Rancourt and Ping (1991) using the Recoil™ software. The goethite impurity was found to be 10.0 (11) % of the total Fe, assuming equal Mössbauer recoilless fraction. The Mössbauer spectrum at 300 K for this sample (Figure F.17) does not show any contribution of a sextet related to magnetically blocked goethite therefore the goethite impurity is superparamagnetic at this temperature. Sw-2 does not show any impurity in its pXRD and, as Sw-1, it shows the typical broad peaks of schwertmannite (Cornell and Schwertmann, 2003). The pXRD coherence length estimates are shown in Table 3.7. The corresponding estimates for Sw-1 should be similar since it has a similar diffractogram to Sw-2, with the effects of the goethite and corundum impurities notwithstanding. The SEM micrographs show spherical aggregates that vary in size up to 500 nm (Figure C.7), similar to those observed for schwertmannite by Kawano and Tomita (2001) and Jönsson et al. (2005).

Table 3.7 Coherence length estimates (L) from pXRD for Sw-2

Miller index	**L (nm)**
(310)	2.0 (2)
(113)	2.4 (5)

The temperature cycle of Sw-1 shows superposed ZFC and FC curves from 210 K to ~ 85 K, below which there is hysteresis and a broad maximum in the ZFC curve, suggesting superparamagnetic behaviour (Figure D.19). At 300 K, the field cycle is non-hysteretic, does not show a sigmoidal curvature and shows small deviations of the data that are within the precision of the instrument (Figure E.50). As indicated previously, the Mössbauer spectrum at this temperature shows a doublet (Figure F.17), indicating the lack of magnetic blocking. At 235 K, the field cycle is non-hysteretic and shows a slight curvature which is shown to be increased at 150 K, where hysteresis is also not resolved (Figures E.51 and E.52). At 4.2 K, the field cycle shows hysteresis (Figure E.53) and the Mössbauer spectrum, as mentioned above, shows a sextet (besides that of the goethite impurity), implying a magnetic blocked state. The progression of higher magnetization values and increasing curvature with decreasing temperature in the field cycles suggest superparamagnetic behaviour from 300 K to 150 K, which extends down to 85 K, based on the superposition of the ZFC and FC curves.

The temperature cycle of Sw-2 shows superposed ZFC and FC curves down to ~ 75 K below which there is hysteresis (Figure D.20). Below 75 K, there is a peak in the ZFC curve at ~ 45 K and another one at ~ 1.8 K which is not completed at this temperature; they represent two main blocking events. The field cycle at 300 K is non-hysteretic and does not show curvature (Figure E.54). At 200 K and 100 K, the field cycles are also non-hysteretic and show increasing curvature with decreasing temperature (Figures E.55 and E.56), in agreement with superparamagnetism. At 1.8 K, the hysteresis in the field cycle represents the magnetic blocked state of the particles that have blocked down to that temperature (Figure E.57). The AC-susceptibility data for Sw-2 also shows evidence of superparamagnetic behaviour; it shows a peak in χ' and there is a frequency-dependency of this parameter below 60 K (Figures 3.12 and 3.13). This frequency-dependency disappears at lower temperatures when approaching the next blocking event or maximum at ~ 1.8 K. The χ'' values are near zero throughout all of the temperature range; as in the case of Gt-2, there is no cumulative effect that can be resolved in the data at lower temperatures due to the occurrence of multiple blocking events.

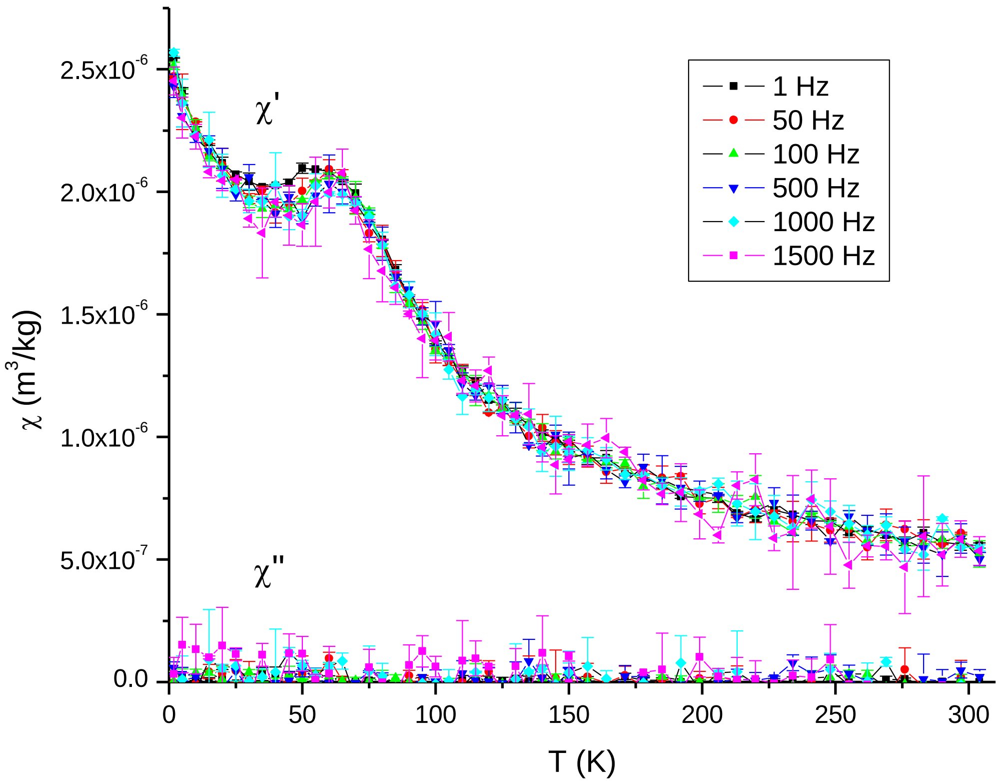

Figure 3.12 AC-susceptibility temperature runs (χ' and χ'') of Sw-2

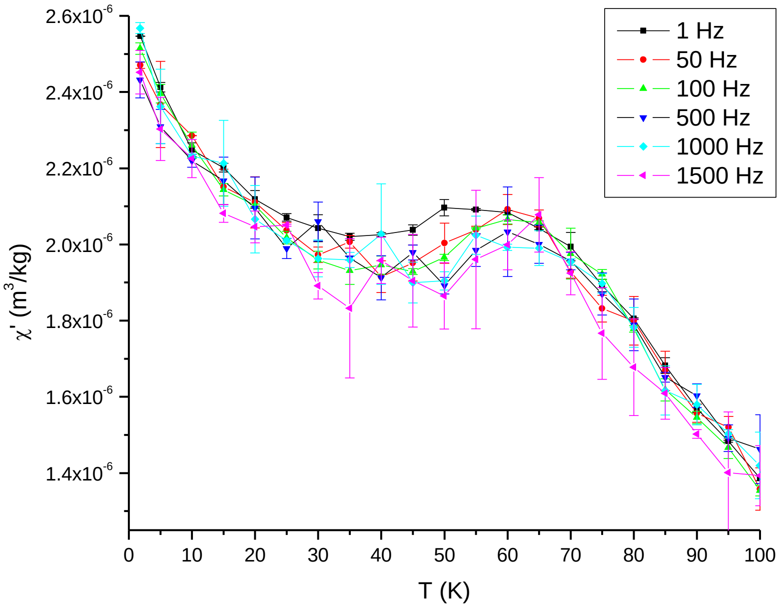

Figure 3.13 Zoom from 0 to 100 K of χ' of Sw-2

Table 3.8 shows the results obtained through the magnetic granulometry method. For Sw-1, the results represent an average that includes the contribution from the superparamagnetic goethite impurity. For the “x < 1” analysis method, the results for Sw-1 from the 235 K and 150 K data are in agreement. The results from either analysis method at each temperature differ in the same way as in the case of Lp-2, that is, they differ based on the different processes that they represent. For both Sw-1 and Sw-2, the results based on the “x >> 1” method show smaller moments and larger intrinsic magnetization values with decreasing temperature. They also show smaller sizes with decreasing temperature, in agreement with a larger fraction of the smaller particles being aligned with the applied field due the lower thermal energy at lower temperatures. For Sw-1, the estimated sizes with this method are bigger than for Sw-2. The results for Sw-1 are based on a lower maximum applied field ($H_{max} = 1$ T) than for Sw-2 ($H_{max} = 7$ T). At lower fields, only the larger particles are aligned with the field and at higher fields, a larger fraction of the smaller particles become aligned and therefore contribute to the estimated average size.

The range of sizes estimated for Sw-2 is approximately 2-5 nm, in agreement with the pXRD sizes estimated (Table 3.7) and is much smaller than the range of sizes of the spherical aggregates seen by SEM (Figure C.7).

Table 3.8 Physical parameters of the schwertmannite samples

	T	**Analysis Method**	$\mathbf{H_{max}}$	**H range**	**{μ}**		**{m}**	**{μ}/{m}**	**d**	**n**	**μ'**	**μ'/n**	**Comment**
	(K)	$x=\mu H/k_BT$	(T)	(T)	$x10^{-21}$ (Am^2)	(μ_B)	$x10^{-21}$ (kg)	(Am^2/kg)	(nm)	$x10^3$		(%)	
Sw-1	300	< 1	1										N/A[1]
	235	< 1	1	0.5-1	2.0 (3)	220 (4)	0.7 (2)	3 (1)	7.1 (8)	4 (1)	44 (7)	1.1 (4)	
	150	< 1	1	0.5-1	1.7 (1)	179 (11)	0.56 (7)	2.9 (4)	6.5 (3)	3.1 (4)	36 (2)	1.2 (2)	
	300	>> 1	1	0.9-1	8.7 (4)	941 (39)	12.4 (5)	0.70 (1)	18.3 (2)	68 (2)	188 (8)	0.28 (2)	
	235	>> 1	1	0.8-1	7.29 (9)	786 (10)	7.18 (8)	1.015 (6)	15.23 (6)	39.2 (4)	157 (2)	0.401 (7)	
	150	>> 1	1	0.8-1	4.98 (5)	537 (6)	3.90 (4)	1.277 (6)	12.43 (4)	21.3 (2)	107 (1)	0.504 (7)	
Sw-2	300	< 1	7										N/A[1]
	200	< 1	7	2-7	0.17 (2)	19 (2)	0.008 (2)	23 (5)	1.6 (1)	0.041 (8)	3.7 (4)	9 (2)	
	100	< 1	7										N/A[2]
	300	>> 1	7	5.8-7	1.30 (3)	140 (4)	0.273 (6)	4.75 (5)	5.12 (4)	1.49 (3)	28 (1)	1.88 (6)	
	200	>> 1	7	6.1-7	0.83 (2)	90 (2)	0.133 (2)	6.28 (5)	4.03 (2)	0.725 (1)	18 (1)	2.48 (6)	
	100	>> 1	7	5.8-7	0.47 (2)	50 (2)	0.50 (1)	9.4 (1)	2.90 (3)	0.271 (8)	10 (1)	3.7 (2)	

[1] Method not applicable due to a zero slope in the χ vs. H^2 graph (C_2=0)

[2] Method not applicable due to lack of a straight line in the χ vs. H^2 graph

3.5 Akaganéites

The diffractogram of Akg-1 shown in Bigham et al. (1990) confirms akaganéite as the only crystalline phase present in this sample. A more recent diffractogram was run in 2006, which shows only akaganéite and therefore proves the lack of phase transformation with time in this sample. The diffractogram of Akg-2 shows less peak broadening than Akg-1, suggesting that the former has a bigger crystallite size and/or a more crystalline structure (Figure B.8). The pXRD coherence lengths estimated from the peak with Miller index (110) are 7.3 (2) nm for Akg-1 and 30 (1) nm for Akg-2.

The SEM micrograph for Akg-1 (Figure C.8 (a)) shows nearly spherical units of 50 to 300 nm in diameter that aggregate into bigger clusters. The SEM image for Akg-2 shows spindle-shaped particles with sizes ranging from 370 x 100 nm to 1250 x 250 nm (Figure C.8 (b)).

The temperature cycle of Akg-1 shows evident hysteresis below ~ 175 K, however, between 175 K and ~ 250 K, the ZFC curve is consistently below the FC curve, suggesting that hysteresis actually starts below 250 K (Figure D.21). At lower temperatures (~ 35 K) the ZFC curve shows a maximum. At 300 K, the field cycle shows curvature and the hysteresis is not resolved (Figure E.58). At this temperature, the Mössbauer spectrum shows a doublet (Figure F.18). The field cycle at 230 K shows an increased curvature with hysteresis not clearly resolved (Figure E.59). At 100 K, there is an evident small hysteresis in the field cycle, indicating magnetic blocking (Figure E.60). At 4.2 K, the field cycle shows hysteresis (Figure E.61) and the Mössbauer spectrum shows a well-developed sextet, indicating a magnetically blocked state (Figure F.18). The latter observations for Akg-1 are in agreement with superparamagnetic behaviour above 250 K and a gradual magnetic blocking process starting below this temperature with a main blocking event at a lower temperature.

The temperature cycle of Akg-2 shows superposed ZFC and FC curves down to ~ 200 K, below which there is evident hysteresis (Figure D.22). Below 200 K, both FC and ZFC curves increase gradually and there are no obvious maxima of the ZFC curve. Above 200 K, there is a local maximum in both curves at ~ 250 K, but there is no hysteresis just below this temperature. The strength of the applied field in a temperature cycle can affect the position of peaks in the ZFC curve, the shape of the FC and ZFC curves and the degree of hysteresis, or separation between them (Section 1.2.2). In order to further investigate the event at 250 K, an additional temperature cycle was run for Akg-2 at a lower applied field (H = 0.1 T) (Figure D.23). In this temperature cycle it is evident that the hysteresis starts just below 250 K, suggesting that the peak at this temperature is one magnetic blocking event, marking the onset of this process. At lower temperatures, it can be seen that other features become more evident due to the lower field strength applied in the temperature cycle. There is a small broad peak in the ZFC curve at ~ 75 K, suggesting an additional noticeable blocking event. Additionally, at the lowest temperatures there is a sudden increase in χ in the FC curve which might be representing another blocking event not completed at 1.8 K. From the previous analysis, it can be said that the temperature cycle data for Akg-2 suggests a magnetic blocking process that starts below ~ 250 K and progresses in a relatively subtle fashion.

The field cycle of Akg-2 at 300 K is non-hysteretic and does not show curvature (Figure E.62). Upon decreasing the temperature down to 200 K and 100 K, the field cycles do not show an increased curvature and remain non-hysteretic (Figures E.63 and E.64), despite the fact that the temperature cycles suggest that magnetic blocking is occurring at these temperatures. The AC-susceptibility data does not show obvious frequency-dependence of χ’ and non-zero values of χ” (Figure 3.14). As with the goethite Gt-2, the magnetic blocking process occurs in multiple events and also in a very gradual way throughout a large temperature range, which makes the previously mentioned effects not evident from the data. At 1.8 K, the field cycle shows curvature but the hysteresis is not resolved (Figure E.65). As suggested by the temperature cycles, the magnetic blocking is not completed at this temperature, explaining the small hysteresis not resolved in this field cycle. As with the temperatures cycles, the field cycles and the AC-susceptibility data also suggest that the blocking process in Akg-2 progresses in a very gradual way.

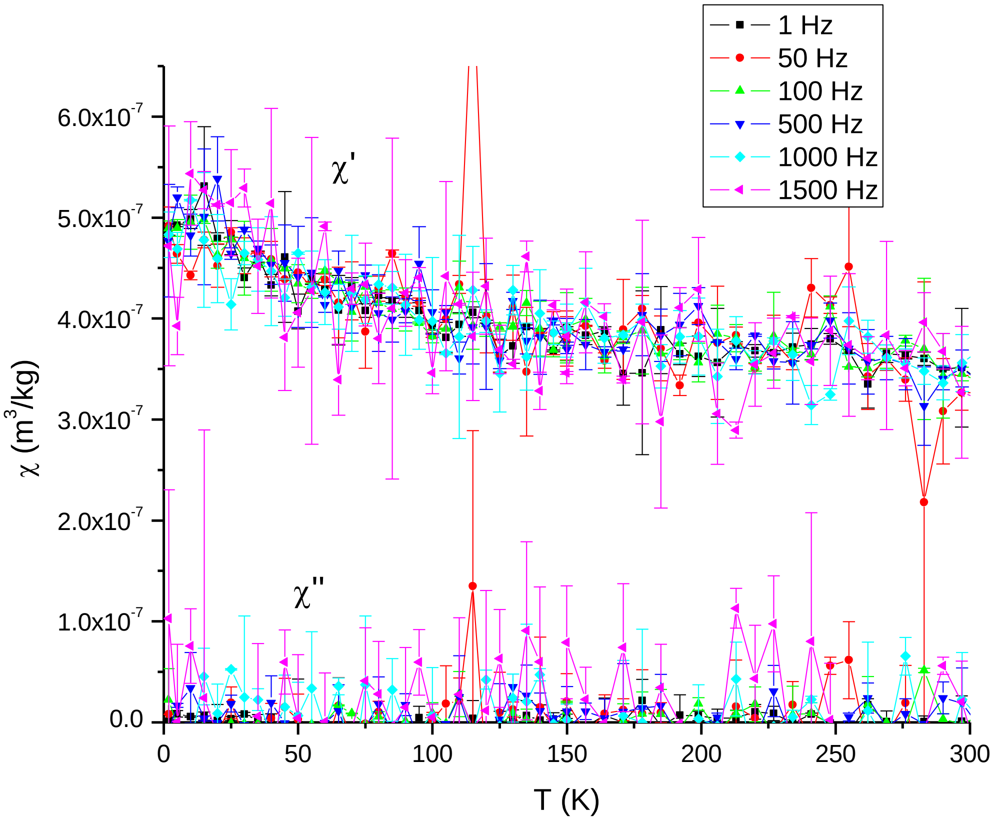

Figure 3.14 AC-susceptibility temperature runs (χ’ and χ”) of Akg-2

The magnetometry data for both akaganéites suggest superparamagnetic behaviour above 250 K therefore the magnetic granulometry method was applied to the field cycles at 300 K; the results are shown in Table 3.9. As previously discussed, the results for Akg-1 obtained with the two different analysis methods differ in agreement with the different processes they represent. The results for Akg-2 obtained with the "x >> 1" method are based on a higher field range than the corresponding results for Akg-1; consequently, the results for Akg-2 include a greater contribution from the smallest particles in its particle size distribution.

Table 3.9 Physical parameters of akaganéite samples from field cycles at 300 K

	H_{max}	**Analysis Method**	**H range**	**$\{\mu\}$**		**$\{m\}$**	**$\{\mu\}/\{m\}$**	**d**	**n**	**μ'**	**μ'/n**	**Comment**
	(T)	$x=\mu H/k_BT$	(T)	x10^{-21} (Am^2)	(μ_B)	x10^{-21} (kg)	(Am^2/kg)	(nm)	x10^3		(%)	
Akg-1	1	< 1	0.5-1	2.6 (2)	281 (17)	0.8 (1)	3.1 (4)	7.7 (3)	5.8 (7)	56 (3)	1.0 (1)	
	1	>> 1	0.8-1	9.39 (4)	1012 (5)	8.43 (4)	1.114 (2)	16.48 (2)	57.1 (2)	202 (1)	0.354 (2)	
Akg-2	7	< 1										N/A[1]
	7	>> 1	5.8-7	1.32 (3)	142 (3)	0.390 (7)	3.38 (3)	5.91 (3)	2.64 (5)	28 (1)	1.08 (3)	

[1] Method not applicable due to a zero slope in the χ vs. H^2 graph (C_2=0)

The estimated particle sizes for Akg-1 are between approximately 8 and 16 nm. As previously indicated, the pXRD size estimate is ~ 7 nm. Bigham et al. (1990) report rod-shaped particles of 3 to 6 nm in diameter for their sample, as seen by transmission electron microscopy (TEM). They also indicate that in a dry state, this sample has a strong tendency to aggregate, which is observed in the SEM micrograph (Figure C.8 (a)), where the spherical units aggregate into bigger clusters. These spherical units might be aggregates themselves of the smaller individual particles given by TEM, pXRD and magnetometry, which are not resolved in the SEM image. For Akg-2, the particle size estimates given by magnetometry and pXRD are smaller than the sizes of the particles seen by SEM (Figure C.8 (b)), which could be aggregates made up of smaller substructures.

Chapter 4 – Discussion

4.1 Superparamagnetic Behaviour

All of the ferrihydrite samples studied and the smallest goethite samples (Gt-1 and Gt-2) show superparamagnetic behaviour from a blocking temperature up to room temperature (300 K), in agreement with the fact that they are magnetically ordered up to high temperatures and have a small particle size. Despite previous claims of low Néel temperatures for lepidocrocite, schwertmannite and akaganéite, these minerals also show a behaviour consistent with superparamagnetism from 300 K down to a blocking temperature, below which they are magnetically blocked.

There are several features of the data that show evidence that the lepidocrocite, schwertmannite and akaganéite samples are not paramagnetic up to 300 K. The curvatures seen in the field cycles, between their respective blocking temperature and 300 K, are typical of superparamagnetism. A field cycle for a Fe^{3+} paramagnetic material would not show curvature for the field and temperature ranges ($|H| \leq 7$ T; $100 \text{ K} \leq T \leq 300$ K) used in the present work (Ashcroft and Mermin, 1976). Additionally, if the samples were paramagnetic, they would follow the Curie-Weiss law above the claimed T_N (Section 1.2.1). Table 4.1 shows the Curie-Weiss temperatures (T_{CW}) estimated from the measured magnetic susceptibility (χ) (given by slope of the field cycles) at the different temperatures above the claimed T_N values. The results show that, for lepidocrocite and schwertmannite, the T_{CW} values are not constant with temperature, in disagreement with the Curie-Weiss law.

Table 4.1 Curie-Weiss temperatures (T_{CW}) and $|T_{CW}|/T_N$ values for the lepidocrocite, schwertmannites and akaganéite samples

Sample	**T (K)**	**χ (x 10^{-7} m^3/kg)**	**T_{CW} (K)**	**$\|T_{CW}\|/T_N$**
Lp-2	300	5.2685 (8)	-670 (17)	9 – 15
	200	7.221 (1)	-508 (13)	7 – 12
	100	12.406 (2)	-312 (7)	4 – 7
Sw-1	300	4.683 (4)	-753 (39)	9 – 11
	235	7.174 (4)	-452 (25)	6
	150	9.652 (4)	-361 (19)	4 – 5
Sw-2	300	4.676 (2)	-651 (8)	8 – 9
	200	5.979 (2)	-544 (8)	7 – 8
Akg-1	300	7.990 (2)	-340 (11)	1 – 23
Akg-2	300	3.332 (1)	-1278 (3)	4 – 85

For all three minerals, paramagnetism can also be discarded based on the relationship between the T_{CW} obtained from the measurements and the previously claimed T_N. This is done by looking at the $|T_{CW}|:T_N$ ratio (Section 1.2.1). The ranges of $|T_{CW}|/T_N$ values, based on the range of claimed T_N, are shown in Table 4.1; they are all above the values expected and experimentally confirmed for antiferromagnetic systems (Section 1.2.1). However, a difference between T_N and T_{CW} can be due to a decrease in the dimensionality of the magnetic structure. As indicated in Section 1.3.2, the low T_N claimed for lepidocrocite has been linked to a possible low dimensionality of the magnetic structure due to the layer-like nature of its crystalline structure. De Jongh and Miedema (1974) have reviewed the theoretical and experimental $|T_{CW}|/T_N$ values for 2-dimensional antiferromagnetic systems with magnetic ions with an atomic spin quantum number (S) of 5/2 and a face-centered type of lattice such as in the case of lepidocrocite, and have found that it does not exceed 2.6. The values of this ratio for the lepidocrocite in this study are clearly larger than this limit. Another reason for high values of $|T_{CW}|/T_N$ (> 10) can be the existence of high degrees of magnetic frustration, where the spins are arranged in a non-collinear fashion (Ramírez, 1994). Lepidocrocite and akaganéite have a collinear antiferromagnetic structure as shown by neutron diffraction and Mössbauer spectroscopy and the unsolved crystalline and magnetic structure of schwertmannite is expected to be similar to that of akaganéite or ferrihydrite, the latter which has also been shown to have an antiferromagnetic structure (Section 1.3.1). Therefore, the $|T_{CW}|/T_N$ values are another indication that those samples are not paramagnetic up to 300 K.

The superparamagnetic behaviour and the associated magnetic blocking process at low temperatures for these three minerals are in agreement with the lack of heat capacity anomalies (usually associated with magnetic ordering) up to 300 K and the variation of the Mössbauer spectra and magnetic susceptibility with temperature and applied field (Section 1.3.2). This is not the first time that the blocking temperature has been misinterpreted as the Néel temperature for iron oxyhydroxide nanoparticles; it also occurred for ferrihydrite (e.g., Coey and Readman, 1973; Zergenyi et al., 2000). However, this was later clarified by neutron diffraction studies confirming the antiferromagnetic structure of ferrihydrite up to high temperatures (e.g., Jansen et al., 2002).

4.2 Physical Parameters

Chapter 3 presented the results for the physical parameters extracted from the analysis of the field cycles, at temperatures where the samples were superparamagnetic, based on the two analysis methods, “$x < 1$” and “$x >> 1$”. The differences in the estimated values (e.g., diameter), obtained by the two different analysis methods using different field ranges at different temperatures, was discussed when presenting the data (e.g., Section 3.3). However, due to the fact that the “x >> 1” method was systematically applicable to all of the samples, the results related to this method are the ones further considered. As opposed to the case of the “x < 1” method, the extraction of the parameters estimated using the “x >> 1” method is not based on an assumption about the type of particle size distribution, in order to directly obtain the average thermal values of the moment and mass of the superparamagnetic particles (Section 2.6.2), and it does not suffer from the effect of instrumental artefacts.

The progressive alignment of smaller particles with the applied field upon decreasing the temperature, as evidenced in the decrease of the average sizes extracted for many samples, suggests a variable size distribution in the samples. In the field cycles, a mixture of different sizes can be evidenced by characteristic shapes (i.e., wasp-waisted, pot-bellied) in the curve, as seen for the goethite Gt-2 sample. Also, the temperature runs (DC and AC) can give a qualitative sense of the size distribution. Due to the intrinsic relationship between the blocking temperature and the particle volume (Section 1.2.2), the number of main magnetic blocking events evidenced in the temperature runs, suggests multiple modes in the size distribution, as it was the case for the goethite Gt-2, akaganéite Akg-2 and schwertmannite Sw-2. Also, the gradual onset of both the hysteresis in the DC temperature cycle and the frequency-dependence of χ' of the 6-line ferrihydrite 6L-Fh-1, for example, likely indicates that the size distribution is broader in this sample than in the two-line ferrihydrite (2L-Fh). This was observed in previous studies of ferrihydrite and the difference in the breadth of the size distribution was confirmed by high-resolution TEM size estimates (Berquó et al., 2007; Carta et al., 2009). However, for the specific case of 2-line ferrihydrite, which has a very small particle size, an increase in the contribution of the surface anisotropy with decreasing particle size can be the cause for having a relaxation time distribution (evidenced in the temperature runs) that is narrower than the actual particle size distribution (Section 1.2.1), thereby causing the significantly sharp peak associated with magnetic blocking in the χ' curve and the sudden onset of hysteresis in the DC temperature cycle. The latter scenario would explain the fact that there is not a large difference in the degree of variation with temperature of the average magnetic sizes estimated between these two types of ferrihydrite (0.7 nm in 2L-Fh and 0.87 nm in the 6L-Fh's), since the estimation of these values is not affected by the magnetic anisotropy energy (Section 2.6.2).

The coherence lengths (L) or crystalline domain sizes estimated from pXRD and the average sizes estimated from magnetometry are in agreement for all of the samples, except for the akaganéites. The agreement between the magnetometry and the pXRD sizes implies that the magnetic domain and the crystalline domain are the same. For all of the samples, both the magnetic sizes and the pXRD sizes are smaller than those estimated from the SEM images, showing a strong tendency of aggregation.

In the case of the ferrihydrites, the SEM images did not provide resolution of individual particles. The average magnetic domain sizes estimated for 2-line and 6-line ferrihydrite were 2.6 and 4.0 nm, respectively, which is in agreement with previous results of particle size obtained by high-resolution TEM (e.g., Michel et al., 2007a; Silva et al., 2008). Similar results were also obtained for ferrihydrite for which magnetic sizes were estimated using neutron diffraction (Seehra et al., 2000).

For the schwertmannites, the pXRD sizes and the average magnetic sizes estimated (2 – 18 nm) are much smaller than the sizes estimated for the spherical or hedge-hog-like aggregates usually seen through electron microscopy (500 – 1000 nm), in the present work and in the literature. Loan et al. (2004) have suggested that schwertmannite is not a single-phase structure and that the needles at the surface (of the hedge-hog-like aggregates) have a different structure than the core. TEM sizes for these needles have been found to be 2 – 30 nm in diameter and 60 – 300 nm in length (Bigham et al., 1994; Loan et al., 2004). The SEM image for the schwertmannite Sw-2 (Figure C.7) does not resolve features within the lower half of the needles' diameter range and its average magnetic size (of a bimodal size distribution) is less than 5 nm. Regardless of the phase structure in schwertmannite, the results suggest that the average magnetic domain size in schwertmannite does not exceed the order of the diameter of the needles at the surface of the aggregates which are usually reported for this mineral.

For the rest of the samples, many of the aggregates seen in the SEM images show well-defined and characteristic morphology, like the laths or needles in the case of the goethites and lepidocrocite and the spindle-like particles of akaganéite (Akg-2), suggesting a type of "oriented aggregate" that does not imply a continuity of either the crystalline domain or the magnetic domain.

The specific case of the akaganéites is an interesting one, since many morphological studies have proposed that these rod- or spindle-shaped particles usually seen in electron microscopy represent superstructures composed of smaller parallel rod-like subunits (< 5 nm in diameter) that have aggregated and experienced secondary nucleation (e.g., Gallagher, 1970; Holm, 1985; Richmond et al., 2006). Therefore both the pXRD and the magnetic sizes estimated may represent these smaller sub-units. As mentioned previously, the magnetic and crystalline domain sizes (from pXRD) for the akaganéites are not in agreement. Based on the diffraction peak used to do the size estimation, the pXRD sizes for the akaganéites represent the coherence length across a conical section of the rods. Accordingly, for Akg-1, the latter dimension is larger than the TEM diameters given by Bigham et al. (1990). The larger average magnetic domain diameter for Akg-1 could be a result of the assumption of a spherical particle shape and/or the use of a maximum applied field of 1 T in its estimation, which would make it biased towards larger particles in the sample's particle size distribution. In the case of Akg-2, the average magnetic domain size estimated is smaller than the crystalline domain size from pXRD. Due to the layered type of antiferromagnetic structure in akaganéite and to the type of crystal symmetry that can be present in this mineral (Section 1.3.1), it is possible to have particles attaching to each other in such a way that there is a continuity of the crystalline domain, but not of the magnetic domain, as a result of the interruption of the alternating sequence of the layers of spins coupled antiferromagnetically.

All of the physical parameters estimated for the P-HFO series of samples show a variation with P concentration that is similar to trends seen by Thibault et al. (2009) using pXRD and Mossbauer data of this P-HFO series of samples, which were interpreted as the effect of a limiting P:Fe ratio of 1:2 of incorporation of P within the HFO structure. Thibault et al. (2009) indicated that up to the latter ratio, P is not only forming a complex at the particle's surface but it is also incorporated within the structure of the HFO. The incorporation of P within the structure can affect the magnetic superexchange paths coupling the Fe^{3+} cations having a direct effect on its magnetism, and this could be the reason of the decreasing average moment and intrinsic magnetization up to the latter P:Fe ratio. The variation of the latter parameters can also be related to the variation in particle size, which shows an increasing trend up to the P:Fe = 1:2 ratio, in the magnetic field range measured ($|H| \leq 1$ T). A limiting P:Fe ratio can explain the qualitative observations of the field cycles and temperature runs. The increasing incorporation of P within the structure would inhibit both the magnetic blocking, evidenced in the temperature runs, and the presence of curvature in the field cycles, which is related to the lower magnetic moment of the superparamagnetic particles (Appendix A).

All samples have a net magnetic moment, a defect moment due to uncompensation of the spins in the antiferromagnetic structure of the superparamagnetic particles. This uncompensation can be due to the presence of defects in the structure and to the non-continuity of this structure at the surface. The origin of this defect moment will be discussed later in Section 4.3. This defect moment is evidenced in the field cycles at the lowest temperatures reached (i.e., 1.8 K and 4.2 K), by showing remanence and hysteresis. The intrinsic magnetization associated with the defect moment was calculated using the magnetic granulometry method. Figure 4.1 shows the extracted intrinsic magnetization ({μ}/{m}) and estimated diameter (d), at the lowest temperature where superparamagnetism was evidenced, for all of the samples. The values of saturation magnetization for magnetite (superparamagnetic to multi-domain) (Goya et al., 2003) and single-domain hematites (González-Lucena, 2004) are included in Figure 4.1 for comparison purposes. The results for 6-line ferrihydrite samples at 162 K from a previous study (Guyodo et al., 2006) using an alternative magnetic granulometry method are included (symbol +) along with the results of the analysis of this published data using the method used in the present work (i.e., Rancourt et al., 2004) (symbol ×).

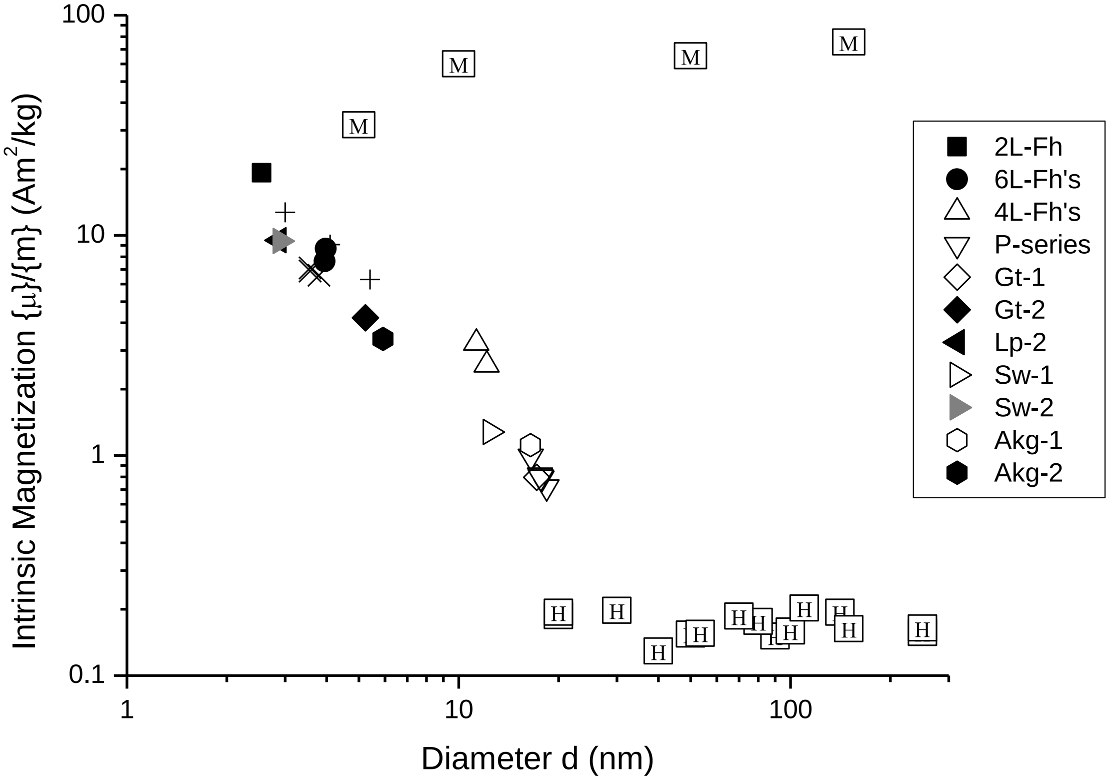

Figure 4.1 Summary graph of intrinsic magnetization and diameter for all samples studied. Solid symbols represent data extracted using H_{max} = 7 T and open symbols represent data extracted using H_{max} = 1 T. Values for magnetite [M] (Goya et al., 2003) and hematite [H] (González-Lucena, 2004) have been added for comparison. Results from Guyodo et al. (2006) (symbols × and +) are also added as explained in the text

All of the superparamagnetic iron oxyhydroxides studied are along the same linear trend in this logarithmic graph. As the particle size decreases, the intrinsic magnetization increases reaching relatively high values that are in the order of those for magnetite nanoparticles, the latter being the most magnetic mineral in surface environments. For all of the samples, the use of even higher applied fields can lead to the estimation of the true average intrinsic magnetizations which can be higher than those estimated here.

The results obtained by Guyodo et al. (2006) for a series of 6-line ferrihydrite samples (symbol +) were obtained applying an alternative magnetic granulometry method based on the use of a modified Langevin function that includes an additional linear term representing the antiferromagnetic susceptibility. These results follow the same linear trend previously explained. The results obtained from analyzing the data published in Guyodo et al. (2006), using the magnetic granulometry used in the present study (i.e., Rancourt et al., 2004) (symbol ×), are in agreement with the other 6-line ferrihydrites considered in the present study and follow the common linear trend among all of the samples in this graph. The results suggest that the inclusion of an additional term for the antiferromagnetic susceptibility in the Langevin expression does not seem to be necessary for the magnetic field strengths and temperatures used in the present study and in the study done by Guyodo et al. (2006). Additionally, the method proposed by Rancour et al. (2004) is simpler, easier to apply and does not require the estimation of the particle size distribution by TEM.

4.3 Moment Formation Mechanism

The general trend of increasing magnetization for smaller particles in antiferromagnetic systems hypothesized by Néel (1961) is evidenced in Figure 4.1. The fact that all of the samples follow a common linear trend suggests a common moment formation mechanism. Based on the idea proposed by Néel (1961) that there is a relationship between the total number of magnetic cations in the particle (n) and the net number of magnetic cations contributing to the observed magnetic moment of the particle (μ'), the moment formation mechanism can be explored using the following general expression:

$$\mu' = A\, n^{\alpha} \tag{4.1}$$

By taking the natural logarithm on both sides of the equation:

$$\ln(\mu') = \ln(A) + \alpha \ln(n) \qquad (4.2)$$

This implies that on a graph of $\ln(\mu')$ vs. $\ln(n)$, a straight line has an intercept equal to $\ln(A)$ and a slope equal to α. Figure 4.2 shows the resultant linear fit for the data. This fit gives: $\alpha = 0.54\ (2)$ and $\ln(A) = -\ 0.6\ (2)$, which implies:

$$\mu' = 0.5\ (1)\ n^{0.54\ (2)} \qquad (4.3)$$

This result is in agreement with an exponent of $\alpha = ½$, which represents the model where there is a random spatial distribution throughout the particle of uncompensation of the spins in the antiferromagnetic structure (Table 1.5). The results also show that the net defect moment of the superparamagnetic particles of iron oxyhydroxides is not only due to the uncompensation of spins as a result of surface effects, which are considerable in nanoparticles, but that it also comes from random uncompensation of the spins in the core of the particles due to defects.

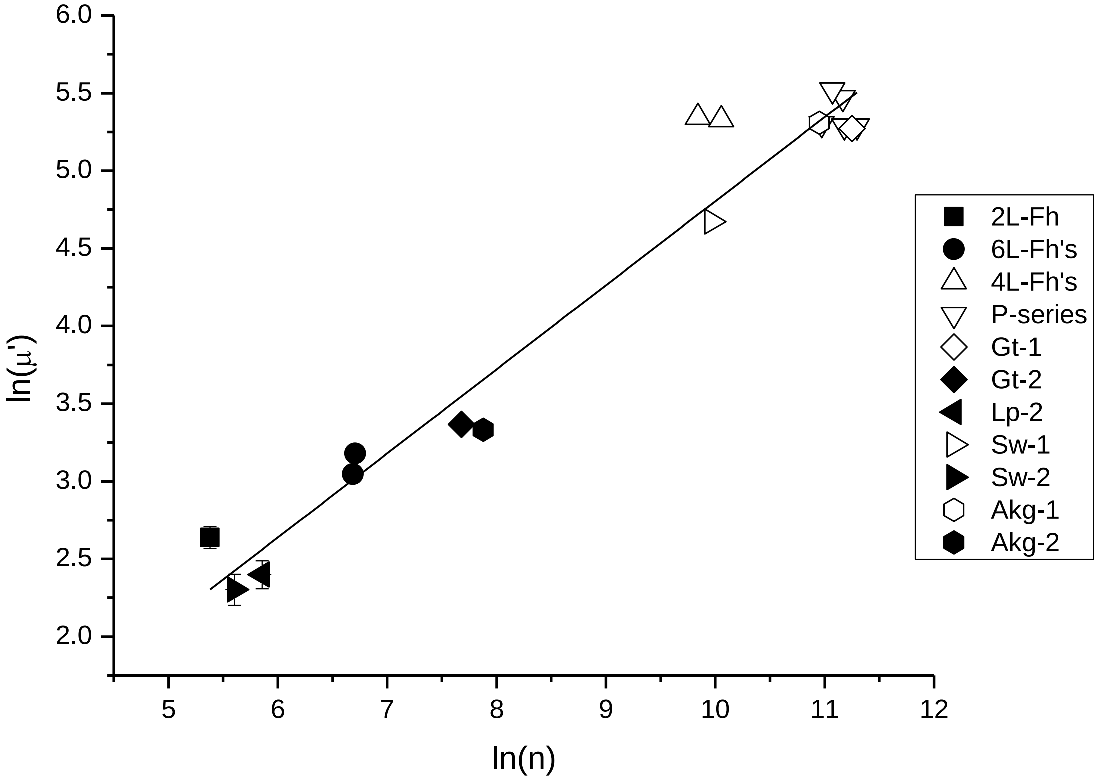

Figure 4.2 Exploration of the moment formation mechanism based on the model $\mu' = A\ n^{\alpha}$

The pre-factor A of 0.5 represents the fraction of magnetic cations for which the random uncompensation model applies, which means that 50 % of the total Fe^{3+} spins in the superparamagnetic particle is randomly uncompensated. Based on the results for μ'/n (%) shown in Chapter 3, the uncompensation generally comes from a small fraction of the total Fe^{3+} spins in the superparamagnetic particle.

It is worth noting here that the resultant common moment formation mechanism for the iron oxyhydroxides considered in the present work has been obtained from the direct analysis of the data without the need of preliminary assumptions such as particle size or stoichiometry (Section 1.3.3). In fact, the same result, within error, is obtained using the n estimated from the measured N (Appendix G) instead of the n based on the stoichiometry of the assumed nominal chemical formulas (Section 1.3).

Conclusions

All of the common iron oxyhydroxide minerals: goethite, ferrihydrite, lepidocrocite, akaganéite and schwertmannite are magnetically ordered at room temperature, as evidenced by their superparamagnetic behaviour associated with their small particle size nature. Previous claims of low Néel temperatures for lepidocrocite, akaganéite and schwertmannite are understood as misinterpreted magnetic blocking temperatures. The results suggest that, like the rest of the iron oxides and iron oxyhydroxides, the Néel temperatures for lepidocrocite, akaganéite and schwertmannite are above room temperature, which is consistent with the relatively strong magnetic exchange couplings.

Future studies of lepidocrocite, akaganéite and schwertmannite should aim at the direct measurement of the magnetic ordering temperature at high temperatures using neutron diffraction (with deuterated samples), heat capacity and thermomagnetic measurements. However, high temperatures are expected to increase the complexity of separating the magnetic and lattice contributions in heat capacity measurements, for instance. Additionally, high temperatures may also lead to phase transformations, as in the case of lepidocrocite, which could prevent the direct observation of the magnetic transition.

The elucidation of the magnetic state of lepidocrocite, akaganéite and schwertmannite has important repercussions in the field of environmental magnetism. It provides a reference for a more accurate discrimination of the superparamagnetic fraction in samples and therefore a more accurate interpretation of the measured signals. Additionally, the strong tendency of these nanoparticles to aggregate, especially in aqueous media, has implications in the natural remanent magnetization of environmental materials. As the iron oxyhydroxide nanoparticles aggregate, they can potentially couple magnetically and become larger stable single-domain magnetic phases with high intrinsic magnetizations, thereby becoming important magnetic remanence carriers. In fact, this may be the case associated with the first report of magnetic remanence in both synthetic and natural ferrihydrite reported by Pannalal et al. (2005).

Besides confirming the magnetic state of the iron oxyhydroxide nanoparticles, the systematic magnetic study complemented with the Mössbauer spectroscopy, pXRD and SEM analyses have enabled their nanoscale (< 10 nm) mineralogical characterization. The study has shown the possible effect of crystal chemical variations, such as those associated with elemental structural incorporation, on the intrinsic physical properties of the material. It has provided qualitative information about the particle size distribution within a sample and quantitative results in the estimation of particle sizes. In particular, the estimation of sizes of magnetic domains can be useful in the study of magnetic coupling in aggregates of nanoparticles.

Additionally, the present study provides experimental evidence for a common magnetic moment formation mechanism of spin uncompensation for the iron oxyhydroxide nanoparticles, confirming a model for small antiferromagnetic particles originally proposed by Louis Néel in 1961. This provides fundamental insight into the magnetic nanostructure of these minerals showing that the defects leading to spin uncompensation, associated with different degrees of structural disorder and stoichiometric variability in these nanoparticles, are randomly distributed throughout their volume. Furthermore, it shows that there is not a significant difference in the defect distribution and defect density in the core and in the surface region of the particle. This could be due, for instance, to the lowering of the surface strain of the particles as a result of water adsorption (e.g., Waychunas and Zhang, 2008); the latter has been evidenced by thermoanalysis for all of the iron oxyhydroxide minerals

(Ishikawa and Inouye, 1976; Cornell and Schwertmann, 2003). Specifically, for the smallest particles (e.g., 2-line ferrihydrite), the case could be that the high strain of the surface region of the particle is extended throughout its entire volume due to its small size. In any case, the elucidation of the magnetic nanostructure of these iron oxyhydroxide mineral nanoparticles also contributes to the characterization of the structure of their surface region; the latter has an effect on the particles' reactivity in the environment.

Acknowledgements

I would like to thank my supervisors Dr. Danielle Fortin and Dr. Gilles Lamarche for welcoming me as a graduate student in 2009. Your continuous scientific guidance, help and encouragement has been crucial for me to complete and finish this thesis. I would like to acknowledge Dr. Denis Rancourt for his guidance and for his help in the conception of this project.

I would like to acknowledge the late Mrs. Anne-Marie Lamarche for her help in the interpretation of published neutron diffraction data. I thank Dr. Andrew Gault for his help in the synthesis of the samples. I also appreciate the helpful discussions I had with Pierre-Jean Thibault and Jean-François Meunier. I thank all of the persons (listed in Chapter 2) who provided samples and performed measurements used in the present work.

I would like to acknowledge the help and support provided by the Dean of the Faculty of Science, Dr. A. E. Lalonde and the Dean of the Faculty of Graduate and Post-doctoral Studies, Dr. Gary Slater. I also would like to thank the reviewers of this thesis: Dr. Richard Cox, Dr Joseph Hodych, Dr. Dogan Paktunc and Dr. Kenneth Torrance for their helpful comments and suggestions.

I am grateful to my friends and peers from both the Physics and Earth Sciences departments for their support. I thank all of my family back in Venezuela for their continuous encouragement. I specially thank mon amour, Oscar, for his continuous support and his patience.

I also would like to acknowledge the financial support from the University of Ottawa in the form of a Graduate Admission Scholarship, an International Tuition Fee Scholarship and Graduate Bursaries.

References

Afanas'ev, A.M. and Chuev, M.A. (2003) "Mössbauer spectra of single-domain particles with rotating magnetic moments" *Journal of Physics: Condensed Matter* 15: 4827-4839

Ashcroft, N. W. and N. D. Mermin (1976) *Solid State Physics*. Holt, Reinhart and Winston: Philadelphia

Berquó, T.S., Banerjee, S.K., Ford, R.G. and Penn, R.L. (2007) "High crystallinity Si-ferrihydrite: An insight into its Néel temperature and size dependence of magnetic properties" *Journal of Geophysical Research* 112: B02102

Bigham, J.M., Schwertmann, U., Carlson, L., and Murad, E. (1990) "A poorly crystallized oxhyhydroxysulfate of iron formed by bacterial oxidation of Fe (II) in acid mine waters" *Geochimica et Cosmochimica Acta* 54: 2743-2758

Bigham, J.M., Carlson, L., and Murad, E. (1994) "Schwertmannite, a new iron oxyhydroxy-sulphate from Pyhäsalmi, Finland, and other localities" *Mineralogical Magazine* 58: 641-648

Bocquet, S., Pollard, R.J., and Cashion, J.D. (1995) "Shape anisotropy in antiferromagnetic superparamagnetic particles" *Journal of Applied Physics* 77 (6): 2809-2810

Bødker, F., Hansen, M.F., Bender Koch, C., Lefmann, K., and Mørup, S. (2000) "Magnetic properties of hematite nanoparticles" *Physical Review B* 61: 6826-6838

Bowden, M.E. and Ryan, M.J. (1991) "Comparison of intensities from fixed and variable divergence X-ray diffraction experiments" *Powder Diffraction* 6: 78–81

Buffle J., De Vitre R. R., Perret D. and Leppard G. G. (1989) "Physico-chemical characteristics of a colloidal iron phosphate species formed at the oxic–anoxic interface of a eutrophic lake" *Geochimica et Cosmochimica Acta* 53: 399–408

Carta, D., Casula, M.F., Corrias, A., Falqui, A., Navarra, G. and Pinna, G. (2009) "Structural and magnetic characterization of synthetic ferrihydrite nanoparticles" *Materials Chemistry & Physics* 113 (1): 349-355

Chambaere, D. and De Grave, E. (1984) "On the Néel temperature of β-FeOOH: structural dependence and its implications" *Journal of Magnetism and Magnetic Materials* 42: 263-268

Coey, J.M.D. and Readman, P.W. (1973) "New spin structure in an amorphous ferric gel" *Nature* 246: 476-478

Coey, J.M.D., Barry, A., Brotto, J.-M., Rakoto, H., Brennan, S., Mussel, W.N., Collomb, A. and Fruchart, D. (1995) "Spin flop in goethite" *Journal of Physics – Condensed Matter* 7 (4): 759-768

Cornell, R. M. and U. Schwertmann. (2003) *The Iron Oxides - Structure, Properties, Reactions, Occurrence and Uses*. VCH: Weinheim. Second Edition. 664 pp.

Cundy, A.B., Hopkinson, L. and Whitby, R.L.D. (2008) "Use of iron-based technologies in contaminated land and groundwater remediation: A review" *Science of the Total Environment* 400: 42-51

De Grave, E., Persoons, R.M., Chambaere, D.G., Vandenberghe, R.E. and Bowen, L.H. (1986) "An ^{57}Fe Mössbauer effect study of poorly crystalline γ-FeOOH" *Physics and Chemistry of Minerals* 13: 61-67

De Grave, E., Da Costa, G.M., Bowen, L.H., Schwertmannn, U. and Vandenberghe, R.E. (1996) "^{57}Fe Mössbauer effect study of Al-substituted lepidocrocites" *Clays and Clay Minerals* 44: 214-219

De Jongh, L.J. and Miedema, A.R. (1974) "Experiments on simple magnetic model systems" *Advances in Physics* 23: 1 -260

Dézsi, I., Keszthelyi, L., Kulgawczuk, D., Molnár, B., and Eissa, N.A. (1967) "Mössbauer study of β- and δ-FeOOH and their disintegration products" *Physica Status Solidi* 22: 617-628

Diakonov, I.I. (1998) "Thermodynamic properties of iron oxides and hydroxides. III. Surface and bulk thermodynamic properties of lepidocrocite (gamma-FeOOH) to 500 K" *European Journal of Mineralogy* 10, 31-41

Dormann, J., Fiorani, D. and Tronc, E. (1997) "Magnetic relaxation in fine-particle systems" In *Advances in Chemical Physics* 98: 283-494; Prigogine, I. and Rice, S.A. Eds.; Wiley: New York

Drits, V.A., Sakharov, B.A., Salyn, A.L., and Manceau, A. (1993) "Structural model for ferrihydrite" *Clay Minerals* 28 (2): 185-208

Duarte, E.L., Itri, L., Lima, E., Baptista, M.S., Berquó, T.S. and Goya, G.F. (2006) "Large magnetic anisotropy in ferrihydrite nanoparticles synthesized from reverse micelles" *Nanotechnology* 17 (22): 5549-5557

Dutkiewicz, S., Follows, M.J., and Parekh, P. (2005) "Interactions of the iron and phosphorus cycles: A three-dimensional model study" *Global Biogeochemical Cycles* 19: GB1021

Dunlop, D.J. and Özdemir, Ö. (1997) *Rock magnetism: Fundamentals and frontiers* Cambridge University Press: New York. 573 pp.

Eggleton, R.A. and Fitzpatrick, R.W. (1990) "New data and a revised structural model for ferrihydrite: Reply" *Clays and Clay Minerals* 38 (3): 335-336

Eneroth, E. and Koch, C.B. (2004) "Fe-hydroxysulphates from bacterial Fe^{2+} oxidation" *Hyperfine Interactions* 156/157: 423-429

Föllmi K. B. (1996) "The phosphorus cycle, phosphogenesis and marine phosphate-rich deposits" *Earth-Science Reviews* 40: 55–124

Forsyth, J.B., Hedley, I.G., and Johnson, C.E. (1968) "The magnetic structure and hyperfine field of goethite (α-FeOOH)" *Journal of Physics C* 1: 179-188

Fortin, D. (1992) *Caractérisation chimique et microscopique des oxyhydroxydes de fer naturels formés "in situ" dans les sédiments lacustres.* Université du Québec. Thèse de doctorat (présentée à l'Institut National de la Recherche Scientifique INRS-eau)

Fortin, D. and Langley, S. (2005) "Formation and occurrence of biogenic iron-rich minerals" *Earth-Science Reviews* 72: 1-19

Fox L. E. (1989) “A model for inorganic control of phosphate concentrations in river waters” *Geochimica et Cosmochimica Acta* 53: 417–428

Gallagher, K.J. (1970) “The atomic structure of tubular subcrystals of β-iron (III) oxide hydroxide” *Nature* 226: 1225-1228

García, K.E., Morales, A.L., Barrero, C.A., Arroyave, C.E., and Greneche, J.M. (2004) “Magnetic and crystal structure refinement in akaganéite nanoparticles” *Physica B* 354: 187-190

Gilles, C., Bonville, P., Wong, K.K.W. and Mann, S. (2000) “Non-Langevin behaviour of the uncompensated magnetization in nanoparticles of artificial ferritin” *The European Physical Journal B* 17: 417-427

González-Lucena, F. (2004) *Mineral magnetism of synthetic microcrystalline and nanophase iron oxides and iron oxyhydroxides*. University of Ottawa. M.Sc. Thesis

Goya, G.F., Berquó, T.S., Fonseca, F.C. and Morales, F.C. (2003) “Static and dynamic magnetic properties of spherical magnetite nanoparticles” *Journal of Applied Physics* 94: 3520-3528

Gualtieri, A.F. and Venturelli, P. (1999) “In situ study of the goethite-hematite phase transformation by real time synchrotron powder diffraction” *American Mineralogist* 84: 895-904

Guo, X. and Chen, F. (2005) "Removal of arsenic by bead cellulose loaded with iron oxyhydroxide from groundwater" *Environmental Science and Technology* 39: 6808-6818

Guyodo, Y., Banerjee, S.K., Penn, R.L., Burleson, D., Berquó, T.S., Seda, T. and Solheid, P. (2006) "Magnetic properties of synthetic six-line ferrihydrite nanoparticles" *Physics of the Earth and Planetary Interiors* 154: 222-233

Guyodo, Y. (2007) "Bio-mediated formation of magnetite and maghemite particles" *The IRM Quaterly* 16 (4): 2-3

Hanesch, M., Stanjek, H., and Petersen, N. (2006) "Thermomagnetic measurements of soil iron minerals: the role of organic carbon" *Geophysical Journal International* 165: 53-61

Harris, J.G.E., Grimaldi, J.E., Awschalom, D.D., Chiolero, A. and Loss, D. (1999) "Excess spin and the dynamics of antiferromagnetic ferritin" *Physical Review B* 60 (5): 3453-3456

Hirt, A.M., Lanci, L., Dobson, J., Weidler, P. and Gehring, A.U. (2002) "Low-temperature magnetic properties of lepidocrocite" *Journal of Geophysical Research-Solid Earth* 107: 2011

Hochella, M.F., Lower, S.K., Maurice, P.A., Penn, R.L., Sahai, N., Sparks, D.L. and Twining, B.S. (2008) "Nanominerals, mineral nanoparticles and Earth systems" *Science* 319: 1631-1635

Hogg, C.S., Malden, P.J., and Meads, R.E. (1975) “Identification of iron impurities in natural kaolinites using the Mössbauer effect” *Mineralogical Magazine* 40: 89-96

Holm, N.G. (1985) “New evidence for a tubular structure of β-iron (III) oxide hydroxide – akaganéite” *Origins of Life* 15: 131-139

Ishikawa, T. and Inouye, K. (1976) “Evolved gas detection of iron oxyhydroxides” *Journal of Thermal Analysis and Calorimetry* 10 (3): 399-410

Jambor, J.L. and Dutrizac, J.E. (1998) “Occurrence and constitution of natural and synthetic ferrihydrite, a widespread iron oxyhydroxide” *Chemical Reviews* 98: 2549-2585

Janney, D.E., Cowley, J.M. and Buseck, P.R. (2000) “Structure of synthetic 2-line ferrihydrite by electron nanodiffraction” *American Mineralogist* 85: 1180-1187.

Jansen, E., Kyek, A., Schäfer, W. and Schwertmann, U. (2002) “The structure of six-line ferrihydrite” *Applied Physics A* 74 (Suppl.): S1004-S1006.

Johnson, C.E. (1969) “Antiferromagnetism of γ-FeOOH: a Mössbauer effect study” *Journal of Physics C: Solid State Physics* 2 (11): 1996

Jönsson, J., Persson, P., Sjöberg, S. and Lövgren, L. (2005) “Schwertmannite precipitated from acid mine drainage: phase transformation, sulphate release and surface properties” *Applied Geochemistry* 20: 179-191

Kawano, M. and Tomita K. (2001) “Geochemical modeling of bacterially induced mineralization of schwertmannite and jarosite in sulfuric acid spring water” *American Mineralogist* 86: 1156-1165

Kilcoyne, S.H. and Cywinski, R. (1995) “Ferritin: a model superparamagnet” *Journal of Magnetism and Magnetic Materials* 140-144: 1466-1467

Kimmel, G. (1987) “High quality X-ray diffraction data using an adjustable divergence slit and thin samples” *Powder Diffraction* 2: 22–27

Kulgawczuk, D.S., Obuszko, Z. and Szytula, A. (1968) “Susceptibility and magnetization of β- and δ- FeOOH” *Physica Status Solidi* 26: K83-K85

Lang, B.E. (2005) *Specific heat and thermodynamic properties of metallic systems: Instrumentation and analysis.* Brigham Young University. Ph.D. Thesis

Lee, G.H., Kim, S.H., Choi, B.J., Huh, S.H., Chang, Y., Kim, B., Park, J., and Oh, S.J. (2004) “Magnetic properties of needle-like α-FeOOH and γ-FeOOH nanoparticles” *Journal of the Korean Physical Society* 45: 1019-1024

Lidiard, A.B. (1954) “Antiferromagnetism” *Reports on Progress in Physics* 17: 201-244

Loan, M., Cowley, J.M., Hart, R. and Parkinson, G.M. (2004) “Evidence on the structure of synthetic schwertmannite” *American Mineralogist* 89: 1735-1742

Mackay, A.L. (1960) “β-Ferric oxyhydroxide” *Mineralogical Magazine* 32: 545-557

Makhlouf, S.A., Parker, F.T. and Berkowitz, A.E. (1997) “Magnetic hysteresis anomalies in ferritin” Physical Review B 55 (22): R14 717-R14 720

Madsen, D.E., Cervera-Gontard, L., Kasama, T., Dunin-Borkowski, R.E., Koch, C.B., Hansen, M.F., Fradsen, C.F. and Mørup, S. (2009) “Magnetic fluctuations in nanosized goethite (α-FeOOH) grains" *Journal of Physics: Condensed Matter* 21: 016007

Majzlan, J., Lang, B.E., Stevens, R., Navrotsky, A., Woodfield, B.F. and Boerio-Goates, J. (2003) "Thermodynamics of Fe oxides: Part I. Entropy at standard temperature and pressure and heat capacity of goethite (α-FeOOH), lepidocrocite (γ-FeOOH), and maghemite (γ-Fe_2O_3)" *American Mineralogist* 88: 846-854

Manceau, A. and Combes, J.M. (1988) "Structure of Mn and Fe oxides and oxyhydroxides: A topological approach by EXAFS" *Physics and Chemistry of Minerals* 15: 283-295

Manceau, A., Nagy, K.L., Spadini, L. and Ragnarsdottir, K.V. (2000) "Influence of anionic layer structure of Fe-oxyhydroxides on the structure of Cd surface complexes" *Journal of Colloid and Interface Science* 228: 306-316

Manceau, A. (2009) "Evaluation of the structural model for ferrihydrite derived from real-space modelling of high-energy X-ray diffraction data" *Clay Minerals* 44 (1): 19-34.

Michel, F.M., Ehm, L., Antao, S.M., Lee, P.L., Chupas, P.J., Liu, G., Strongin, D.R., Schoonen, M.A.A., Phillips, B.L. and Parise, J.B. (2007a) "The structure of ferrihydrite, a nanocrystalline material" *Science* 316 (5832): 1726-1729

Michel, F.M., Ehm, L., Liu, G., Han, W.Q., Antao, S.M., Chupas, P.J., Lee, P.L., Knorr, K., Eulert, H., Kim, J., Grey, C.P., Celestian, A.J., Gillow, O.J., Schoonen, M.A.A., Strongin, D.R. and Parise, J.B. (2007b) "Similarities in 2- and 6-line ferrihydrite based on pair distribution function analysis of X-ray total scattering" *Chemistry of Materials* 19: 1489-1496

Michel, F.M., Barrón, V., Torrent, J., Morales, M.P., Serna, C.J., Boily, J.-F., Liu, Q., Ambrosini, A., Cismasu, A.C. and Brown, G.E. Jr. (2010) "Ordered ferrimagnetic form of ferrihydrite reveals links among structure, composition, and magnetism" *Proceedings of the National Academy of Sciences of the United States of America* 107 (7): 2787-2792

Morris, R.V., Golden, D.C., Bell III, J.F., Shelfer, T.D., Scheinost, A.C., Hinman, N.W., Furniss, G., Mertzman, S.A., Bishop, J.L., Ming, D.W., Allen, C.C. and Britt, D.T. (2000) "Mineralogy, composition, and alteration of Mars Pathfinder rocks and soils: Evidence from multispectral, elemental, and magnetic data on terrestrial analogue, SNC meteorite, and Pathfinder samples" *Journal of Geophysical Research* 105: 1757-1817

Morrish, A.H. (1965) *The Physical Principles of Magnetism*. Wiley: New York. 680 pp.

Mørup, S. and Hansen, M.F. (2007) "Superparamagnetic Particles" In *Handbook of Magnetism and Advanced Magnetic Materials (Novel Materials)* 4: 1-18; H. Kronmüller and S. Parkin. Eds. Wiley: England

Murad, E. (1979) "Mössbauer and X-ray data on β-FeOOH (akaganéite)" *Clay Minerals* 14: 273-283

Murad, E. and Schwertmann, U. (1984) “The influence of crystallinity on the Mössbauer spectrum of lepidocrocite” *Mineralogical Magazine* 48: 507-511

Murad, E., Bigham, J.M., Bowen, L.H., and Schwertmann, U. (1990) “Magnetic properties of iron oxides produced by bacterial oxidation of Fe^{2+} under acid conditions” *Hyperfine Interactions* 58: 2373-2376

Murad, E. and Rojík, P. (2005) “Iron mineralogy of mine-drainage precipitates as environmental indicators: review of current concepts and a case study from the Sokolov Basin, Czech Republic” *Clay Minerals* 40 (4): 427-440

Murakami, T., Sato, T., Ohnuki, T. and Isobe, H. (2005) “Field evidence for uranium “nanocrystallization” and its implications for uranium transport” *Chemical Geology* 221: 117-126

Navrotsky, A., Mazeina, L. and Majzlan, J. (2008) “Size-driven structural and thermodynamic complexity in iron oxides” *Science* 319: 1635-1638

Néel, L. (1961) “Superparamagnétisme des grains très fins antiferromagnétiques” *Comptes-Rendus Hebdomadaires des Séances de L'Académie des Sciences* 252: 4075-4080

Olés, A., Szytula, A. and Wanic, A. (1970) “Neutron diffraction study of γ-FeOOH” *Physica Status Solidi* 41: 173-177

Pan, Y., Brown, A. and Brydson, R. (2006) “Electron beam damage studies on 6-line ferrihydrite” *Journal of Physics: Conference Series* 26: 46–49

Pankhurst, Q.A., and Pollard, R.J. (1992) “Structural and magnetic properties of ferrihydrite” *Clays and Clay Minerals* 40 (3): 268-272

Pannalal, S., Crowe, S., Cioppa, M., Symons, D., Sturm, A., and Fowle, D. (2005) “Room-temperature magnetic properties of ferrihydrite: A potential magnetic remanence carrier?” *Earth and Planetary Science Letters* 236: 856-870

Pedersen, T.P. (1999) “Schwertmannite and awaruite as alteration products in iron meteorites” *Meteoritics and Planetary Science* 34 (Suppl.): A90-A90

Peters, C. and Dekkers, M.J. (2003) “Selected room temperature magnetic parameters as a function of mineralogy, concentration and grain size” *Physics and Chemistry of the Earth* 28: 659-667

Poddar, P., Gass, J., Rebar, D.J., Srinath, S., Srikanth, H., Morrison, S.A. and Carpenter, E.E. (2006) “Magnetocaloric effect in ferrite nanoparticles” *Journal of Magnetism and Magnetic Materials* 307: 227-231

Pollard, R.J. and Pankhurst, Q.A. (1992) “A comment on the detection of speromagnetism in insulators by Mössbauer spectroscopy” *Journal of Physics: Condensed Matter* 4: L317-L323

Pollard, R.J., Cardile, C.M., Lewis, D.G., and Brown, L.J. (1992) “Characterization of FeOOH polymorphs and ferrihydrite using low-temperature, applied-field, Mössbauer spectroscopy” *Clay Minerals* 27: 57-71

Post, J.E., Heaney, P.J., Von Dreele, R.B. and Hanson, J.C. (2003) "Neutron and temperature-resolved synchrotron X-ray powder diffraction study of akaganéite" *American Mineralogist* 88: 782-788

Punnoose, A., Magnone, H., Seehra, M.S. and Bonevich, J. (2001) "Bulk to nanoscale magnetism and exchange bias in CuO nanoparticles" *Physical Review B* 64: 174420

Punnoose, A., Phanthavady, T., Seehra, M.S., Shah, N. and Huffman, G.P. (2004) "Magnetic properties of ferrihydrite nanoparticles doped with Ni, Mo, and Ir" *Physical Review B* 69: 054425

Ramírez, A.P. (1994) "Strongly geometrically frustrated magnets" *Annual Review of Materials Research* 24: 453-480

Rancourt, D.G. and Ping, J.Y. (1991) "Voigt-based methods for arbitrary shape static hyperfine parameter distributions in Mössbauer spectroscopy" *Nuclear Instruments and Methods in Physics Research* B58: 85-97

Rancourt, D.G., McDonald, A.M., Lalonde, A.E. and Ping, J.Y. (1993) "Mössbauer absorber thicknesses for accurate site populations in Fe-bearing minerals" *American Mineralogist* 78: 1-7

Rancourt, D.G. (1998) "Mössbauer spectroscopy in clay science" *Hyperfine Interactions* 117: 3-38

Rancourt, D.G., González-Lucena, F. and Thibault, P.-J. (2004) "Magnetic granulometry from equilibrium magnetization measurements: Mineral magnetometry of superparamagnetic particles and application to synthetic ferrihydrites" *American Mineralogist* 89: 987-997

Rancourt, D.G. and Meunier, J.-F. (2008) "Constraints on structural models of ferrihydrite as a nanocrystalline material" *American Mineralogist* 93: 1412-1417

Reynolds, R.C. Jr. (1989) "Diffraction by small and disordered crystals" In *Modern Powder Diffraction. Reviews in Mineralogy* 20: 145-181; Bish, D.L.and Post, J.E. Eds. Mineralogical Society of America: USA

Richardson, J.T., Yiagas, D.I., Turk, B., Forster, K. And Twigg, M.V. (1991) "Origin of superparamagnetism in nickel oxide" *Journal of Applied Physics* 70 (11): 6977-6982

Richmond, W.R., Cowley, J.M., Parkinson, G.M. and Saunders, M. (2006) "An electron microscopy study of β-FeOOH (akaganéite) nanorods and nanotubes" *CrystEngComm* 8: 36-40

Rose J., Manceau A., Bottero J.-Y., Masion A. and García F. (1996) "Nucleation and growth mechanism of Fe oxyhydroxide in the presence of PO_4 ions. 1. Fe K-edge EXAFS study" *Langmuir* 12: 6701–6707

Sako, S., Umemura, Y., Ohshima, K., Sakai, M. and Bandow, S. (1995) "Magnetic property of antiferromagnetic MnO ultra-fine particle" *Journal of the Physical Society of Japan* 65 (1): 280-284

Schwertmann, U. and Cornell, R.M. (2000) *Iron oxides in the laboratory* VCH: Weinheim. Second edition. 188 pp.

Schwertmann, U., Friedl, J. and Kyek, A. (2004) “Formation and properties of a continuous crystallinity series of synthetic ferrihydrites (2- to 6-line) and their relation to FeOOH forms” *Clays and Clay Minerals* 52: 221-226

Seehra, M.S., Babu, V.S., Manivannan, A. and Lynn, J.W. (2000) “Neutron scattering and magnetic studies of ferrihydrite nanoparticles” *Physical Review B* 61 (5): 3513-3518

Silva, N.J.O., Amaral, V.S., Carlos, L.D., Rodríguez-González, B., Liz-Marzán, L.M., Berquó, T.S., Banerjee, S.K., de Zea Bermudez, V., Millán, A. and Palacio, F. (2008) “Evidence of random magnetic anisotropy in ferrihydrite nanoparticles based on the analysis of statistical distributions” *Physical Review B* 77: 134426

Szytula, A., Burewicz, A., Dimitrijevic, Ž., Krasnicki, S., Rzany, H., Todorovic, J., Wanic, A. and Wolski, W. (1968) “Neutron diffraction studies of α-FeOOH” *Physica Status Solidi* 26: 429–434.

Szytula, A., Balanda, M., and Dimitrijevic, Ž. (1970) “Neutron diffraction studies of β-FeOOH” *Physica Status Solidi A* 3: 1033-1037

Tauxe, L., Mullender, T.A.T. and Pick, T. (1996) “Potbellies, wasp-waists, and superparamagnetism in magnetic hysteresis” *Journal of Geophysical Research* 101: 571-584

Thibault, P.-J., Rancourt, D.G., Evans, R.J. and Dutrizac, J.E. (2009) “Mineralogical confirmation of a near-P:Fe=1:2 limiting stoichiometry ratio in colloidal P-bearing ferrihydrite-like hydrous ferric oxide” *Geochimica et Cosmichimica Acta* 73: 364-376

Thompson, R. and Oldfield, F. (1986) *Environmental Magnetism* Allen & Unwin: London

Towe, K. M. and Bradley, W. F. (1967) “Mineralogical constitution of colloidal "hydrous ferric oxides"” *Journal of Colloid and Interface Science* 24: 384-392

Vlasov, A.Y. and Rukosuev, M.N. (1974) “Low-temperature neutron diffraction of α and β iron hydroxides and the Morin points of hematites made from α, β, γ and δ-FeOOH” *Soviet Physics Journal* 15 (8): 1226-1229

Waychunas, G.A., Kim, C.S. and Banfield, J.F. (2005) “Nanoparticulate iron oxide minerals in soils and sediments: unique properties and contaminant scavenging mechanisms” *Journal of Nanoparticle Research* 7: 409-433

Waychunas, G.A. and Zhang, H. (2008) “Structure, chemistry, and properties of mineral nanoparticles” *Elements* 4: 381-387

Webb, J., St. Pierre, T.G., Tran, K.C., Chua-anusorn, W., Macey, D.J. and Pootrakul, P. (1996) “Biologically significant iron(III) oxyhydroxy polymers: Mössbauer spectroscopic study of ferritin and hemosiderin in pancreas tissue of β-thalassemia/hemoglobin E disease” *Inorganica Quimica Acta* 243: 121-125

Webmineral.com “jPOWD Applet for Goethite mineral structure data” 1999, 2010 <http://webmineral.com/jpowd/JPX/jpowd.php?target_file=Goethite.jpx>; “jPOWD Applet for Lepidocrocite mineral structure data”, 1963, 2010 <http://webmineral.com/jpowd/JPX/jpowd.php?target_file=Lepidocrocite.jpx>;

"jPOWD Applet for Akaganeite mineral structure data", 1991, 2010 <http://webmineral.com/jpowd/JPX/jpowd.php?target_file=Akaganeite.jpx>

Weckler, B. and Lutz, H.D. (1998) "Lattice vibration spectra. Part XCV. Infrared spectroscopic studies on the iron oxide hydroxides goethite (α), akaganéite (β), lepidocrocite (γ), and feroxyhite (δ)" *European Journal of Solid State and Inorganic Chemistry* 35: 531-544

Wyckoff R. W. G. (1963) *Crystal Structures* Vol. 1 Interscience: New York. Second Edition

Yamamoto, N. (1968) "The magnetic properties of the synthetic iron oxyhydrates" *Bulletin of the Institute for Chemical Research, Kyoto University* 46: 275-282

Yamamoto, N., Shinjo, T., Kiyama, M., Bando, Y., and Takada, T. (1968) "Mössbauer effect of α-FeOOH and β-FeOOH: making use of oriented particles" *Journal of the Physical Society of Japan* 25: 1267-1271

Zergenyi, R.S., Hirt, A.M. Zimmermann, S., Dobson, J.P. and Lowrie, W. (2000) "Low-temperature magnetic behavior of ferrihydrite" *Journal of Geophysical Research* 105 (B4): 8297-8303

Zhang, X.X. (2006) "Magnetic relaxation and quantum tunneling of magnetization" In *Handbook of Advanced Magnetic Materials (Nanostructural Effects)* 1: 147-177; Liu, Y. Sellmyer, D.J. and Shindo, D. Eds. Springer: New York

Zhang, L.-Y., Xue, D.-S. and Fen, J. (2006) "Magnetic properties of amorphous β-FeOOH nanowire arrays" *Journal of Magnetism and Magnetic Materials* 305: 228-232

Appendix A – Simulations of Superparamagnetism for FeOOH

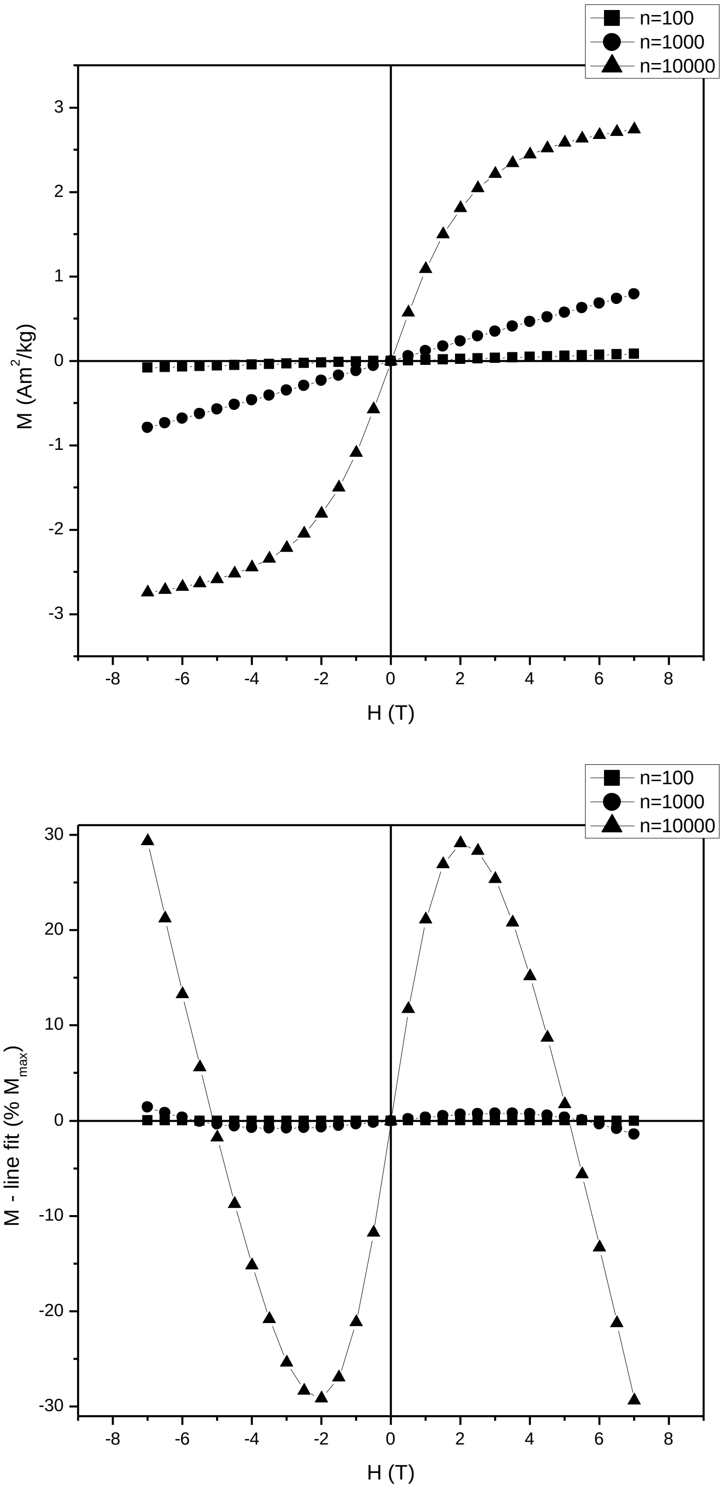

Figure A.1 Field cycle simulations for the model μ' = A n at 300 K, where A=0.01 (top) and corresponding curvature graphs (bottom)

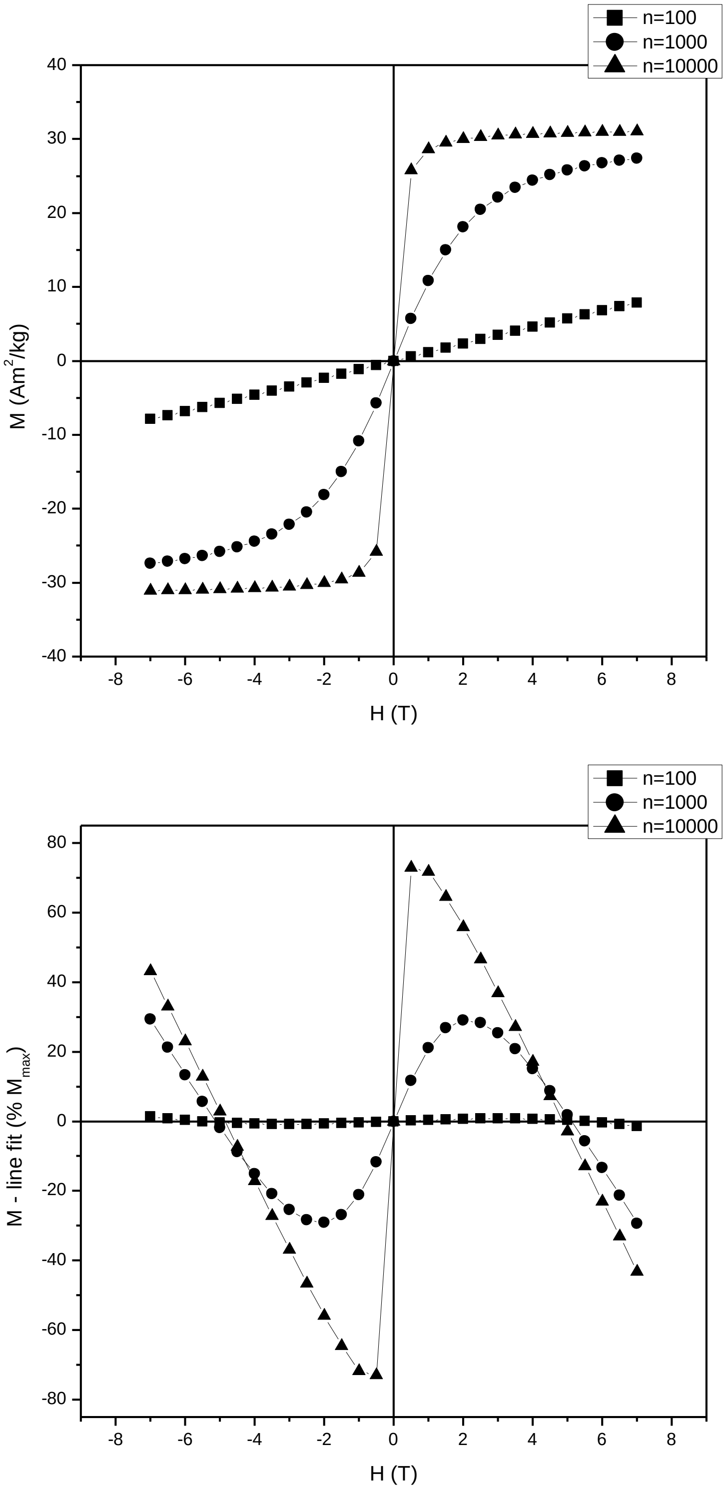

Figure A.2 Field cycle simulations for the model μ' = A n at 300 K, where A=0.1 (top) and corresponding curvature graphs (bottom)

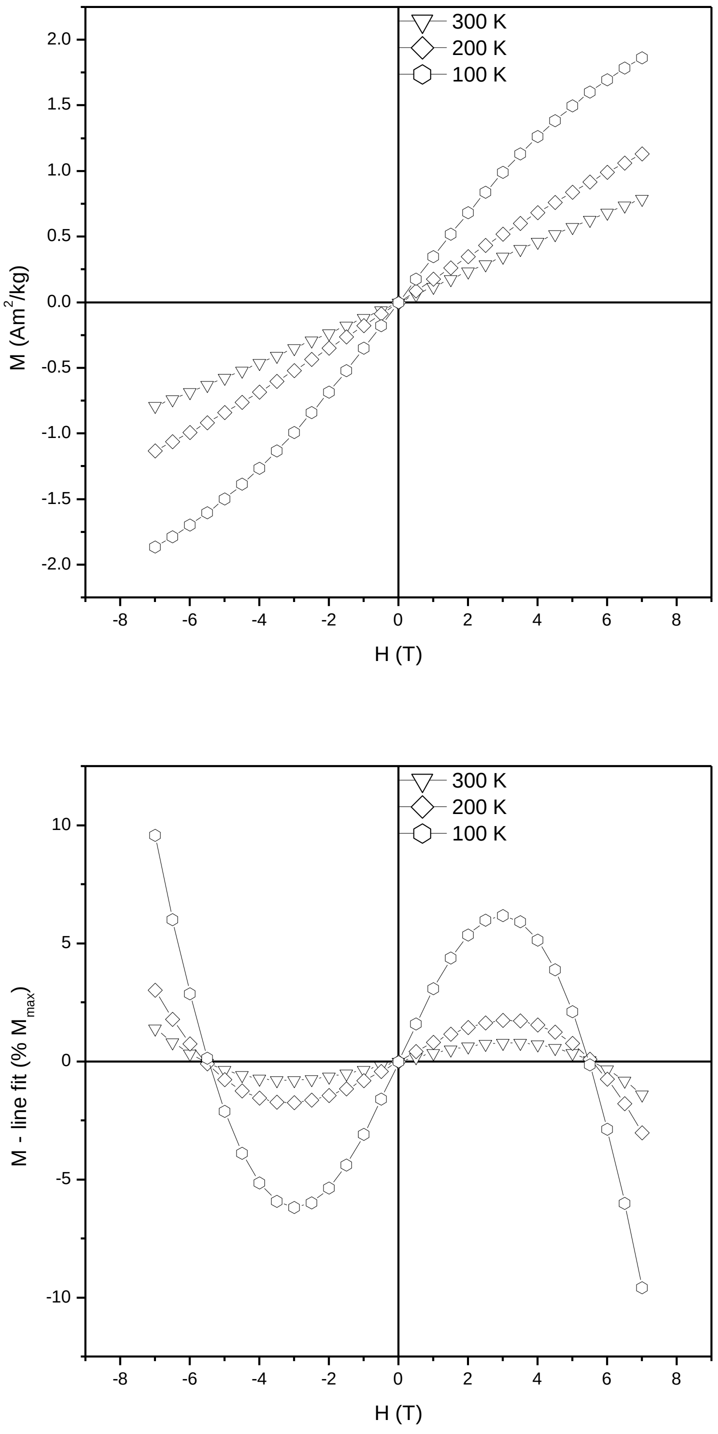

Figure A.3 Temperature dependence of field cycle simulations for the model μ' = A n, where A=0.01 and n=1000 (top) and corresponding curvature graphs (bottom)

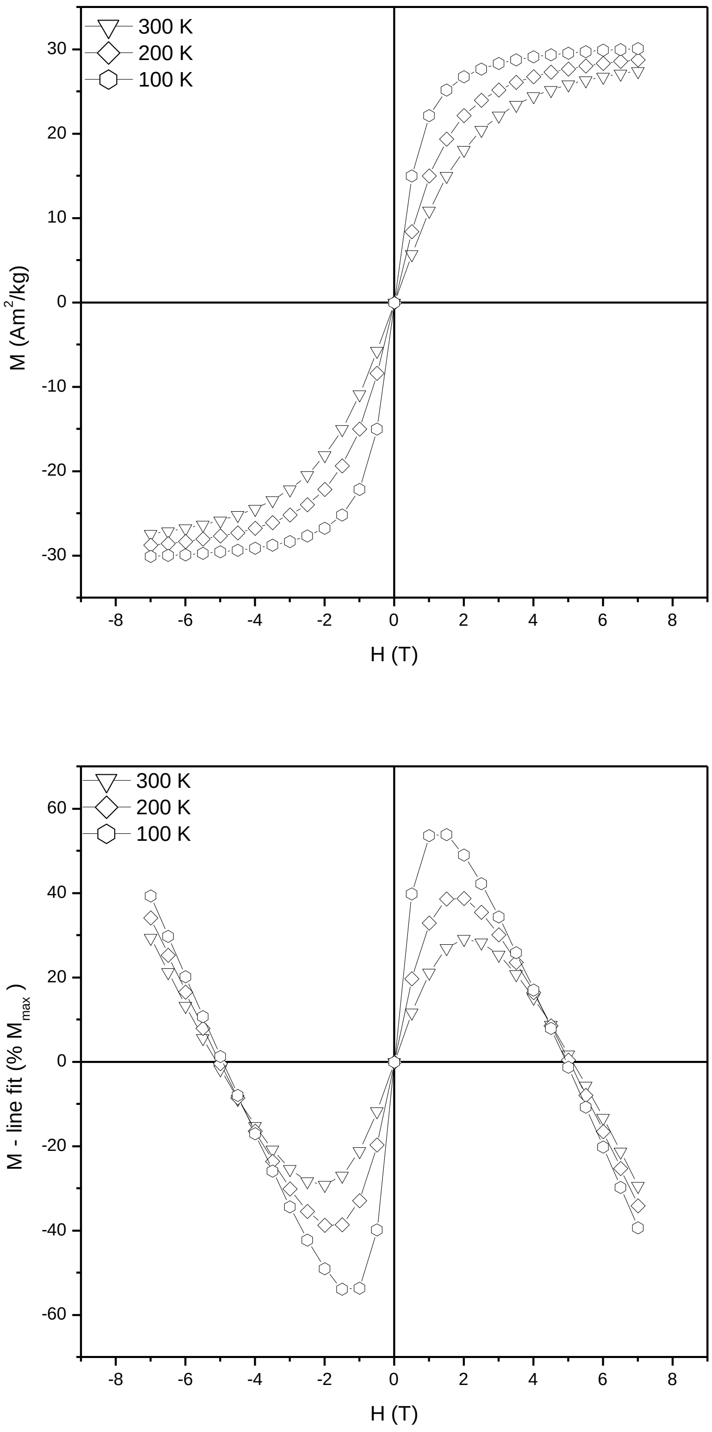

Figure A.4 Temperature dependence of field cycle simulations for the model $\mu' = A\ n$, where A=0.1 and n=1000 (top) and corresponding curvature graphs (bottom)

Appendix B – Powder X-ray Diffractograms (pXRD)

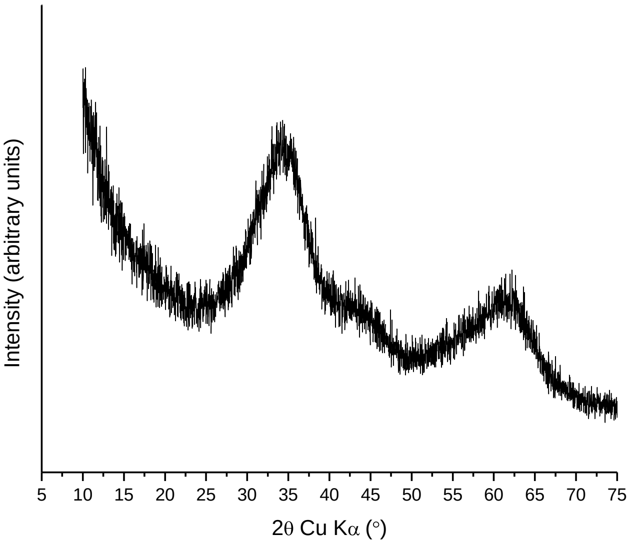

Figure B.1 pXRD of 2L-Fh

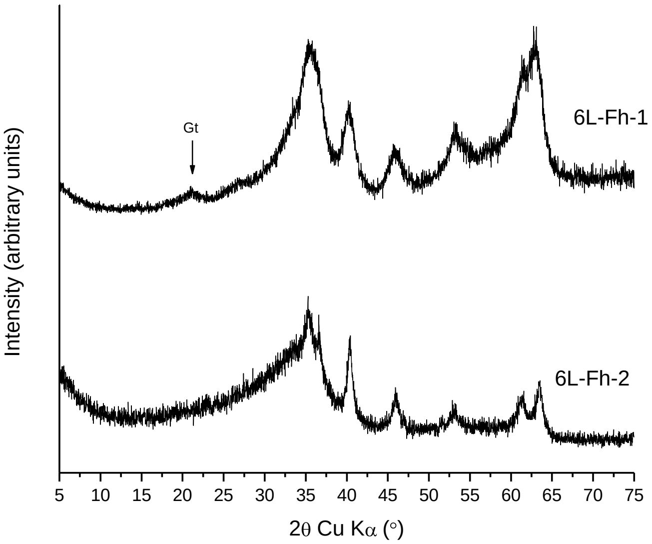

Figure B.2 pXRD of 6L-Fh-1 (top) showing a goethite (Gt) impurity, and 6L-Fh-2 (bottom)

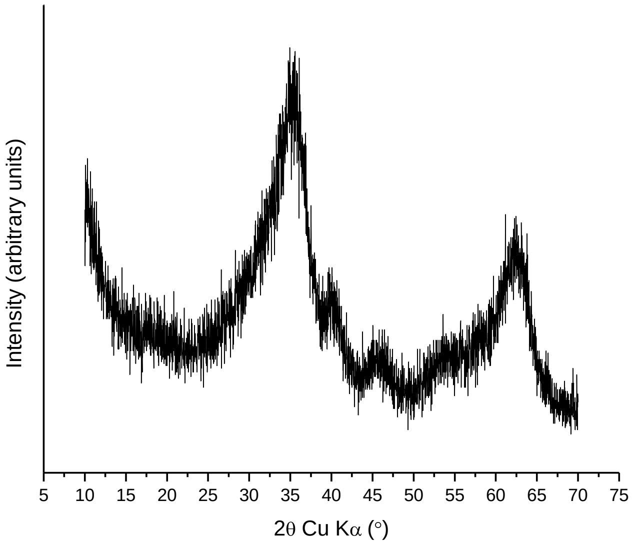

Figure B.3 pXRD of 4L-Fh

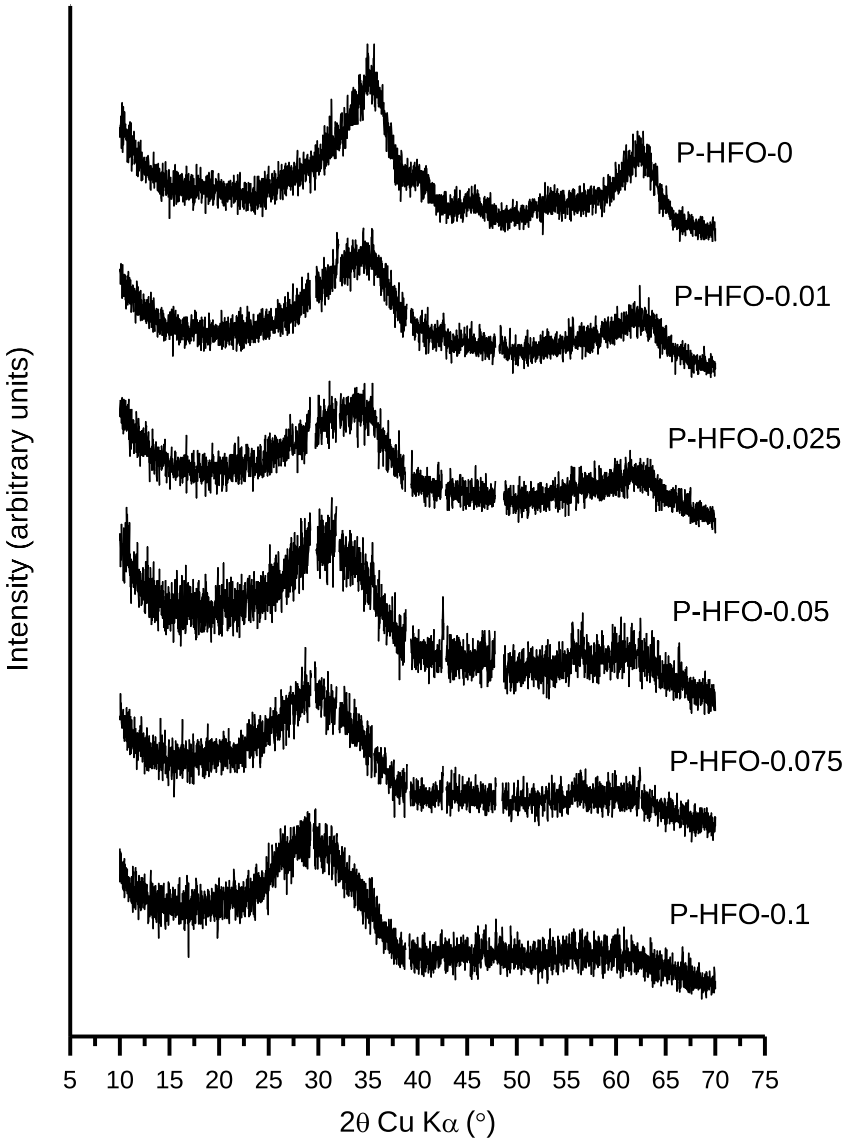

Figure B.4 pXRD of P-HFO series samples (as indicated). Intensities have been scaled and shifted for clarity. The gaps in the data are removed peaks of $NaNO_3$ impurities resulting from the syntheses

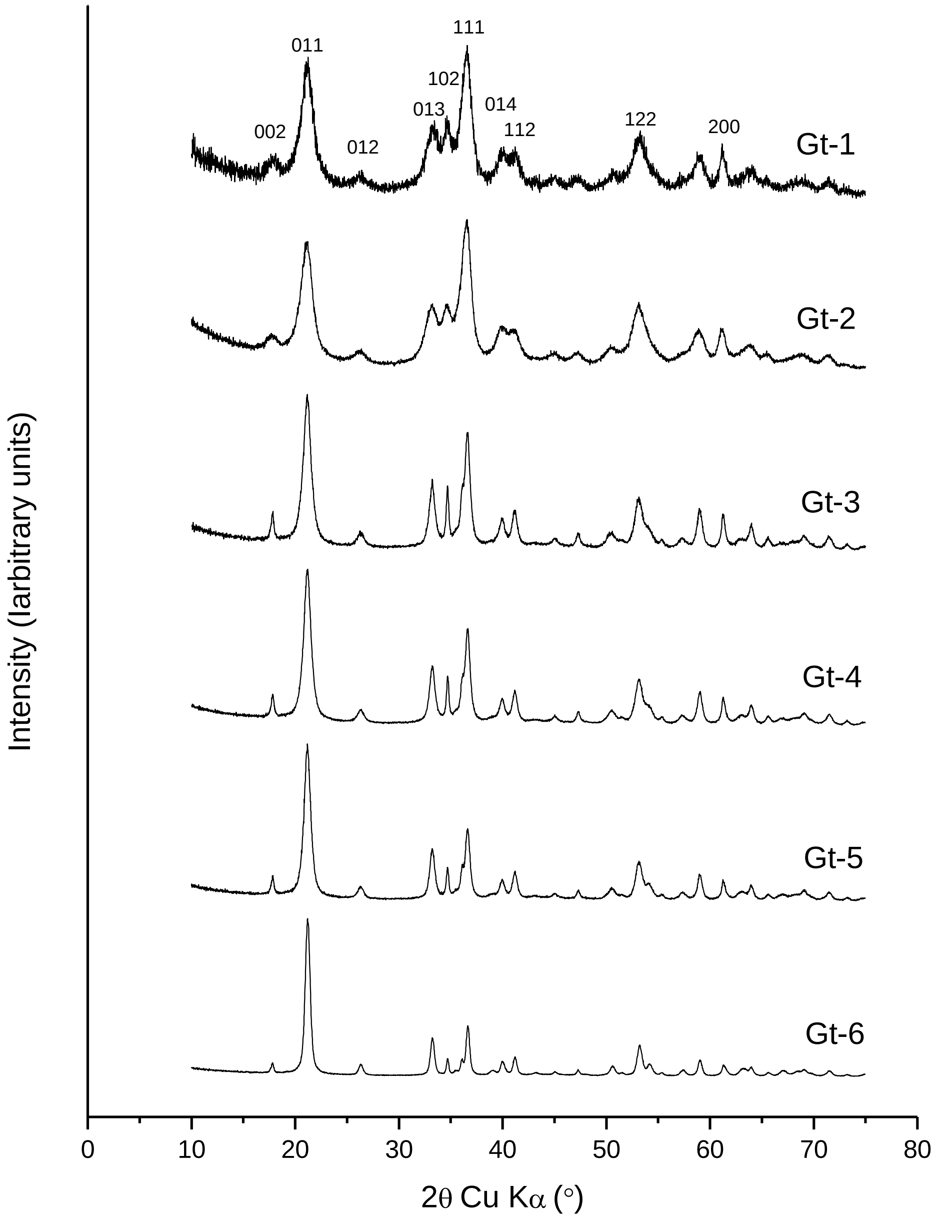

Figure B.5 pXRD of goethite (Gt) samples: Gt-1, Gt-2, Gt-3, Gt-4, Gt-5 and Gt-6 (as indicated) with peaks indexed based on the Gt JCPDS-PDF# 29-0713

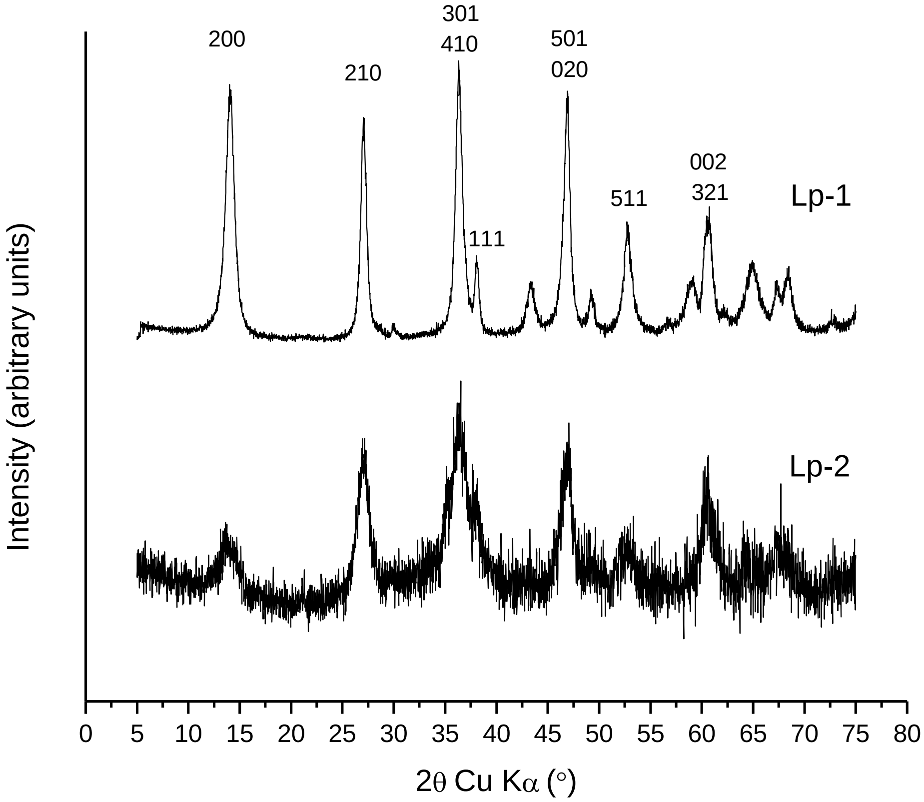

Figure B.6 pXRD of Lp-1 (top) and Lp-2 (bottom) with major peaks indexed based on the Lp JCPDS-PDF# 44-1415

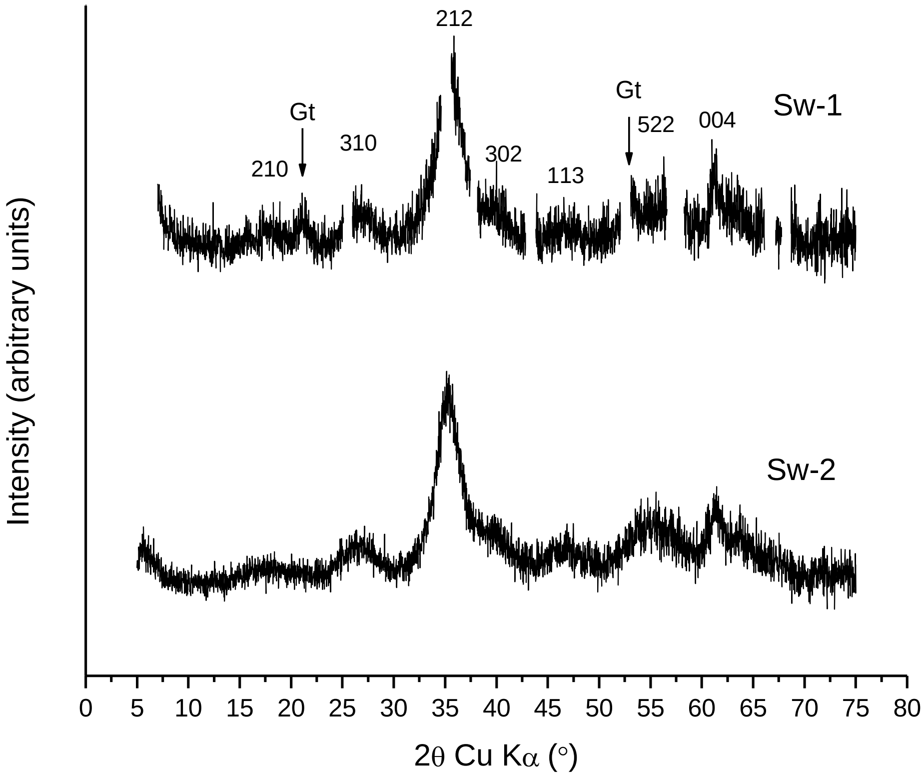

Figure B.7 pXRD of Sw-1 (top) and Sw-2 (bottom) with major peaks indexed based on the Sw JCPDS-PDF# 47-1775. The gaps in the data of Sw-1 are removed peaks of a corundum impurity from the mortar used in the pXRD sample preparation

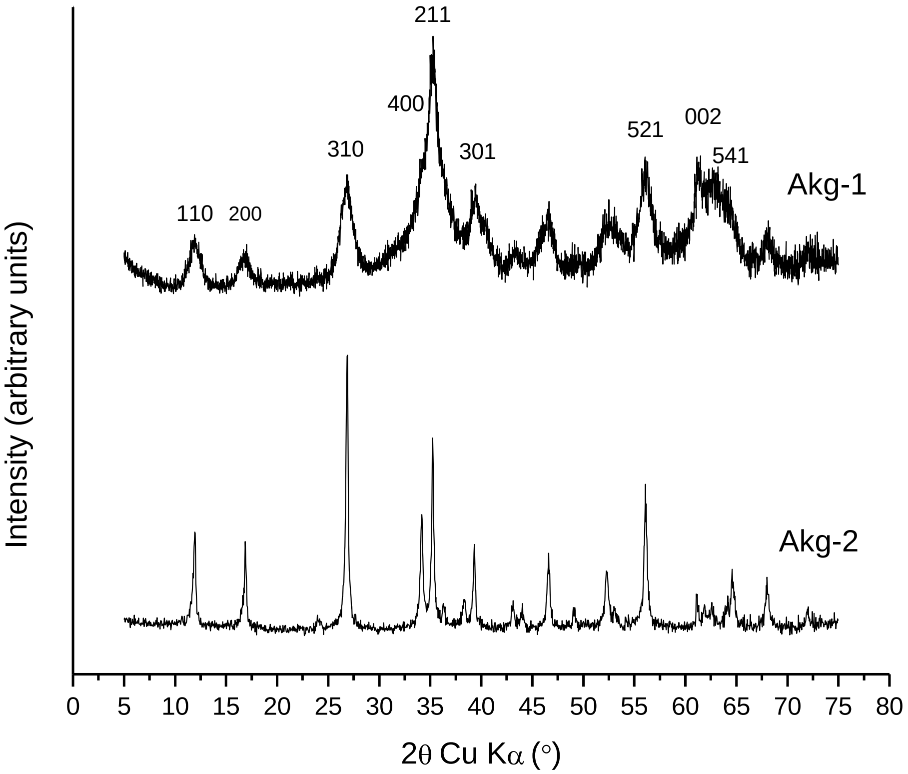

Figure B.8 pXRD of Akg-1 (top) and Akg-2 (bottom) with major peaks indexed based on the Akg JCPDS-PDF# 34-1266. The peaks (211) and (002) of Akg-1 have contributions of a corundum impurity from the mortar used in the pXRD sample preparation

Appendix C – SEM Micrographs

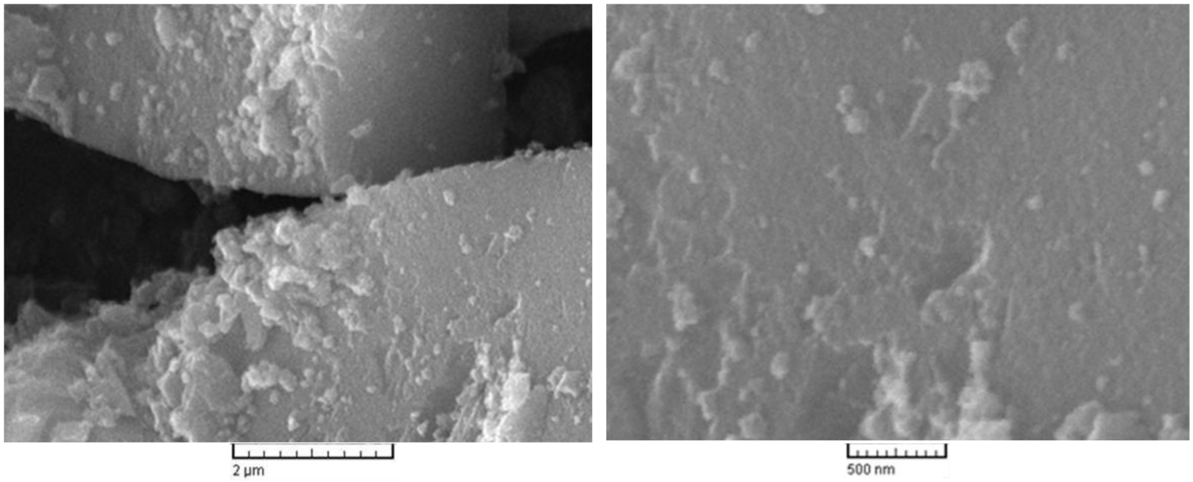

Figure C.1 Scanning electron micrographs of 2L-Fh

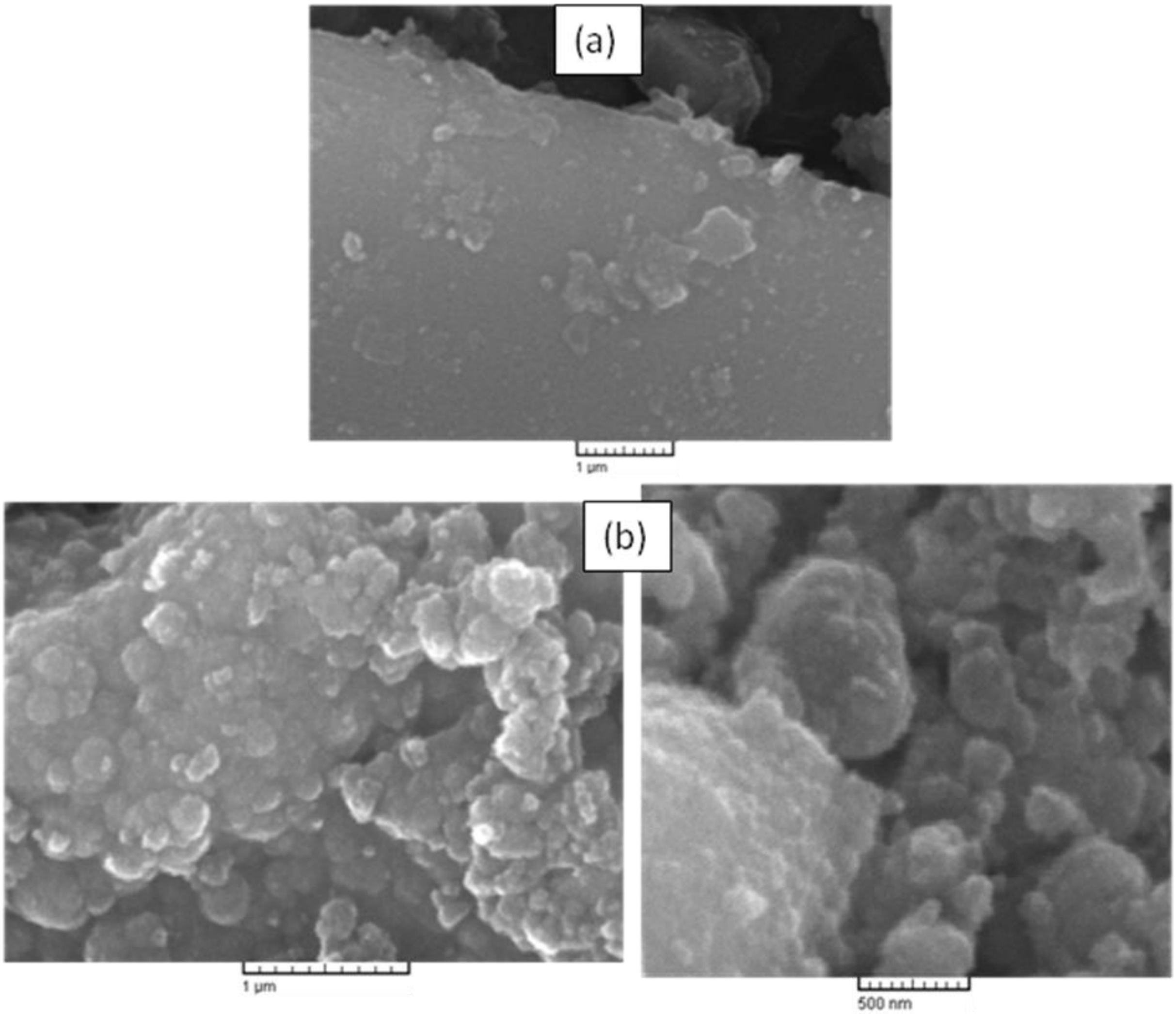

Figure C.2 Scanning electron micrographs of (a) 6L-Fh-1; (b) 6L-Fh-2

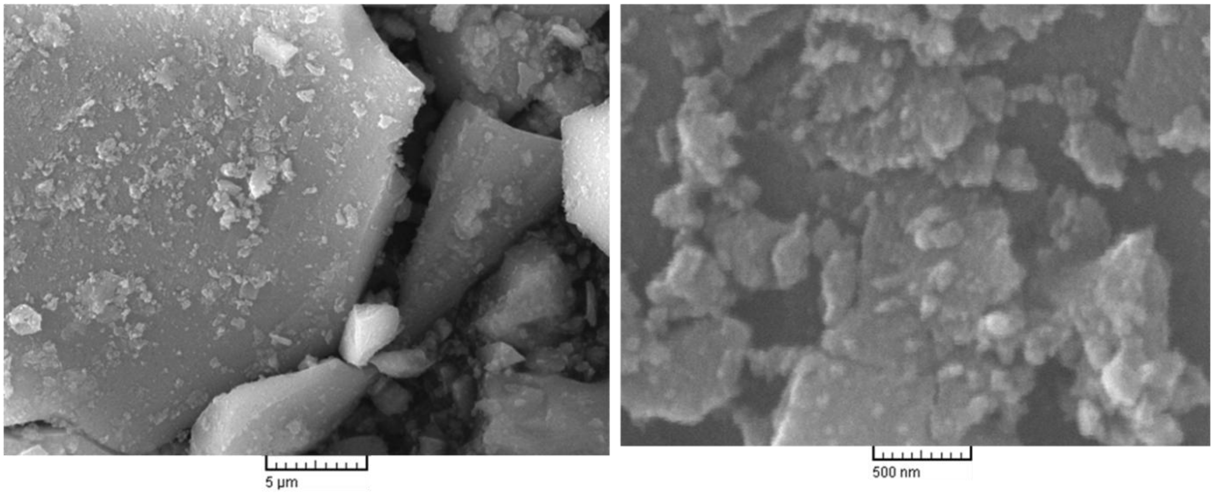

Figure C.3 Scanning electron micrographs of 4L-Fh

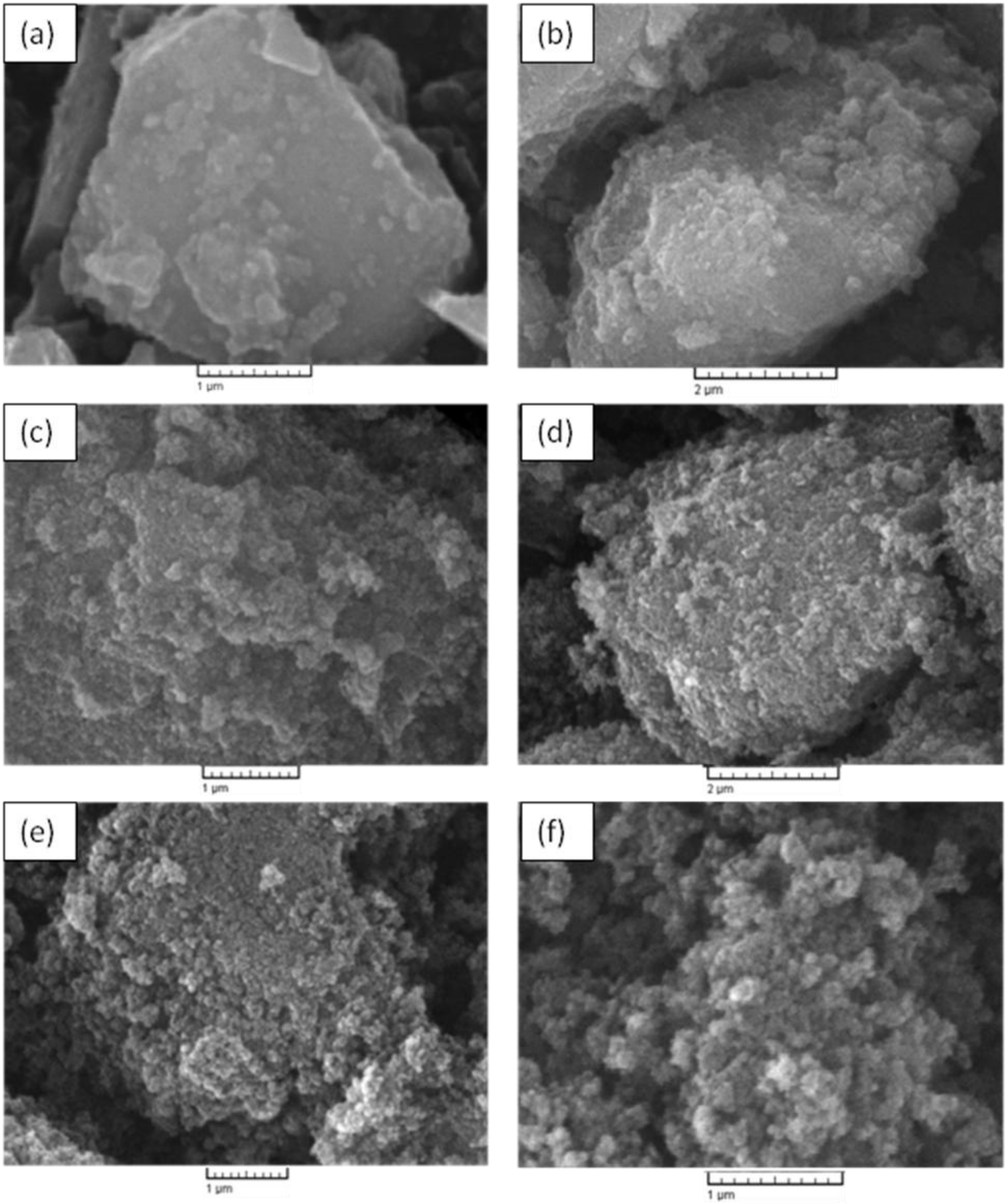

Figure C.4 Scanning electron micrographs of (a) P-HFO-0; (b) P-HFO-0.01; (c) P-HFO-0.025; (d) P-HFO-0.05; (e) P-HFO-0.075; (f) P-HFO-0.1

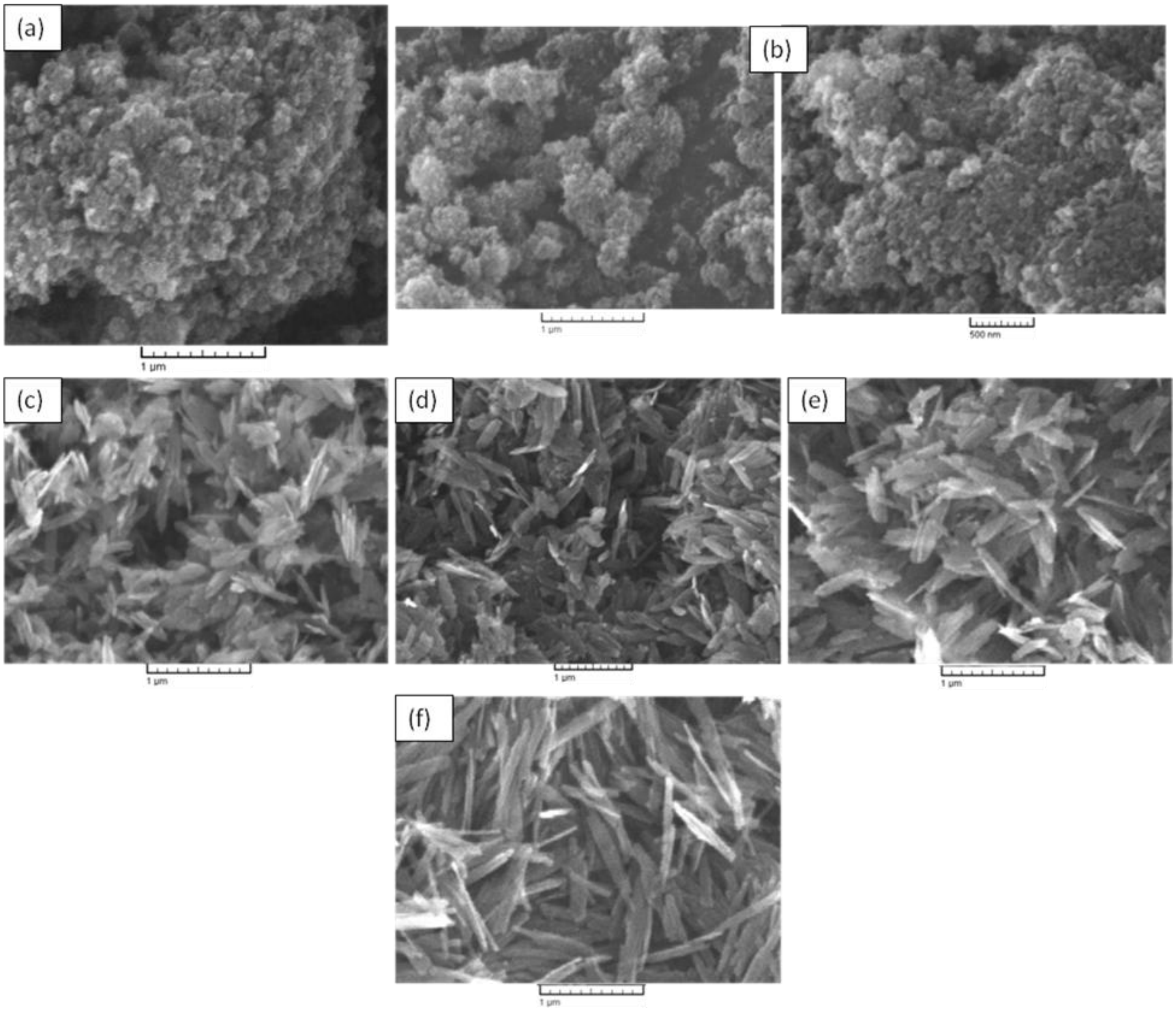

Figure C.5 Scanning electron micrographs of (a) Gt-1; (b) Gt-2; (c) Gt-3; (d) Gt-4; (e) Gt-5; (f) Gt-6

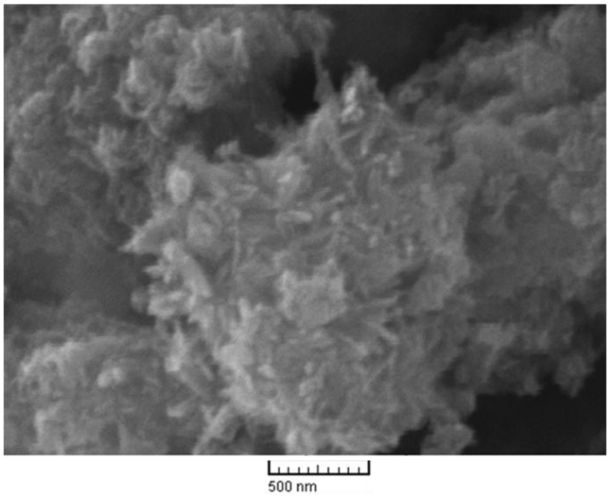

Figure C.6 Scanning electron micrograph of Lp-2

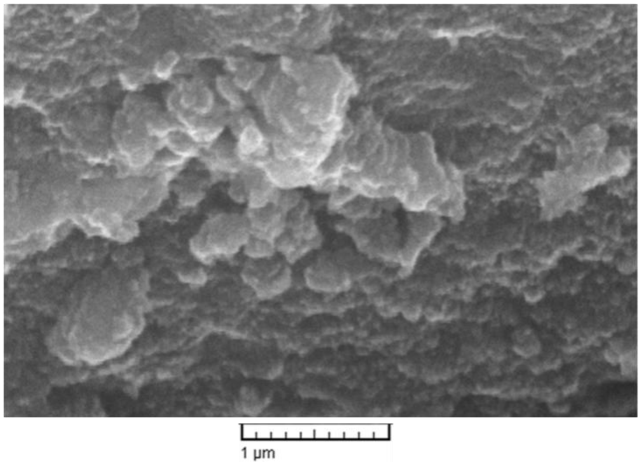

Figure C.7 Scanning electron micrograph of Sw-2

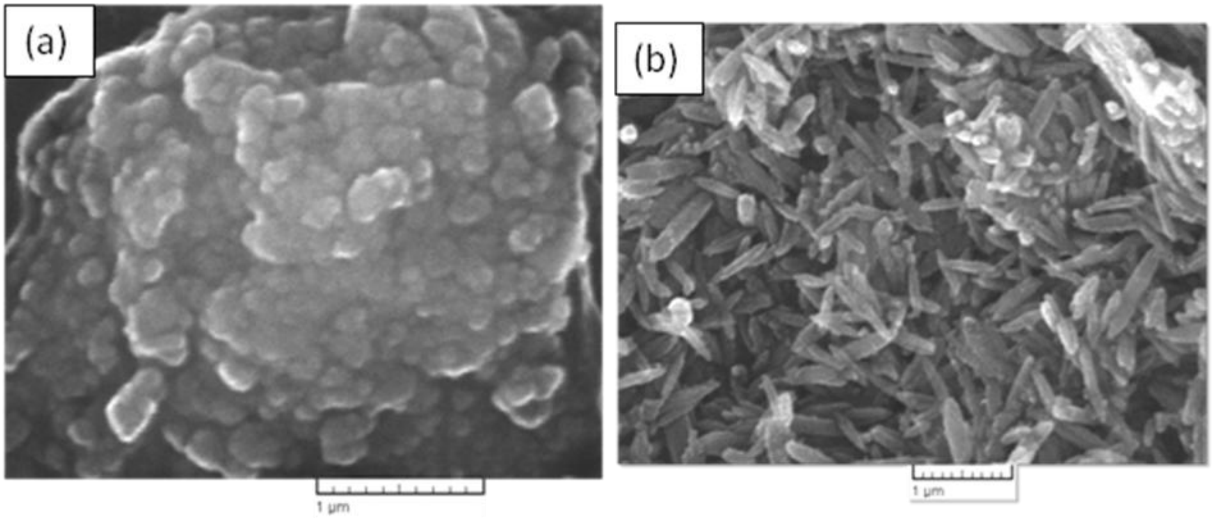

Figure C.8 Scanning electron micrographs of (a) Akg-1; (b) Akg-2

Appendix D – Temperature Cycles

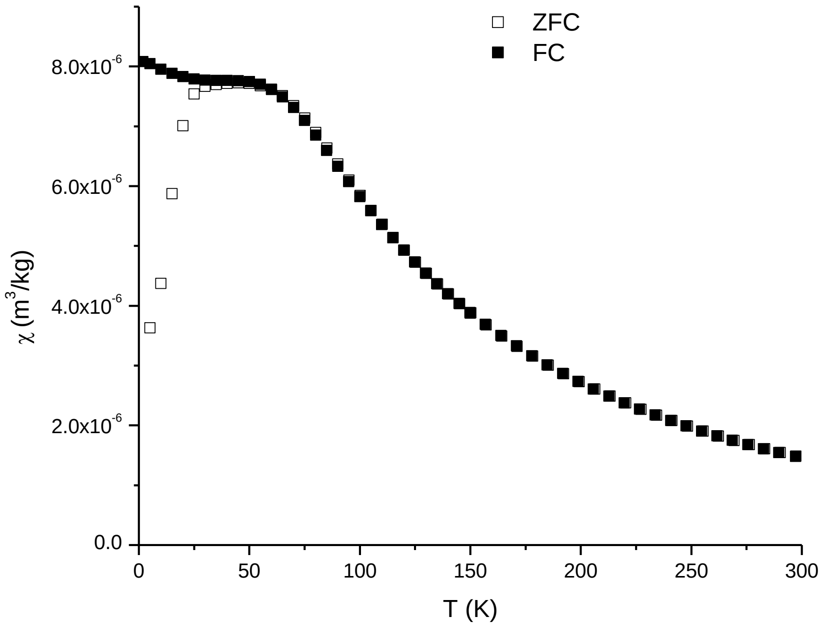

Figure D.1 Zero-field-cooled (ZFC) and field-cooled (FC) curves of 2L-Fh

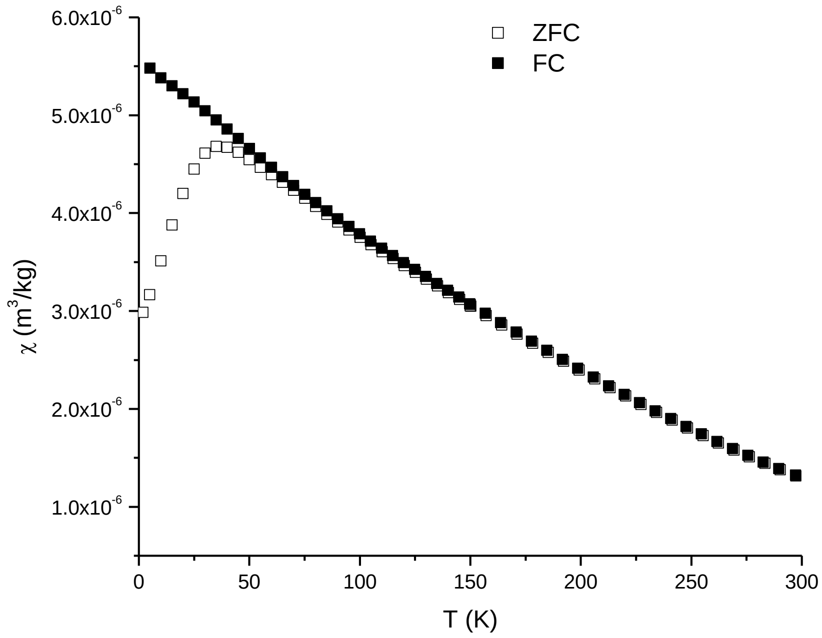

Figure D.2 Zero-field-cooled (ZFC) and field-cooled (FC) curves of 6L-Fh-1

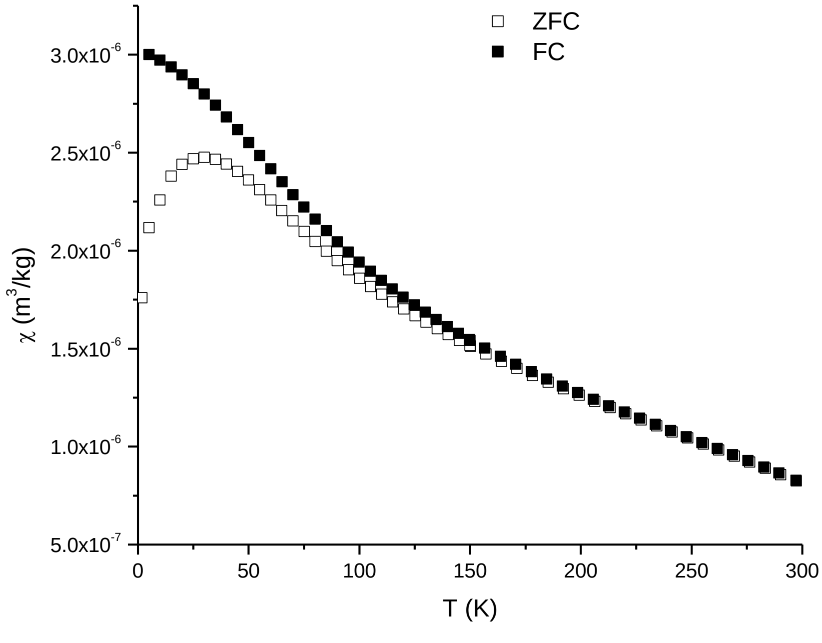

Figure D.3 Zero-field-cooled (ZFC) and field-cooled (FC) curves of 6L-Fh-2

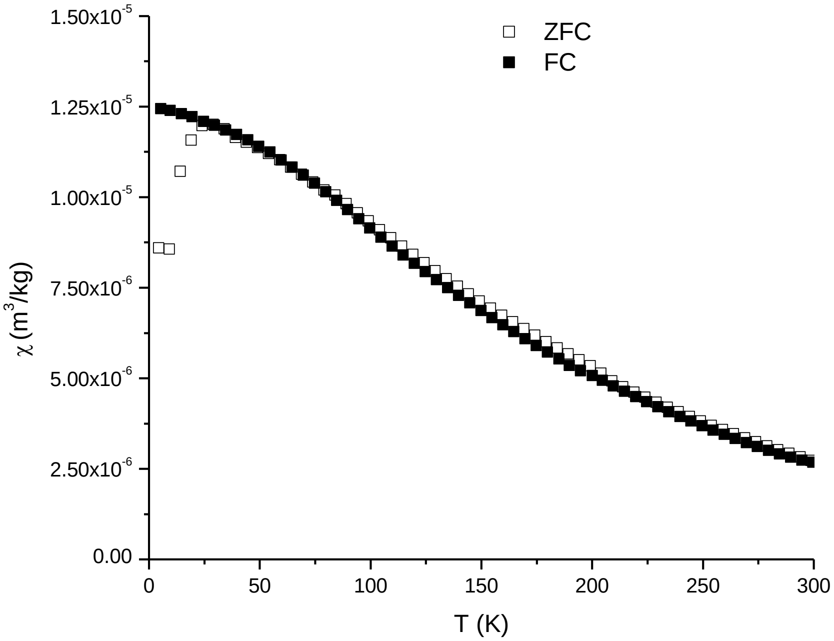

Figure D.4 Zero-field-cooled (ZFC) and field-cooled (FC) curves of 4L-Fh

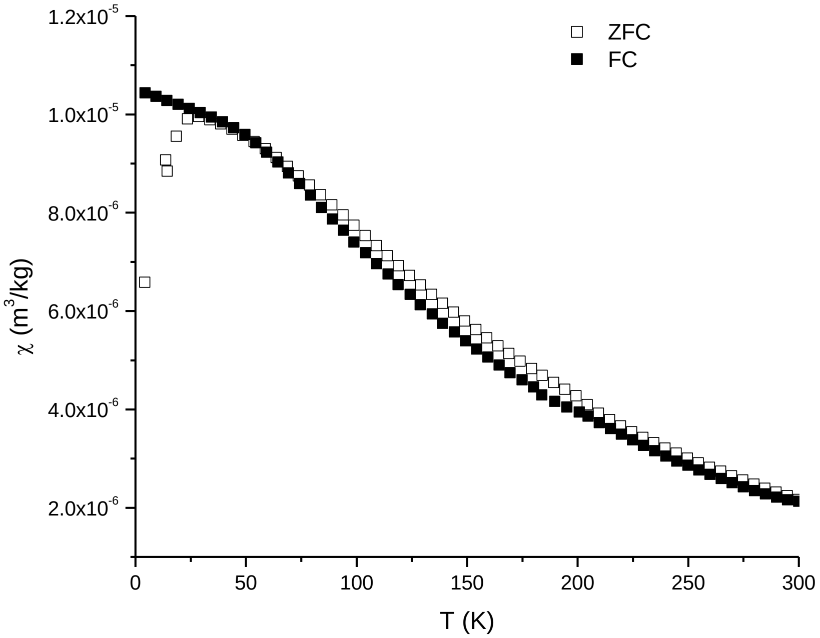

Figure D.5 Zero-field-cooled (ZFC) and field-cooled (FC) curves of P-HFO-0

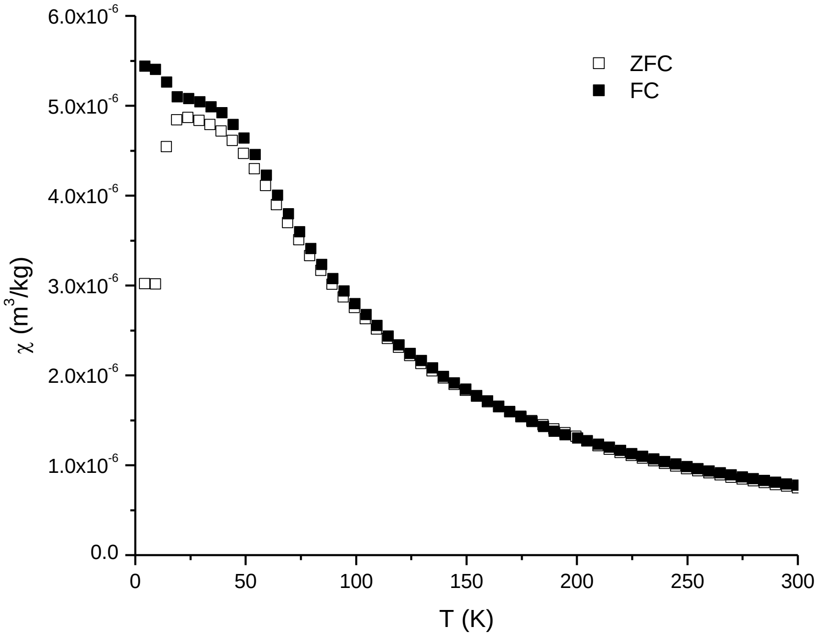

Figure D.6 Zero-field-cooled (ZFC) and field-cooled (FC) curves of P-HFO-0.01

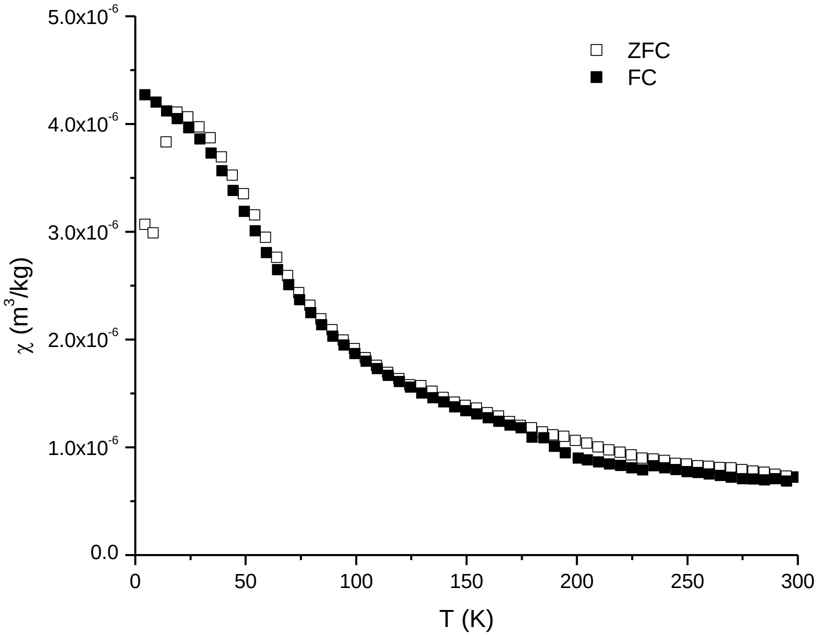

Figure D.7 Zero-field-cooled (ZFC) and field-cooled (FC) curves P-HFO-0.025

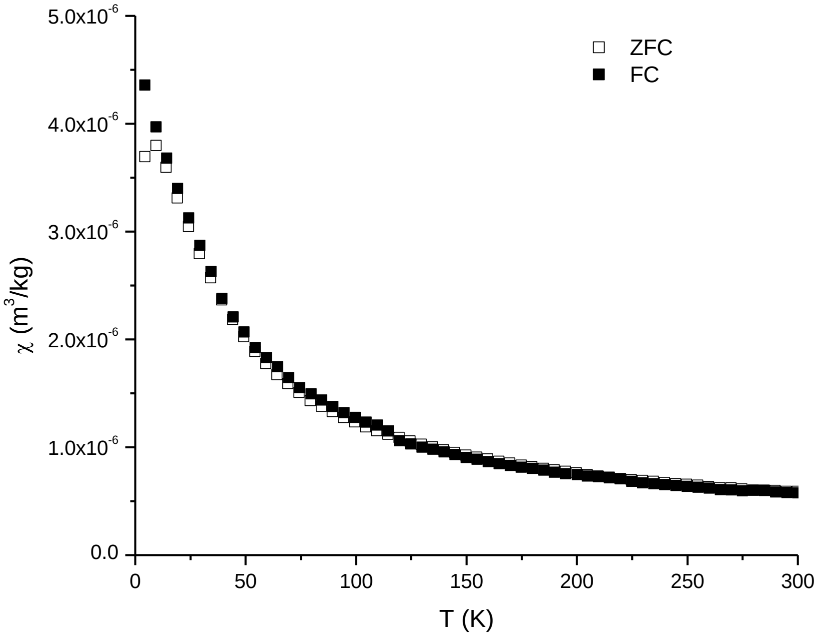

Figure D.8 Zero-field-cooled (ZFC) and field-cooled (FC) curves of P-HFO-0.05

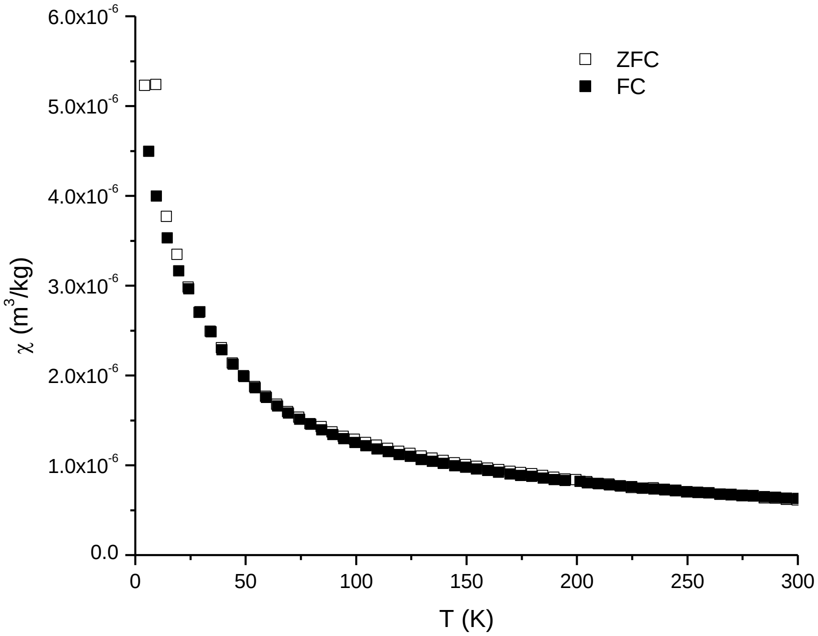

Figure D.9 Zero-field-cooled (ZFC) and field-cooled (FC) curves of P-HFO-0.075

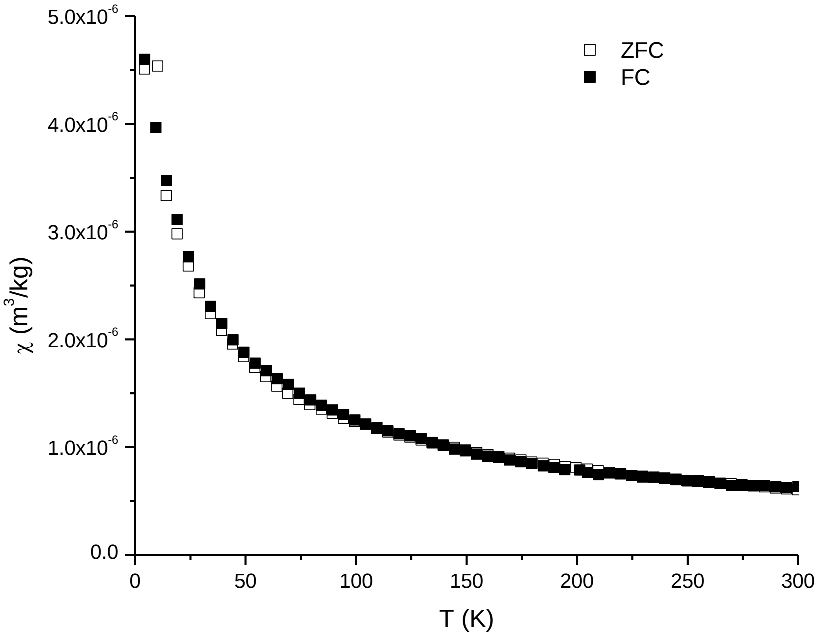

Figure D.10 Zero-field-cooled (ZFC) and field-cooled (FC) curves of P-HFO-0.1

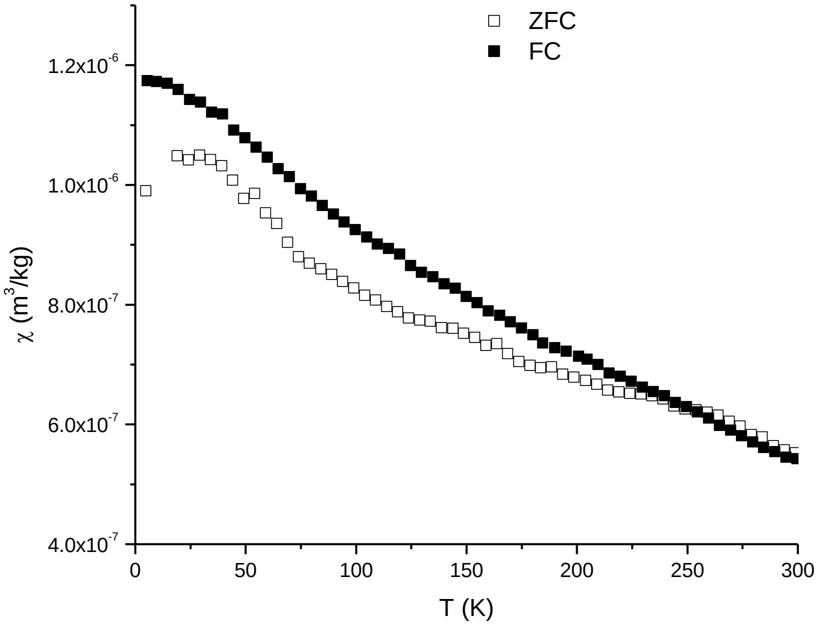

Figure D.11 Zero-field-cooled (ZFC) and field-cooled (FC) curves of Gt-1

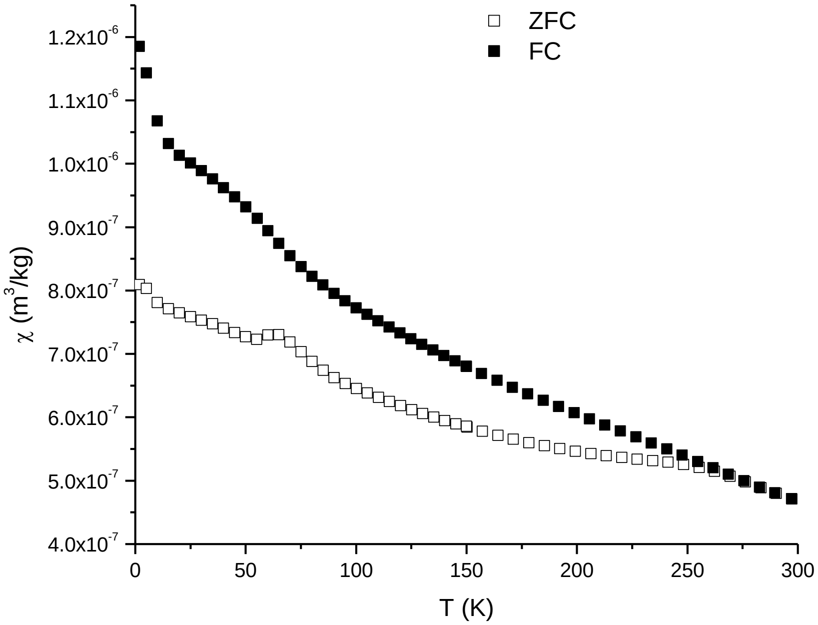

Figure D.12 Zero-field-cooled (ZFC) and field-cooled (FC) curves of Gt-2

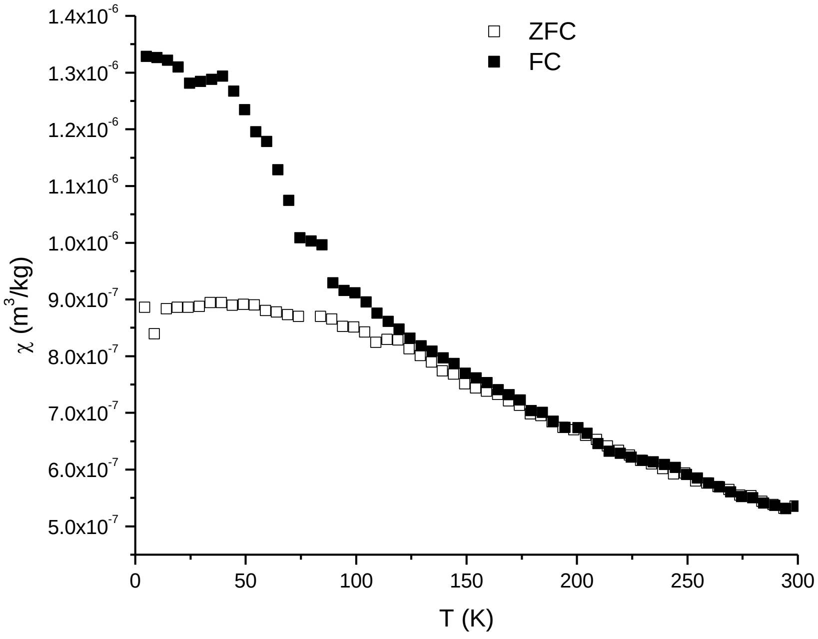

Figure D.13 Zero-field-cooled (ZFC) and field-cooled (FC) curves of Gt-3

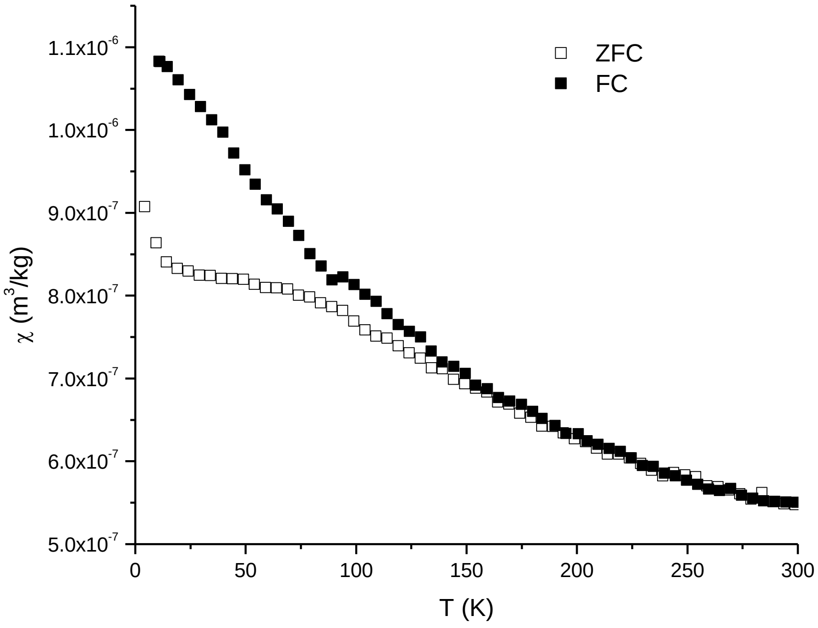

Figure D.14 Zero-field-cooled (ZFC) and field-cooled (FC) curves of Gt-4

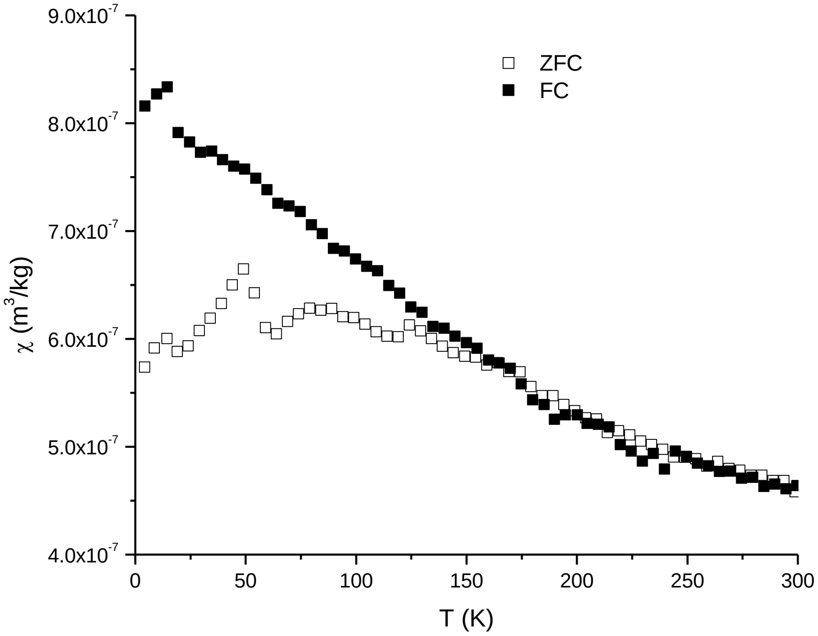

Figure D.15 Zero-field-cooled (ZFC) and field-cooled (FC) curves of Gt-5

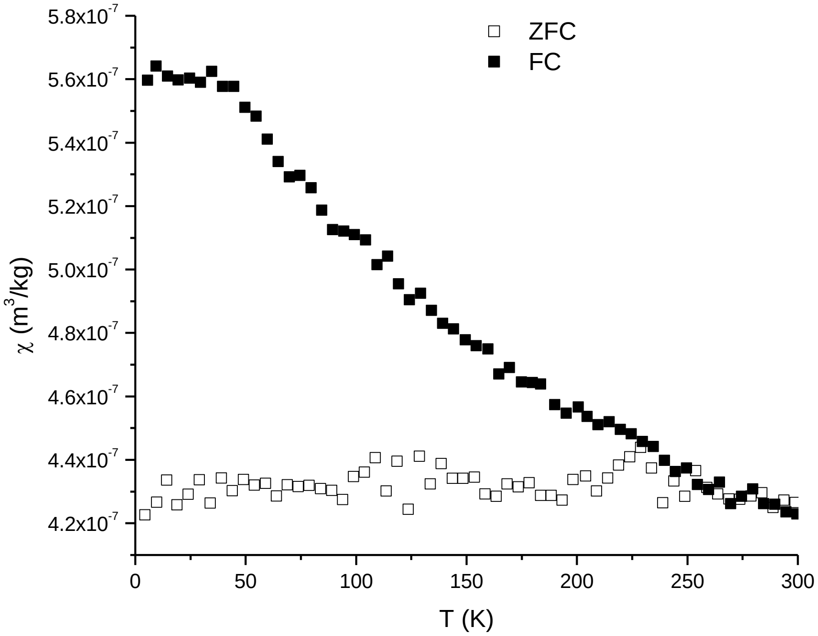

Figure D.16 Zero-field-cooled (ZFC) and field-cooled (FC) curves of Gt-6

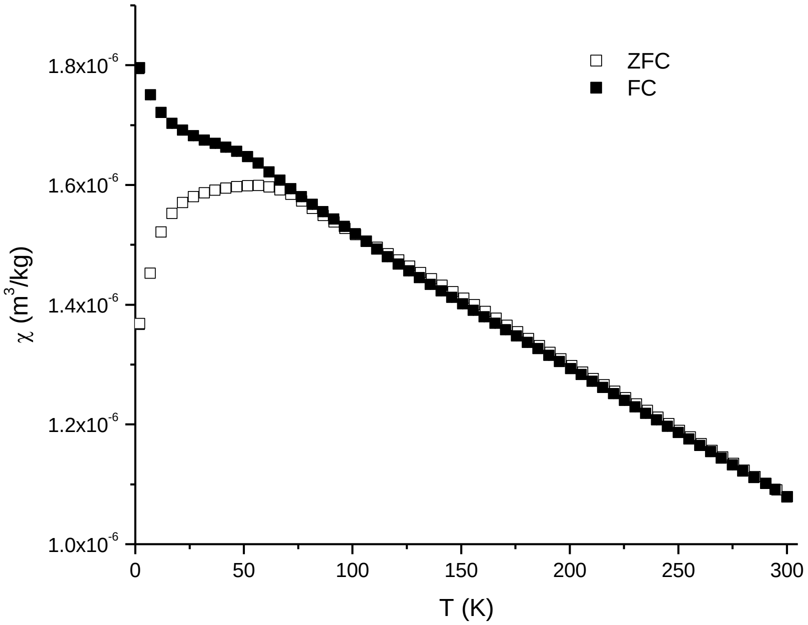

Figure D.17 Zero-field-cooled (ZFC) and field-cooled (FC) curves of Lp-1

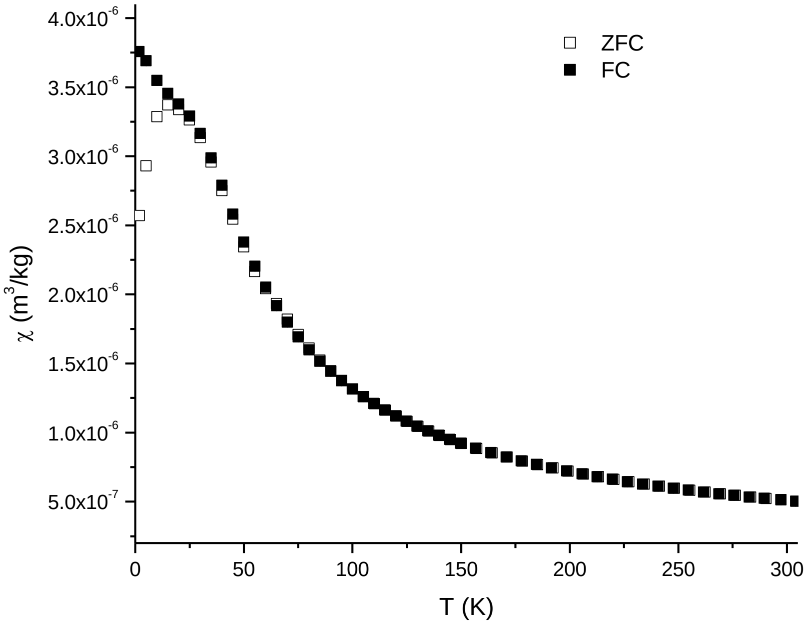

Figure D.18 Zero-field-cooled (ZFC) and field-cooled (FC) curves of Lp-2

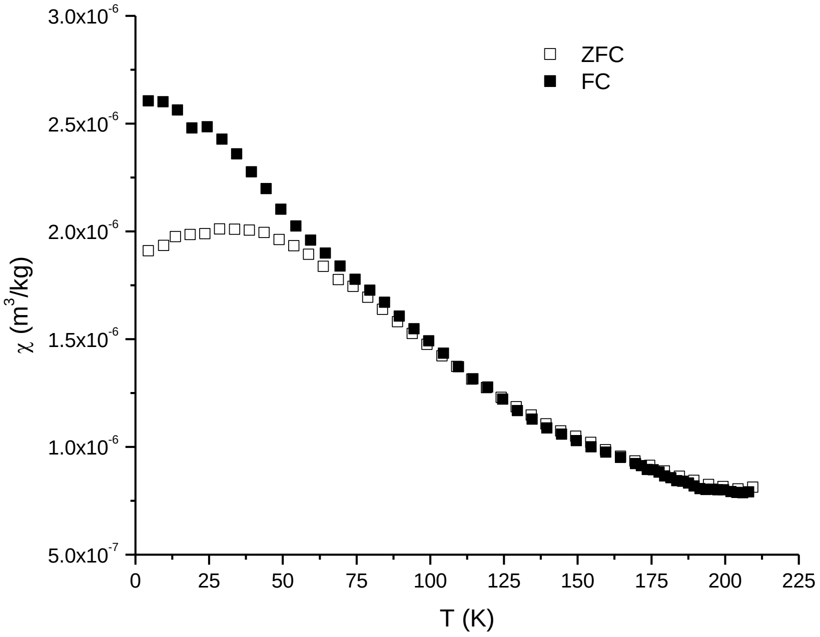

Figure D.19 Zero-field-cooled (ZFC) and field-cooled (FC) curves of Sw-1

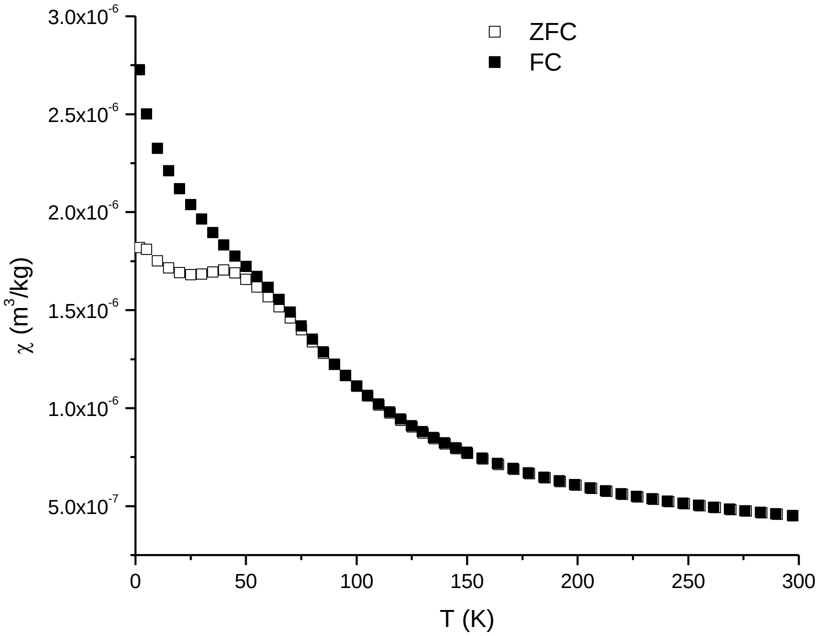

Figure D.20 Zero-field-cooled (ZFC) and field-cooled (FC) curves of Sw-2

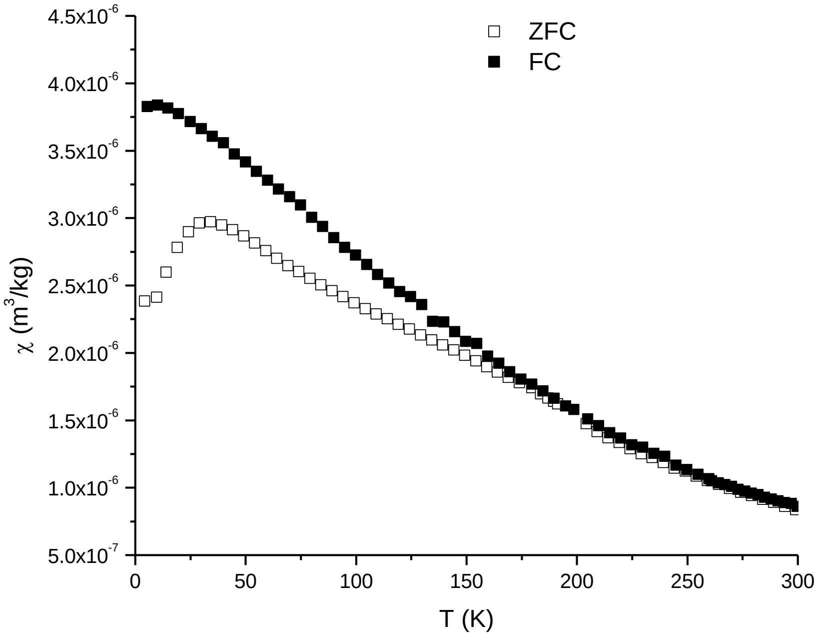

Figure D.21 Zero-field-cooled (ZFC) and field-cooled (FC) curves of Akg-1

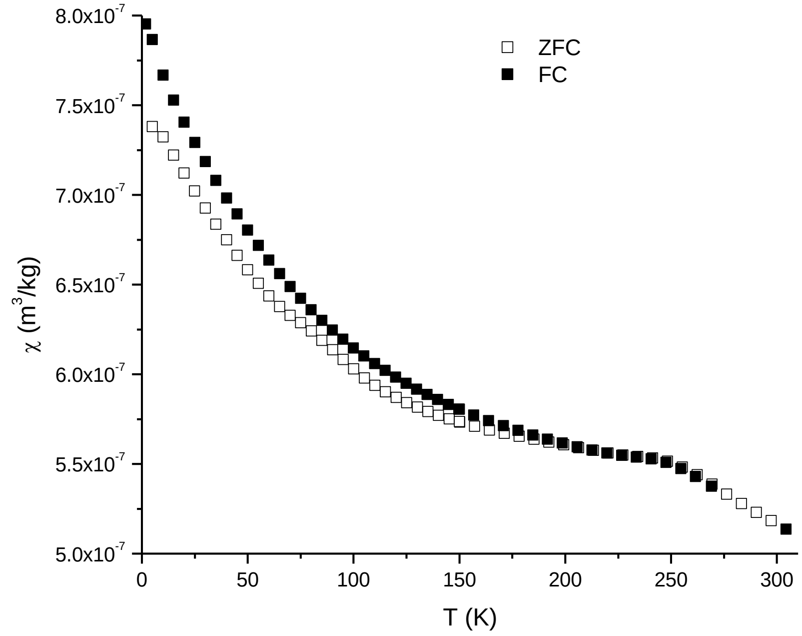

Figure D.22 Zero-field-cooled (ZFC) and field-cooled (FC) curves of Akg-2. The lack of FC data between 275 and 300 K is due to an instrumental artefact

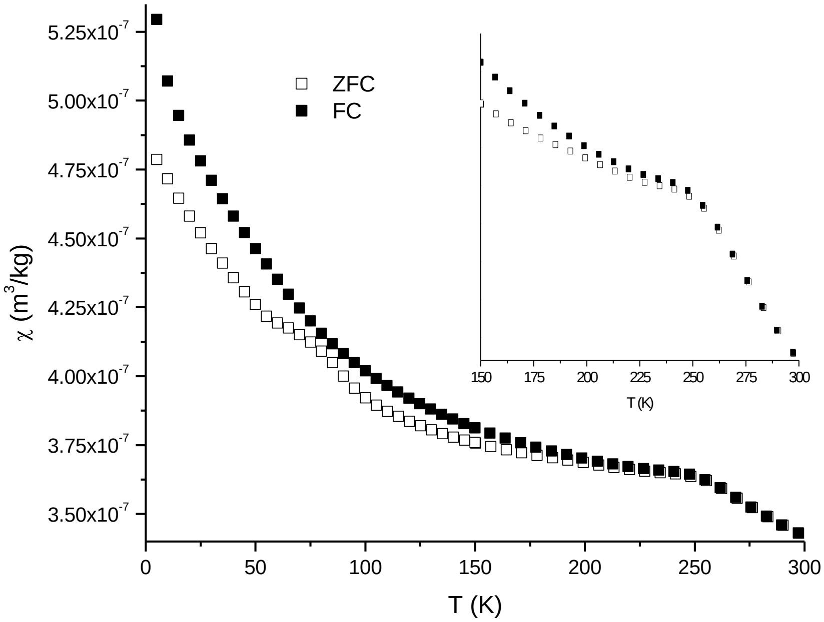

Figure D.23 Zero-field-cooled (ZFC) and field-cooled (FC) curves of Akg-2 measured applying a lower magnetic field, H = 0.1 T; and zoom from 150 K to 300 K (inset)

Appendix E- Field Cycles

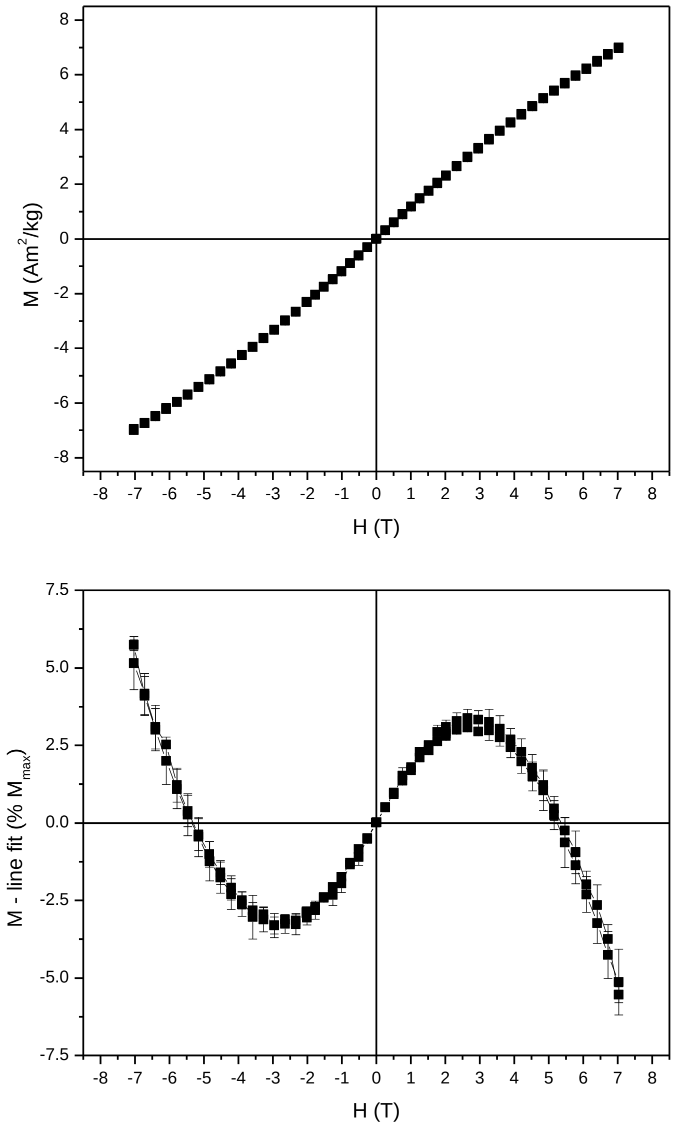

Figure E.1 Field cycle of 2L-Fh at 300 K (top) and corresponding curvature graph (bottom)

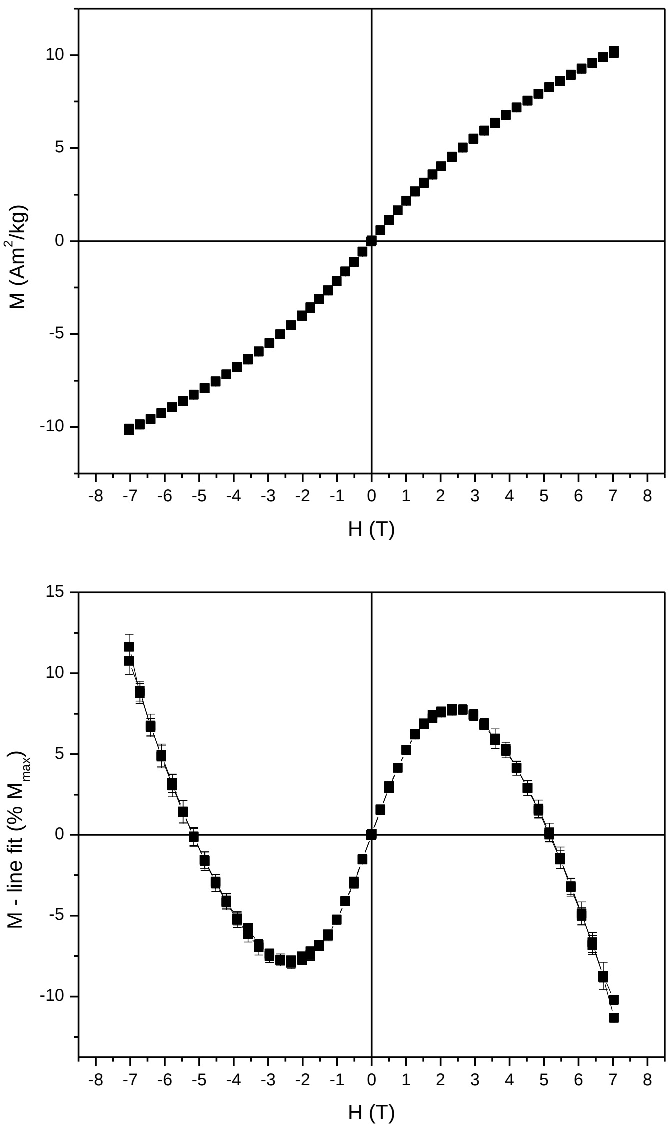

Figure E.2 Field cycle of 2L-Fh at 200 K (top) and corresponding curvature graph (bottom)

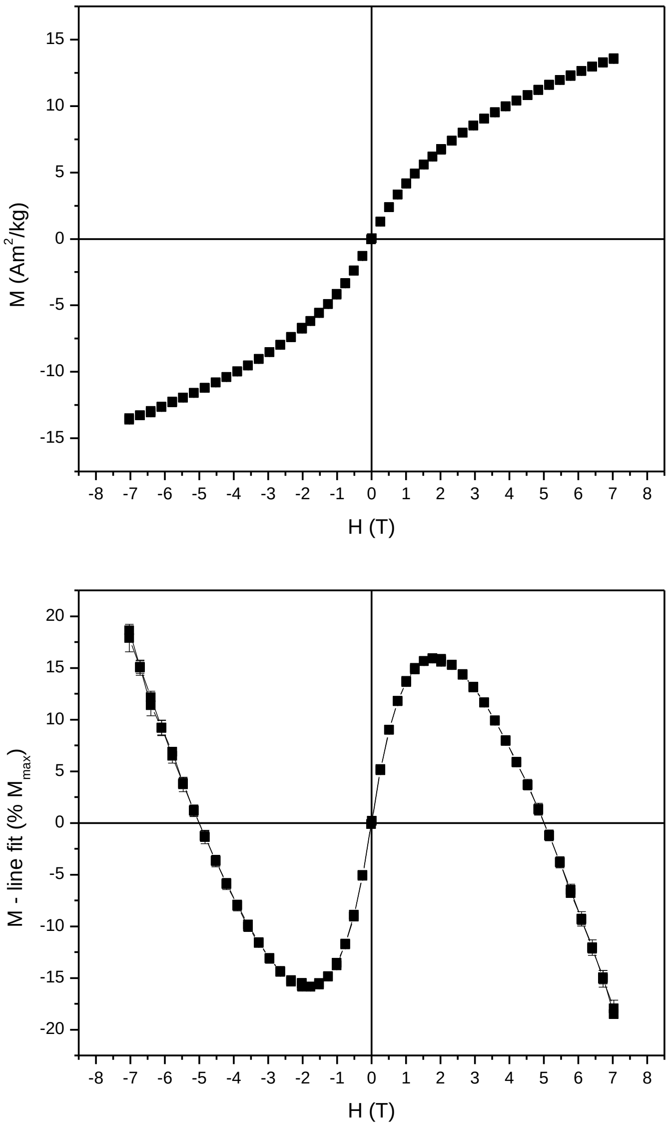

Figure E.3 Field cycle of 2L-Fh at 100 K (top) and corresponding curvature graph (bottom)

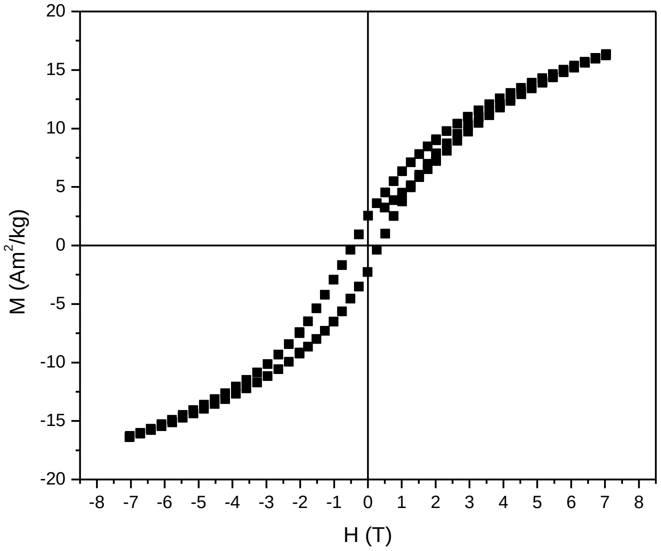

Figure E.4 Field cycle of 2L-Fh at 1.8 K

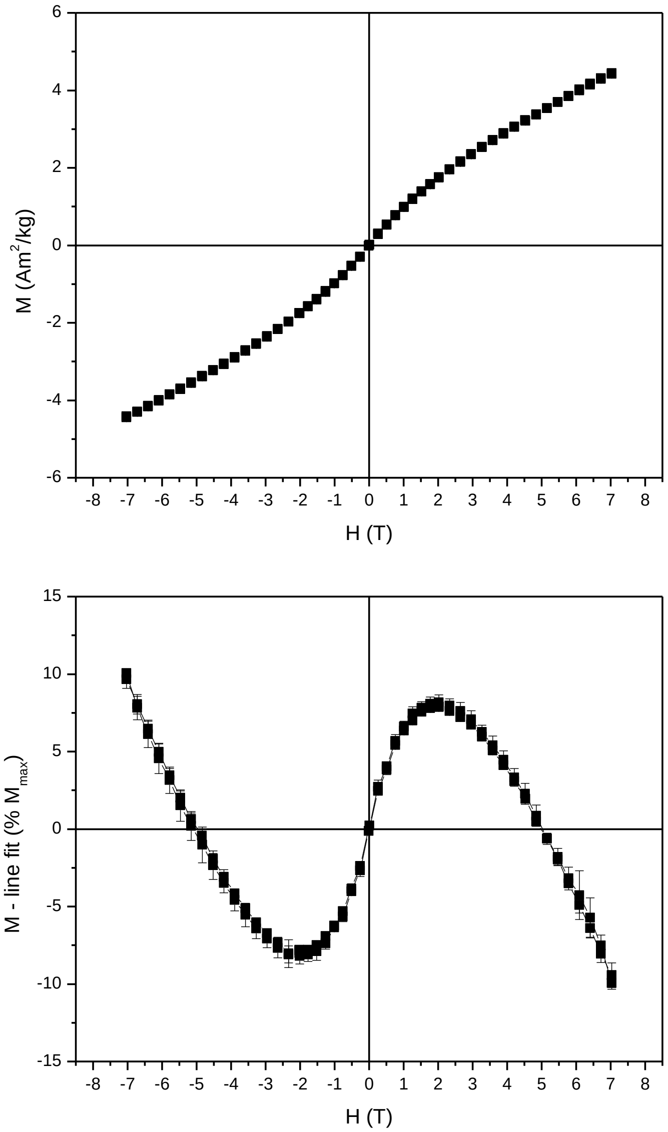

Figure E.5 Field cycle of 6L-Fh-1 at 300 K (top) and corresponding curvature graph (bottom)

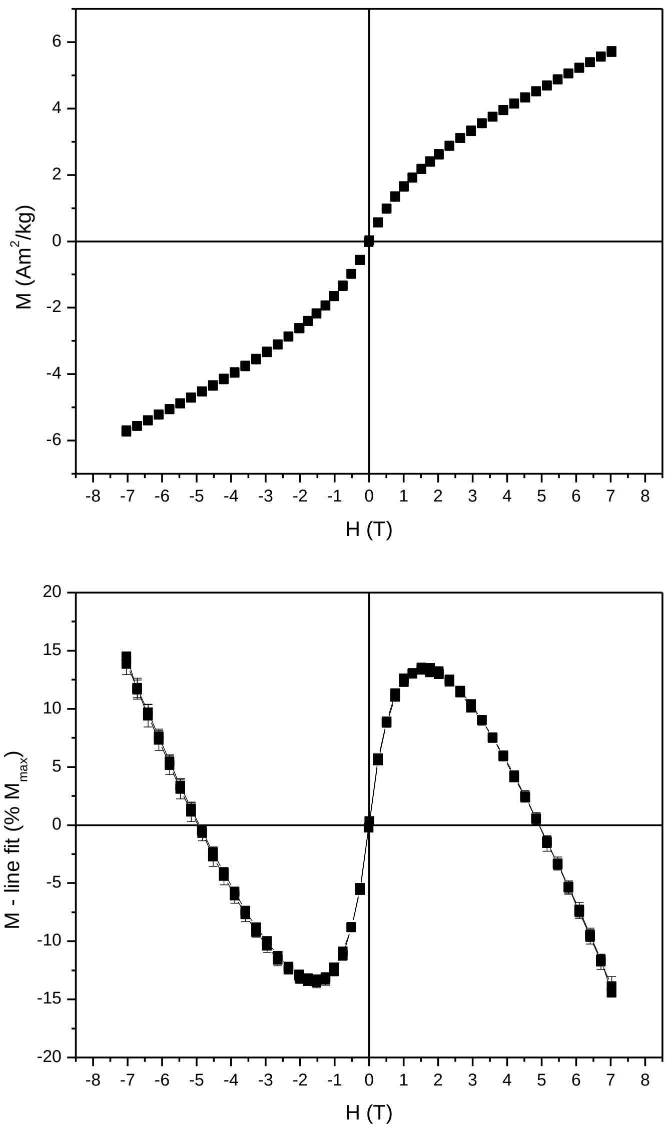

Figure E.6 Field cycle of 6L-Fh-1 at 200 K (top) and corresponding curvature graph (bottom)

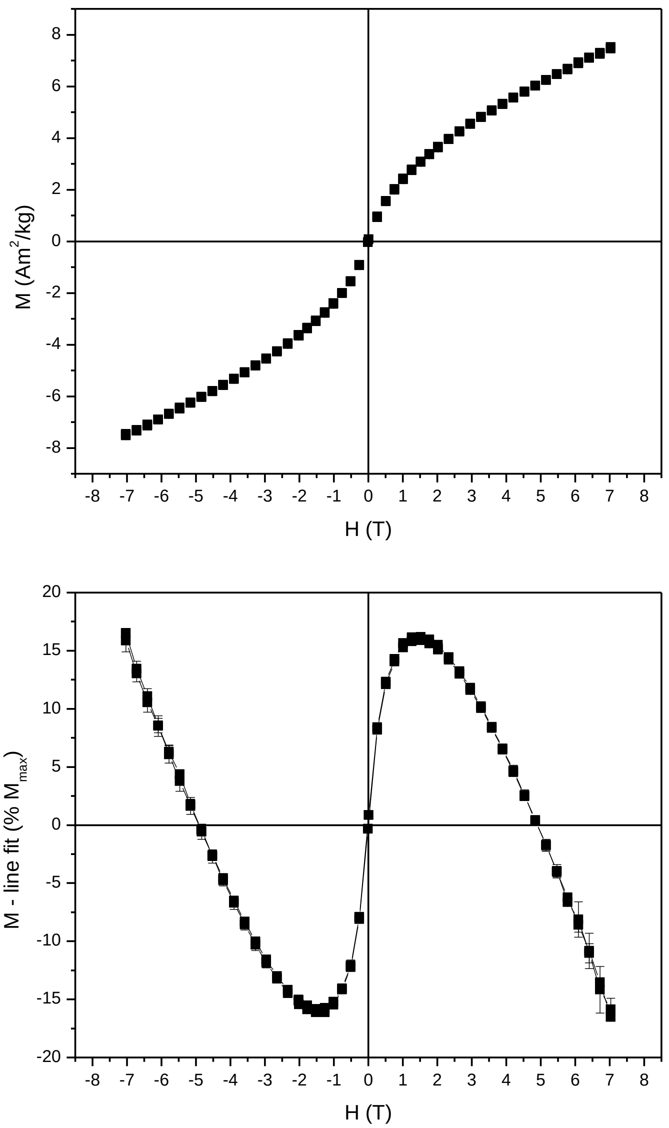

Figure E.7 Field cycle of 6L-Fh-1 at 100 K (top) and corresponding curvature graph (bottom)

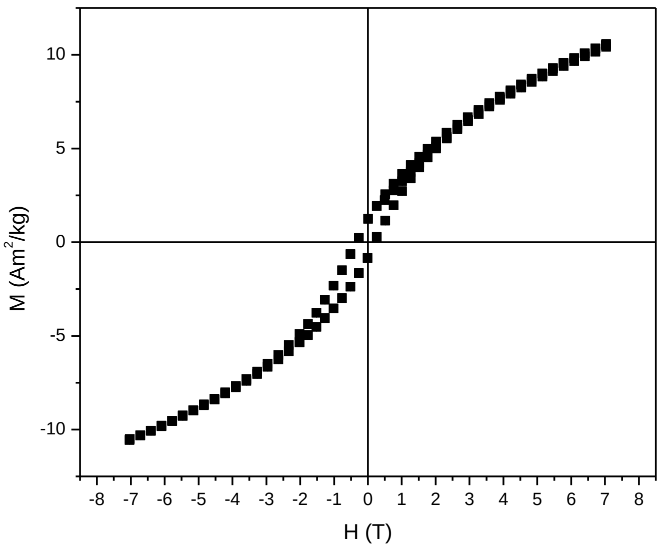

Figure E.8 Field cycle of 6L-Fh-1 at 1.8 K

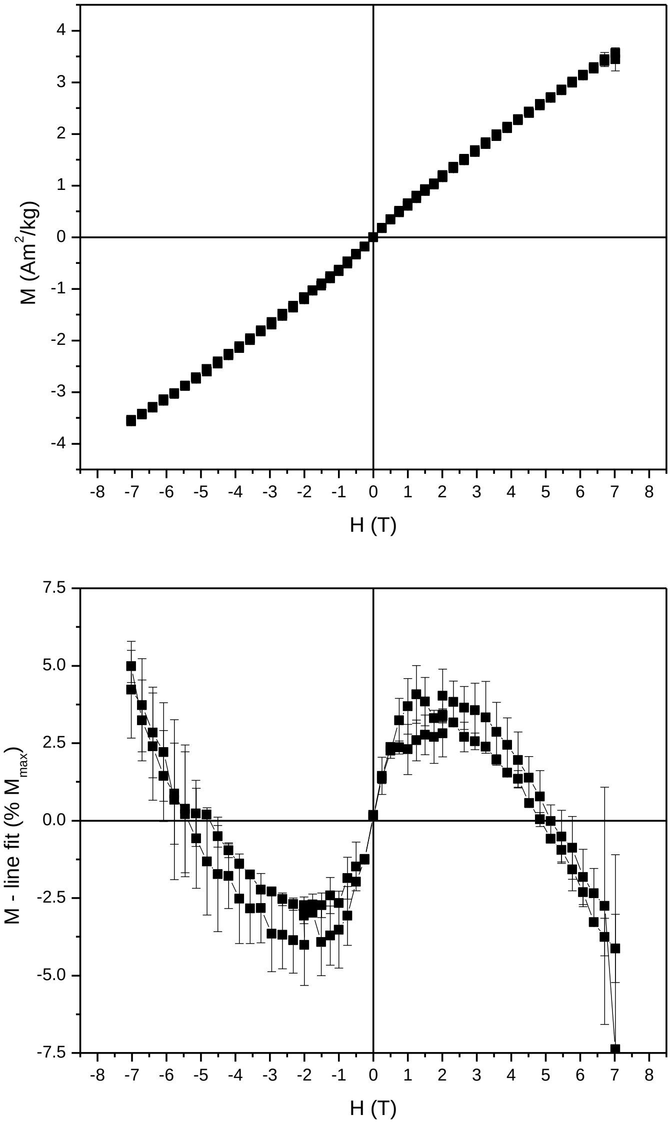

Figure E.9 Field cycle of 6L-Fh-2 at 300 K (top) and corresponding curvature graph (bottom)

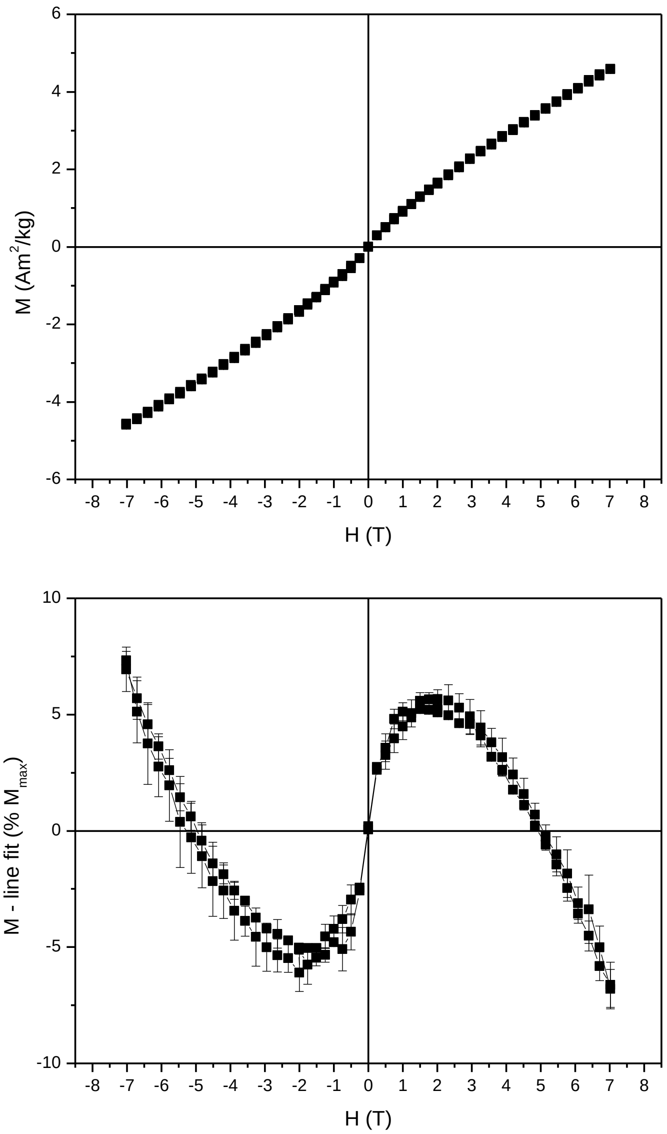

Figure E.10 Field cycle of 6L-Fh-2 at 200 K (top) and corresponding curvature graph (bottom)

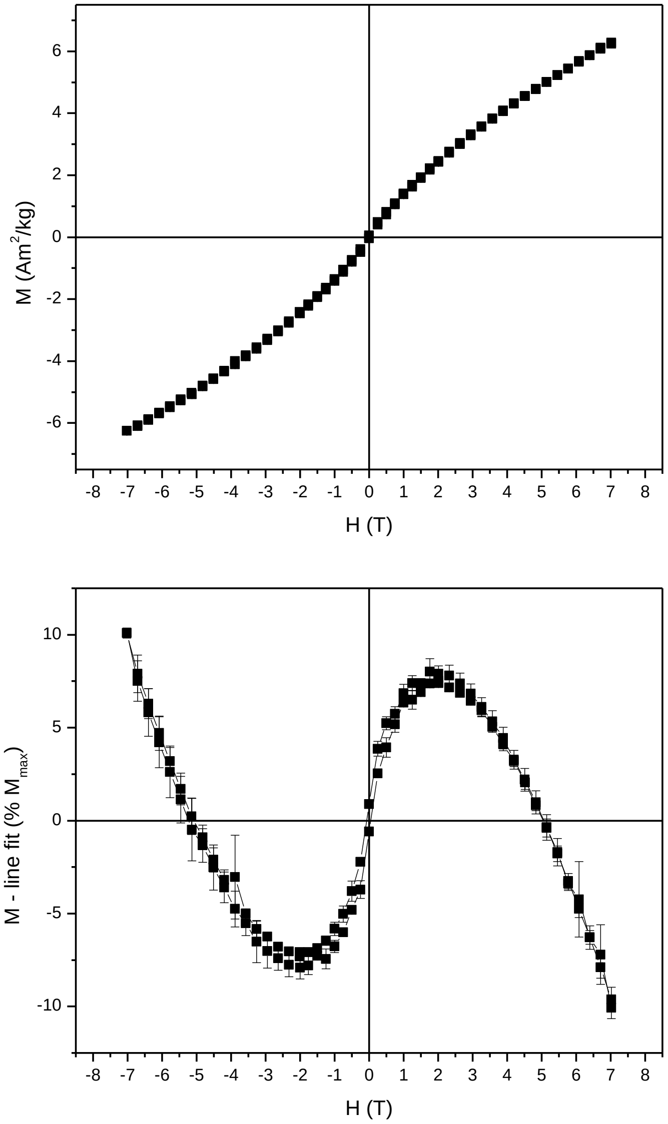

Figure E.11 Field cycle of 6L-Fh-2 at 100 K (top) and corresponding curvature graph (bottom)

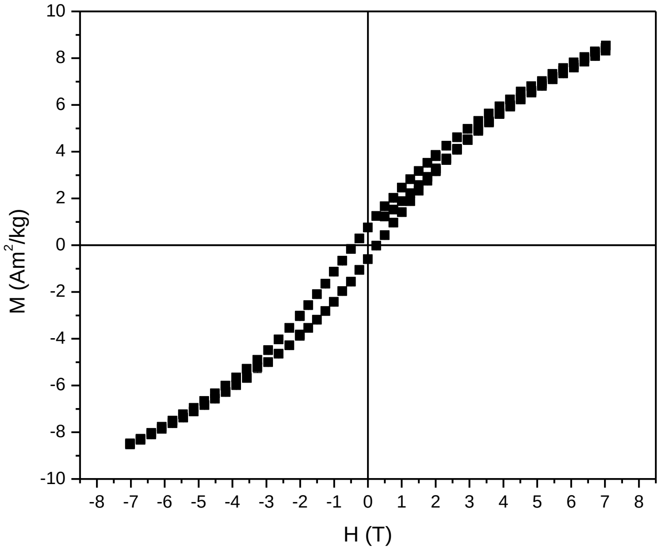

Figure E.12 Field cycle of 6L-Fh-2 at 1.8 K

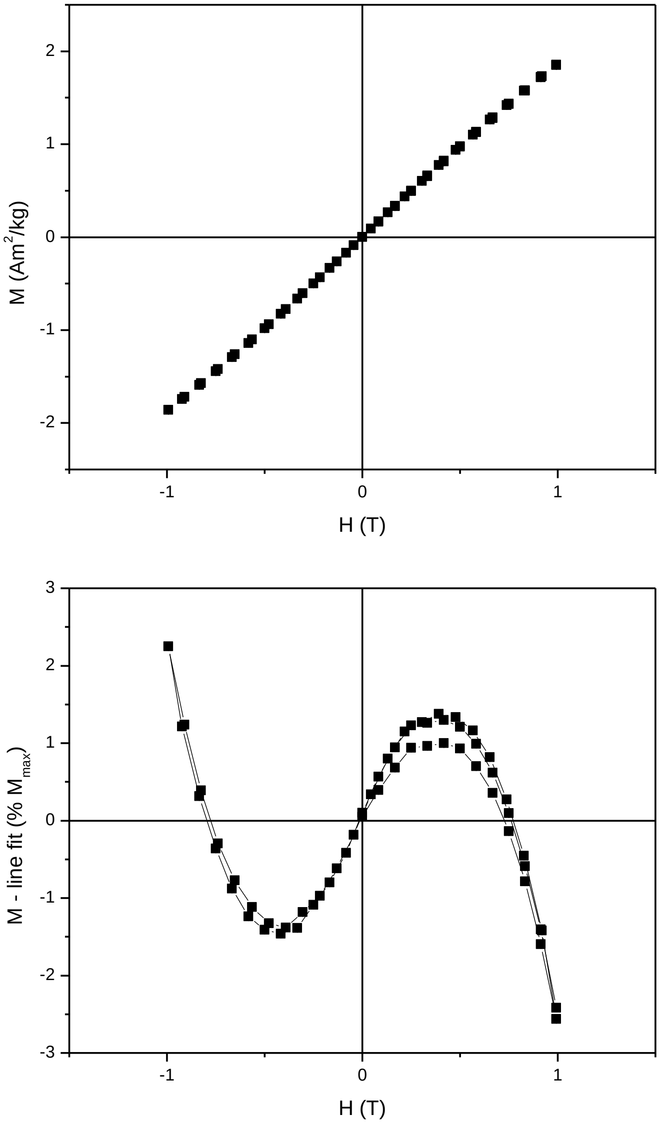

Figure E.13 Field cycle of 4L-Fh at 300 K (top) and corresponding curvature graph (bottom)

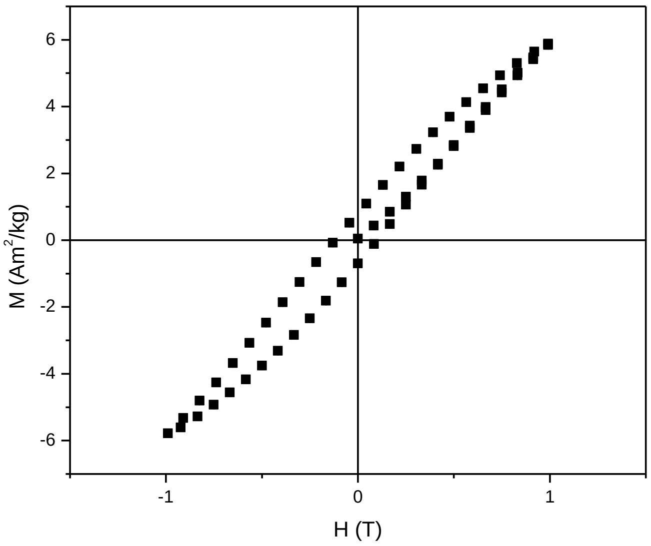

Figure E.14 Field cycle of 4L-Fh at 4.2 K

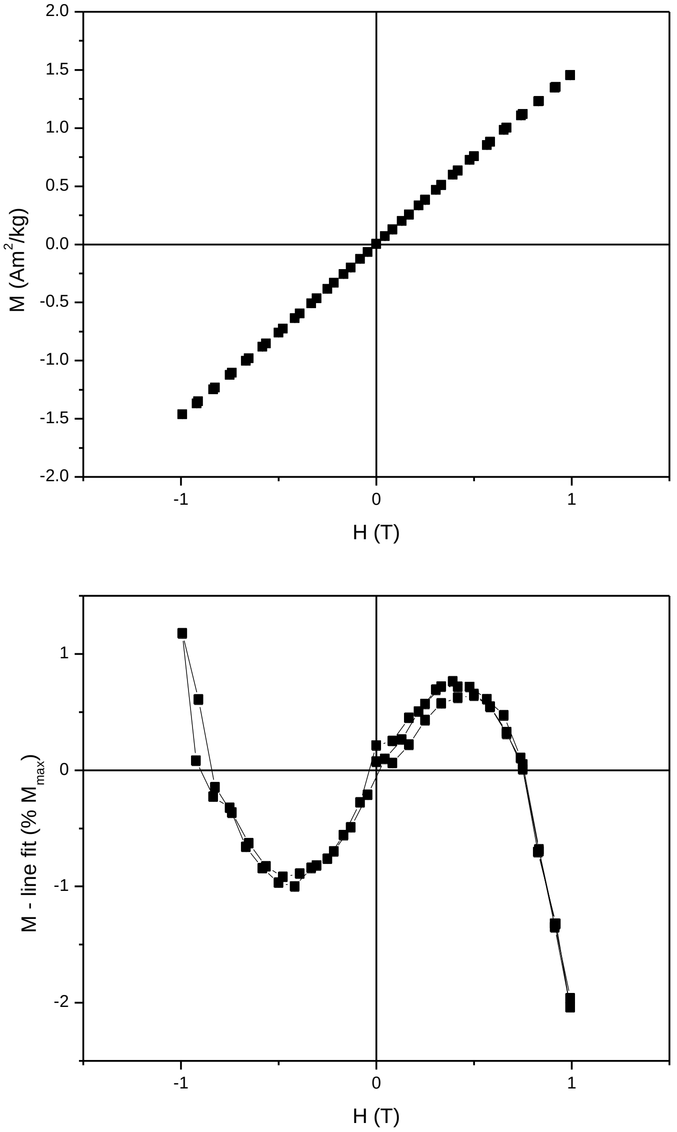

Figure E.15 Field cycle of P-HFO-0 at 300 K (top) and corresponding curvature graph (bottom)

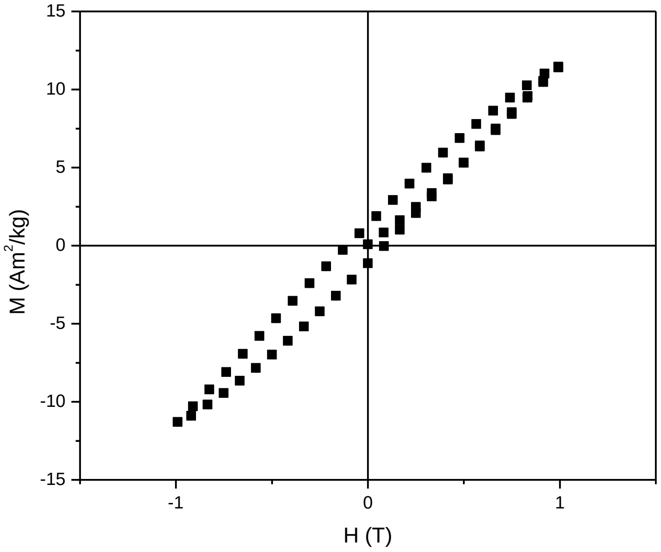

Figure E.16 Field cycle of P-HFO-0 at 4.2 K

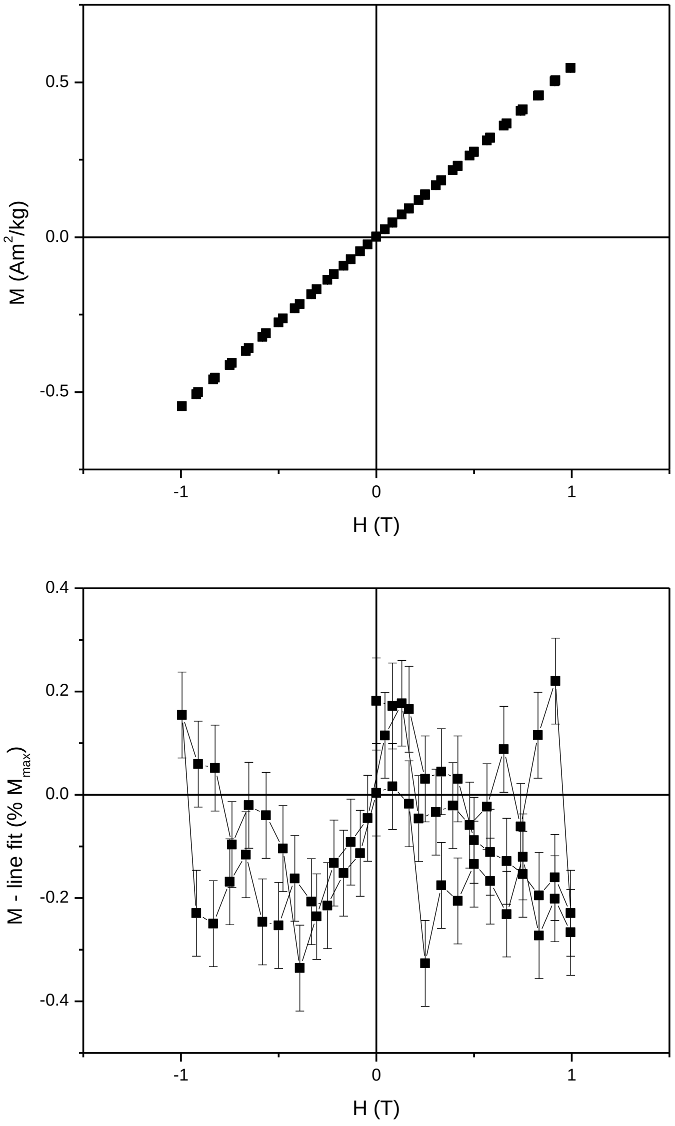

Figure E.17 Field cycle of P-HFO-0.01 at 300 K (top) and corresponding curvature graph (bottom)

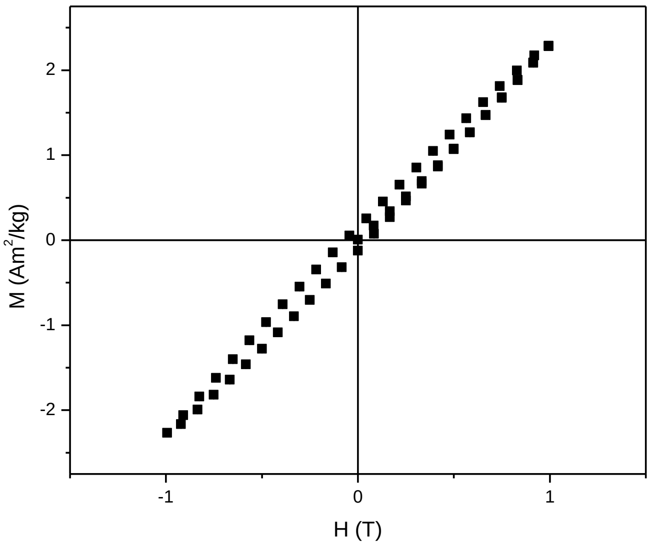

Figure E.18 Field cycle of P-HFO-0.01 at 4.2 K

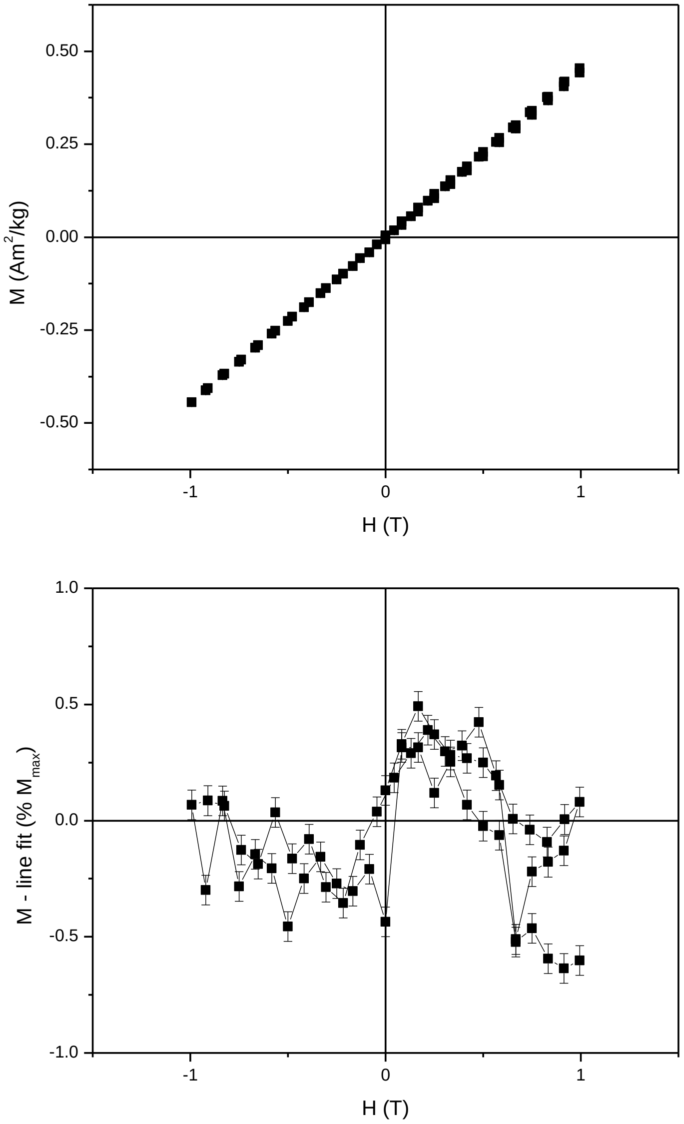

Figure E.19 Field cycle of P-HFO-0.025 at 300 K (top) and corresponding curvature graph (bottom)

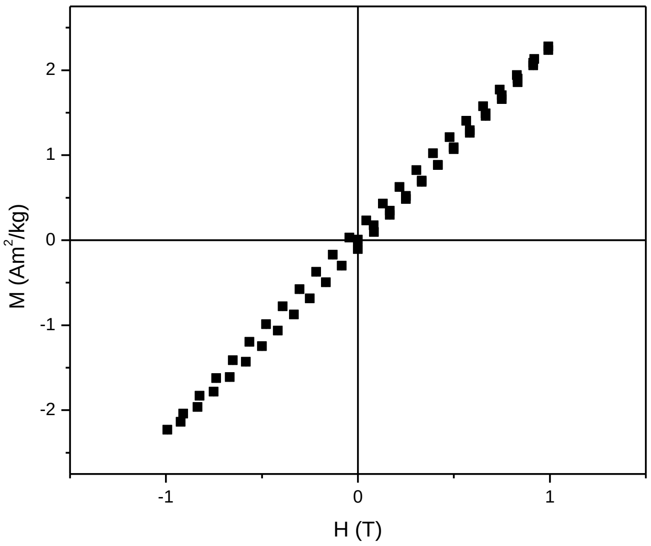

Figure E.20 Field cycle of P-HFO-0.025 at 4.2 K

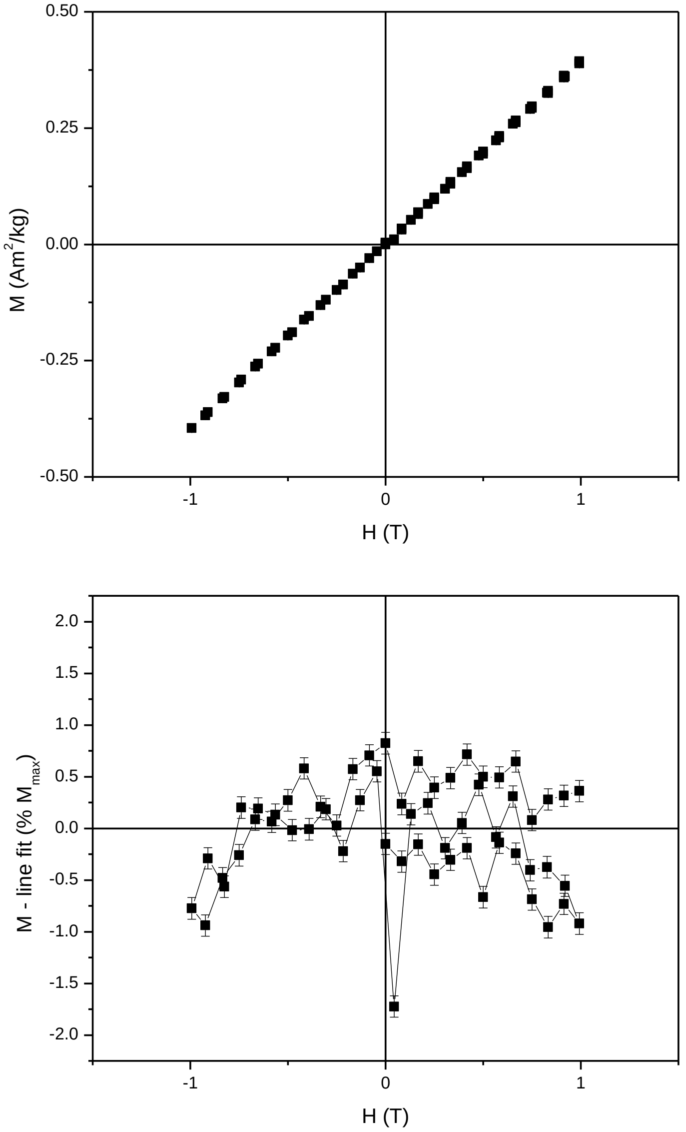

Figure E.21 Field cycle of P-HFO-0.05 at 300 K (top) and corresponding curvature graph (bottom)

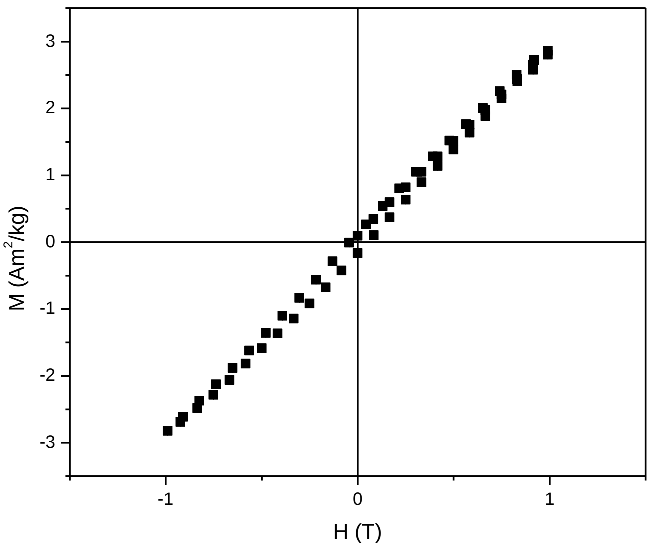

Figure E.22 Field cycle of P-HFO-0.05 at 4.2 K

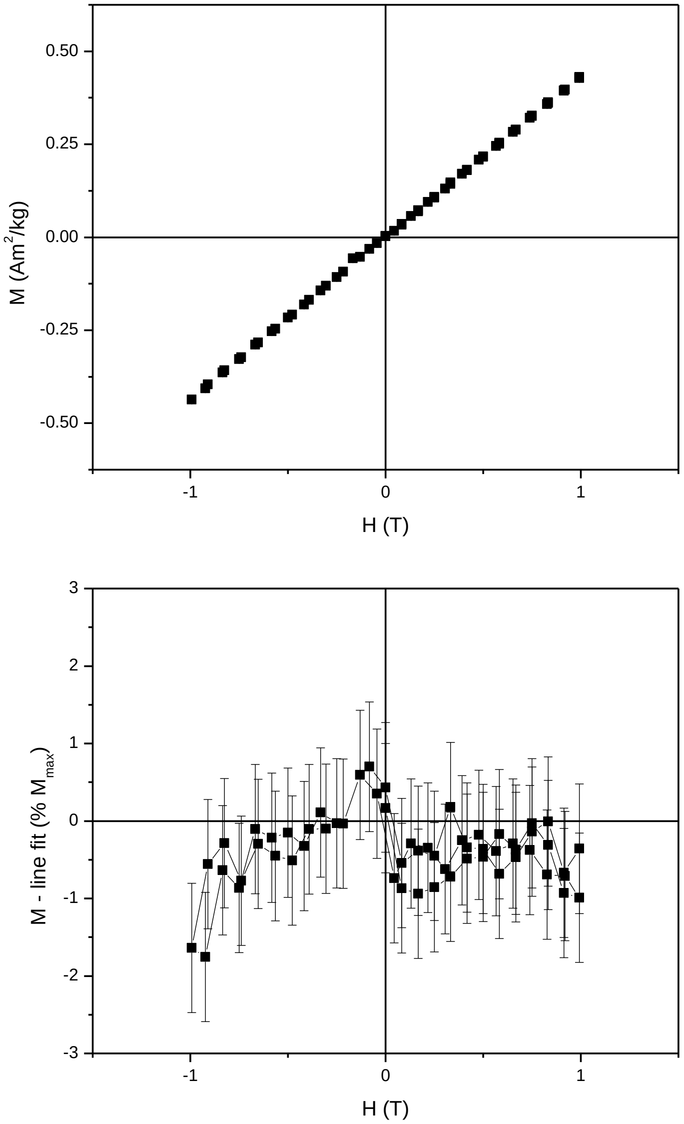

Figure E.23 Field cycle of P-HFO-0.075 at 300 K (top) and corresponding curvature graph (bottom)

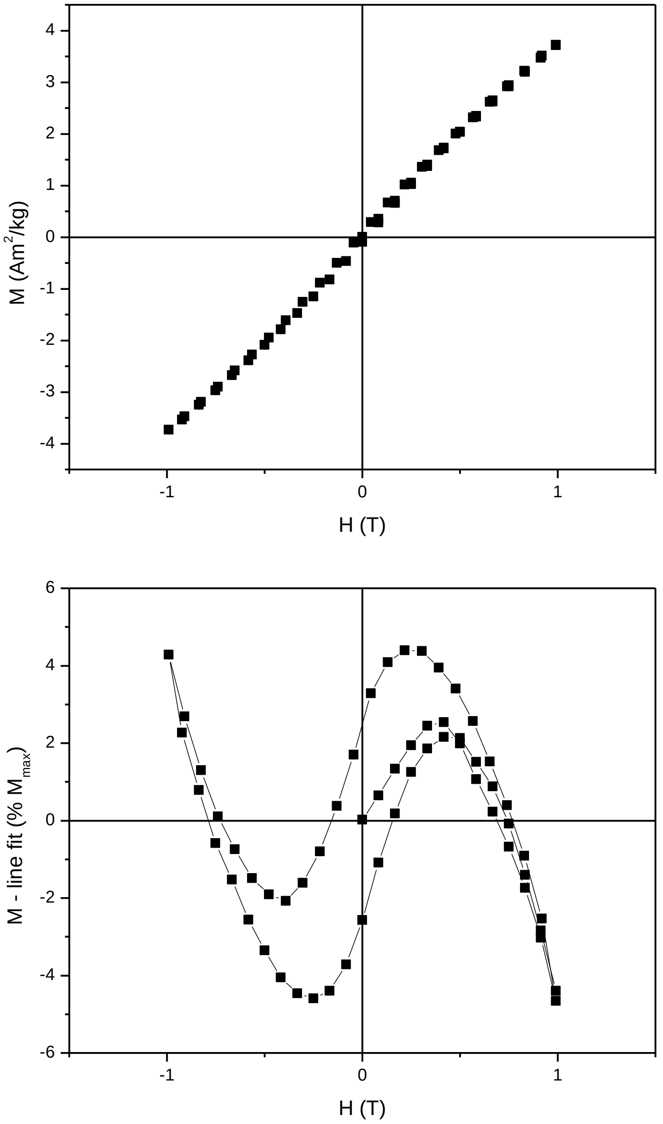

Figure E.24 Field cycle of P-HFO-0.075 at 4.2 K (top) and corresponding curvature graph (bottom)

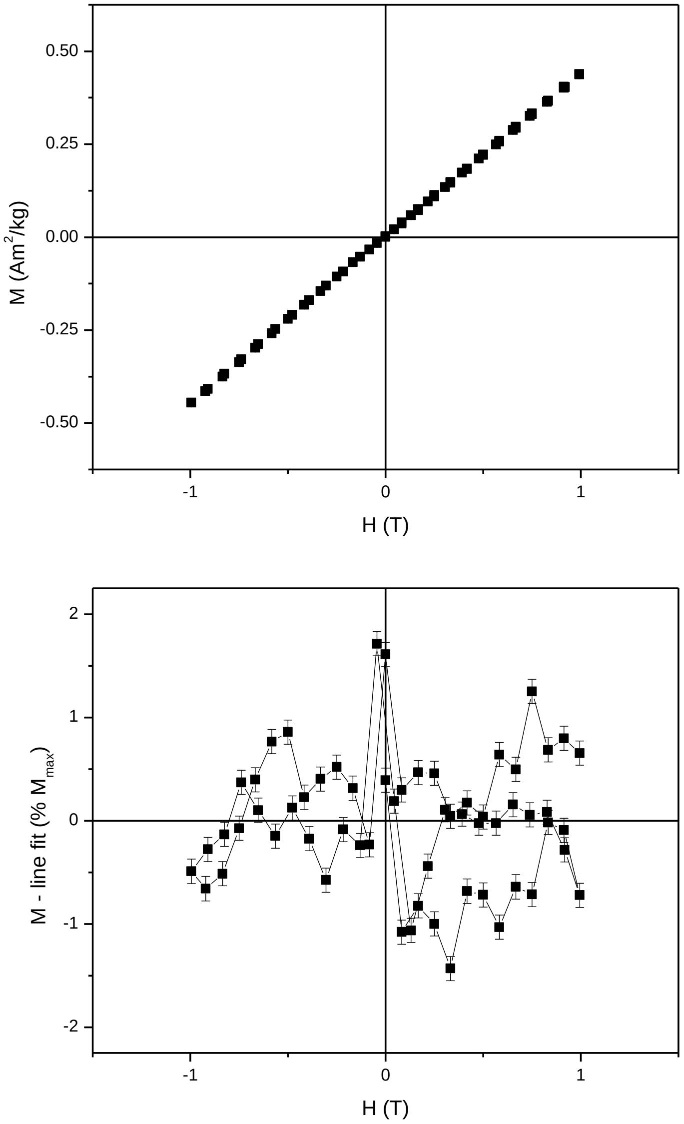

Figure E.25 Field cycle of P-HFO-0.1 at 300 K (top) and corresponding curvature graph (bottom)

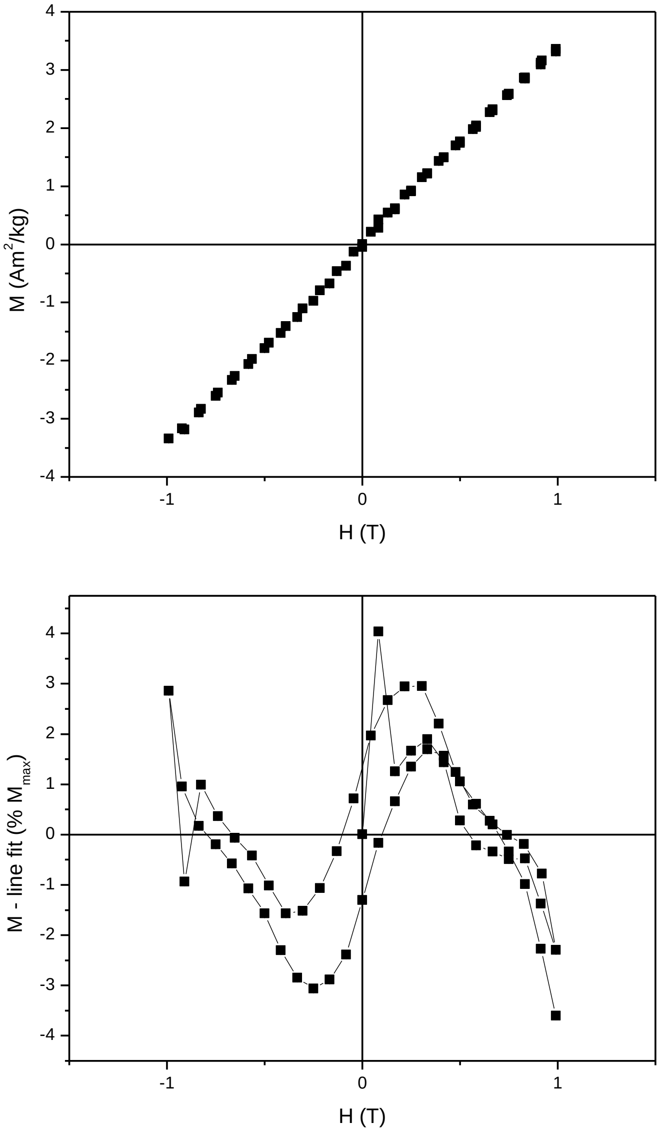

Figure E.26 Field cycle of P-HFO-0.1 at 4.2 K (top) and corresponding curvature graph (bottom)

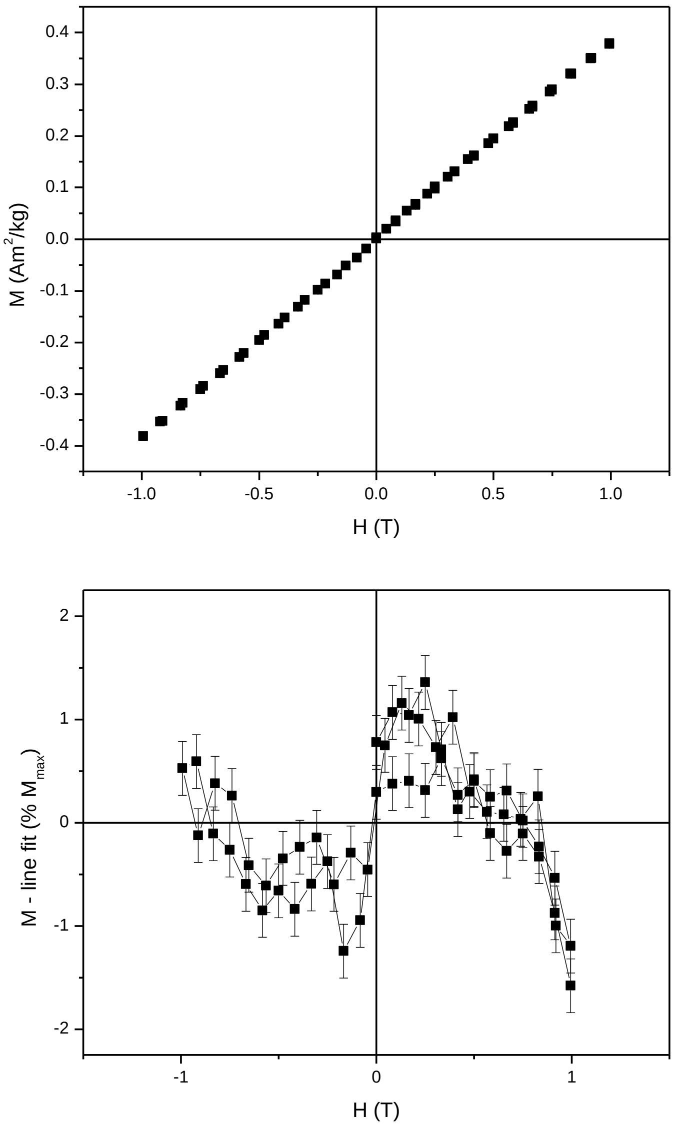

Figure E.27 Field cycle of Gt-1 at 300 K (top) and corresponding curvature graph (bottom)

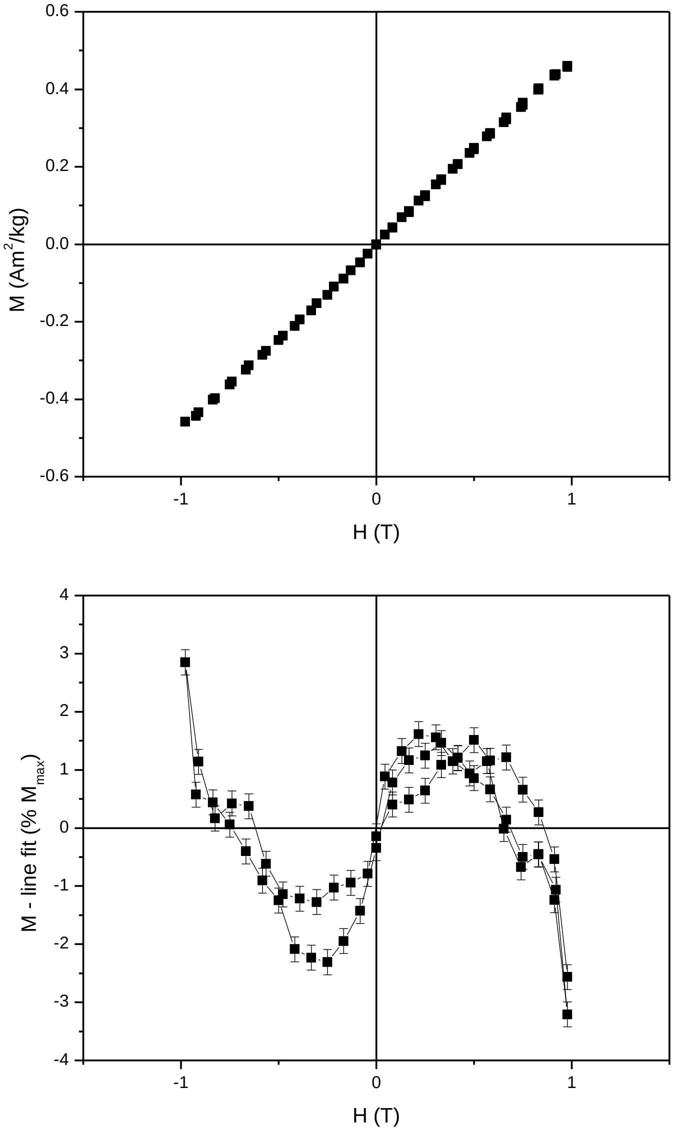

Figure E.28 Field cycle of Gt-1 at 270 K (top) and corresponding curvature graph (bottom). The separation of the curves is due to instrumental noise and is not consistent with hysteresis

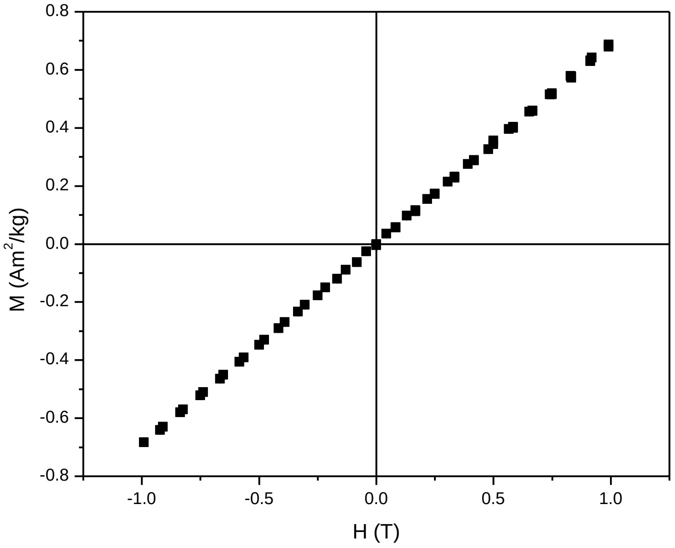

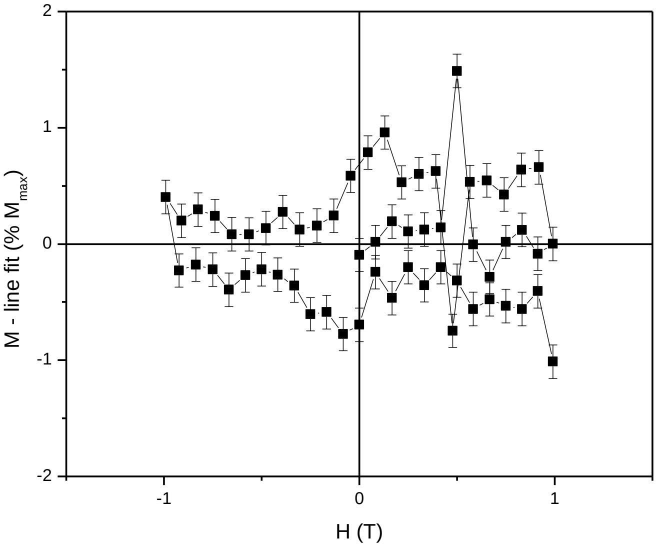

Figure E.29 Field cycle of Gt-1 at 4.2 K (top) and corresponding curvature graph (bottom)

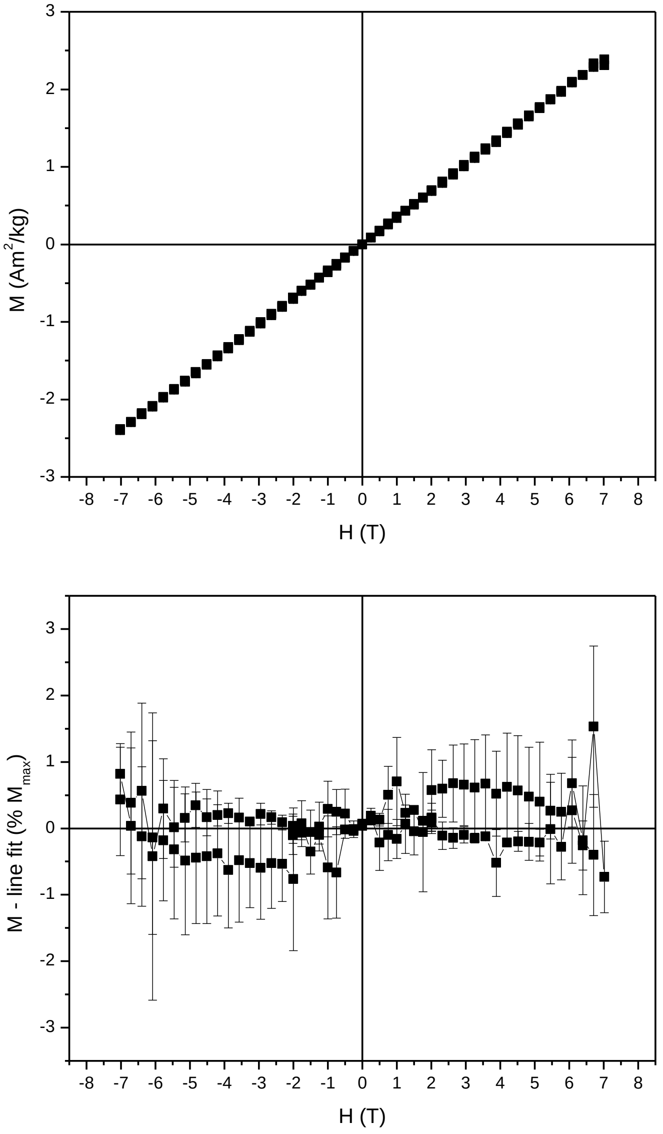

Figure E.30 Field cycle of Gt-2 at 300 K (top) and corresponding curvature graph (bottom)

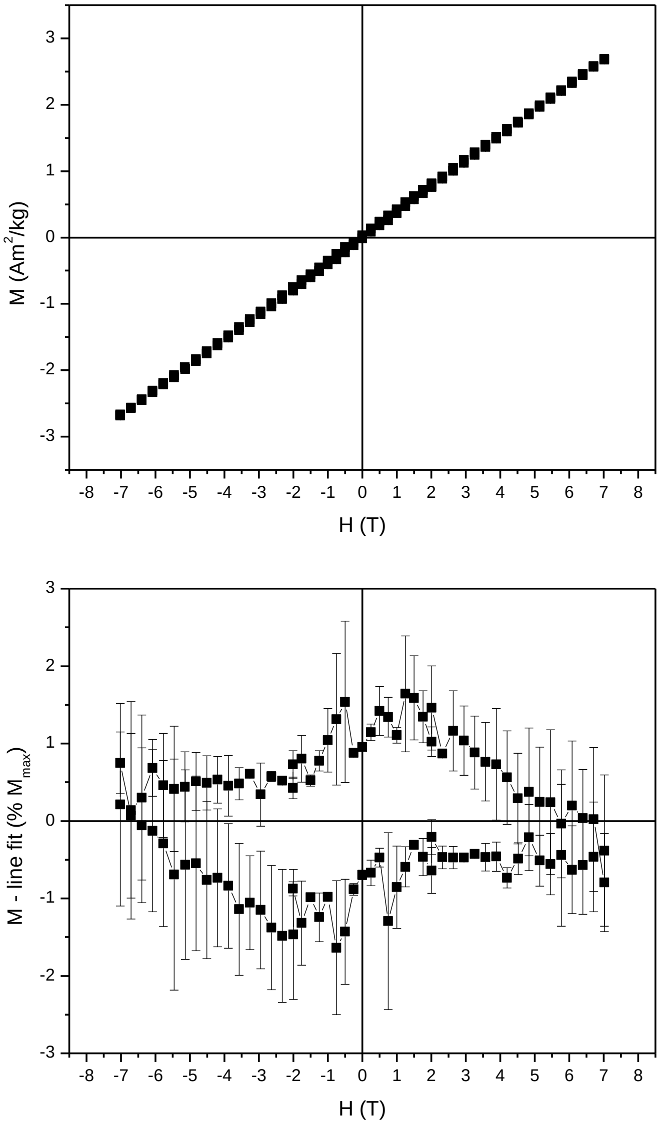

Figure E.31 Field cycle of Gt-2 at 200 K (top) and corresponding curvature graph (bottom)

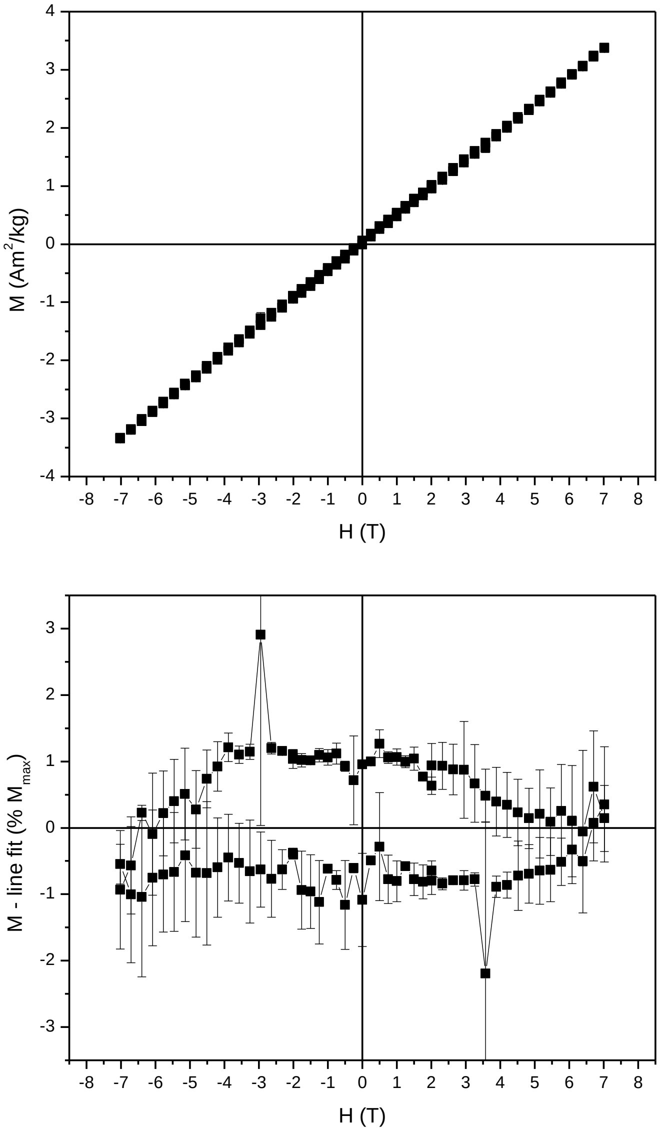

Figure E.32 Field cycle of Gt-2 at 100 K (top) and corresponding curvature graph (bottom)

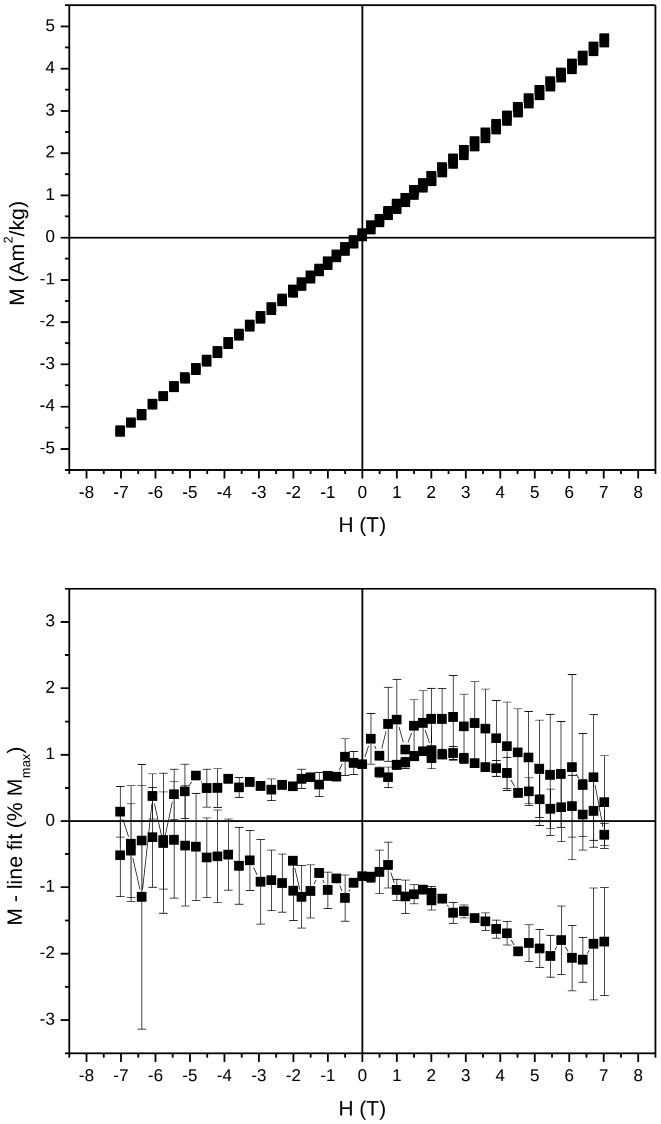

Figure E.33 Field cycle of Gt-2 at 1.8 K (top) and corresponding curvature graph (bottom); the evident deviation of the lower branch at positive fields is due to an instrumental artefact

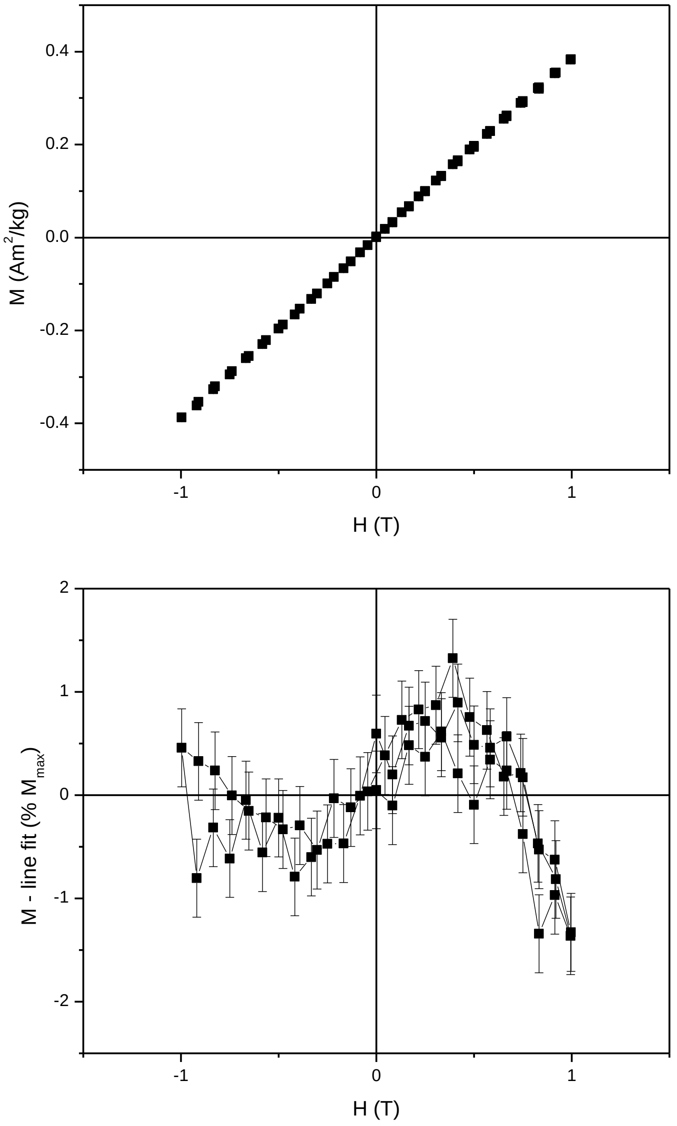

Figure E.34 Field cycle of Gt-3 at 300 K (top) and corresponding curvature graph (bottom)

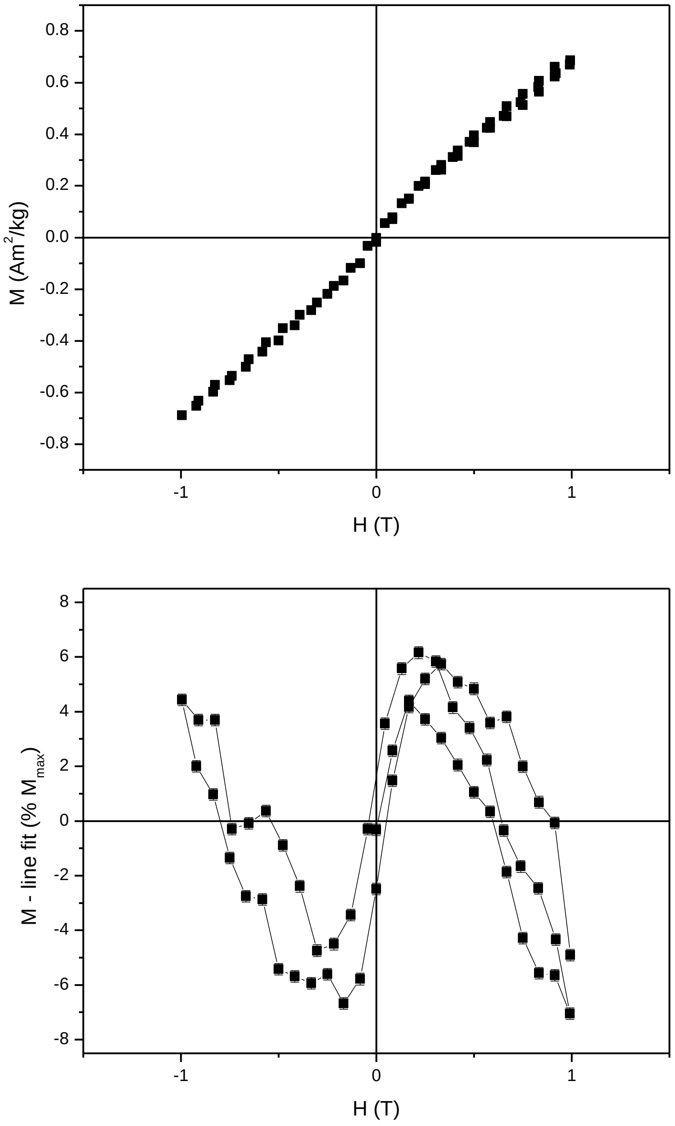

Figure E.35 Field cycle of Gt-3 at 4.2 K (top) and corresponding curvature graph (bottom)

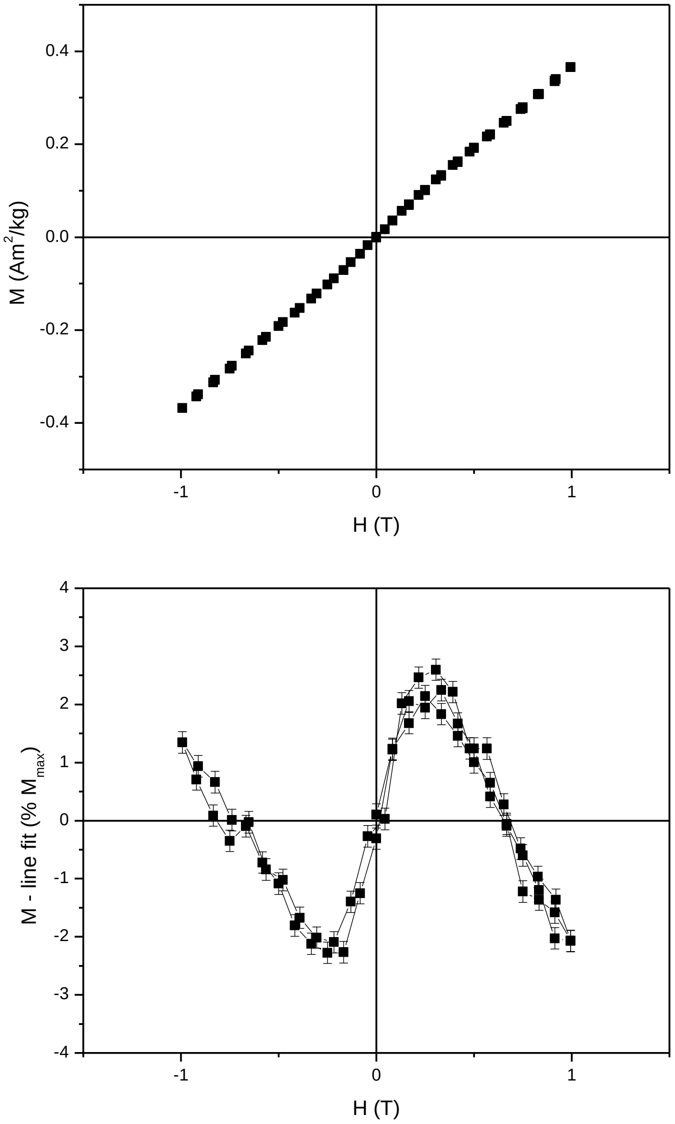

Figure E.36 Field cycle of Gt-4 at 300 K (top) and corresponding curvature graph (bottom)

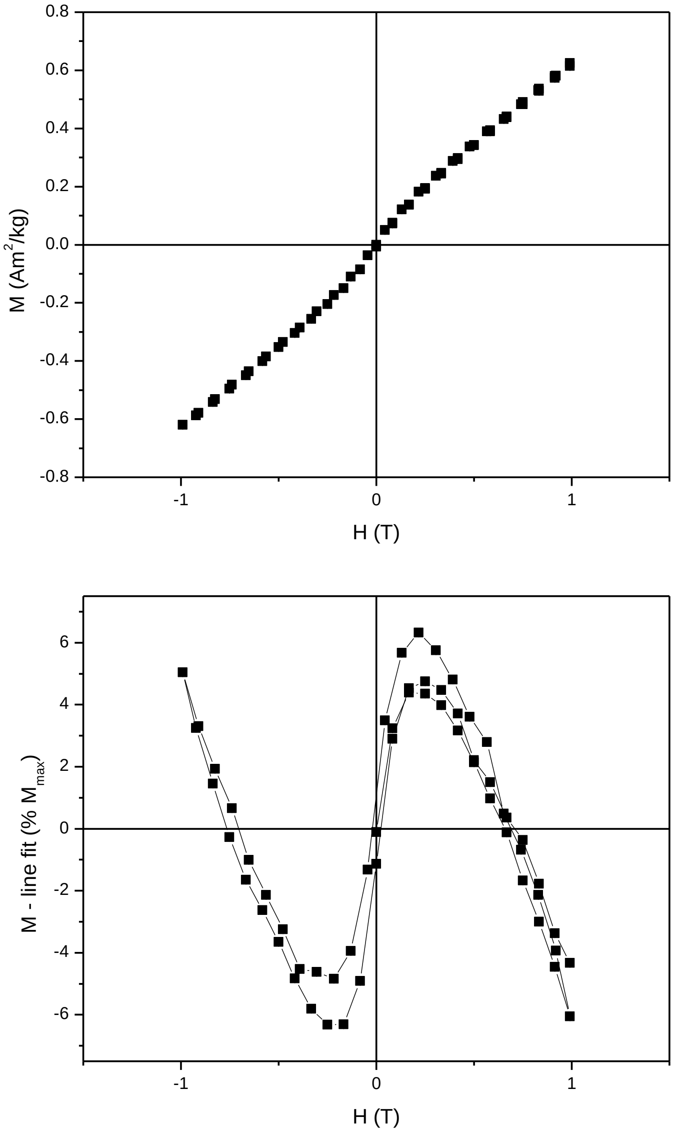

Figure E.37 Field cycle of Gt-4 at 4.2 K (top) and corresponding curvature graph (bottom)

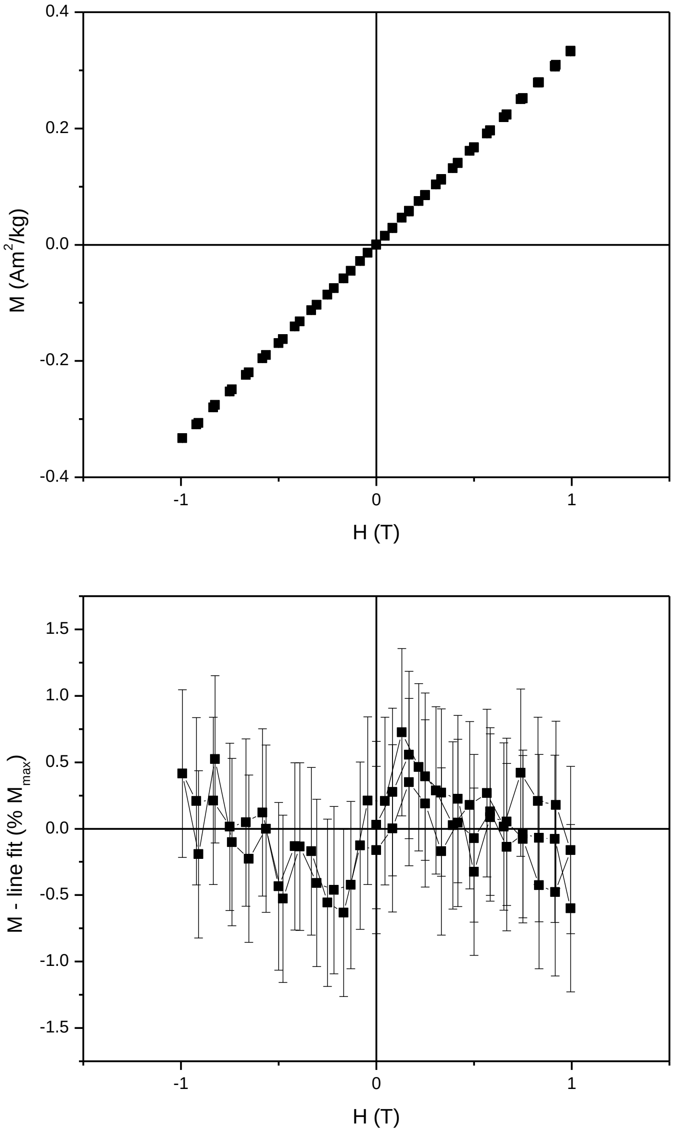

Figure E.38 Field cycle of Gt-5 at 300 K (top) and corresponding curvature graph (bottom)

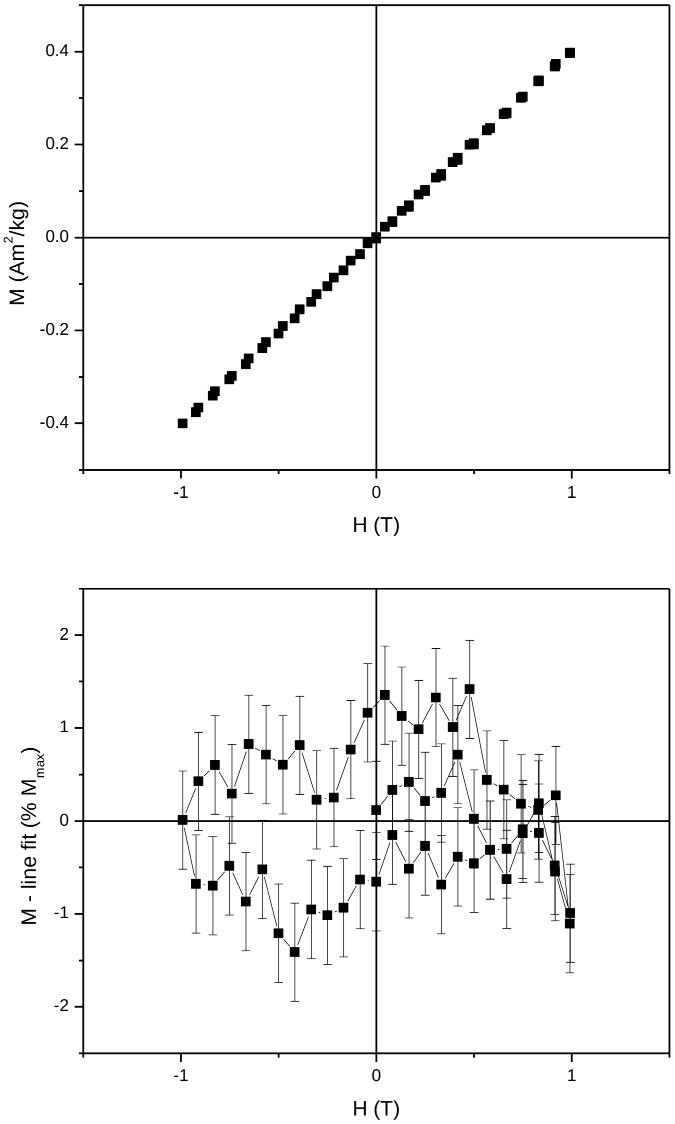

Figure E.39 Field cycle of Gt-5 at 4.2 K (top) and corresponding curvature graph (bottom)

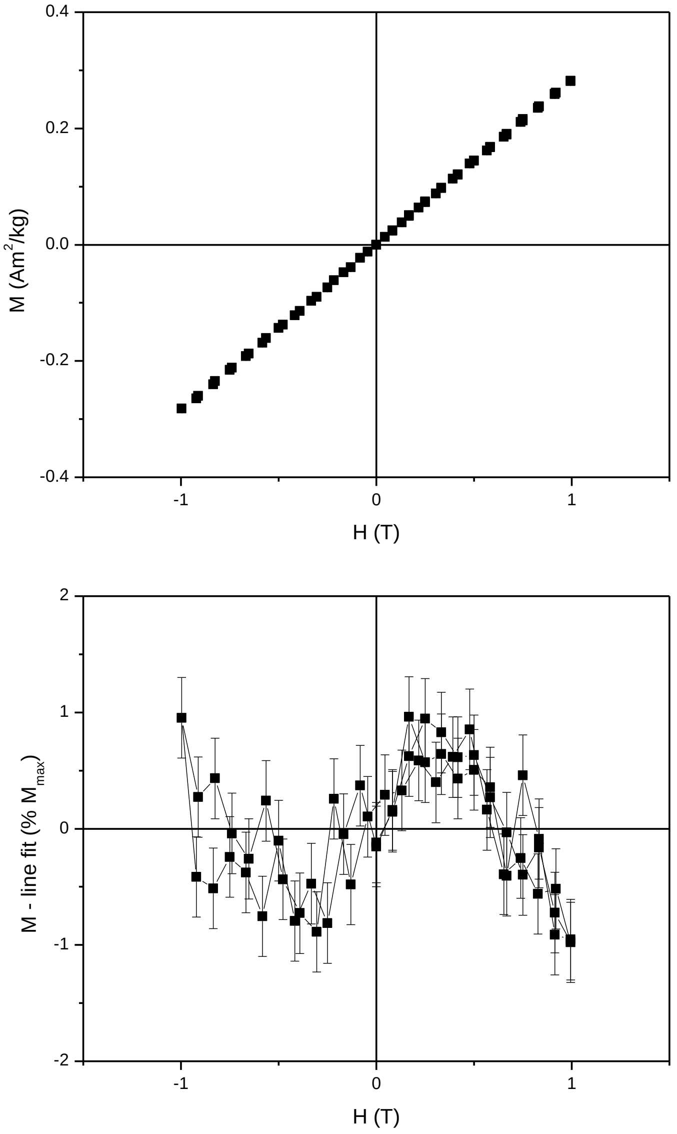

Figure E.40 Field cycle of Gt-6 at 300 K (top) and corresponding curvature graph (bottom)

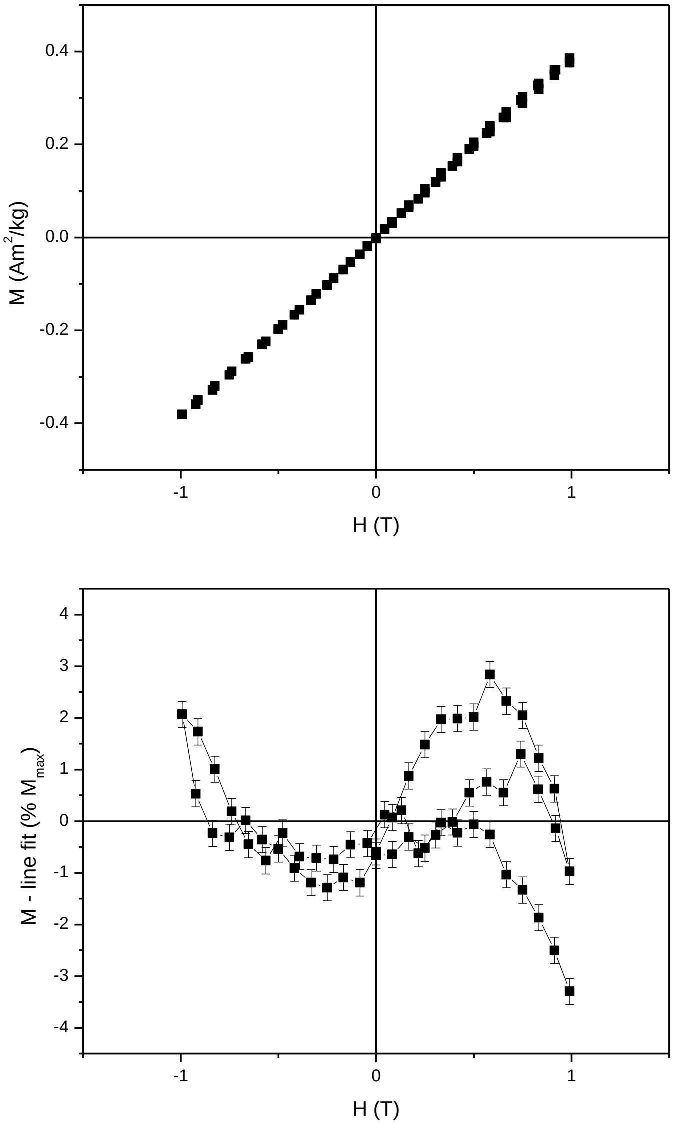

Figure E.41 Field cycle of Gt-6 at 4.2 K (top) and corresponding curvature graph (bottom); the evident deviation of the lower branch at positive fields is due to an instrumental artefact

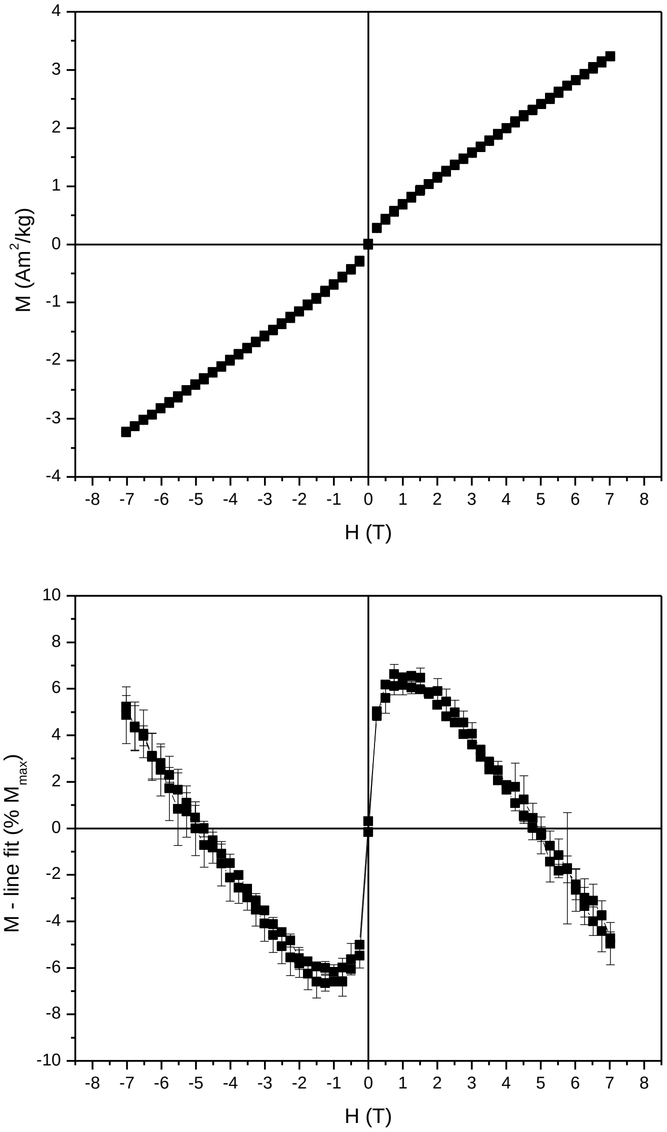

Figure E.42 Field cycle of Lp-1 at 300 K (top) and corresponding curvature graph (bottom)

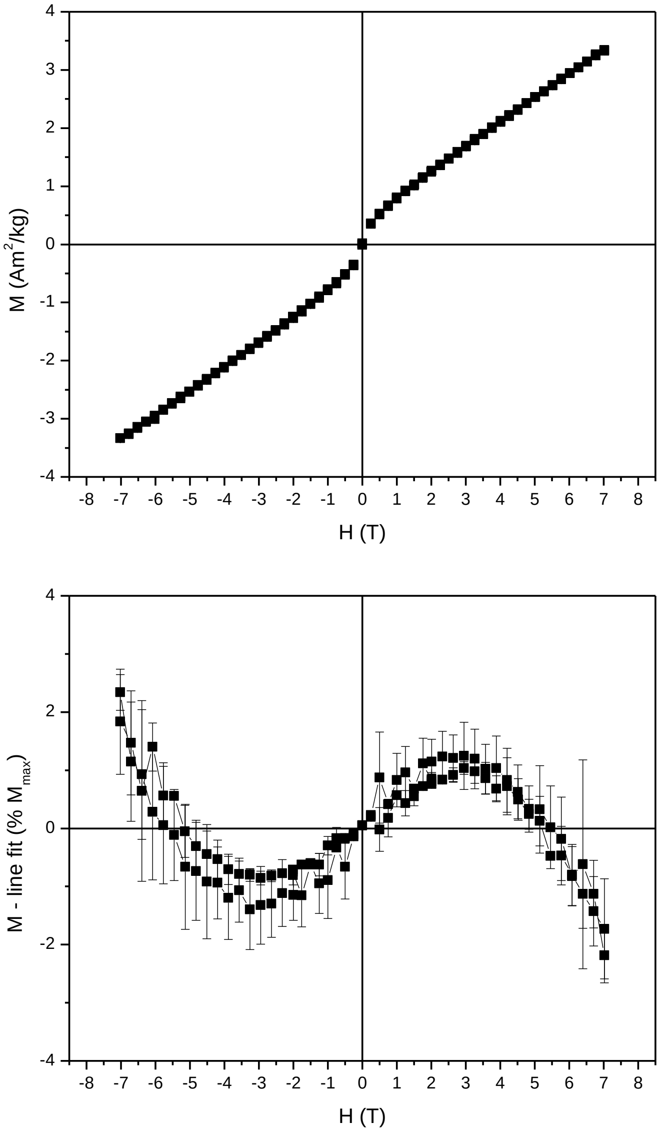

Figure E.43 Field cycle of Lp-1 at 200 K (top) and corresponding curvature graph (bottom)

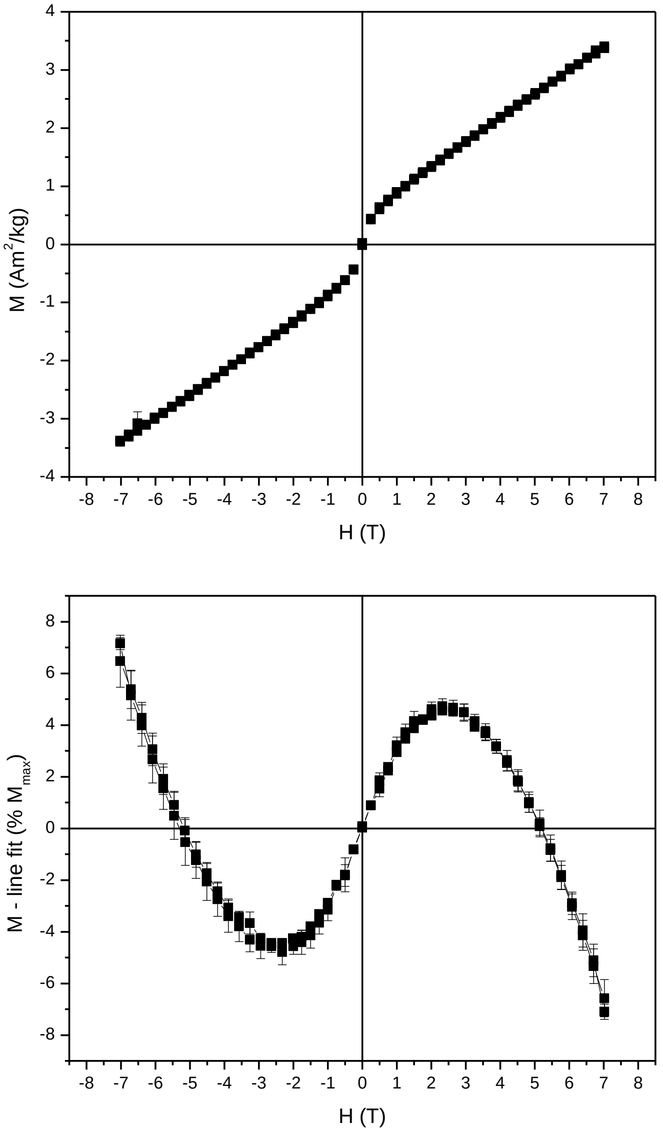

Figure E.44 Field cycle of Lp-1 at 100 K (top) and corresponding curvature graph (bottom)

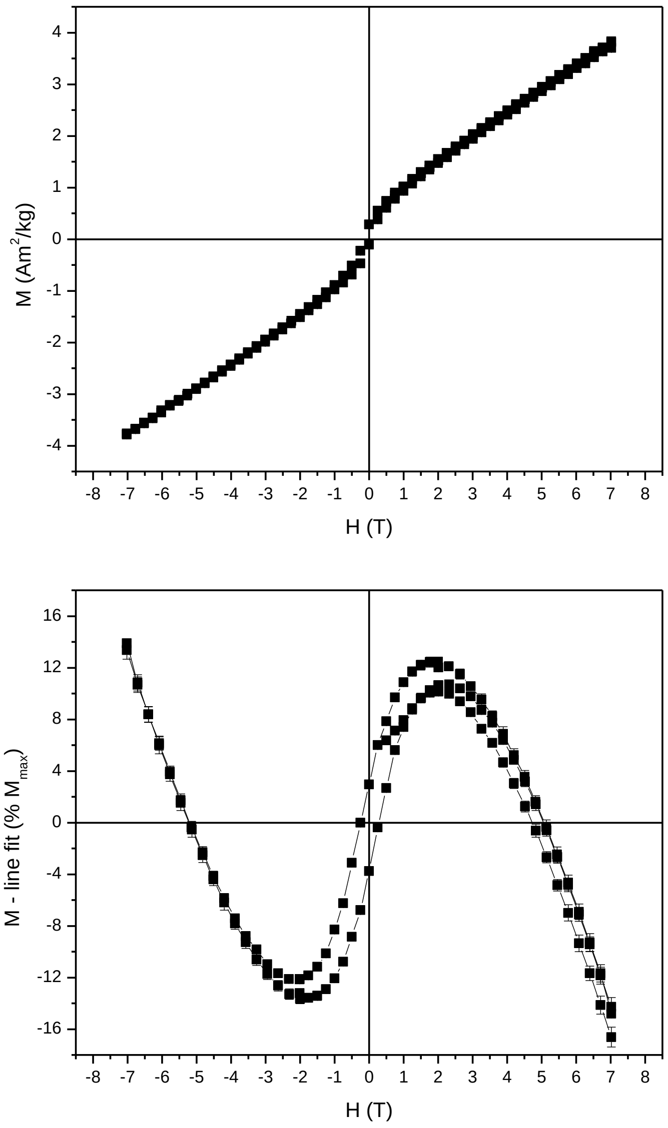

Figure E.45 Field cycle of Lp-1 at 1.8 K (top) and corresponding curvature graph (bottom)

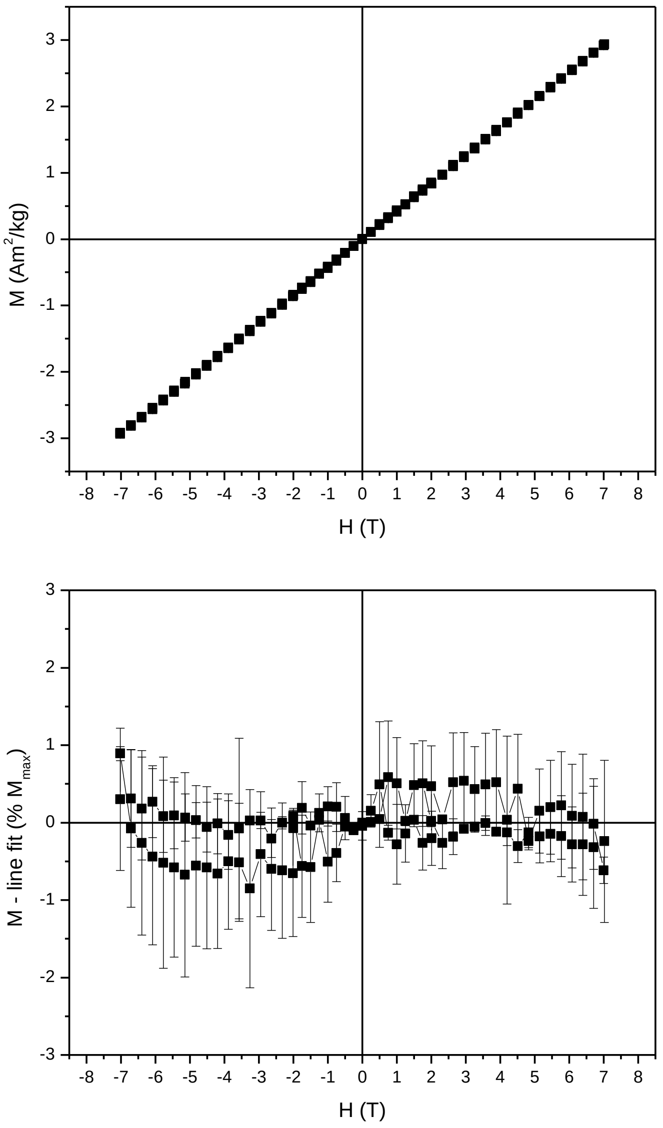

Figure E.46 Field cycle of Lp-2 at 300 K (top) and corresponding curvature graph (bottom)

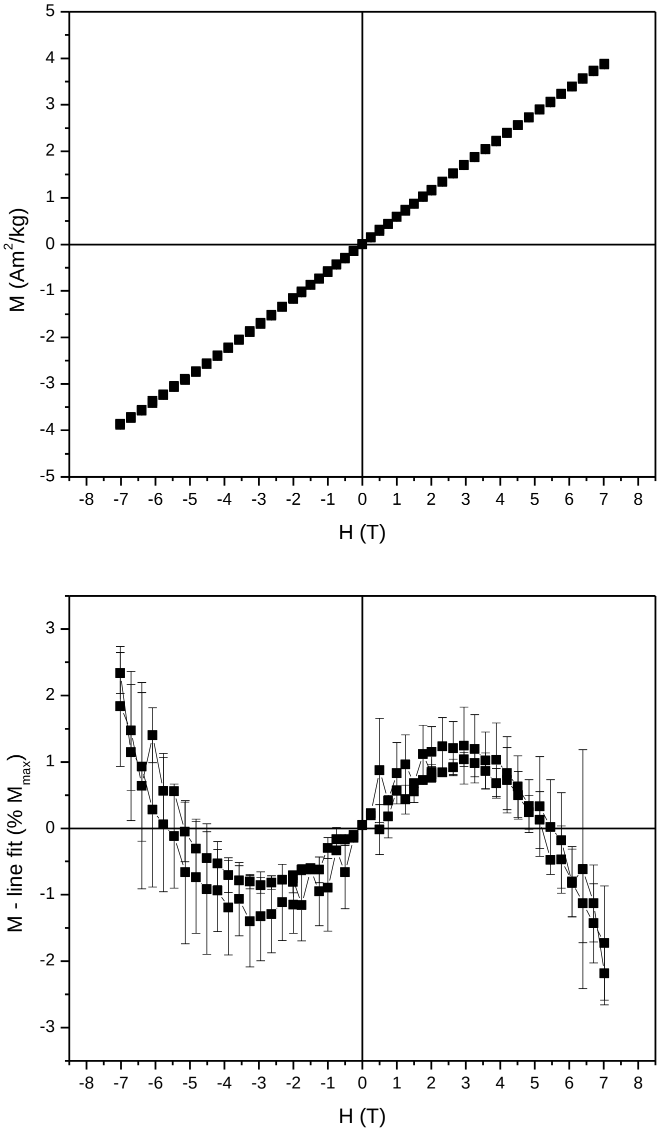

Figure E.47 Field cycle of Lp-2 at 200 K (top) and corresponding curvature graph (bottom)

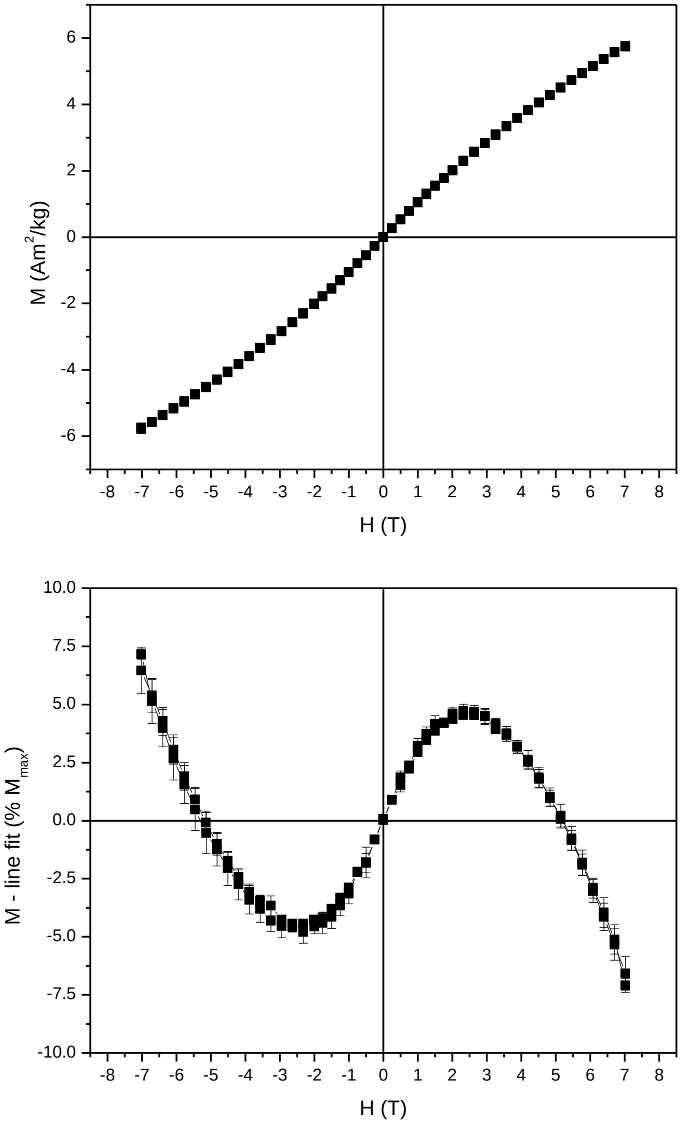

Figure E.48 Field cycle of Lp-2 at 100 K (top) and corresponding curvature graph (bottom)

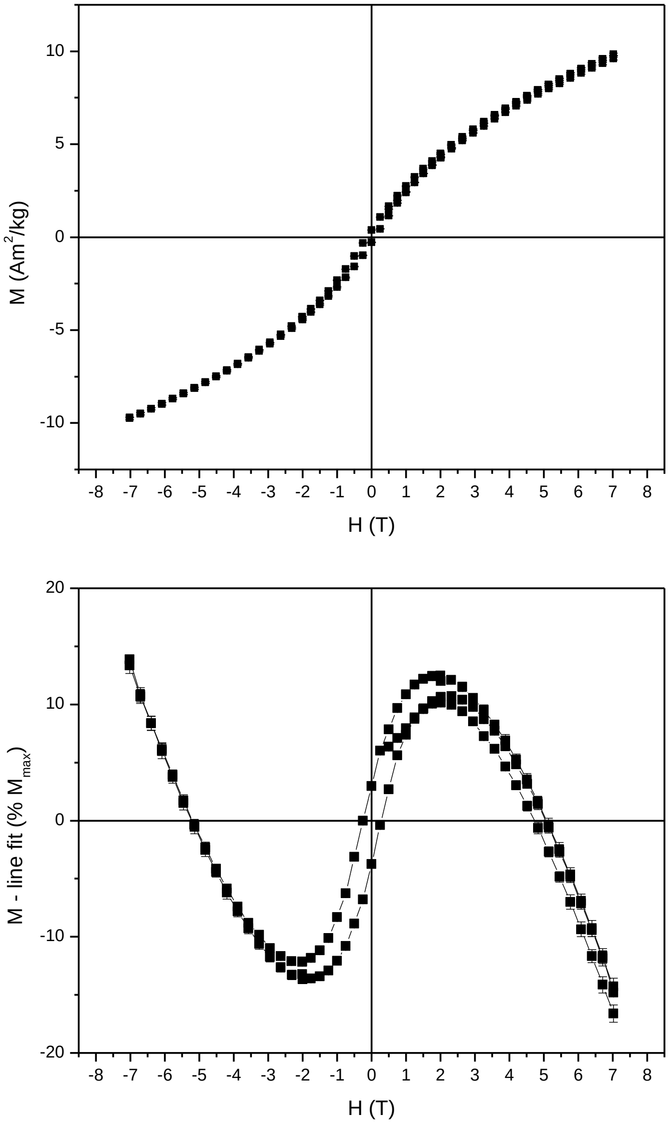

Figure E.49 Field cycle of Lp-2 at 1.8 K (top) and corresponding curvature graph (bottom)

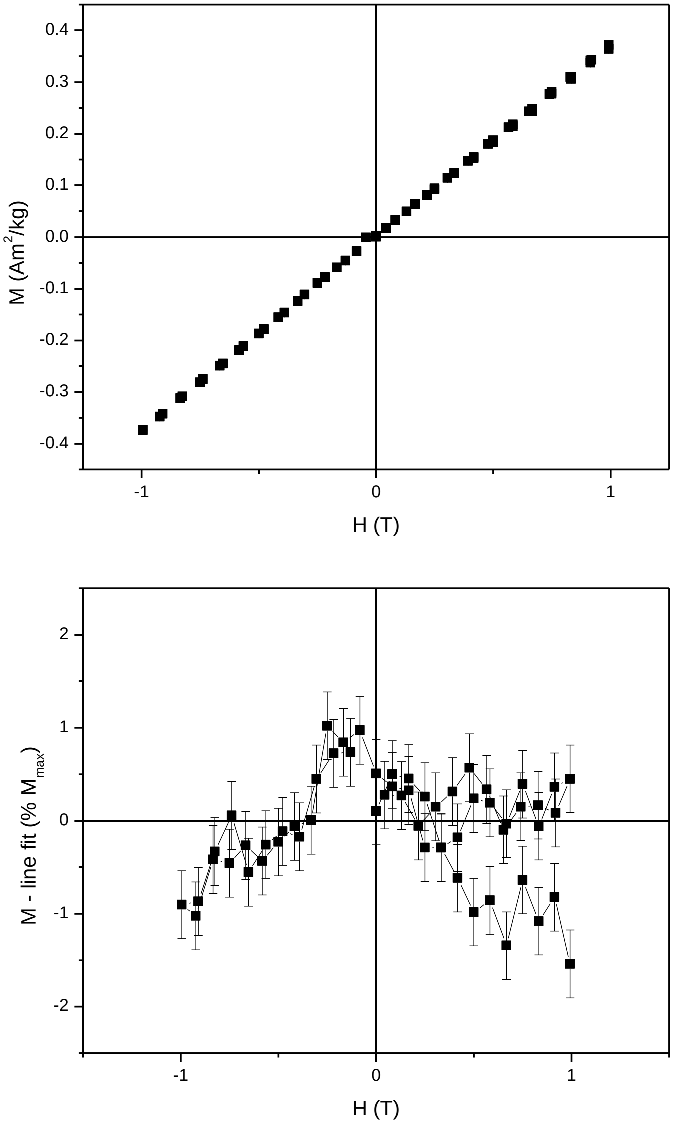

Figure E.50 Field cycle of Sw-1 at 300 K (top) and corresponding curvature graph (bottom)

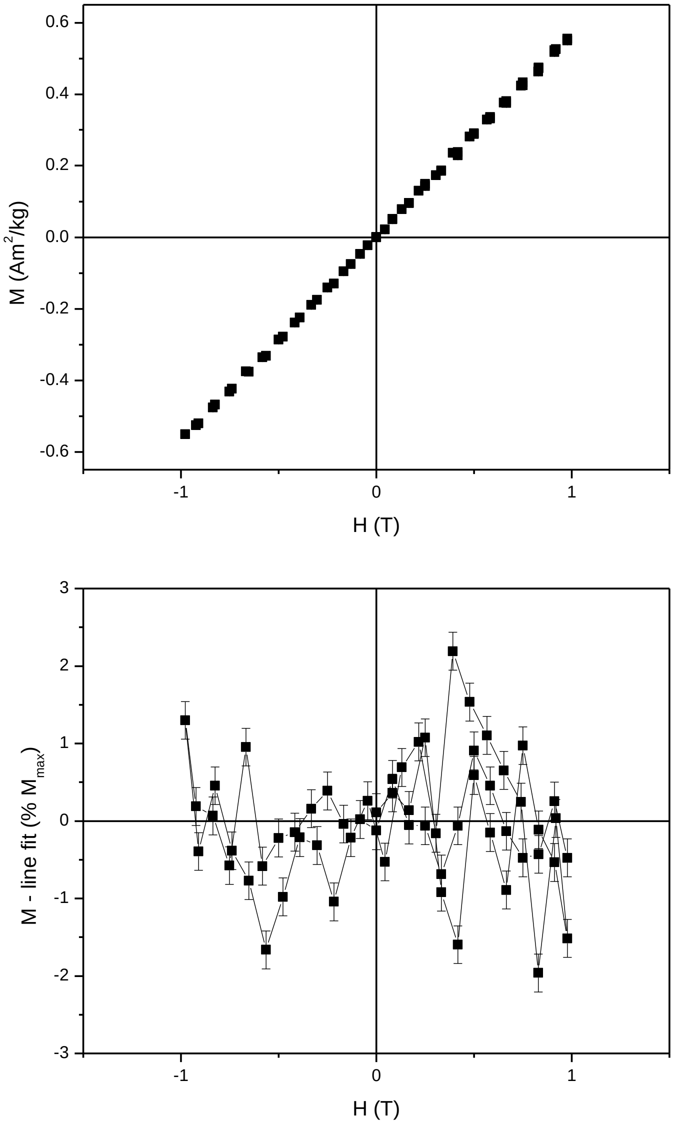

Figure E.51 Field cycle of Sw-1 at 235 K (top) and corresponding curvature graph (bottom)

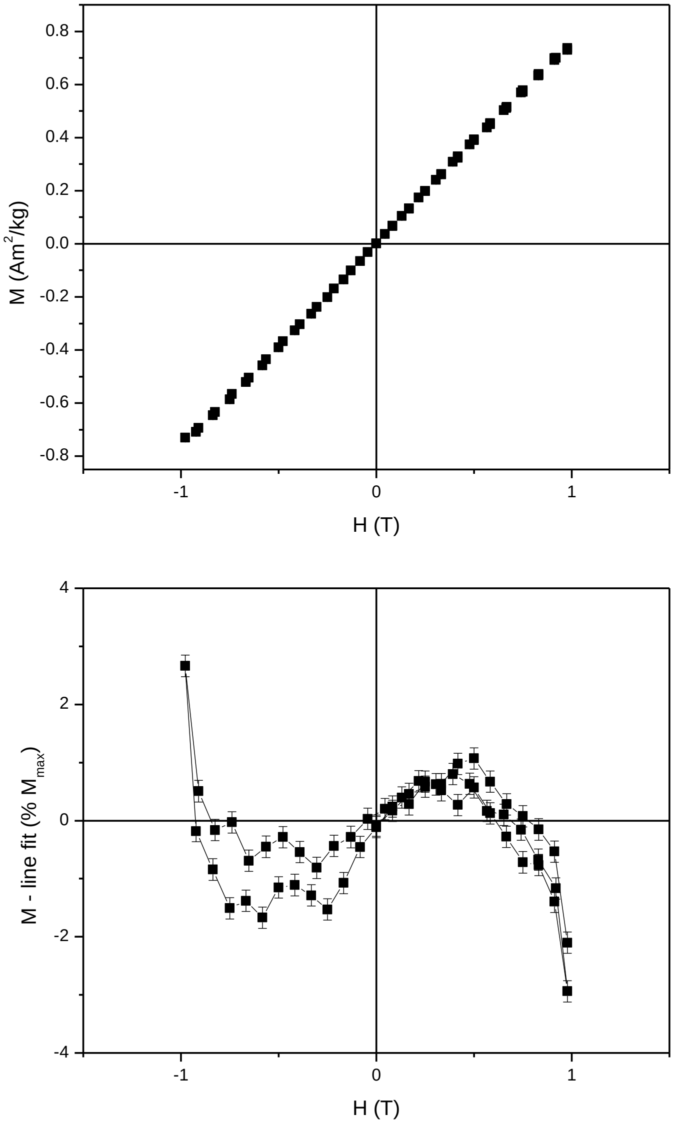

Figure E.52 Field cycle of Sw-1 at 150 K (top) and corresponding curvature graph (bottom)

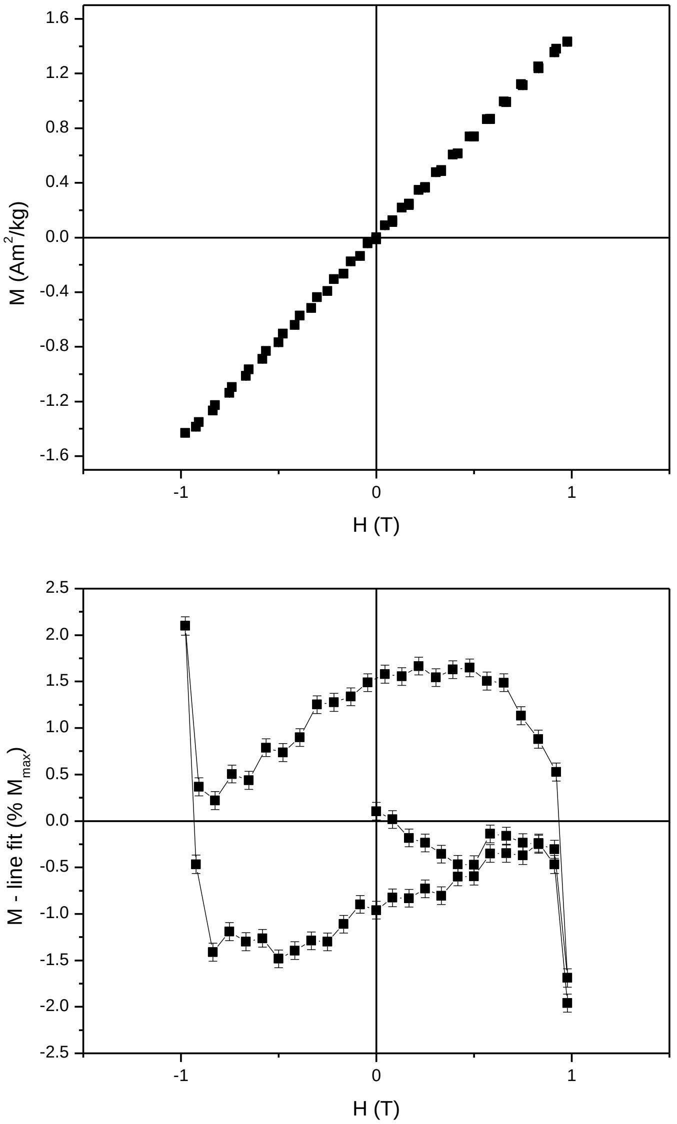

Figure E.53 Field cycle of Sw-1 at 4.2 K (top) and corresponding curvature graph (bottom)

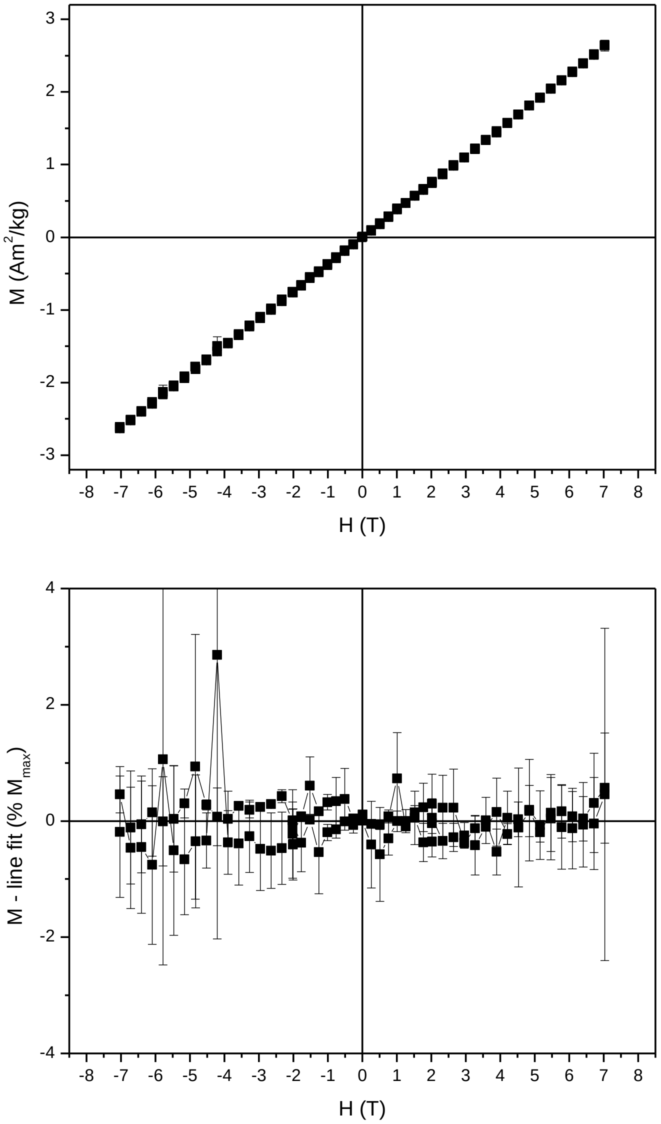

Figure E.54 Field cycle of Sw-2 at 300 K (top) and corresponding curvature graph (bottom)

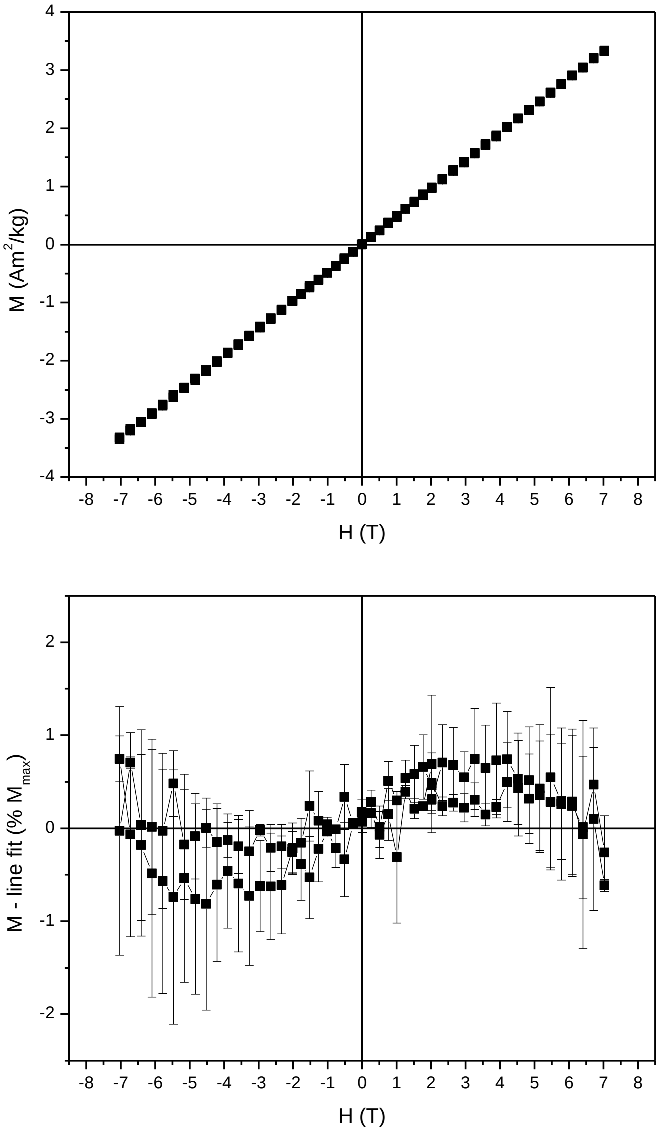

Figure E.55 Field cycle of Sw-2 at 200 K (top) and corresponding curvature graph (bottom)

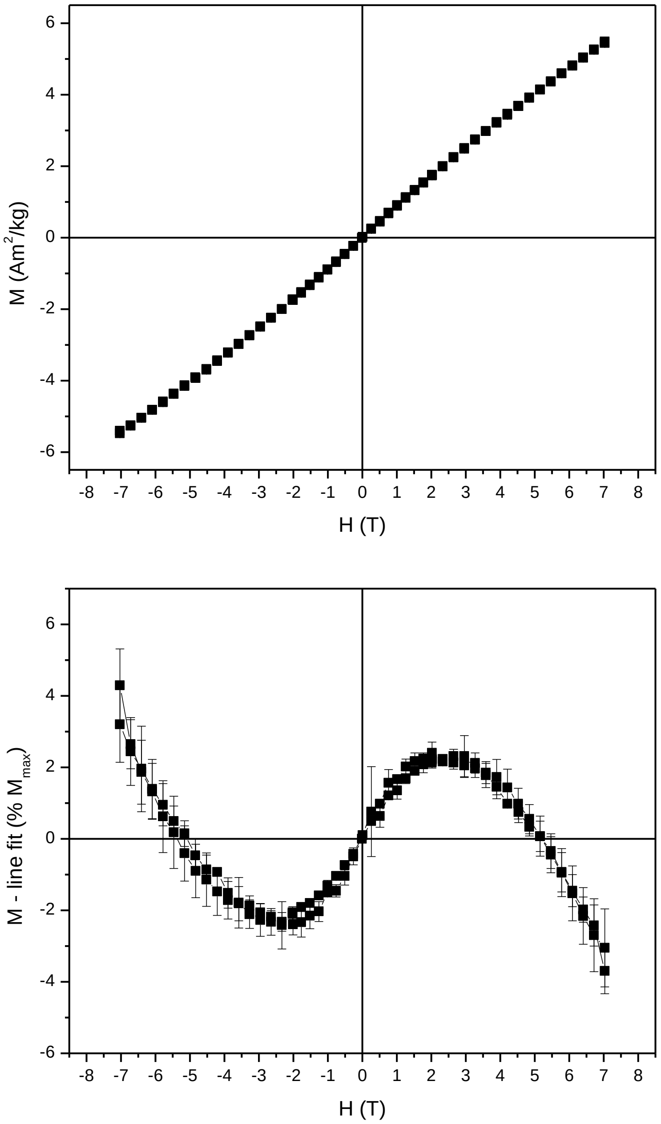

Figure E.56 Field cycle of Sw-2 at 100 K (top) and corresponding curvature graph (bottom)

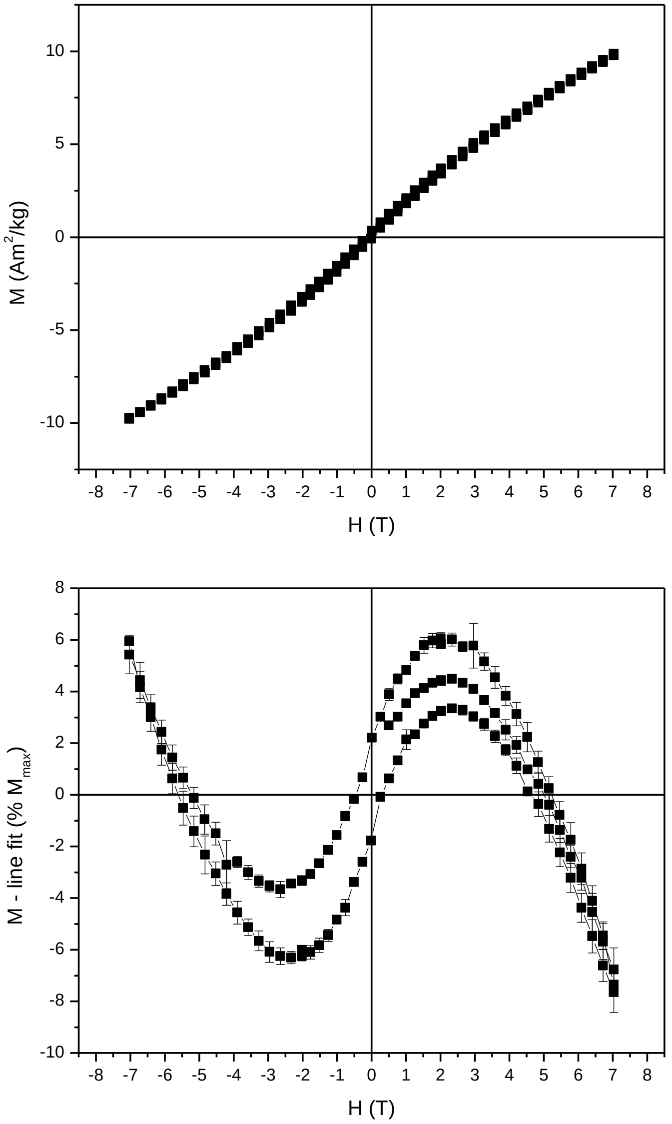

Figure E.57 Field cycle of Sw-2 at 1.8 K (top) and corresponding curvature graph (bottom)

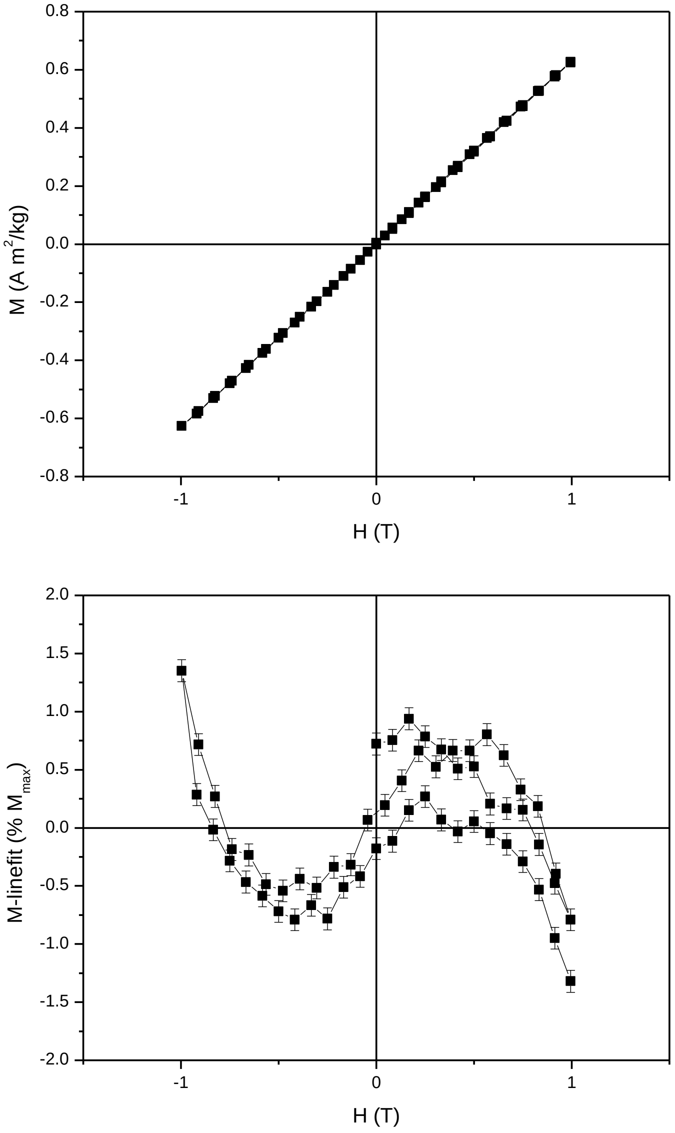

Figure E.58 Field cycle of Akg-1 at 300 K (top) and corresponding curvature graph (bottom)

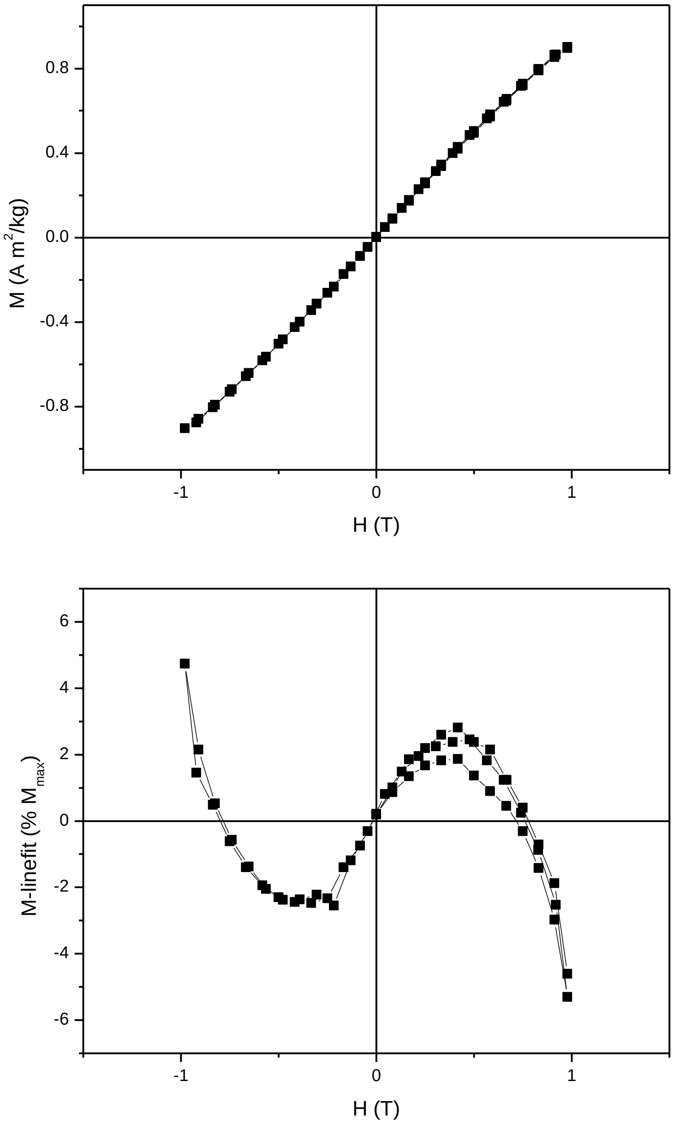

Figure E.59 Field cycle of Akg-1 at 230 K (top) and corresponding curvature graph (bottom)

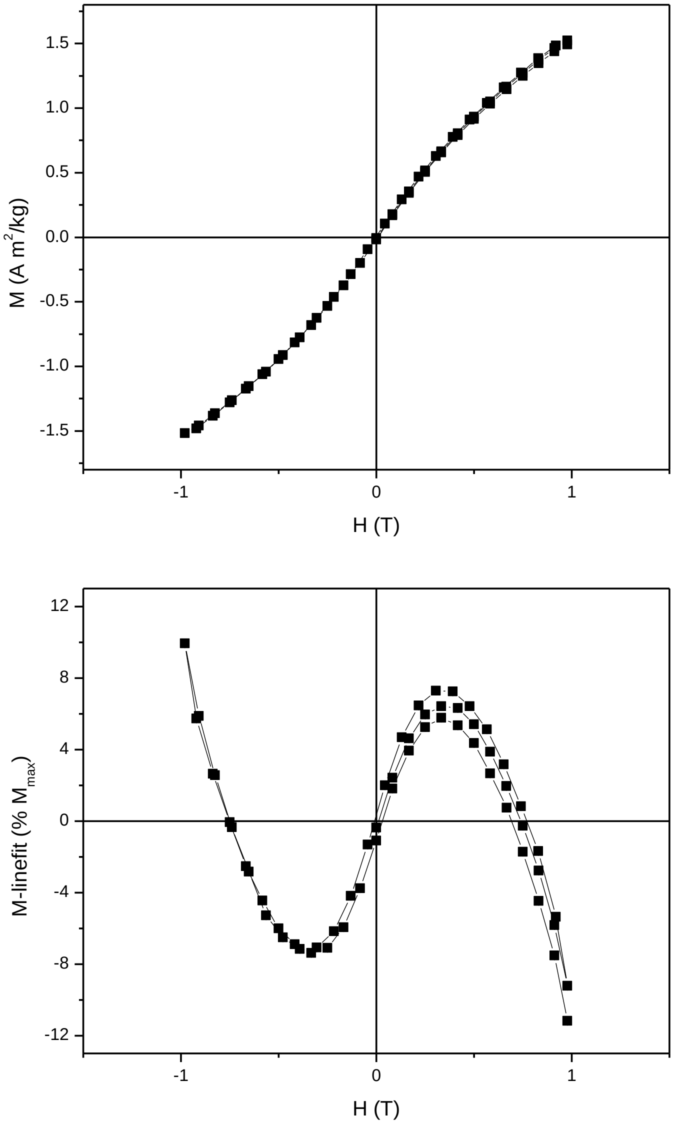

Figure E.60 Field cycle of Akg-1 at 100 K (top) and corresponding curvature graph (bottom)

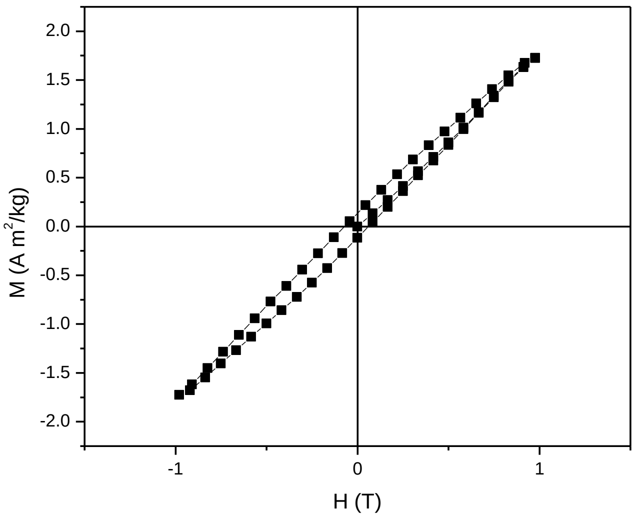

Figure E.61 Field cycle of Akg-1 at 4.2 K

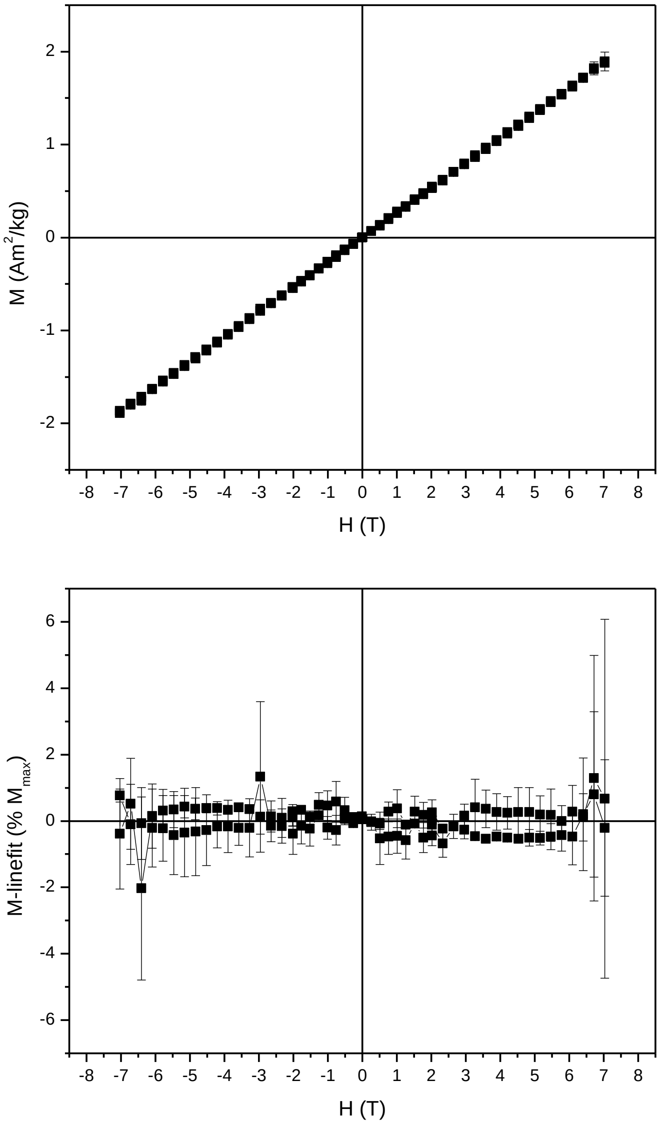

Figure E.62 Field cycle of Akg-2 at 300 K (top) and corresponding curvature graph (bottom)

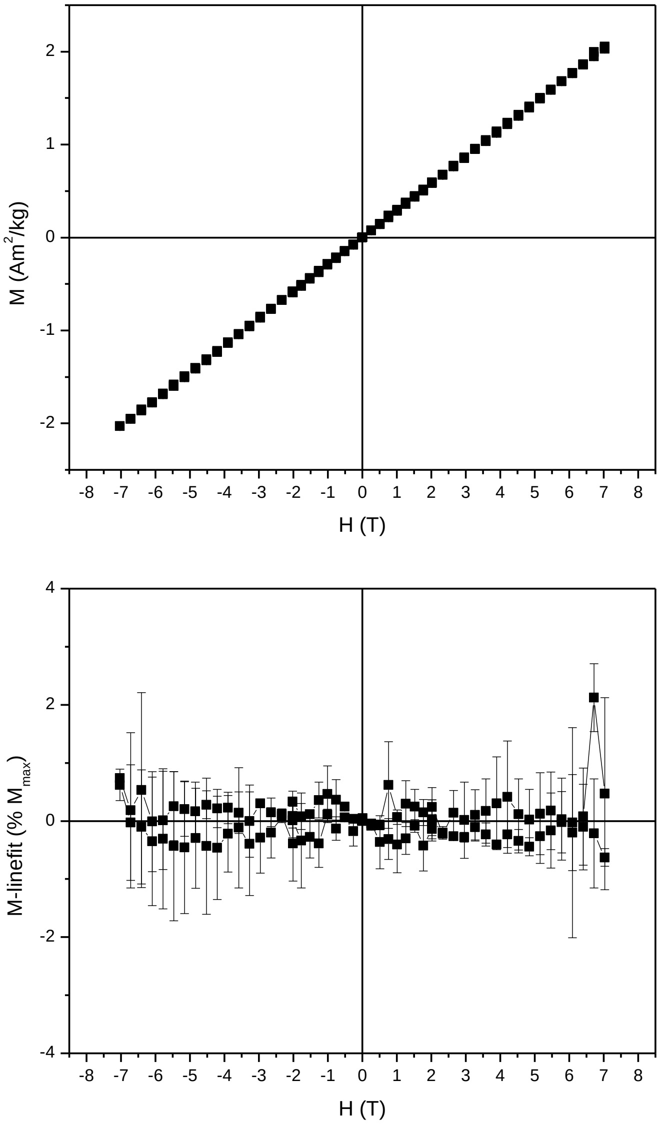

Figure E.63 Field cycle of Akg-2 at 200 K (top) and corresponding curvature graph (bottom)

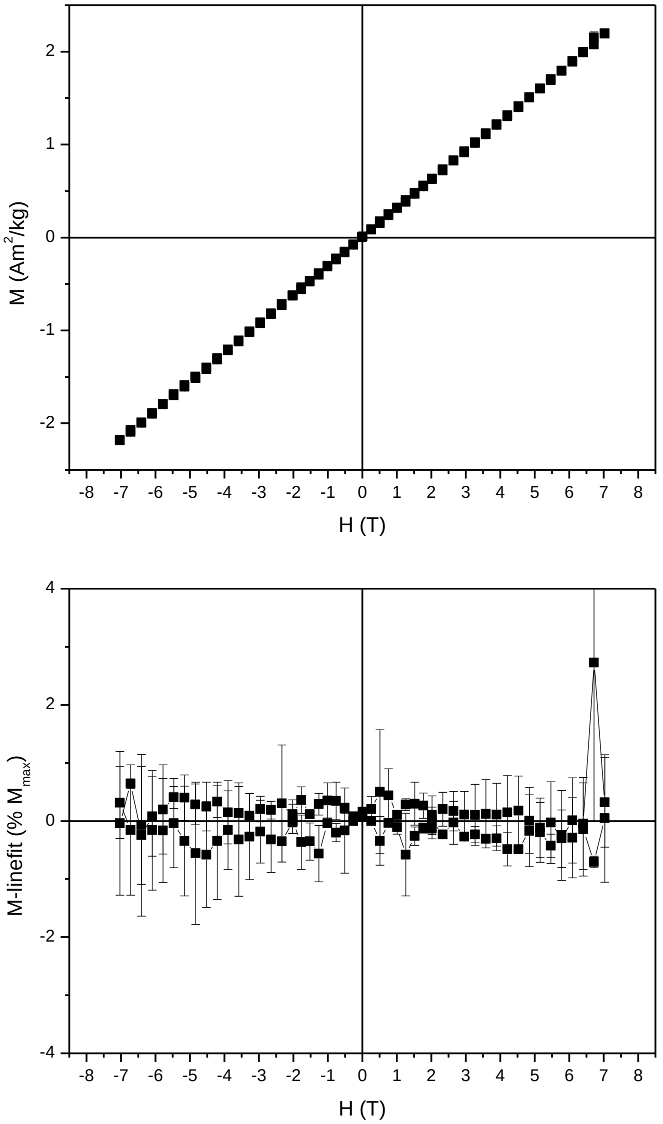

Figure E.64 Field cycle of Akg-2 at 100 K (top) and corresponding curvature graph (bottom)

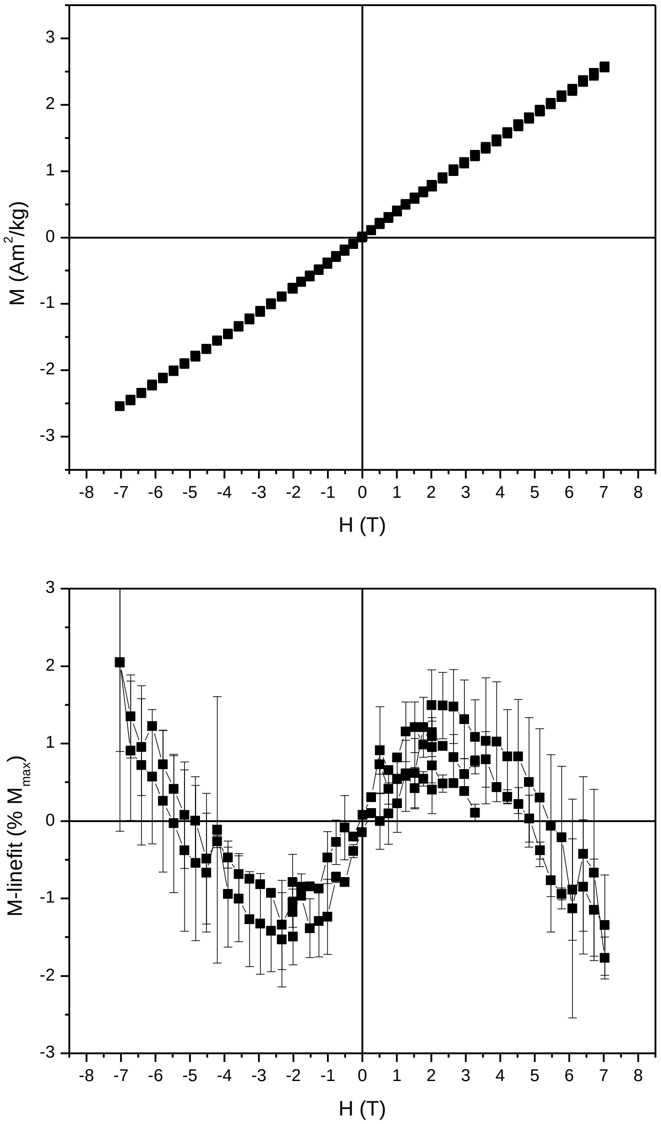

Figure E.65 Field cycle of Akg-2 at 1.8 K (top) and corresponding curvature graph (bottom)

Appendix F – Mössbauer Spectra

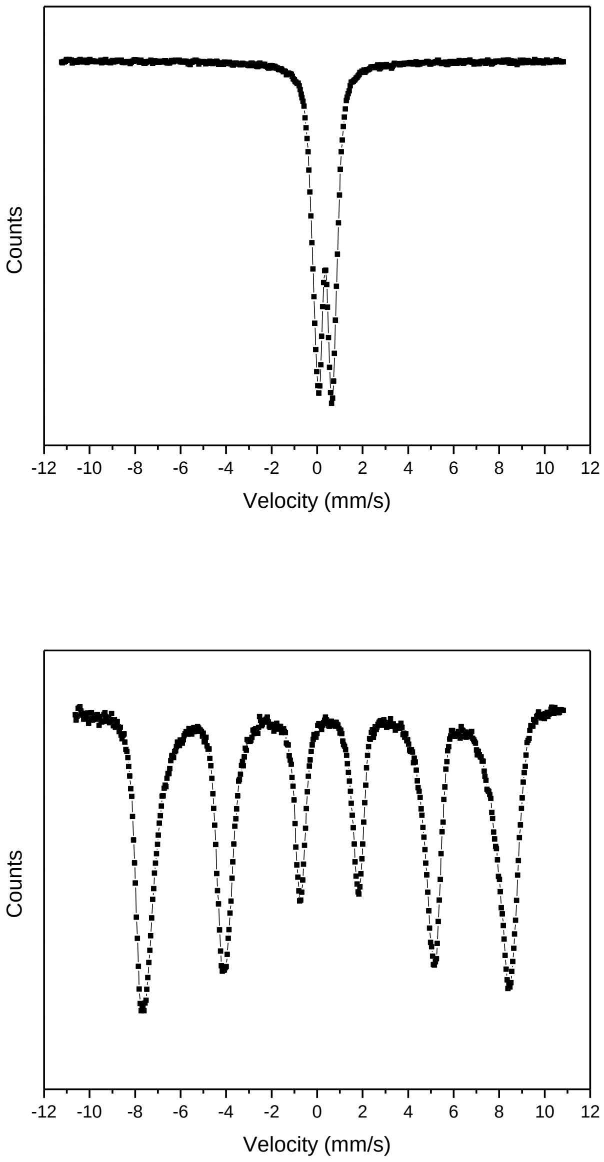

Figure F.1 Mössbauer spectra of 6L-Fh-1 at 300 K (top) and 4.2 K (bottom)

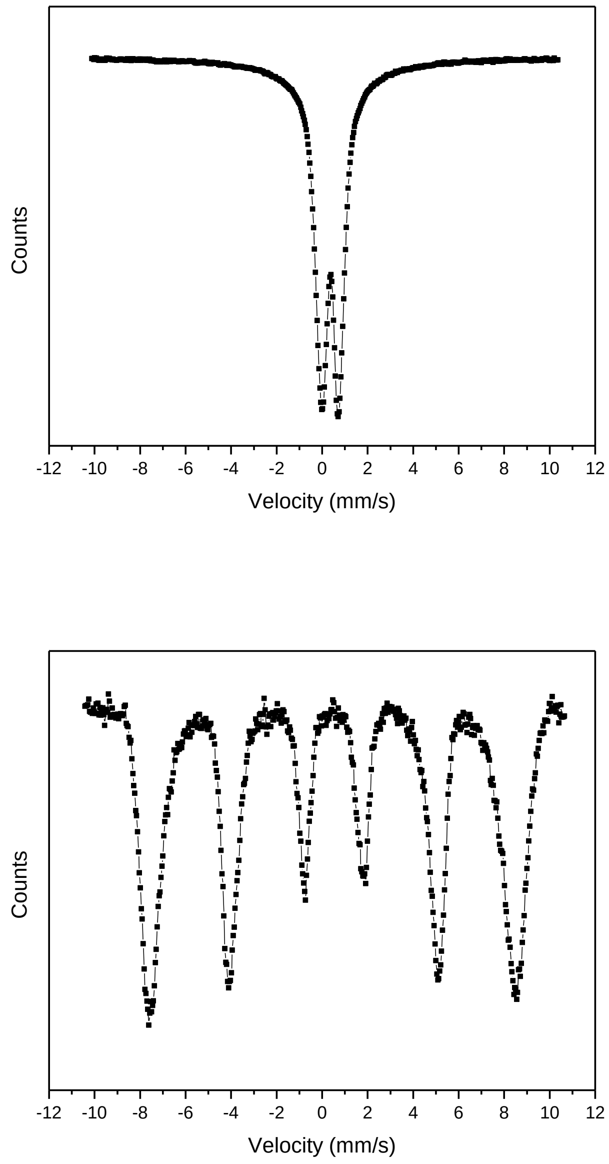

Figure F.2 Mössbauer spectra of 6L-Fh-2 at 300 K (top) and 4.2 K (bottom)

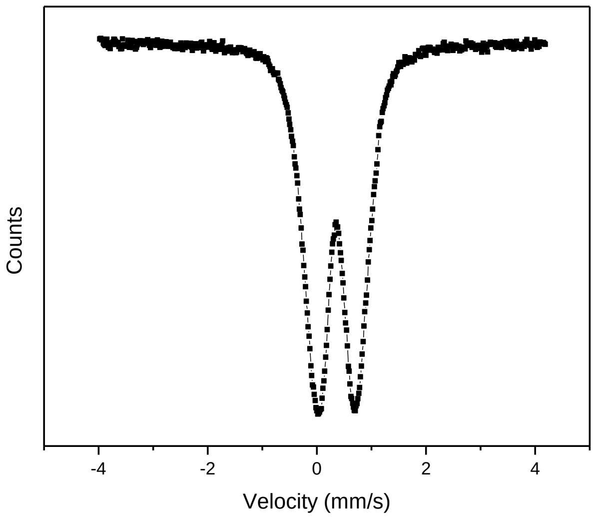

Figure F.3 Mössbauer spectrum of 4L-Fh at 300 K

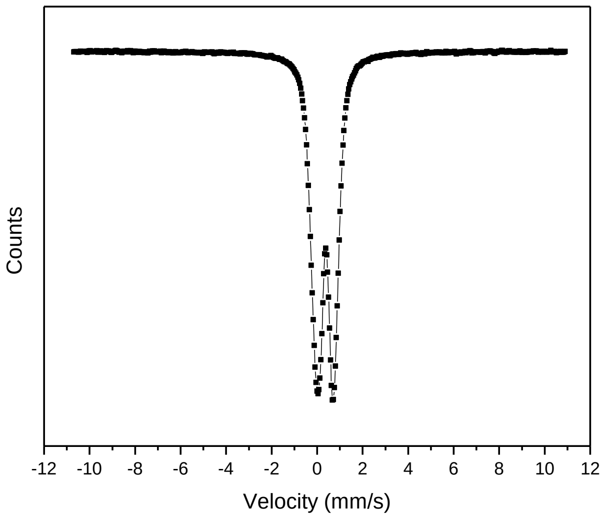

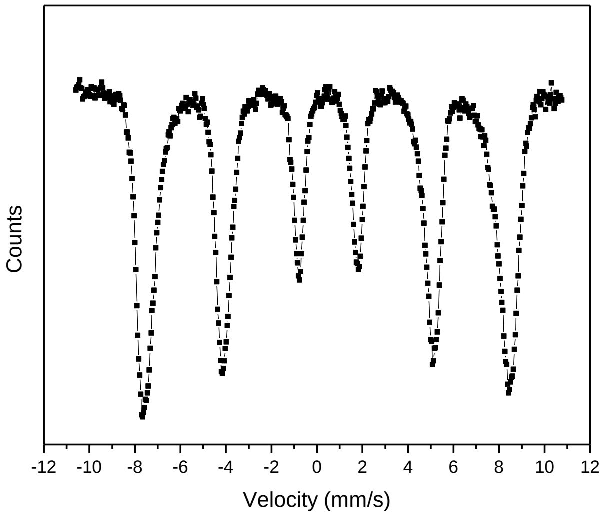

Figure F.4 Mössbauer spectra of P-HFO-0 at 300 K (top) and 4.2 K (bottom)

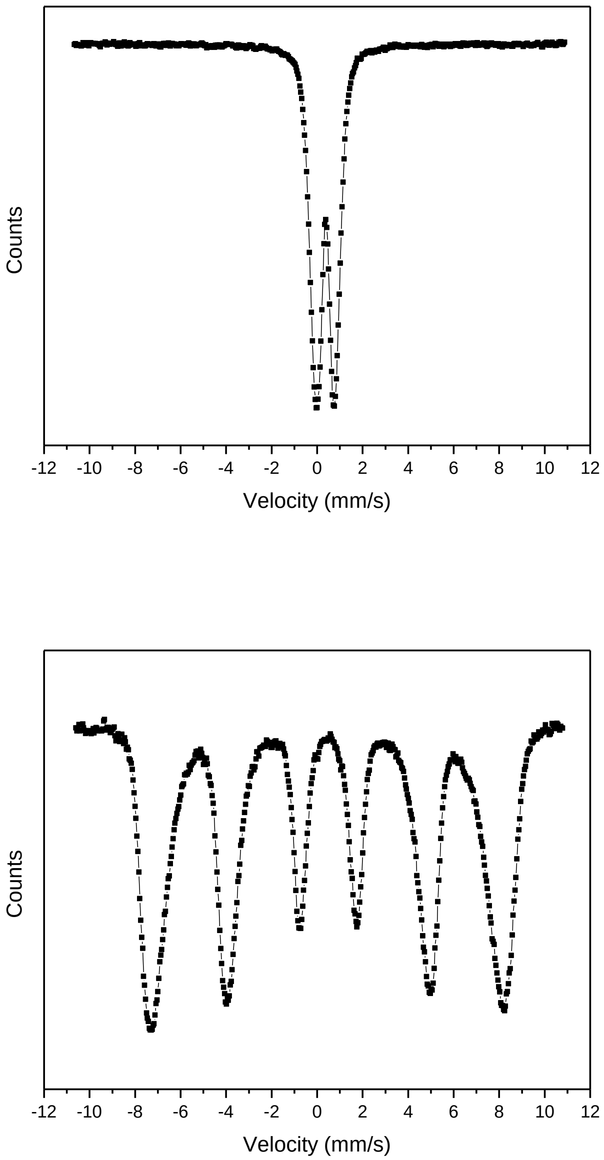

Figure F.5 Mössbauer spectra of P-HFO-0.01 at 300 K (top) and 4.2 K (bottom)

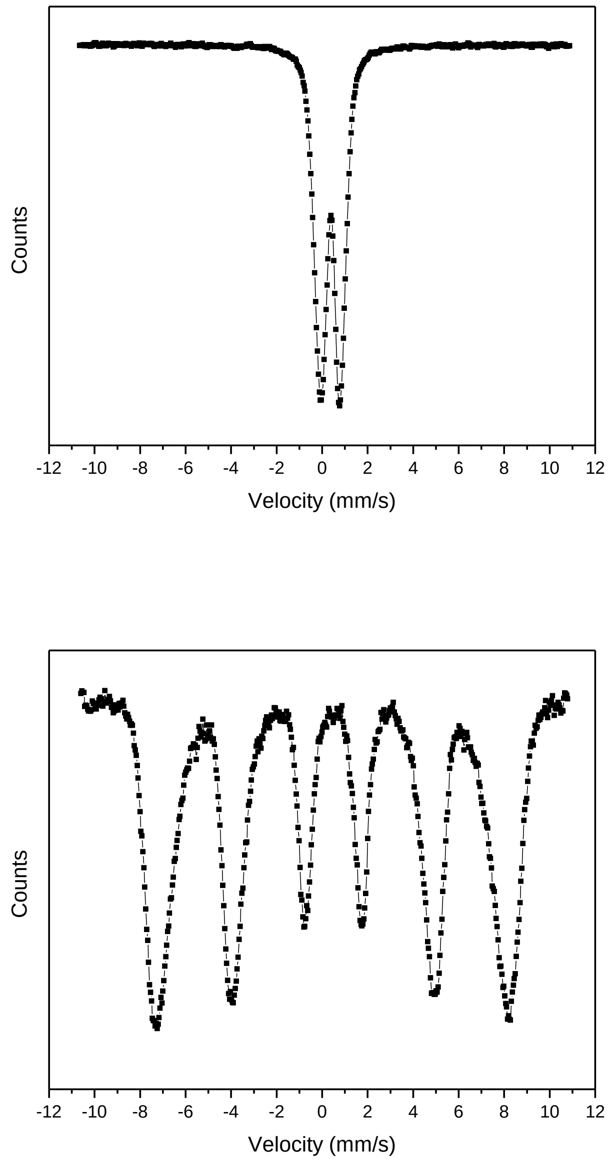

Figure F.6 Mössbauer spectra of P-HFO-0.025 at 300 K (top) and 4.2 K (bottom)

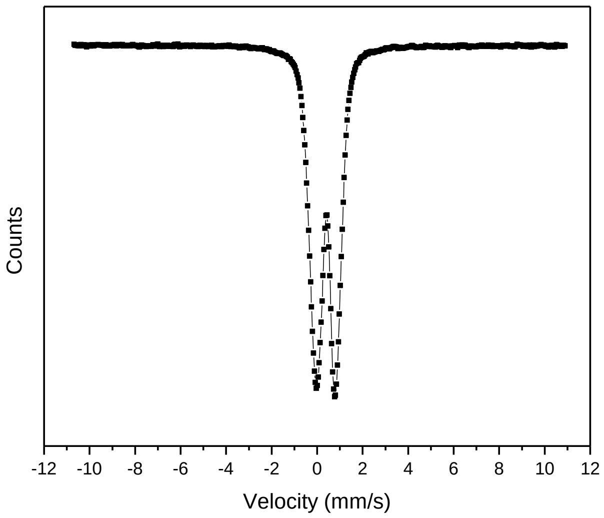

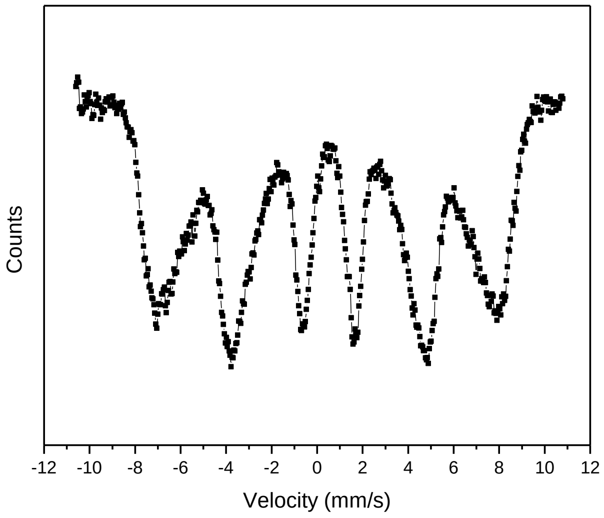

Figure F.7 Mössbauer spectra of P-HFO-0.05 at 300 K (top) and 4.2 K (bottom)

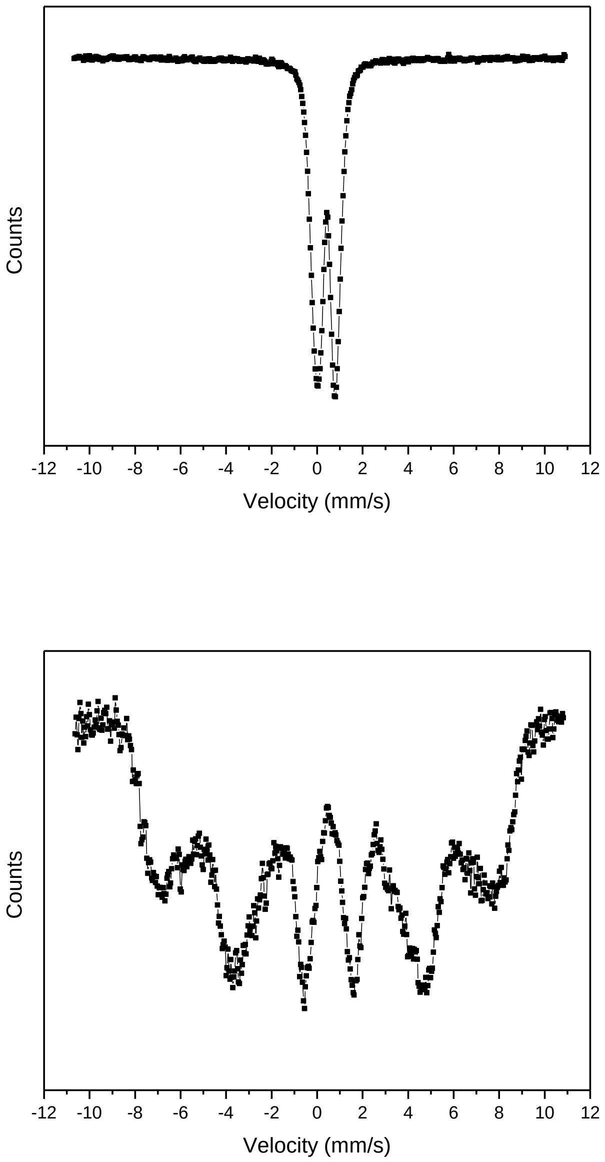

Figure F.8 Mössbauer spectra of P-HFO-0.075 at 300 K (top) and 4.2 K (bottom)

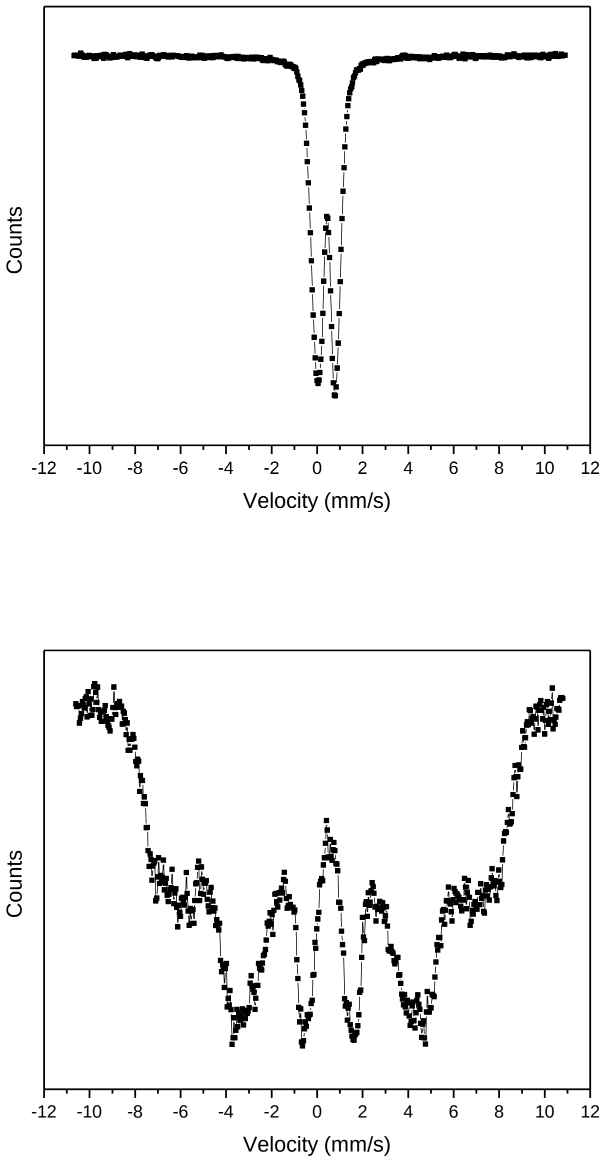

Figure F.9 Mössbauer spectra of P-HFO-0.1 at 300 K (top) and 4.2 K (bottom)

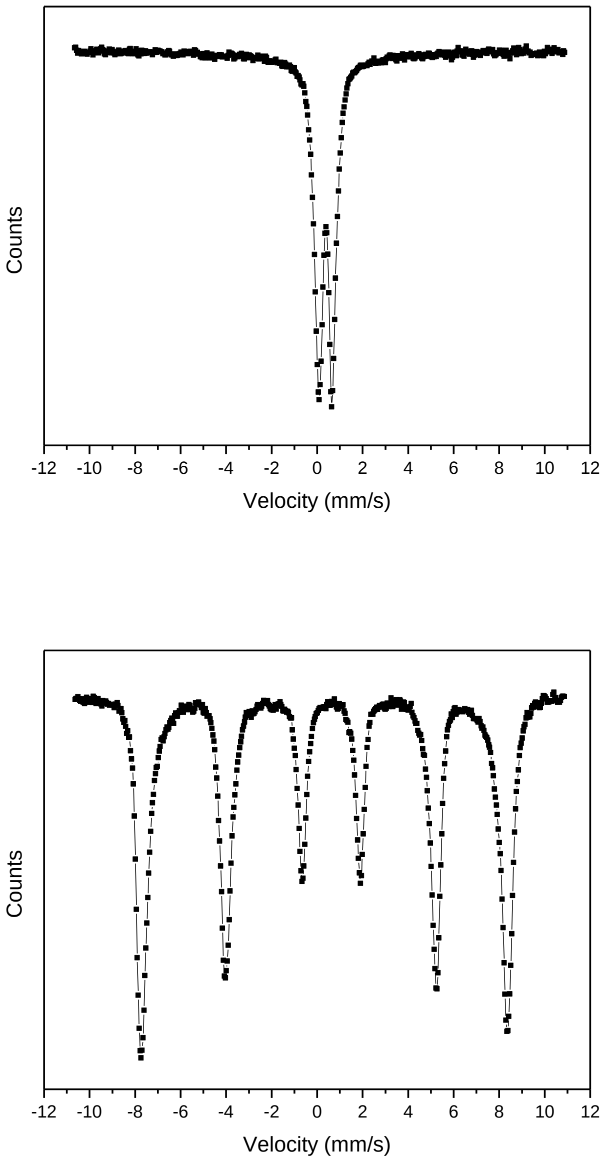

Figure F.10 Mössbauer spectra of Gt-1 at 300 K (top) and 4.2 K (bottom)

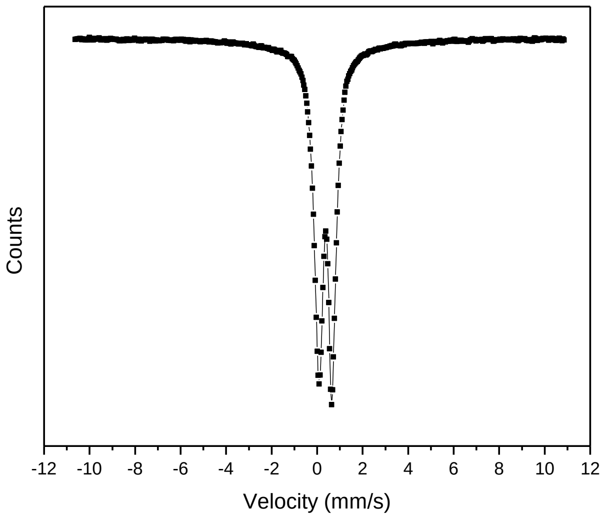

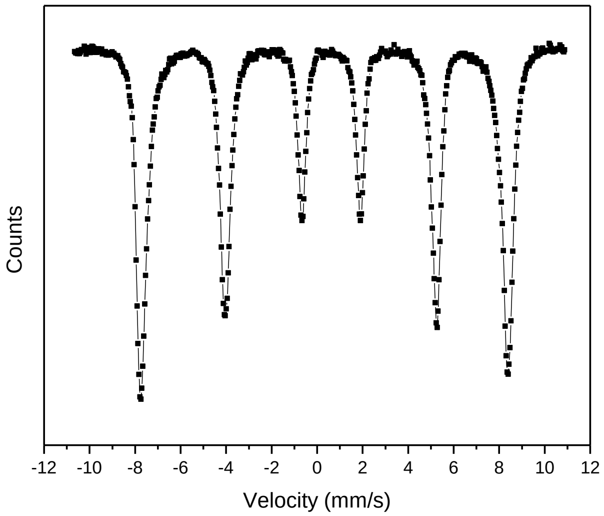

Figure F.11 Mössbauer spectra of Gt-2 at 300 K (top) and 4.2 K (bottom)

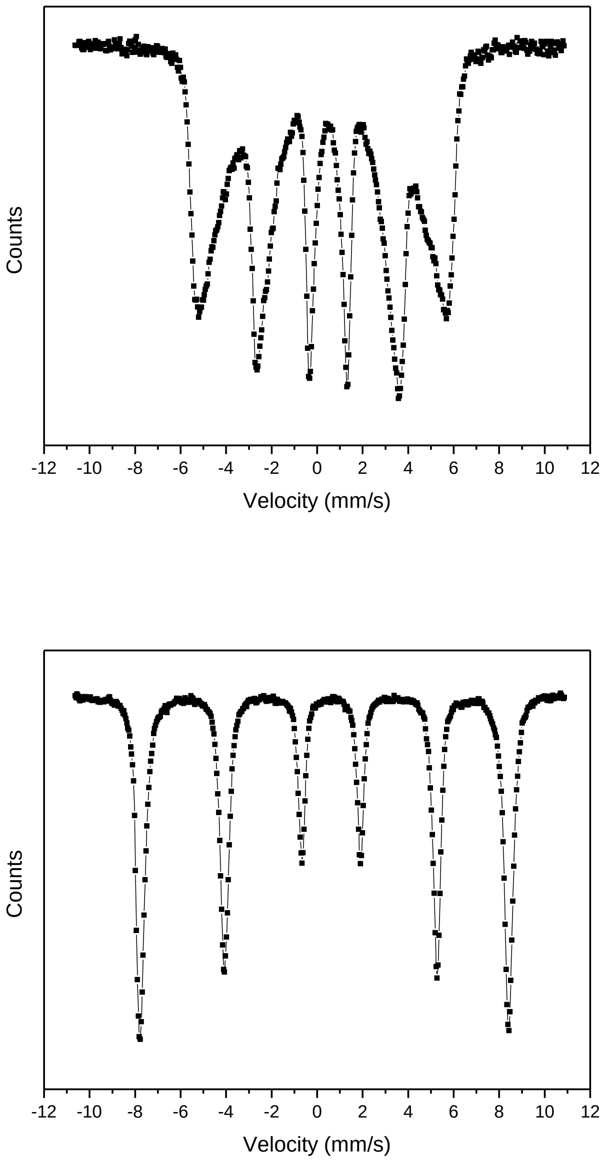

Figure F.12 Mössbauer spectra of Gt-3 at 300 K (top) and 4.2 K (bottom)

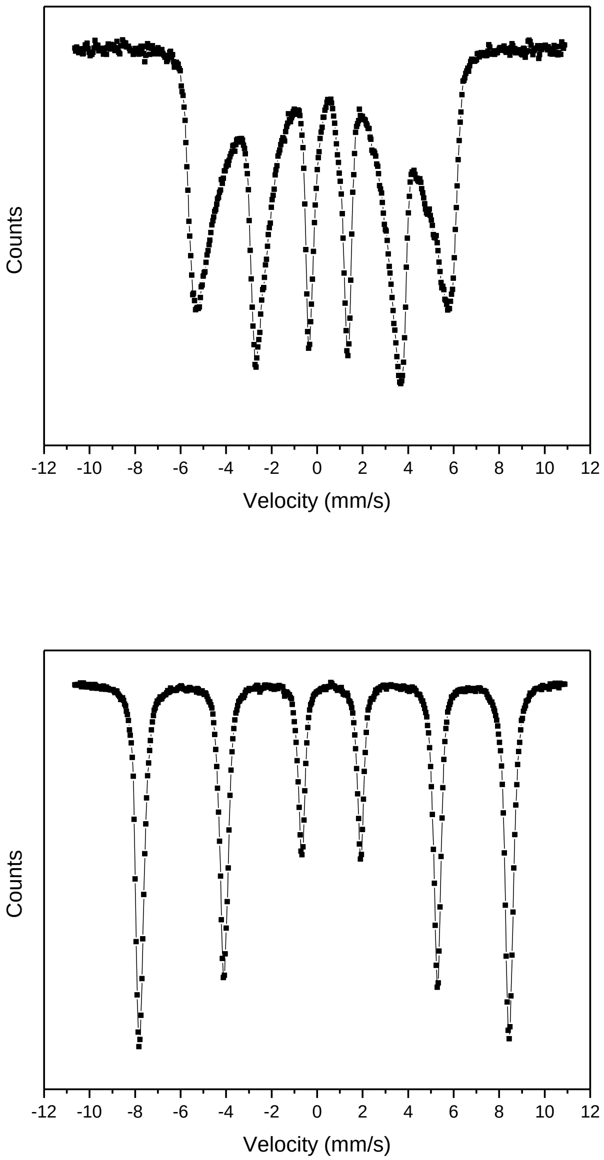

Figure F.13 Mössbauer spectra of Gt-4 at 300 K (top) and 4.2 K (bottom)

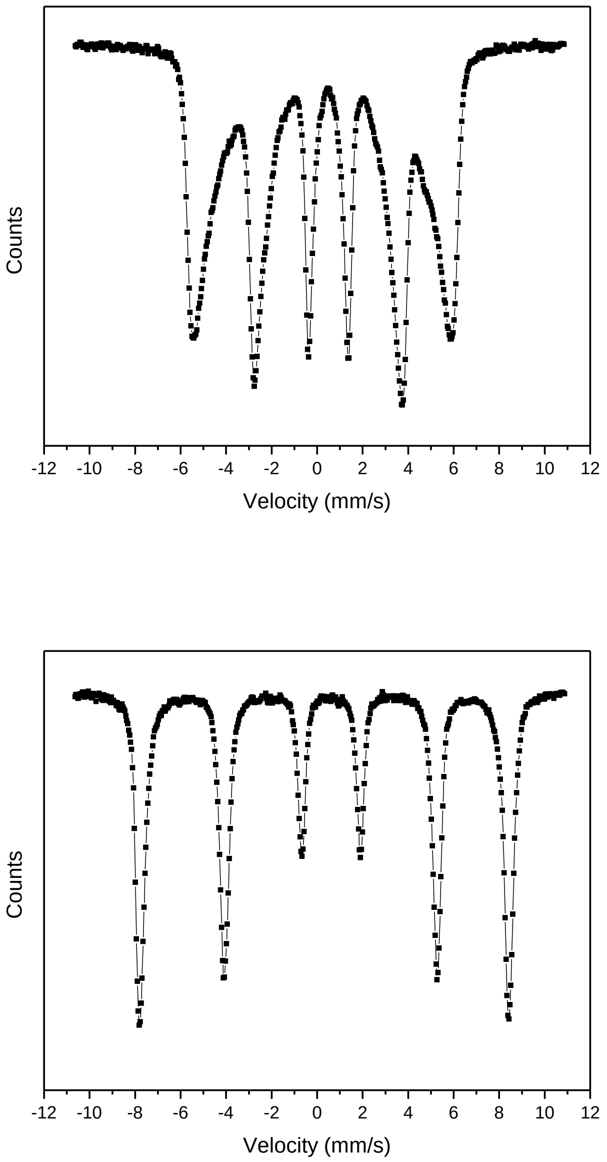

Figure F.14 Mössbauer spectra of Gt-5 at 300 K (top) and 4.2 K (bottom)

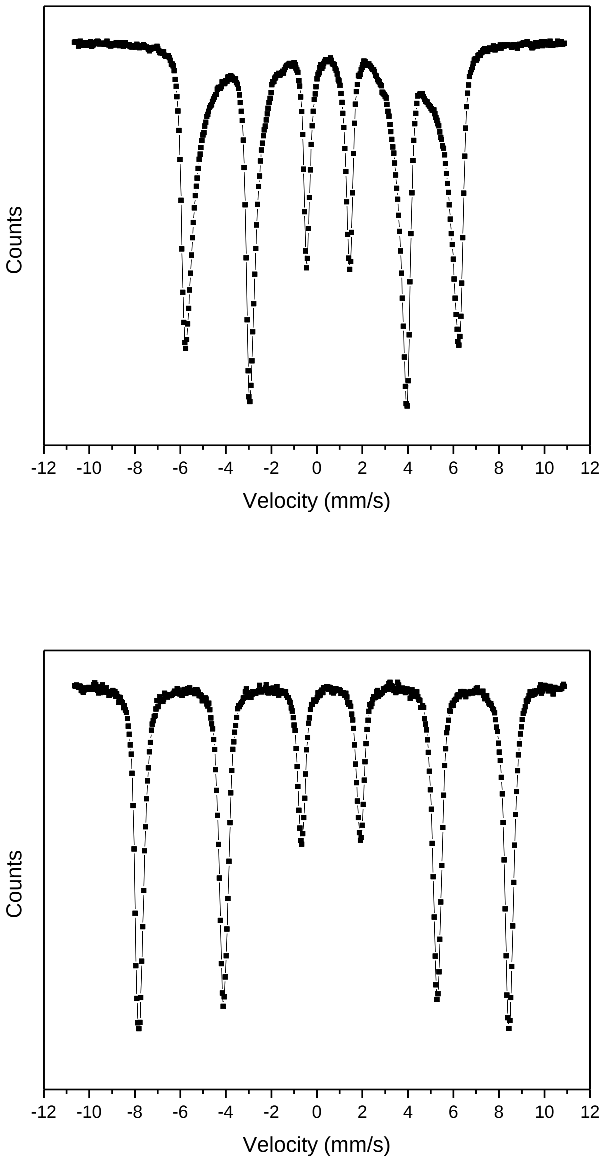

Figure F.15 Mössbauer spectra of Gt-6 at 300 K (top) and 4.2 K (bottom)

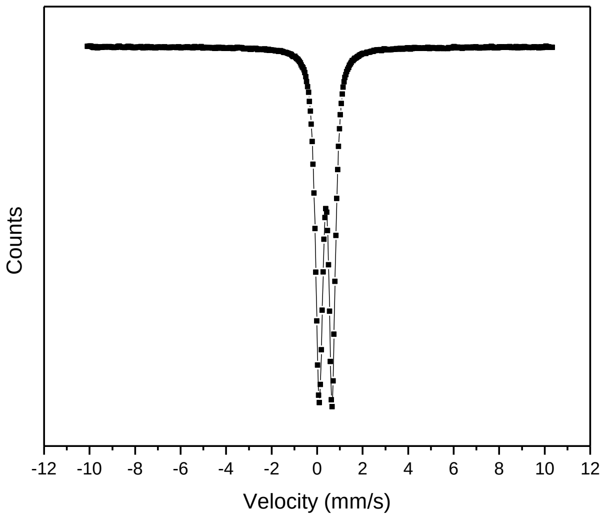

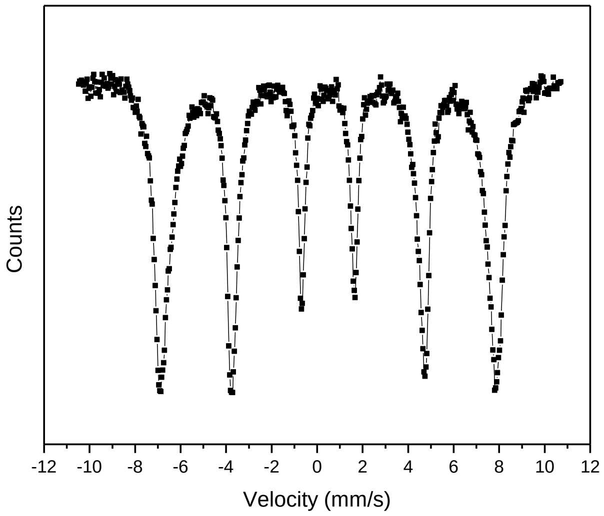

Figure F.16 Mössbauer spectra of Lp-1 at 300 K (top) and 4.2 K (bottom)

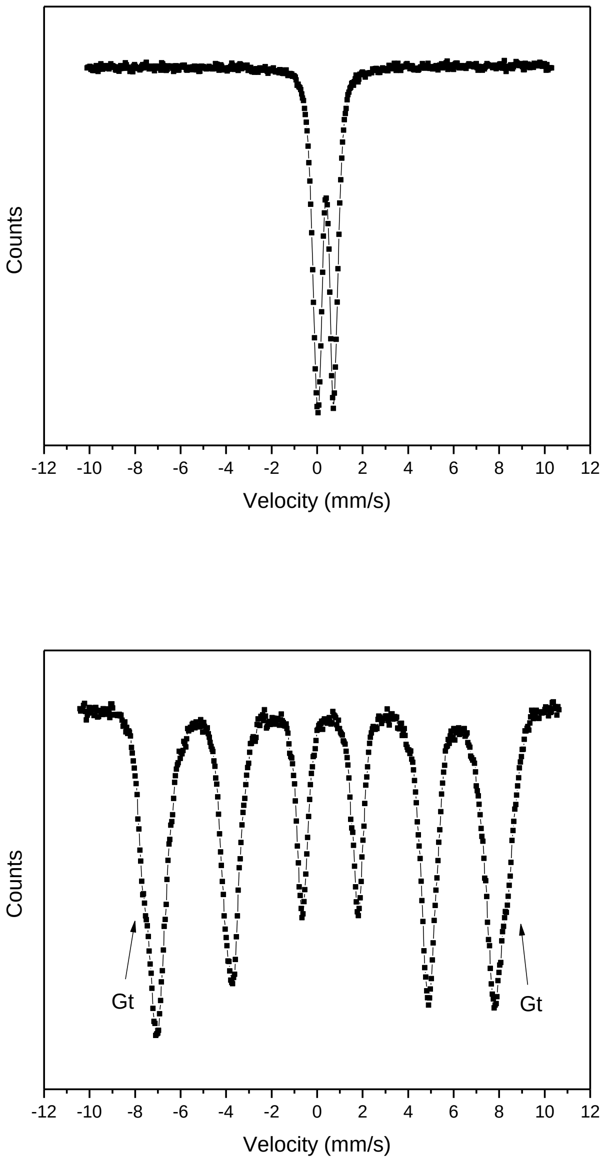

Figure F.17 Mössbauer spectra of Sw-1 at 300 K (top) 4.2 K (bottom) showing the contribution of the Gt impurity

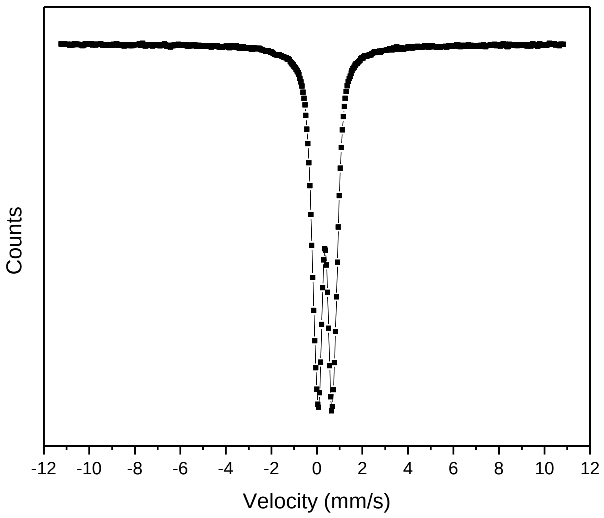

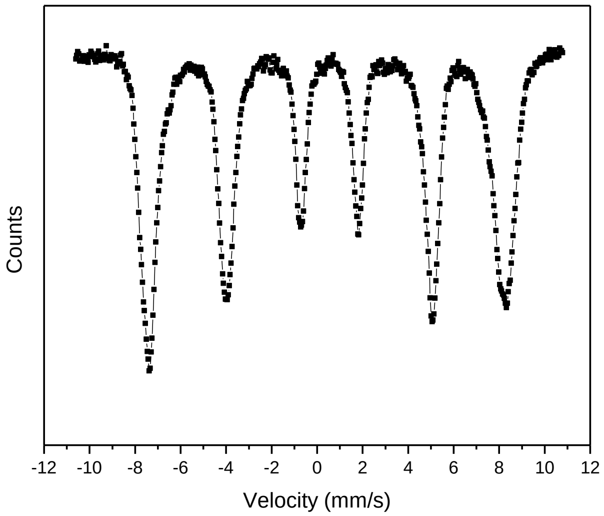

Figure F.18 Mössbauer spectra of Akg-1 at 300 K (top) and 4.2 K (bottom)

Appendix G – Iron Concentration

Table G.1 Iron weight percentage (Fe wt %) and derived number of Fe atoms per mass (N) estimated from the weight loss measurements

Sample name	Fe (wt %)	N (x 10^{24} Fe/kg)
2L-Fh	59.0 (3)	6.36 (3)
6L-Fh-1	60.8 (3)	6.56 (3)
6L-Fh-2	60.6 (5)	6.53 (5)
4L-Fh	58.8 (2)	6.34 (2)
P-HFO-0	54.791 (1)	5.9083 (1)
P-HFO-0.01	52.8 (2)	5.69 (2)
P-HFO-0.025	55.071 (1)	5.9385 (1)
P-HFO-0.05	52.160 (3)	5.6246 (3)
P-HFO-0.075	53.987 (3)	5.8216 (3)
P-HFO-0.1	56.016 (1)	6.0404 (1)
Gt-1	56.25 (7)	6.066 (8)
Gt-2	56.88 (8)	6.133 (9)
Gt-3	59.2 (1)	6.39 (1)
Gt-4	59.2 (2)	6.38 (2)
Gt-5	59.6 (1)	6.43 (9)
Gt-6	60.76 (8)	6.553 (9)
Lp-1	61.38 (2)	6.619 (2)
Lp-2	52 (1)	5.6 (1)
Sw-1	50.1 (2)	5.40 (2)
Sw-2	45.2 (5)	4.87 (5)
Akg-1	52 (1)	5.6 (1)
Akg-2	53.4 (1)	5.76 (1)